Magnetization Reversal in Cylindrical Nanowires and in Nanowires with Perpendicular Magnetic Anisotropy

Judith Kimling

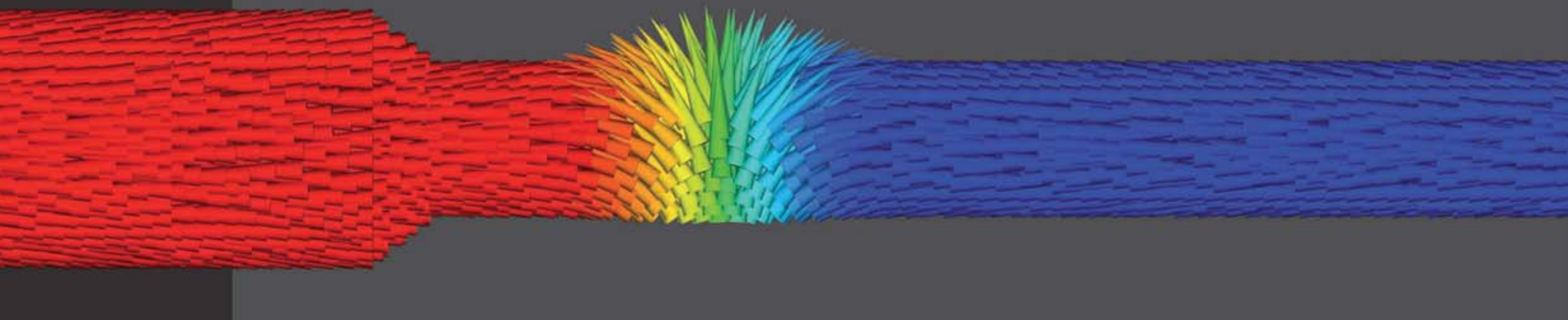

Cuvillier Verlag Göttingen
Internationaler wissenschaftlicher Fachverlag

Magnetization Reversal in Cylindrical Nanowires and in Nanowires with Perpendicular Magnetic Anisotropy

MAGNETIZATION REVERSAL IN CYLINDRICAL NANOWIRES AND IN NANOWIRES WITH PERPENDICULAR MAGNETIC ANISOTROPY

Dissertation

zur Erlangung des Doktorgrades

des Fachbereichs Physik

der Universität Hamburg

vorgelegt von

Judith Valentina Kimling
geb. Moser
aus
Ellwangen

Hamburg
2012

Bibliografische Information der Deutschen Nationalbibliothek
Die Deutsche Nationalbibliothek verzeichnet diese Publikation in der Deutschen Nationalbibliografie; detaillierte bibliografische Daten sind im Internet über **http://dnb.d-nb.de** abrufbar.
1. Aufl. - Göttingen: Cuvillier, 2013
Zugl.: Hamburg, Univ., Diss., 2012

ISBN 978-3-95404-518-1

Gutachter der Dissertation:	PD Dr. Guido Meier Prof. Dr. Manfred Albrecht
Gutachter der Disputation:	PD Dr. Guido Meier Prof. Dr. Kornelius Nielsch
Datum der Disputation:	14.12.2012
Vorsitzender des Prüfungsausschusses:	Dr. Stefan Mendach
Vorsitzender des Promotionsausschusses:	Prof. Dr. Peter Hauschildt
Dekan der MIN-Fakultät:	Prof. Dr. Heinrich Graener

Nonnenstieg 8, 37075 Göttingen
Telefon: 0551-54724-0
Telefax: 0551-54724-21
www.cuvillier.de

Gedruckt auf umweltfreundlichem, säurefreiem Papier aus nachhaltiger Forstwirtschaft.

Abstract

Deposition of magnetic materials in self-organized pores of an alumina membrane provides the unique ability to process large amounts of nanowires with complex shape and uniform properties. For both fundamental research and technological applications it is of interest to understand and control the magnetization reversal and the pinning of magnetic domain walls in so-prepared structures. The present work provides new insights into the magnetic behavior of electrochemically synthesized nanowires by applying established methods such as magnetoresistance measurements and magnetic force microscopy as well as a novel photoemission electron microscopy method developed at the synchrotron light source BESSY II in Berlin, Germany. Recording both the electrons emitted directly from the surface of a nanoobject as well as the ones bounced out of the substrate by the transmitted x rays in the object's shadow, surface and bulk magnetizations can be probed separately. The individual switching of two coaxial nanomagnets, namely an iron oxide tube and an enclosed nickel core, is successfully demonstrated.

Magnetization reversal of individual straight nickel wires with diameters between 40 nm and 350 nm is studied experimentally and by micromagnetic simulations performed with nmag. The results are analyzed by comparison to analytical models. For the preparation of domain walls in electrochemically synthesized nanowires three different methods are explored. While the manipulation with a focused Ga^+ ion beam rather decreases the nucleation field than induces pinning sites, reliable domain-wall preparation is shown in bent wires. A main focus of this work lies on magnetization reversal in cylindrical wires with one or more diameter modulations. It is found that domain walls stop their propagation when approaching a modulation from a thin towards a thicker segment. A model based on magnetic charges is proposed that accounts for the experimentally observed behavior and predicts what is also confirmed by micromagnetic simulations: while the exact shape of a modulation is of minor importance, the force experienced by a domain wall and thereby the pinning potential can be tuned by changing the aspect ratio of a modulation.

The last part of this thesis reports on domain nucleation and pinning of domain walls in flat nanowires with perpendicular magnetic anisotropy patterned by electron-beam lithography, sputter deposition of a Co/Pt multilayer, and lift-off processing. Magnetization reversal was imaged by transmission X-ray microscopy at the Advanced Light Source in Berkeley, CA, USA. It is found that the nucleation field in Co/Pt wires can be tuned and reduced by up to 60 percent by designing triangular-pointed ends. In order to clarify the origin of the reduction of the nucleation field micromagnetic simulations are employed. The effect cannot be explained by the geometry variation alone, but is attributable to a local reduction of the perpendicular anisotropy caused by shadowing of the resist mask during sputter deposition of the multilayer. Related aspects concerning the creation of pinning sites for domain walls are addressed.

Zusammenfassung

Die vorliegende Arbeit gewährt neue Einblicke in das magnetische Verhalten elektrochemisch synthetisierter Nanodrähte. Hierfür werden sowohl etablierte Methoden wie Magnetowiderstandsmessungen und magnetische Rasterkraftmikroskopie als auch ein im Rahmen dieser Arbeit neu entwickeltes Verfahren zur Untersuchung komplexer magnetischer Strukturen angewendet. Letzteres nutzt die Strahlenquelle des Berliner Elektronen Synchrotrons BESSY II und basiert auf der konventionell nur oberflächensensitiven Photoemissions-Elektronenmikroskopie. Es werden sowohl die Photoelektronen detektiert, die direkt aus der Oberfläche eines Nanoobjekts emittiert werden, als auch diejenigen, die von den das Objekt durchdringenden Röntgenstrahlen im Schatten des Objekts aus dem Substrat ausgeschlagen werden. Dadurch gelingt es, Bilder der gesamten Magnetisierung, also von der Oberfläche und aus dem Inneren der Nanostruktur, aufzunehmen. Das Potential der Methode wird durch die Untersuchung von Eisenoxidröhren, die einen Nickel-Kern enthalten, demonstriert. Dabei lässt sich individuelles Schalten der beiden koaxialen Nanomagnete nachweisen.

Darüberhinaus beschäftigt sich die Arbeit sowohl experimentell als auch in mikromagnetischen Simulationen mit den Ummagnetisierungsvorgängen einzelner gerader Nickel-Nanodrähte mit Durchmessern zwischen 40 nm und 350 nm. Die Ergebnisse werden unter anderem anhand analytischer Modelle interpretiert. Für die Präparation von Domänenwänden in elektrochemisch synthetisierten Nanodrähten werden drei verschiedene Methoden erprobt. Während die Manipulation mit einem fokussierten Gallium-Ionenstrahl eher das Nukleationsfeld um circa 10 Prozent verringert, als Pinningzentren zu kreieren, gelingt es durch das Anlegen externer Magnetfelder zuverlässige Domänenwandpräparation in geknickten Drähten zu demonstrieren. Ein Schwerpunkt liegt auf der Untersuchung zylindrischer Drähte mit einer oder mehreren Durchmessermodulationen. Es wird gezeigt, dass Domänenwände stoppen, wenn sie von einem dünnen Segment aus auf die Modulation zu einem dickeren Segment hin zulaufen. Zur Erklärung des experimentell beobachteten Verhaltens wird ein Modell aufgestellt, welches auf magnetischen Ladungen beruht und zudem mikromagnetische Simulationen bestätigt: während die genaue Form einer Modulation nur eine untergeordnete Rolle spielt, kann die von der Domänenwand erfahrene Kraft durch das Aspektverhältnis der Modulation eingestellt werden.

Der letzte Abschnitt der vorliegenden Arbeit beschäftigt sich mit der Nukleation und dem Pinnen von Domänenwänden in lithographisch hergestellten Co/Pt-Multischichtdrähten mit senkrechter Anisotropie. Mittels Transmissions-Röntgenmikroskopie an der Advanced Light Source in Berkeley (USA) wird gezeigt, dass das Feld, bei dem Domänenwände in einen Draht injiziert werden, justiert und um bis zu 60 Prozent reduziert werden kann, indem man Drähte mit spitzen Enden herstellt. Mikromagnetische Simulationen belegen, dass die Verringerung dieses Nukleationsfeldes nicht durch die geometrische Variation allein erklärbar ist, sondern sich auf eine Verminderung der lokalen senkrechten Anisotropie zurückführen lässt. Für letztere wiederum sind präparationsbedingte Abschattungseffekte verantwortlich.

Contents

1 Introduction

The performance of magnetic nanostructures is determined by their precisely engineered design and material properties. Therefore, their detailed inspection is indispensable prior to sensitive applications in many fields that range from local drug delivery or hyperthermia tumor treatment [Pan03] to high-density information storage [Ter05]. One focus of this work lies on establishing a novel x-ray method based on conventionally surface-sensitive photoemission electron microscopy that allows for the element-specific magnetic imaging of composite nanostructures as well as for the separate imaging of surface and bulk contributions [Kim11]. In particular in the field of magnetic data storage, industrial progress and underlying research have been exceptionally close ever since. Reaching fundamental limits such as superparamagnetism of down-scaled bits and unaddressability of non-perfect self-organized structures demands completely new concepts. In this respect, the so-called racetrack memory was proposed [Par05, Par08]. This non-volatile shift register is based on the effect that domain walls can be displaced by spin-polarized currents [Ber84, Klä03a, Tho07]. Franken *et al.* recently demonstrated a comparable concept based on field-driven domain-wall motion [Fra12c]. The precondition for the realization of such shift registers is to understand and control the pinning and the simultaneous propagation of domain walls in a periodic potential. Other promising applications basing on domain-wall motion are logic devices [All05] and lab-on-chip devices where microbeads trapped in the stray-fields of domain walls are employed for the directed transportation of biomolecules and cells [Bry10, Rap12]. Systematic studies of field- and current-driven domain-wall dynamics are prerequisites for the realization of the above mentioned devices. These studies require the reliable preparation of domain walls. Since high current densities can change or destroy the structures investigated, weak pinning potentials allowing for the depinning of domain walls at low current densities are desirable. It is decisive for the preparation of a domain wall at such pinning sites, that the domain wall is injected into a wire at fields smaller than the field required to depin the domain wall from the respective pinning site.

The perspective of this work is to find reliable methods for the preparation of domain walls in two different kinds of ferromagnetic nanostructures, namely lithographically patterned wires of Co/Pt multilayers with perpendicular magnetic anisotropy and electrochemically synthesized nickel and nickel-iron wires. Both systems are among the most promising candidates for novel devices that are based on the propagation of domain walls. Furthermore, they can serve as model systems for fundamental studies.

Systems with high uniaxial out-of-plane anisotropy as Co/Pt multilayers are characterized by comparably small domain-wall widths. Thus, they allow for higher storage density compared to in-plane magnetized materials. It has been shown both theoretically [Tat04, Xia06] and experimentally [Bou08, Alv10] that the non-adiabatic spin transfer, an effect that increases with decreasing domain-wall width, contributes to the efficiency of current-driven domain-wall motion. Another advantage of systems with high perpendicular magnetic anisotropy is that one-dimensional models can be applied to analyze their domain walls, which exhibit nearly perfect Bloch or Néel spin structures [Bou11], whereas in soft-magnetic wires with a stray-field driven in-plane magnetization complex two-dimensional spin structures with intrinsic degrees of freedom occur [Hay06b]. The simple domain-wall structure is also the reason why for example Co/Pt layered structures with out-of-plane anisotropy are frequently used to investigate the intrinsic domain wall resistance [Has06, Azi06, Fra12b]. Furthermore, for Bloch walls in perpendicularly magnetized wires the domain-wall resistance is not masked by contributions of the anisotropic magnetoresistance as the magnetization is orthogonal to the current direction everywhere.

Anodization of aluminum templates allows for the creation of pores with modulated diameters [Lee06]. The pores can be covered by atomic-layer deposition or filled by electrochemical deposition to synthesize complex three-dimensional nanostructures replicating the variations of the pore diameter [Pit09, Cho10, Pit11]. The possibility of cheap mass production of uniform particles with diameters down to a about 20 nm and aspect ratios up to 1000 makes this synthesis approach highly attractive for technological applications. It has been predicted that domain walls in cylindrical nanowires can act as massless objects [Yan10]. This implies that there is no Walker breakdown restricting the domain-wall velocity, and accordingly no fundamental limit for the performance of devices that are based on the fast movement of domain walls. Another aspect that is of interest for such applications is that there exists no threshold current for the displacement of massless domain walls. Soft-magnetic cylindrical wires are often declared as model systems for numerical simulations and analytical calculations based on infinite cylinders [Aha97a]. The validity of this approach is critically discussed in this work.

This thesis is structured as follows: chapter 2 gives an overview of the underlying physics. Section 2.1 focuses on the fundamentals of ferromagnetism including domain-wall theory. Section 2.2 deals with the preparation, depinning, and motion of domain walls in ferromagnetic nanowires. Introductions to magnetoresistive effects and to the x-ray magnetic circular dichroism (XMCD) effect, which is the basis of magnetic imaging using polarized x rays, follow in Secs. 2.3 and 2.4. Chapters 3 through 6 are dedicated to cylindrical nanowires. Chapter 3 gives an introduction to micromagnetic simulations and presents some results to illustrate the influence different energies have on the magnetic behavior of nanostructures. The synthesis of cylindrical nanowires as well as the methods employed for their characterization, namely magnetoresistance measurements, magnetic force microscopy, and photoemission electron microscopy, are presented in chapter 4. Section 4.4 includes publication [Kim11] dealing with photoemission electron microscopy of three-dimensional magnetization configurations in core-shell nanostructures. Chapter 5 covers the results on straight nickel wires which are analyzed on the basis of the analytical curling model and micromagnetic simulations. The feasibility of controlled domain-wall preparation in wires manipulated with a focused ion beam, in bent wires, and in wires with diameter modulations serving as tailored pinning sites is the subject matter of chapter 6. Experimental aspects and results on Co/Pt multilayer wires are presented in chapter 7 that includes publication [Kim13]. Additional details on the sample preparation and magnetic imaging by transmission x-ray microscopy are given in the Appendix Secs. B.3 and B.6, respectively. The work closes with a conclusion in chapter 8.

2 Fundamentals

In this work, magnetization reversal in two different kinds of ferromagnetic nanostructures, namely cylindrical nanowires and flat wires of Co/Pt multilayers, is studied. This chapter gives an overview of the underlying physics. The first section starts with the fundamentals of ferromagnetism and domain theory. Subsections 2.1.5 and 2.1.6 discuss the Stoner-Wohlfarth model of coherent rotation and the curling model, two models for the analytical treatment of magnetization reversal. The section closes with an introduction to micromagnetism, the basis for micromagnetic simulations. Section 2.2 deals with the preparation, depinning, and motion of domain walls in ferromagnetic nanowires. An introduction to spin-dependent transport and a phenomenological overview of magnetoresistive effects follows in Sec. 2.3. In Sec. 2.4 the x-ray magnetic circular dichroism (XMCD) effect, which is the basis of magnetic imaging using polarized x rays, is explained.

2.1 Ferromagnetism

Magnetism has been an active field of study for more than 2 500 years [Stö06]. Many theoretical and experimental approaches have generated a variety of definitions and concepts. Addressing all exciting aspects of the topic lies beyond the scope of this work. This section is limited to the basics and to the aspects directly related to this work: the microscopic origin of ferromagnetism, vector fields used for its description, as well as energy considerations and reversal modes regarding the formation of ferromagnetic patterns, so-called domains.

2.1.1 Origin of ferromagnetism

In a free atom, there are three origins of a magnetic moment: the spin of the electron, the orbital angular momentum of the electron with respect to the movement around the core, and changes of the orbital angular momentum induced by an external magnetic field [Spa11]. The latter leads to diamagnetism, while the other two aspects are the sources of paramagnetism. Some paramagnetic materials show a phase transition at the so-called Curie temperature. Below this temperature cooperative magnetic ordering appears, and the material is ferromagnetic. Classical magnetic dipole-dipole interactions between adjacent ions are not strong enough to account for such a spontaneous magnetization, since ordering is easily destroyed by thermal fluctuations at temperatures above a few millikelvin [Kop07]. The orientation of the magnetic moments in a ferromagnet is a quantum-mechanical phenomenon [Blu01]. The basic interaction is the exchange interaction. The Hamiltonian considering the exchange energy between two fermionic particles with spins $\vec{S_i}$ and $\vec{S_j}$ is given by [Whi07]

$$\hat{H}_{\mathrm{ex}} = -2J\vec{S_i} \cdot \vec{S_j}. \tag{2.1}$$

J is the coupling constant depending on the difference between the symmetric and the antisymmetric product state of the single-particle wavefunctions. This Hamiltonian is the basis of some fundamental models for the description of ferromagnetic behavior. The most popular of these models is the **Heisenberg model** where the interaction between the individual spins in a three-dimensional lattice is described by the Heisenberg Hamiltonian

$$\hat{H} = -\sum_{i \neq j} J_{ij}\vec{S_i} \cdot \vec{S_j} \tag{2.2}$$

with the exchange integral $J_{ij} = \int\int \psi_i(\vec{r}_1)\psi_j(\vec{r}_2)\frac{e^2}{4\pi\epsilon_0 r_{12}}\psi_i^*(\vec{r}_2)\psi_j^*(\vec{r}_1)d\vec{r}_1 d\vec{r}_2$ [Hei28]. ψ_{ij} are the single-particle wavefunctions, $\epsilon_0 \cong 8.854 \cdot 10^{-12}\,\frac{\mathrm{As}}{\mathrm{Vm}}$ is the permittivity of vacuum, and $e \cong 1.602 \cdot 10^{-19}$ C is the elementary charge.

If J is positive the system prefers parallel spin orientation and the material is ferromagnetic. For negative J antiparallel alignment is favored and the material shows an antiferromagnetic spin structure. Only in few materials the exchange interaction is strong enough to force an alignment of adjacent spins. If there is no overlap of the electron wave functions the Hamiltonian is zero and magnetic ordering cannot be explained by direct exchange interaction [Stö06]. Indirect exchange interaction can be mediated by a diamagnetic ion between two magnetic ions, e.g. manganese oxide, or via excited states, e.g. europium oxide [Mat61]. Another type of indirect exchange is the Ruderman-Kittel-Kasuya-Yoshida (RKKY) interaction [Rud54]. This long-range interaction is caused by the coupling of the magnetic moments of well-shielded, low lying shells to the conduction electrons. It shows an oscillatory behavior depending on the distance between two ions [Nol86]. The RKKY interaction is responsible for the coupling between magnetic layers, the basis of giant magnetoresistance (GMR).

In the $3d$ transition metals iron, cobalt, and nickel as well as in their alloys, the main exchange interaction is mediated by the conduction electrons. The origin of ferromagnetic order in such systems can be described by the **Stoner model of ferromagnetism**, which incorporates the exchange interaction into the itinerant electron model [Sto38]. The model considers the density of states $D(E)$ as consisting of two subbands $D_\uparrow(E)$ and $D_\downarrow(E)$ for electrons with spin up and spin down, respectively.

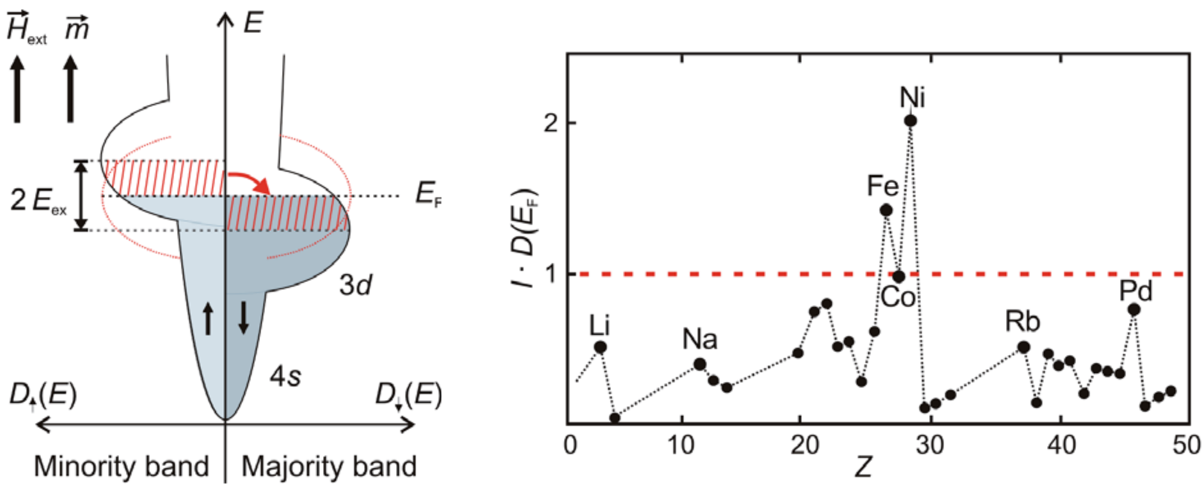

(a) (b)

Figure 2.1: (a) Schematic of the spin-projected density of states of a $3d$ transition metal. Due to the exchange interaction the energy of the $3d$ electrons with a spin orientation antiparallel to the direction of an external field $\vec{H}_{\mathrm{ext}}$ is lower by the exchange splitting $2\,E_{\mathrm{ex}}$ what leads to a population change as indicated by the red shaded regions. The gray areas mark the resulting filled electron states below the Fermi energy E_{F}. The band with the larger amount of electrons with spin down is called 'majority band', while the other one is referred to as 'minority band' carrying the minority electrons. (b) Product of the density of states at the Fermi level $D(E_{\mathrm{F}})$ and exchange integral I as a function of the atomic number Z. If the Stoner criterion $I \cdot D(E_{\mathrm{F}}) \geq 1$ is fulfilled, a metal is ferromagnetic. After [Iba99].

In the presence of a magnetic field the degeneracy of electrons with opposite spin orientation is lifted and the two subbands get shifted by $\pm E_{\mathrm{ex}}$. Electrons change from one subband to the other as indicated by the red shaded areas in Fig. 2.1(a). The increase in kinetic energy pays off by the energy reduction due to exchange interaction. The resulting difference in the number of electrons with spin up and spin down, also referred to as 'minority' and 'majority' electrons, leads to an effective magnetic moment $\vec{m}$. This magnetic moment is not necessarily an integer multiple of the Bohr magneton[1], as it is observed in iron (2.2 μ_{B}/atom), cobalt (1.7 μ_{B}/atom), and nickel (0.6 μ_{B}/atom)[O'H00]. The model predicts a ferromagnetic ordering if the **Stoner criterion**

$$I \cdot D(E_{\mathrm{F}}) \geq 1 \tag{2.3}$$

is fulfilled [Sto38]. I is an exchange integral, and $D(E_{\mathrm{F}})$ is the density of states at the Fermi level.

---

[1] The Bohr magneton is defined as $\mu_{\mathrm{B}} = \frac{e\hbar}{2m_{\mathrm{e}}} \cong 9.27 \cdot 10^{-24}\,\mathrm{Am}^2$. $m_{\mathrm{e}} \cong 9.109 \cdot 10^{-31}$ kg is the electron mass, $\hbar$ is Planck's constant divided by 2π.

In Fig. 2.1(b) the product $D(E_\mathrm{F}) \cdot I$ is plotted for some materials. The $3d$ transition metals iron (Fe), cobalt (Co), and nickel (Ni) are ferromagnetic as predicted by the Stoner criterion. While I is element specific and not depending on the local environment, $D(E_\mathrm{F})$ is influenced by adjacent ions. Atoms at interfaces have less neighbors, i.e. the coordination number is decreased. As a consequence the $3d$ band carrying the magnetic moment gets narrower and tends to the bandstructure of a free atom [Bob04]. The bandwidth is inversely proportional to the density of states at the Fermi level. That is why more metals satisfy the Stoner criterion if surface effects come into play. Palladium (Pd) and platinum (Pt) for example can be ferromagnetic if they are prepared as thin films [Blü95].

2.1.2 Magnetic anisotropy

Anisotropy means that a physical property is a function of direction. The spontaneous magnetization of a ferromagnet is not oriented arbitrarily but aligned along preferential directions, the so-called easy axes (EA). Without this anisotropy magnetic order could hardly be observed, especially in two dimensional systems such as thin films [Bla94]. The reason for this is the short-range character of the exchange interaction. Magnetic anisotropy is usually caused by different contributions made up of surface and volume parts. The individual contributions are discussed below.

Surface and interface anisotropy originate from missing neighbors. At interfaces the overlap of the electron shells is reduced. This modifies the exchange energy and results in an anisotropic magnetization behavior [Cho69].

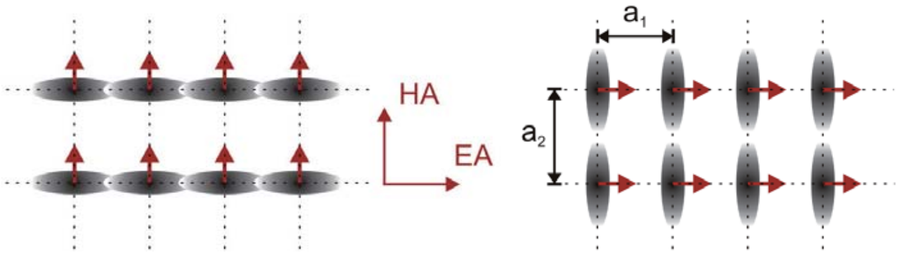

(a) (b)

Figure 2.2: Microscopic origin of magnetocrystalline anisotropy. The gray shaded ellipses represent non-spherical charge distributions caused by spin-orbit interaction. In a cubic crystal with two different lattice constants a_1 and $a_2 > a_1$ the overlap of electron shells varies depending on the orientation of the associated magnetic moments indicated by the red arrows. For a hard axis (HA) magnetization the overlap is large (a), while for a magnetization along the easy axis (EA) the overlap and the concomitant exchange and electrostatic energy are reduced (b). After [Kit05].

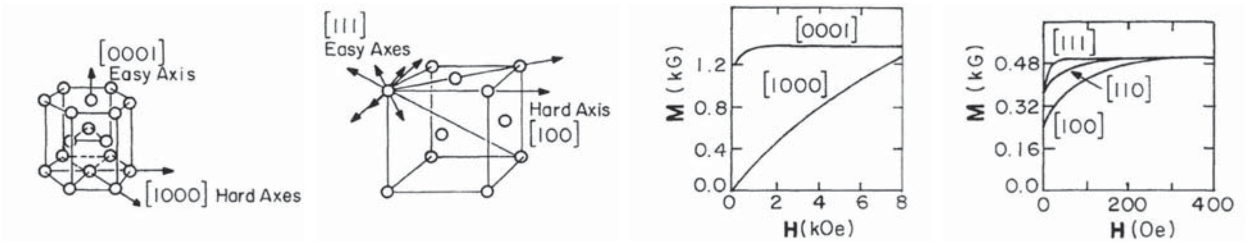

(a) (b) (c) (d)

Figure 2.3: (a) Hexagonal lattice structure of cobalt. (b) Face-centered cubic (fcc) structure of nickel. Magnetization versus field curves of (c) cobalt and (d) nickel for an external magnetic field H applied along different crystal axes. Reprinted with permission from [O'H00]. Copyright 2000 by John Wiley and Sons.

The volume anisotropy has several origins. **Magnetocrystalline anisotropy** reflects the symmetry of the crystal lattice [Kit49]. Its microscopic origin is illustrated in Fig. 2.2. The electron distribution of an atom is coupled to the spin direction. It is not always spherical but can be deformed by spin-orbit interaction. If in addition the crystal field seen by an atom is of low symmetry, an anisotropic interaction of the electron shells with the crystal field can be observed. Phenomenologically the magnetocrystalline anisotropy is defined as the largest difference of spin-orbit energy for a sample magnetized along two different directions. For strong spin-orbit interaction and anisotropic crystal fields as they are typical for rare-earth metals, the magnetocrystalline anisotropy is high [Bré07]. If the coupling of the orbital angular momentum to the lattice is stronger than the spin-orbit coupling, a rather weak magnetocrystalline anisotropy is observed. The latter is generally the case in $3d$ transition metals. Nevertheless, magnetocrystalline anisotropy can play a role in these materials, and shall be discussed for cobalt and nickel in the following.

Figure 2.3 shows the crystal structures of cobalt and nickel as well as their magnetization versus field curves[2] along different crystal axes. The hexagonal crystal structure of cobalt results in a uniaxial magnetocrystalline anisotropy with an easy axis along the c axis (<0001> direction). As revealed by the magnetization curves in Fig. 2.3(c) high external fields are required to align the magnetic moments of cobalt parallel to the basal plane. The magnetic field required to saturate the magnetization of a sample along a hard axis is called anisotropy field H_a. It is a quantitative measure for the strength of the magnetocrystalline anisotropy.

In systems with one preferred direction as cobalt or thin films with uniaxial magnetic anisotropy, the anisotropy energy density is given by [Hub09]

$$\epsilon_{\mathrm{uniaxial}} = K_{\mathrm{u1}} \sin^2 \theta + K_{\mathrm{u2}} \sin^4 \theta + ... \tag{2.4}$$

---

[2] Magnetization curves are discussed in more detail in the respective paragraph of Sec. 2.1.4.

where θ is the angle between the magnetization direction and the easy axis. K_{u1} and K_{u2} are the anisotropy constants. At room temperature only the lowest order terms of the energy densities have to be considered, since contributions of higher orders are averaged out by thermal excitations.

Nickel usually crystallizes in a face centered cubic (fcc) structure as shown in Fig. 2.3(b). Like iron and permalloy nickel has a cubic anisotropy which in bulk is described by the energy density

$$\epsilon_{\mathrm{cubic}} = K_{\mathrm{c1}}(\alpha_1^2\alpha_2^2 + \alpha_2^2\alpha_3^2 + \alpha_3^2\alpha_1^2) + K_{\mathrm{c2}}(\alpha_1^2\alpha_2^2\alpha_3^2) + \dots \, . \tag{2.5}$$

α_j are the direction cosine of the magnetization with respect to the cubic axes. The anisotropy constants of selected materials are listed in Table 2.1 together with some other material constants.

To get an impression of the influence of the magnetocrystalline anisotropy on the magnetic behavior let us consider a spherical sample of nickel saturated along the hard axis [100]. Figure 2.3(d) depicts the corresponding magnetization curve. If the applied field H is reduced below the anisotropy field of about 23 mT, the magnetization starts to rotate away from the hard axis, either toward the adjacent <110> directions or to one of the four nearest <111> directions. Only if H is decreased below 15 mT the magnetization steadily rotates toward one of the four easy axes in <111> direction with positive components along [100] to minimize the energy. When H is reduced to zero, all moments lie in <111> directions. This leads to a remanent magnetization of about $1/\sqrt{3}$ of the saturation magnetization M_{s} [O'H00].

All anisotropy contributions mentioned so far can somehow depend on **magneto-elastic effects** which are negligible in most cases when it comes to domain theory. In cubic crystals such as nickel one of them, namely magnetostriction, can play a role [Lee71]. Magnetostriction means the deformation of a ferromagnet during the magnetization process [Hor71]. It is related to the magnetocrystalline anisotropy since it also originates from spin-orbit interactions. The inverse magnetostrictive effect gives rise to a stress sensibility of magnetic materials that can influence the

Material	Co	Ni	Fe	$Ni_{80}Fe_{20}$	Fe_3O_4
Structure	hcp	fcc	bcc	fcc	spinel
Exchange stiffness A (10^{-11}J/m)	1.3	1.0	2.5	1.3	1.0
Saturation magnetization M_{s} (10^6 A/m)	1.44	0.483	1.71	0.8	0.48
Anisotropy constant K_1 (10^4J/m^3)	41	-0.45	4.8	-0.03	-0.9
Anisotropy constant K_2 (10^4J/m^3)	15	-0.23	-1.0	-	-

Table 2.1: Fundamental magnetic data at room temperature [Sch91, O'H00, Gol03].

domain structure. In systems with high uniaxial anisotropy domains are magnetized parallel to each other, and their deformations are identical. Magneto-elastic energy only appears in the domain walls, but it is usually negligible compared to the other energy contributions [Hub09].

The total anisotropy energy of a sample is given by

$$E_{\text{anisotropy}} = \sum_i \int \epsilon_i(\vec{m}(\vec{r}))d^3r. \tag{2.6}$$

The summation over i indicates that depending on the sample energy densities ϵ_i of different origin have to be considered. Contributions of the **shape anisotropy** which originates from long-range dipole-dipole interactions [Stö06] are not contained in this energy term. They are accounted for by the stray-field energy discussed later.

The effective anisotropy constant K_{eff} of a thin film includes contributions of the surface anisotropy K_{S} and the volume anisotropy K_{V}. Under the convention that $\frac{K_{\text{S}}}{t}$ represents the difference between the anisotropy of the interface atoms with respect to the bulk atoms, K_{eff} is given by

$$K_{\text{eff}} = K_{\text{V}} + \frac{2K_{\text{S}}}{t}, \tag{2.7}$$

where t is the layer thickness [Joh96]. Figure 2.4 shows how the easy axis of a Co/Pd multilayer stack changes from in-plane to out-of-plane with increasing thickness t of the ferromagnetic cobalt layer.

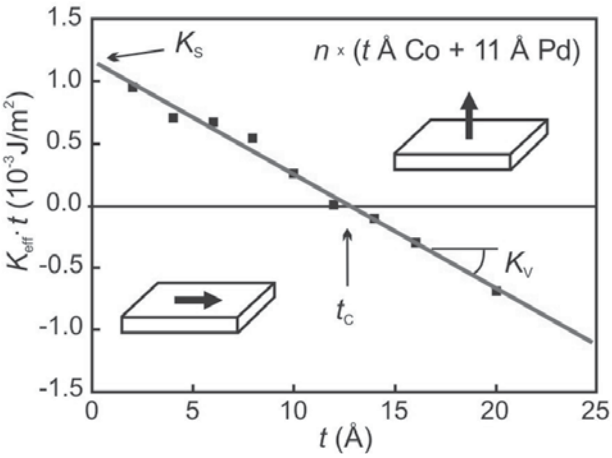

Figure 2.4: Dependence of the magnetic anisotropy energy on the cobalt layer thickness t in a Co/Pd multilayer film studied by den Broeder *et al.* [Bro91]. While the surface anisotropy K_{S} favors a magnetization perpendicular to the interfaces, the volume anisotropy K_{V} tends to pull the easy axis in the plane. Depending on t different anisotropy contributions are dominant [Cho69].

2.1.3 Vector fields for the macroscopic description

For the macroscopic description of ferromagnetism the spins or microscopic moments $\vec{m}$ are replaced by a vector field $\vec{M} = M_{\mathrm{s}}\vec{m}(\vec{r})$ where $|\vec{m}(\vec{r})|^2 = 1$. This magnetization $\vec{M}$ of a solid is defined as the magnetic moment per volume and measured in units of $[\frac{\mathrm{A}}{\mathrm{m}}]$. The relation between the magnetization and the strength of an external magnetic field $\vec{H}$ is given by the magnetic susceptibility χ:

$$\vec{M} = \chi\vec{H}. \tag{2.8}$$

Since the response of a magnetic material can depend on the direction of the applied magnetic field, χ is a tensor. The origins of this anisotropy were discussed in Sec. 2.1.2. A material is ferromagnetic if $|\chi| >> 1$. The spontaneous magnetization of a ferromagnet usually does not vanish in the absence of an external magnetic field. This means the susceptibility χ is not constant but depends on the magnetic history. Such a behavior is called hysteretic. If $|\chi| > 0$ and the magnetization is only stable in the presence of an external field, a material is paramagnetic. In diamagnetic materials ($|\chi| < 0$) the induced magnetization reduces the effective field inside the solid. The magnetic induction $\vec{B}$ is related to $\vec{H}$ via the permeability constant $\mu_0 = 4\pi \cdot 10^{-7}\frac{\mathrm{Vs}}{\mathrm{Am}}$:

$$\vec{B} = \mu_0(\vec{H} + \vec{M}) = \mu_0(1 + \chi)\vec{H} = \mu_0\mu_{\mathrm{r}}\vec{H}. \tag{2.9}$$

The permeability $\mu_{\mathrm{r}} = (1 + \chi)$ is a material parameter which in vacuum is equal to one. From Maxwell's equation

$$\vec{\nabla} \cdot \vec{B} = 0 \tag{2.10}$$

and Gauss' theorem $\int\int\int \vec{\nabla} \cdot \vec{B}\ dV = \int\int \vec{B} \cdot \vec{n}\ dS$ we know that the total flux of magnetic induction through a closed surface with normal vector $\vec{n}$ is zero. This means that there are no magnetic monopoles acting as sources of magnetic flux [Stö06]. Combining equation 2.9 and 2.10 one can derive

$$\vec{\nabla} \cdot \vec{M} = -\vec{\nabla}(\mu_0\vec{H}) \tag{2.11}$$

to define a magnetic stray field. The sinks and sources of the magnetization $\vec{M}$ can be considered as magnetic charges generating the stray field $\vec{H}_{\mathrm{s}}$ surrounding a ferromagnet. Since $\vec{\nabla} \cdot \vec{M}$ is not defined at the surface, magnetic surface charges are described by [Mil07]

$$\sigma = \vec{M} \cdot \vec{n}. \tag{2.12}$$

Inside the material the field created by magnetic charges is often called demagnetization field $\vec{H}_{\mathrm{demag}}$. It is typically aligned antiparallel to the magnetization $\vec{M}$.

2.1.4 Domain theory

A ferromagnet is usually not magnetized homogeneously but consists of several domains. Domains are regions of uniform magnetization. They are separated by domain walls, regions where the magnetization direction changes gradually. The origin of domains can be understood considering the structures illustrated in Fig. 2.5. A uniformly magnetized body and the surrounding stray field $\vec{H}_\mathrm{s}$ are drafted in Fig. 2.5(a). The **stray-field energy** is given by

$$E_\mathrm{strayfield} = \frac{1}{2}\mu_0 \int \vec{H}_\mathrm{s}^2 d^3r. \tag{2.13}$$

It can also be expressed as the potential energy of the magnetic moments in the demagnetization field $\vec{H}_\mathrm{demag}$ inside the sample:

$$E_\mathrm{demag} = -\frac{1}{2}\mu_0 M_\mathrm{s} \int \vec{m}(\vec{r}) \cdot \vec{H}_\mathrm{demag}(\vec{r}) d^3r. \tag{2.14}$$

The stray-field energy can be reduced by the formation of ferromagnetic domains. If a part of the magnetization is rotated as illustrated in Fig. 2.5(b), the stray field is decreased. On the other hand a gradient in the magnetization as it occurs in the domain wall (dotted line) leads to an increase of the **exchange energy** that can be approximated by

$$E_\mathrm{ex} = A \int \left[(\vec{\nabla} m_x)^2 + (\vec{\nabla} m_y)^2 + (\vec{\nabla} m_z)^2 \right] d^3r. \tag{2.15}$$

A is a material constant called exchange stiffness which is proportional to the exchange integral. The process illustrated in Figs. 2.5 (a) through (c) energetically pays out until the energy cost to form another domain wall exceeds the gain in stray-field energy. By the formation of closure domains as shown in Fig. 2.5(d) the stray field can nearly be reduced to zero.

The actual domain configuration in a sample is the consequence of an interplay of multiple energy contributions. Besides the often dominant stray-field energy and the exchange energy additional energy terms have to be considered. One of them is the **anisotropy energy** which was already addressed in Sec. 2.1.2. It considers the dependence of the energy of a ferromagnet on the angle between the magnetization and the structural axes of the material. If a sample is exposed to an external magnetic field the potential energy of the magnetic moments has to be considered. It is given by their orientation relative to the external field $\vec{H}_\mathrm{ext}$ and described by the **Zeeman energy**

$$E_\mathrm{Zeeman} = -\mu_0 \int \vec{M} \cdot \vec{H}_\mathrm{ext} d^3r = -\mu_0 M_\mathrm{s} \int \vec{m}(\vec{r}) \cdot \vec{H}_\mathrm{ext}(\vec{r}) d^3r. \tag{2.16}$$

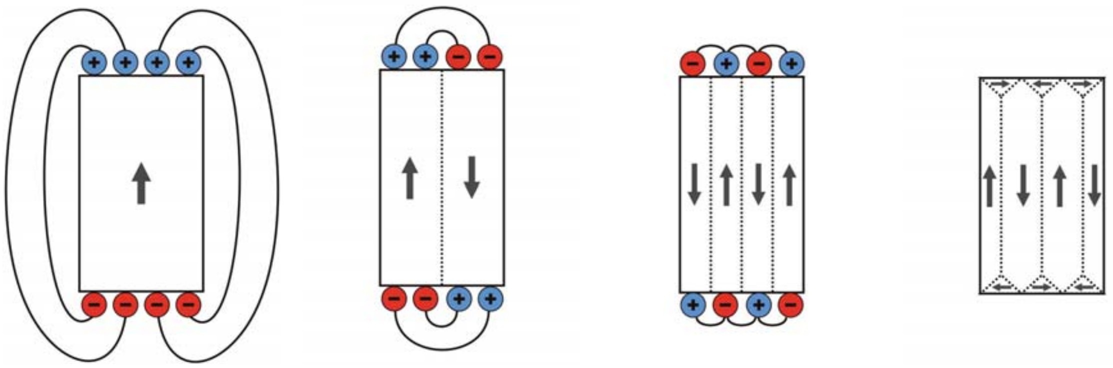

(a) (b) (c) (d)

Figure 2.5: Origin of ferromagnetic domains after [Kit49]. Where magnetization vectors have perpendicular components at the sample surface positive and negative magnetic charges are the sources and sinks of a magnetic stray field. The associated stray-field energy can be reduced by the formation of domains. This process illustrated in (a) through (d) energetically pays off until the cost of exchange energy for the formation of an additional domain wall (dotted lines) exceeds the gain in stray-field energy.

The total free energy E_{tot} of a ferromagnet is given by the sum of the energy contributions discussed above:

$$E_{\mathrm{tot}} = E_{\mathrm{ex}} + E_{\mathrm{strayfield}} + E_{\mathrm{Zeeman}} + E_{\mathrm{anisotropy}} + E_{\mathrm{magneto-elastic}}. \tag{2.17}$$

To give an impression of the impact of the individual energy terms, their coefficients, definitions, and ranges are listed in Table 2.2.

E_{tot} can be treated as a thermodynamic potential. Solving the variational problem $\partial E_{\mathrm{tot}}/\partial M = 0$ under the constraint that $|\vec{m}| = 1$ one can derive stable configurations of the magnetization $\vec{M}(\vec{r})$ in a ferromagnet that minimize the total free energy. This approach is the basis of both domain theory and micromagnetism.

Energy term	Coefficient	Definition	Range
Exchange energy	A	Material constant	$10^{-12} - 2\cdot10^{-11}\,\mathrm{J/m}$
Stray-field energy	K_{d}	$K_{\mathrm{d}} = \mu_0 M_{\mathrm{s}}^2/2$	$0 - 3\cdot10^{6}\,\mathrm{J/m^3}$
Zeeman energy	H_{ext} M_{s}	External field Material constant	depending on H_{ext} $10^{5} - 2\cdot10^{6}\,\mathrm{A/m}$
Anisotropy energies	$K_{\mathrm{u}}, K_{\mathrm{c}}, \ldots$	Material constants	$\pm(10^{2} - 2\cdot10^{7})\,\mathrm{J/m^3}$
Magnetostrictive self energy	$C\lambda^2$	C=shear modulus	$0 - 10^{3}\,\mathrm{J/m^3}$

Table 2.2: Coefficients, definitions and ranges of the energy terms discussed above [Hub09].

Hysteresis curves and magnetization reversal

Possible domain configurations derived by the analysis of energy densities can be used for the construction of magnetization versus field curves. The domain patterns found in a sample often do not necessarily represent a state of global energy minimum but depend on the history of the sample. The reason for this are blocked transitions between equilibrium states leading to hysteresis [Hub09]. Thus, magnetization curves are often called hysteresis loops or curves. The anisotropy energy of a uniaxial system can be determined from the difference of the magnetization work for the external field being applied perpendicular and parallel to the easy axis, respectively [Kis03].

The shape of magnetization curves provides information about the reversal mechanism of a sample [O'H00, Kis03, Smy91]. This is illustrated by means of Fig. 2.6. We consider a ferromagnetic disc with uniaxial in-plane anisotropy. In the initial state shown in Fig. 2.6(a) the net magnetization is zero since the disc is divided into two oppositely magnetized domains of the same size. Within these domains the magnetization is aligned along the easy axis (EA). The domains are separated by a domain wall. In an applied magnetic field the magnetic microstructure changes to reduce the energy of the sample. A change of the sample magnetization can take place via two independent processes [Kit49]:

1. Rotation of the magnetization towards the direction of an external field.
2. Nucleation or growth of domains which are oriented favorably with respect to the external field at the cost of other domains.

The two mechanisms are sketched in Figs. 2.6(b) and (c). If the external field is not oriented along the EA but for example along the hard axis (HA) as shown in Fig. 2.6(b), the magnetization experiences a torque and becomes tilted towards the direction of the external field. The resulting magnetization versus field curve is shown in Fig. 2.6(d). Starting with a demagnetized sample in the origin of the graph the magnetization component along the field axis increases linearly with the value of the applied field as the magnetization rotates. This process is usually reversible. When the magnetic moments in the sample are completely aligned along the field direction, the magnetization reaches a maximum value, the saturation magnetization M_s. The field at which this value is reached is called saturation field H_s. For a hard-axis loop H_s is equal to the anisotropy field H_a. If the external field is applied along the EA of the structure, the favorably oriented domain starts to grow and the domain wall is moved, compare Fig. 2.6(c). A typical hysteresis curve along the EA is shown in Fig. 2.6(e). Coming from positive saturation the structure is homogeneously magnetized and the magnetization corresponds to the saturation magnetization M_S. If the applied field is reduced the magnetization slightly decreases at some point. This can indicate the nucleation of domains. The value of the magnetization of the sample when the external field is reduced to zero is called remanent magnetization M_r. If an

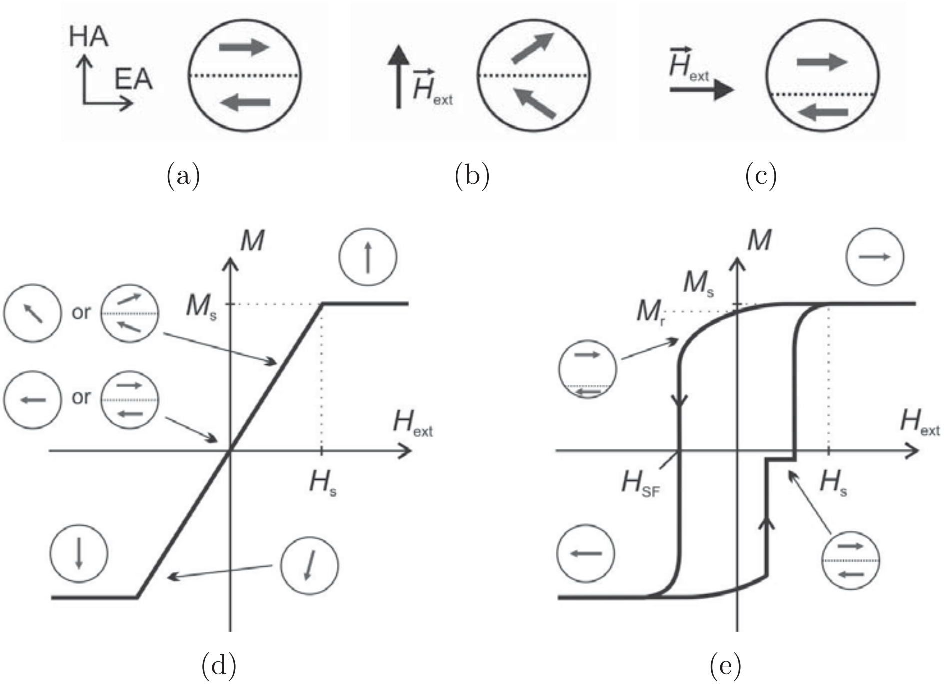

(a) (b) (c)

(d) (e)

Figure 2.6: (a) Initial state with two domains in which the magnetization is aligned along the easy axis (EA). (b) If an external field $\vec{H}_{\text{ext}}$ is applied along the hard axis (HA) the magnetization is rotated. (c) For $\vec{H}_{\text{ext}}$ applied parallel to the EA domains with a magnetization aligned along the direction of $\vec{H}_{\text{ext}}$ tend to grow on the cost of other domains. (d) and (e) are typical HA and EA magnetization versus field curves, respectively. The insets display possible magnetic configurations during the field sweeps. H_{s} and M_{s} are the saturation field and magnetization, H_{SF} is the switching field, and M_{r} is the remanent magnetization in zero field.

increasing negative field is applied a sudden jump of the magnetization to negative values occurs. Such a point of instability close to a saturated or nearly saturated state is referred to as switching field H_{SF}, at which the main part of the magnetization in a nanostructure reverses. In larger samples or for an array of nanostructures a particular switching field is difficult to define. Then, the field required to eliminate the remanent magnetization is often referred to as the coercive field.

If magnetization reversal takes place via the propagation of domain walls it appears that a wall does not move through the sample at once but that it is stopped. In the hysteresis curve such so-called pinning events are indicated by steps as shown in the loop in Fig. 2.6(e) for the sweep into positive field direction. Domain wall propagation is usually not reversible, since the wall energy depends on the position in a sample. One reason for this are intrinsic defects such as surface roughness, grain boundaries, and inclusions. Pinning of domain walls is discussed in more detail in Sec. 2.2 dealing with ferromagnetic nanowires.

Domain walls

So far we talked about domain walls without defining their inner structure. The appearance and configuration of a domain wall depend on the material and the geometry of the sample it exists in. Here, the discussion shall be limited to the most simplest case, a planar 180-degrees wall in an infinite uniaxial medium. The domain walls expected in the structures investigated in the frame of this work are described in the respective sections together with other properties of the samples.

Two possible rotation modes of the magnetization in the transition between two oppositely oriented domains are illustrated in Fig. 2.7. Subfigure (a) shows a so-called Bloch wall in which the magnetic moments rotate parallel to the plane of the wall. Bloch walls are the most common domain-wall type, since they can be nearly free of magnetic charges and thus almost stray-field free, and have the lowest energy in bulk materials [Hub09]. Figure 2.7(b) depicts the rotation mode of a Néel wall, where the magnetic moments in the center of the wall point perpendicular to the plane of the wall. Néel walls are often observed in thin films where they can reduce surface charges by rotating the magnetic moments in the surface plane [Stö06]. Bloch walls and Néel walls are the limiting cases of more complex domain-wall types which occur depending on the dimensions and the anisotropy of a sample or nanostructure [Ram96].

The width of a domain wall is given by an interplay of exchange energy and anisotropy energy. Without a continuous rotation of the magnetic moments at the interface between two domains the magnetization vectors of adjacent domains would be anti-parallel to each other. In this case the creation of a domain wall would not cost anisotropy energy. However, the cost of exchange energy would be significant. The exchange energy can be reduced by distributing the rotation of the magnetization over several moments. The width l_{DW} of a domain wall can be derived by minimizing the sum of exchange energy and anisotropy energy with respect to the amount of spin pairs over which the rotation occurs. It can be approximated by [Lil50]

$$l_{\mathrm{DW}} \approx \pi \sqrt{\frac{A}{K}}. \tag{2.18}$$

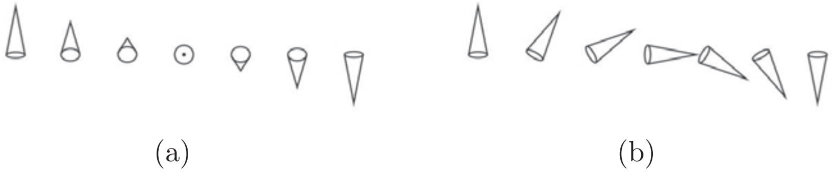
(a) (b)

Figure 2.7: Schematic of the magnetization in (a) a Bloch domain wall and (b) a Néel domain wall.

where A is the exchange stiffness constant and K is the anisotropy constant of the material. In soft-magnetic materials the domain-wall width is in the order of 200 nm, while in high-anisotropy systems it can be a few nanometers only. Equation 2.18 implies the definition of a material-characteristic length scale, the exchange length l_{ex} governed by the square root of the ratio between exchange stiffness A and the energy cost of having spins aligned away from the easy axis:

$$l_{\mathrm{ex}} = \sqrt{\frac{A}{K}}. \tag{2.19}$$

Depending on the leading anisotropy contribution, the anisotropy K in Eq. 2.19 is the magnetocrystalline anisotropy or the shape anisotropy $K_{\mathrm{d}} = \frac{\mu_0 M_{\mathrm{s}}^2}{2}$ [Stö06, Kro62]. The exchange length represents the distance over that the magnetization is expected to change orientation in the presence of magnetic anisotropies. If the dimensions of a sample are in the order of the exchange length, the formation of domains is energetically unfavorable. Magnetization reversal can then be described by the Stoner-Wohlfarth model discussed in the following paragraph.

2.1.5 Stoner-Wohlfarth model

Below a critical size related to the exchange length l_{ex} small particles do not fall apart into domains. Since the energy cost to form a domain wall exceeds the gain in stray-field energy they show a homogeneous magnetization. The easy magnetization direction is given by the effective anisotropy of the structure. Such particles reverse their magnetization in a reversal mode described by the Stoner-Wohlfarth model of coherent rotation [Sto48, Tan08]. Strictly speaking the model only applies for particles that reverse their magnetization uniformly. It is based on considering ellipsoidal particles that distinguish themselves by having homogeneous demagnetization fields. Given by the shape anisotropy, the magnetic easy axis of a spheroid is along the long axis. Particles of deviating shape can also be treated with the Stoner-Wohlfarth model. A sphere for example that has no shape anisotropy but magnetocrystalline anisotropy or strain-induced anisotropy could be described by the same physics with redefined parameters.

The angular dependence of the critical field $H_{\mathrm{c}}^{\mathrm{coh}}$ at which the magnetization reverses coherently resulting from the Stoner-Wohlfarth model is given by

$$H_{\mathrm{c}}^{\mathrm{coh}}(\theta) = \frac{H_{\mathrm{a}}^{\mathrm{coh}}}{\left(\cos^{2/3}\theta + \sin^{2/3}\theta\right)^{3/2}} \tag{2.20}$$

where θ is the angle between the direction of the external field $\vec{H}_{\mathrm{ext}}$ and the easy axis as illustrated in Fig. 2.8(a). The normalized critical field is plotted in Fig. 2.8(b) and

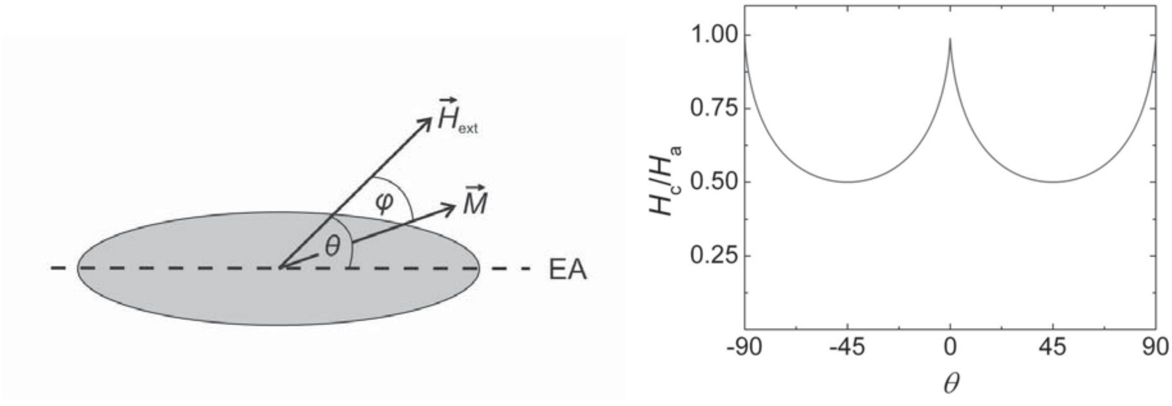

(a) (b)

Figure 2.8: (a) Schematic of a Stoner-Wohlfarth ellipsoid. θ and φ are the angles between the direction of the external field $\vec{H}_{\text{ext}}$ and the easy axis (EA) and the magnetization $\vec{M}$, respectively. (b) Angular dependence of the normalized critical field resulting from the Stoner-Wohlfarth model of coherent rotation.

can be either a coercive field if the coherent magnetization reversal occurs gradually or a switching field if the magnetization suddenly jumps into a new direction. $H_{\text{a}}^{\text{coh}}$ is the anisotropy field that gives the upper limit for the critical field [Liu05]. The magnitude of the anisotropy field usually depends on its definition. A frequently used expression is [Hub09, Aha86][3]

$$H_{\text{a}}^{\text{coh}} = -\frac{2K_1}{\mu_0 M_{\text{s}}} + N_{||} M_{\text{s}} - N_{\perp} M_{\text{s}}. \tag{2.21}$$

$N_{||}$ and $N_{\perp}$ are the demagnetization factors along the major and minor axes of a prolate spheroid, respectively. For a long ellipsoid of rotation they are given by

$$N_{||} = \frac{1}{n^2-1} \frac{n}{\sqrt{n^2-1}} \ln(n - 1 + \sqrt{n^2-1}) \tag{2.22}$$

and

$$N_{\perp} = \frac{1 - N_{||}}{2} \tag{2.23}$$

where $n = l/d$ is the aspect ratio of the length l and the diameter d [Liu05]. Equation 2.21 consists of three terms, the first of which accounts for the contribution of magnetocrystalline anisotropy. The other two summands represent the contribution of shape effects.

---

[3] In Aharoni's formula K_1 is the absolute value of the anisotropy constant $|K_1|$ [Aha86].

2.1.6 Magnetization reversal by curling

Deviations of the Stoner-Wohlfarth theory describe related reversal mechanisms named curling or buckling. These modes occur if particles are still too small to contain domain walls but allow for a non-uniform magnetization rotation at critical fields below the Stoner-Wohlfarth limit. Buckling is a reversal mode that is only expected in particles with large aspect rations in a small interval at the transition from coherent rotation to curling [Fre57, Aha86]. Due to its minor significance it shall not be discussed here.

The curling mode is illustrated in Fig. 2.9(c) for an infinite cylinder in comparison to magnetization reversal in unison as described by the Stoner-Wohlfarth model (a) and magnetization buckling (b). Magnetization reversal via curling avoids the stray field that has to be overcome during coherent rotation. The last term of Eq. 2.21 accounting for this stray-field contribution is therefore replaced by an exchange-stiffness term reflecting the dimensions of the particle [Hub09]:

$$H_{\mathrm{n}}^{\mathrm{curl}} = -\frac{2K_1}{\mu_0 M_{\mathrm{s}}} + N_{||} M_{\mathrm{s}} - \frac{M_{\mathrm{s}}}{2}\frac{k}{S^2}. \tag{2.24}$$

The geometrical factor k is plotted in Fig. 5.3. For an infinite cylinder $k = 1.079$, for a prolate spheroid with an aspect ratio of 4.2:1 $k = 1.2049$, for a sphere $k = 1.3793$ [Aha97a]. S is the reduced radius r/r_{c}. The critical radius r_{c} is the threshold radius for the transition from coherent rotation to curling related to the exchange length. It will be discussed in more detail in Sec. 5.1.

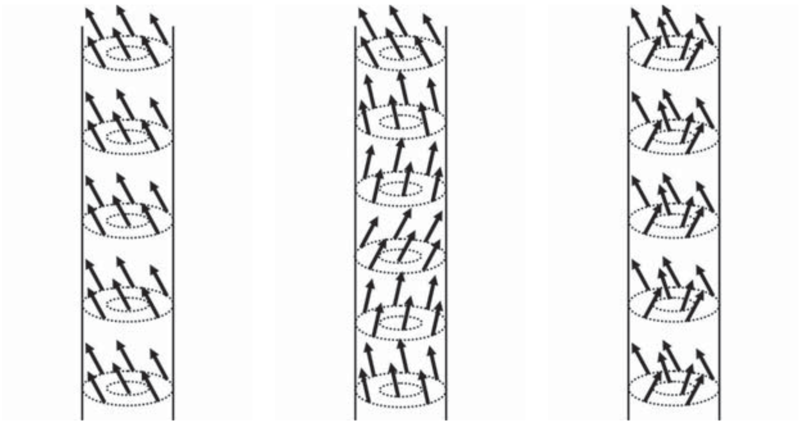

(a) (b) (c)

Figure 2.9: Modes of magnetization reversal in infinite cylinders: (a) Coherent rotation, (b) magnetization buckling, and (c) curling. The arrows indicate the local magnetization directions. Based on [Fre57] and [Sko06].

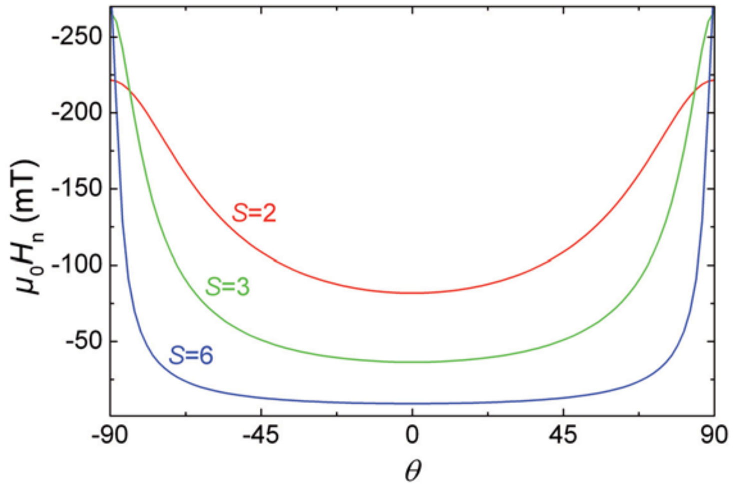

Figure 2.10: Angular dependence of the nucleation field of infinite cylinders with reduced radii of $S = 2$ (red curve), $S = 3$ (green), and $S = 6$ (blue) resulting from the curling model. As saturation magnetization $M_s = 4.83 \cdot 10^5 \frac{A}{m}$ for bulk nickel at room temperature is used.

If the influence of magnetocrystalline anisotropy (first summand of Eq. 2.24) is negligible the angular dependence of the nucleation field is given by [Aha97a]

$$H_n(\theta) = \frac{M_s}{2} \frac{\left(2N_\perp - \frac{k}{S^2}\right)\left(2N_{||} - \frac{k}{S^2}\right)}{\sqrt{\left(2N_{||} - \frac{k}{S^2}\right)^2 \sin^2\theta + \left(2N_\perp - \frac{k}{S^2}\right)^2 \cos^2\theta}}. \tag{2.25}$$

Equation 2.25 has a minimum at $\theta = 0°$. $H_n(\theta)$ is plotted for infinite nickel cylinders with reduced radii of $S = 2$ (red curve), $S = 3$ (green curve), and $S = 6$ (blue curve) in Fig. 2.10.

A precondition for the analytical treatment of magnetization reversal by curling is that the magnetization stays uniform and constant up to a critical field value [Hub09]. This field where the magnetic moments of a previously saturated particle cease to be aligned in parallel is defined as nucleation field H_n [Fre57]. For magnetization reversal via curling the switching field is assumed to be close to this nucleation field.

2.1.7 Micromagnetism

Analytical treatment of magnetization reversal is possible if the magnetization stays uniform up to the switching point. Strictly speaking this is only the case for magnetically homogeneous samples with ellipsoidal shape, compare Secs. 2.1.5 and 2.1.6. For more complex particles the reversal process has to be studied numerically. The basis for this are the micromagnetic equations, a set of coupled differential equations that can be derived by applying a variational principle on the total free energy of a ferromagnet (Eq. 2.17). A consequence of the variational principle is that the torque on the magnetization has to vanish in an effective field H_{eff}:

$$\vec{M} \times \vec{H}_{\mathrm{eff}} = 0. \tag{2.26}$$

The effective field is defined by differentiating Eq. 2.17:

$$\begin{aligned} \vec{H}_{\mathrm{eff}} &= -\frac{1}{\mu_0}\frac{\partial E_{\mathrm{tot}}}{\partial \vec{M}} \qquad (2.27) \\ &= \frac{2A}{\mu_0 M_{\mathrm{s}}^2}\vec{\nabla}^2\vec{M} + \vec{H}_{\mathrm{strayfield}} + \vec{H}_{\mathrm{ext}} - \frac{M_{\mathrm{s}}}{\mu_0}\sum_i \frac{\partial \epsilon_i}{\partial \vec{m}} - \frac{M_{\mathrm{s}}}{\mu_0}\frac{\partial \epsilon_{\mathrm{magneto-elastic}}}{\partial \vec{m}}. \end{aligned}$$

The equation of motion for the magnetization $\vec{M}$ is given by [Stö06]

$$\frac{d\vec{M}}{dt} = -\gamma \vec{M} \times \vec{H}_{\mathrm{eff}} + \frac{\alpha}{M_{\mathrm{s}}}\vec{M} \times \frac{d\vec{M}}{dt} + \vec{T} \tag{2.28}$$

where $\gamma = \frac{\mu_0 g e}{2 m_{\mathrm{e}}} \cong g \cdot 1.105 \cdot 10^5 \frac{\mathrm{m}}{\mathrm{As}}$ is the gyromagnetic ratio for a free electron with a Landé factor $g \approx 2$. Without the last summand $\vec{T}$ Eq. 2.28 is called Landau-Lifshitz-Gilbert (LLG) equation. The first term describes a precession of $\vec{M}$ around the axis of the effective field $\vec{H}_{\mathrm{eff}}$. The second summand is a damping term. It includes the dimensionless phenomenological damping parameter α, and is required to relax the system into an equilibrium state in which the magnetization points along $\vec{H}_{\mathrm{eff}}$ [Stö06]. The last summand $\vec{T}$ is an extension to the LLG equation describing the torque that spin currents impose on the magnetization of a sample.[4] The existence of this so-called spin-transfer torque was predicted in 1978 [Ber78] and experimentally observed in magnetic thin films some years later [Fre85] by Berger *et al.*. Since high current densities were required to observe wall displacement, the effect did not attract a lot of attention at that time. With the improvement of nanofabrication and the prospect of technological applications the research interest in spin-transfer torque has risen in the last decade. A variety of expressions for $\vec{T}$ has been derived to date to account for experimental observations with respect to current-induced domain-wall motion in ferromagnetic multilayers [Slo96] and nanowires [Zha04, Thi05, Krü07].

The LLG equation can be solved numerically. This is usually done by means of micromagnetic simulations. Micromagnetic simulations are the subject matter of chapter 3 where after a short introduction results are presented to illustrate the influence of the individual energy terms in Eq. 2.17 on the magnetic behavior of the cylindrical nanostructures studied in the frame of this work.

---

[4] Charge currents can also contribute to the term $\vec{T}$ via the so-called domain-drag force imposed by Eddy currents at a domain wall. For details see Ref. [Ber74].

2.2 Domain walls in ferromagnetic nanowires

The study of domain walls in confined geometries as ferromagnetic nanowires is of interest for several reasons. First, domain walls in bulk materials change their structure at the surface because there the dipole fields are strongest [Hub09]. In addition, many experimental techniques are limited to surfaces and thin films. Furthermore, in comparison to bulk material the confined geometry of wires offers better control of domain walls, and their dimensions can be accomplished by micromagnetic simulations. This is crucial for systematic studies and a basic understanding of domain-wall structure and dynamics. Besides the incentive of fundamental research huge ambition in domain-wall research has been launched by the proposal of domain wall based memory [Par08] and logic devices [All05]. Compared to contemporary technology such devices would combine merits as non-volatility, high speed and density, as well as low power consumption. Section 2.2.1 describes different methods of domain-wall preparation in ferromagnetic wires, Sec. 2.2.2 deals with depinning.

2.2.1 Preparation of domain walls

In this section established methods for the preparation of domain walls in ferromagnetic wires are reviewed. The preparation of a domain wall usually consists of two steps. First, the domain wall has to be injected into the wire. Then the wall has to be localized. This is typically done at a pinning site.

Domain-wall injection

Different methods for the injection of a domain wall are illustrated in Figs. 2.11 through 2.13. The sketches show soft-magnetic wires with an in-plane easy axis along the wire.[5] All methods presented base upon the application of a magnetic field. The second method employs a local magnetic Oersted field. In all cases we start with considering a single domain state of the wire as shown in the subfigures (a). These initial states are prepared by saturating the wires in a positive magnetic field pointing horizontally to the right. At remanence the shape anisotropy forces the magnetization to align parallel to the edges of the wires.

In a bend wire a domain wall can be prepared by applying an external magnetic field perpendicular to the wire as illustrated in Fig. 2.11(b) [Nah09]. When the field is turned off, a domain wall is formed in the curve, see Fig. 2.11(c). In the situation shown, the magnetizations of the domains separated by the wall point towards each

---

[5] The most widely studied material in this respect is permalloy ($Ni_{80}Fe_{20}$), combining desirable properties as negligible magnetocrystalline anisotropy and near-zero magnetostriction.

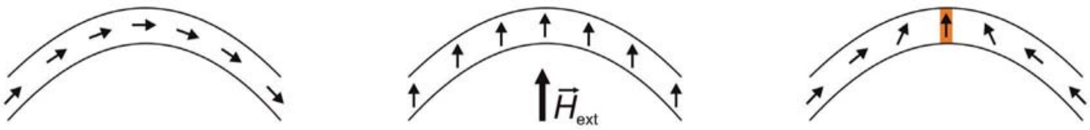

(a) (b) (c)

Figure 2.11: Schematic of the preparation of a domain wall in a bent soft-magnetic wire by the application of an external field $\vec{H}_{\text{ext}}$. The small arrows indicate the local magnetization directions.

other. Such a transverse domain wall is called head-to-head domain wall. By choosing the direction of the applied field (in this case up or down) one can select whether to prepare the latter domain-wall type or its counterpart, a tail-to-tail wall.

A method for the preparation of a domain wall in a straight wire is illustrated in Fig. 2.12. The gray area indicates a lead fabricated above the wire. The Oersted field accompanying a current pulse sent through this lead can reverse a segment of the wire underneath the lead. Since high current densities can destroy the structure, the effective field acting on the wire segment is often increased by applying a background field $\vec{H}_{\text{back}}$ supporting the Oersted field. Once the magnetization of the wire segment underneath the strip line is reversed, there are two domain walls in the wire, see Fig. 2.12(b). Due to the background field these domain walls move into opposite directions. The domain wall on the right hand side propagates into the wire, while the other one is annihilated at the left wire end. This procedure is frequently employed both in wires with in-plane [Ste12] and out-of-plane [Koy11] anisotropy. A variation of the method is the application of a local Oersted field at the end of a wire where the high demagnetization field replaces the external background field $\vec{H}_{\text{back}}$ and a domain wall can be nucleated as demonstrated by Himeno *et al.* [Him03].

A domain wall can also be injected into a wire using a design as shown in Fig. 2.13 [Shi99]. One side of a ferromagnetic wire is connected to a large area called nucleation pad. If an increasing reverse field antiparallel to the initial magnetization direction

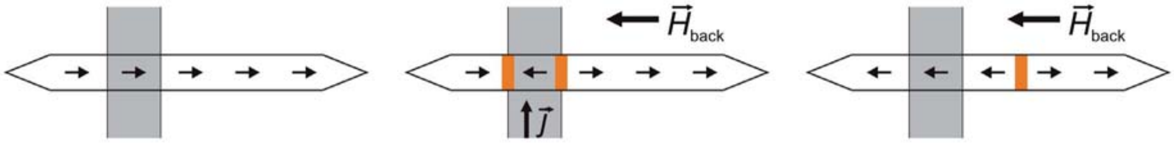

(a) (b) (c)

Figure 2.12: Schematic of domain wall (orange) nucleation using the Oersted field around a lead (gray) through which a current $\vec{j}$ is sent. The process is supported by an external background field $\vec{H}_{\text{back}}$.

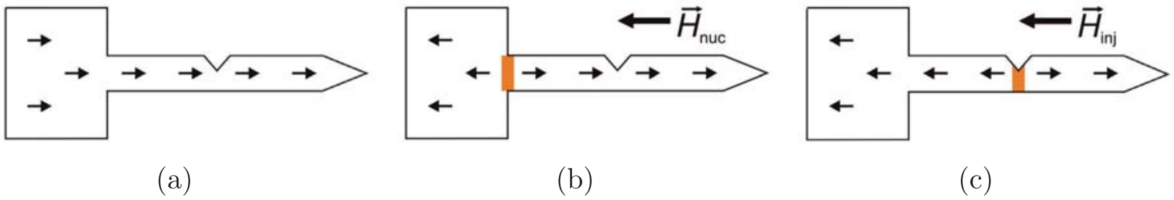

Figure 2.13: Schematic of domain-wall preparation in a soft-magnetic wire with nucleation pad and notch. At the nucleation field $\vec{H}_{\mathrm{nuc}}$ the magnetization of the pad reverses (b), at the injection field $\vec{H}_{\mathrm{inj}}$ a domain wall propagates through the wire and gets pinned at the notch.

of the wire is applied, magnetization reversal starts in this pad due to increased demagnetizing fields when the field value H_{nuc}, the nucleation field, is reached. A domain wall is then pinned at the transition between nucleation pad and wire, compare Fig. 2.13(b). As soon as the applied reverse field reaches the value H_{inj}, this domain wall is injected into the wire. The notch shown in the center of the wire is one out of many possibilities to implement a pinning site.

Domain-wall pinning

A frequently appearing and sometimes undesirable kind of pinning sites are defects inherent in the material of a nanostructure. Such intrinsic defects can be caused by surface and edge roughness, grain boundaries, and inclusions to mention a few. The impact of a defect on the energy of a domain wall in a material with an anisotropy constant K is illustrated in Fig. 2.14. A nonmagnetic inclusion or a grain with an anisotropy $K_{\mathrm{l}} < K$ (left, green) reduces the local energy of a domain wall, since in the area of such a defect the magnetization $\vec{M}$ does not need to rotate at all or rotates over a longer distance (compare Eq. 2.18) what lowers the exchange energy. If the local effective anisotropy K_{h} of an inclusion is higher than the anisotropy K of the surrounding material, the inclusion acts like an energy barrier that constricts the propagation of the domain wall through the defect (right hand side of Fig. 2.14, red). Defects occur naturally but they can also be created on purpose, for example by local ion irradiation. The modification of magnetic material parameters can be caused by radiation-induced structural changes as well as by ion implantation. For more information the reader may refer to reference [Cha98] and the review article by Fassbender *et al.* [Fas04], as well as to publication [Vog10] appended to this thesis in Sec. A.2.

Another possibility to create pinning sites in a wire is by means of geometrical modifications. A representative for such pinning sites is a triangular-shaped notch as the one shown in Fig. 2.13. The pinning potential of notches and anti-notches with a

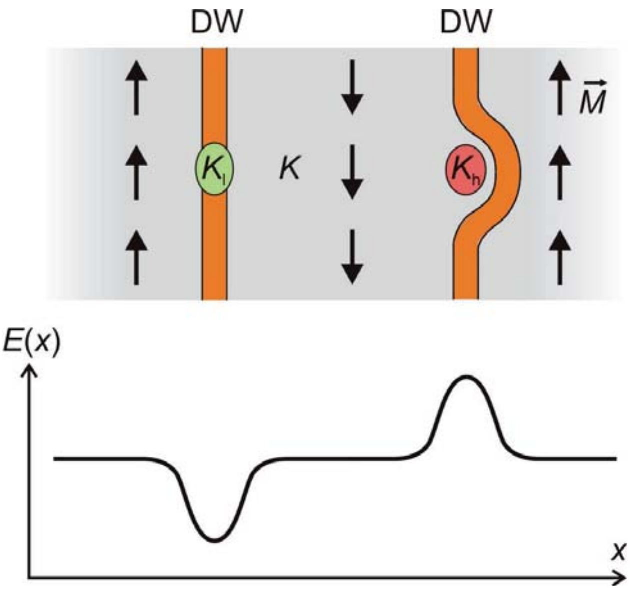

Figure 2.14: Ferromagnetic material (gray) with anisotropy constant K and two domain walls (orange). A defect with $K_\mathrm{l} < K$ pins a domain wall by locally lowering its energy, while an inclusion with $K_\mathrm{h} > K$ poses a barrier to its motion. The lower panel depicts the domain-wall energy as a function of the position in the material in the absence of an external field. After [O'H00].

variety of different shapes and dimensions has been extensively studied by several groups [Klä03b, Him03, Pet08, Im09, Gla12]. It was found that the energy landscape created by a lateral modulation not only depends on the geometry of the modulation but also on the structure of the domain wall [Hay06b]. The two fundamental types of domain walls occurring in flat soft-magnetic wires are transverse walls as illustrated in Figs. 2.15(a) and (b) and vortex walls as shown in (c) and (d). The sense of rotation of the magnetization across these walls can be clockwise ((a) and (c)) or counterclockwise ((b) and (d)). In a simple model for a clockwise oriented transverse wall the notch can be considered as a potential well in which the domain wall is trapped since its energy is lowered by decreasing the length of the wall. Furthermore, the alignment of the magnetization parallel to the edges of the notch reduces magnetic charges. For a counterclockwise oriented transverse wall, however, the energy landscape created by the notch looks different. The notch constitutes a potential barrier, since a wall located right a the notch would cause a comparably high stray field. The propagation of such a domain wall has to be considered as a repulsion from or transmission through the barrier rather than pinning and depinning. Comparable considerations can be made for vortex type domain walls.

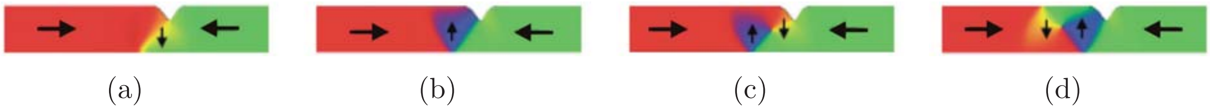
(a) (b) (c) (d)

Figure 2.15: Models of transverse (a, b) and vortex-type (c, d) domain walls with clockwise (a, c) and counterclockwise (b, d) sense of rotation. Reprinted with permission from [Hay06b]. Copyright 2006 by the American Physical Society.

2.2.2 Depinning and motion of domain walls

In principle a domain wall can be depinned from or pushed past a pinning site by one or a combination of the following three processes:

- Application of a magnetic field
- Thermal activation
- Spin-momentum transfer

The Zeeman energy of domains with magnetization components aligned antiparallel to an external field is increased. To reduce the total energy of the system domains aligned in parallel tend to grow at the cost of others, a process which can take place via field-induced domain-wall motion. For a theoretical treatment of depinning a domain wall can be considered as a quasi-particle [Gar95]. The potential landscape shown in Fig. 2.16 can be used to describe both the depinning from a potential well and the transmission through a potential barrier. E_0 is the depth or height of the potential in the absence of an external magnetic field. The application of external fields shifts the energy landscape as illustrated by the blue and green curves in Fig. 2.16 for two field values H_1 and $H_2 > H_1$. An analytical expression for the barrier height derived by Garg is given by

$$E(H) \approx E_0 \left(1 - \frac{H}{H^0_{\mathrm{depin}}}\right)^{3/2} \tag{2.29}$$

where H^0_{depin} is the depinning field at zero Kelvin [Gar95]. The lower the effective barrier height the higher is the chance of depinning by thermal activation. The average depinning time τ can be expressed by an Arrhenius law:

$$\tau(T,H) = \tau_0 \, e^{\frac{E(H)}{k_{\mathrm{B}}T}} \, . \tag{2.30}$$

τ_0 is the inverse attempt frequency which lies in the order of 10^9 to 10^{10} $\frac{1}{s}$. Measuring the temperature dependent depinning probabilities for varying strengths and opposite directions of an applied magnetic field provides information about the heights of energy barriers at pinning sites [Len10, Wut12]. Thermal activation imposes a stochastic nature on domain-wall depinning and propagation. Additional complexity of domain-wall processes originates from intrinsic degrees of freedom which are not incorporated in the above quasi-particle model. Before a domain wall is depinned, it can be deformed or even transformed into another domain-wall type [Klä05, Hay06a, Klä08]. Briones *et al.* proposed a description of the depinning process that accounts for the variety of possible processes via which a domain wall can be depinned from a certain pinning site [Bri11].

A precondition for the realization of devices like the race-track memory is the synchronous movement of several domain walls [Par08]. To achieve this, main efforts of

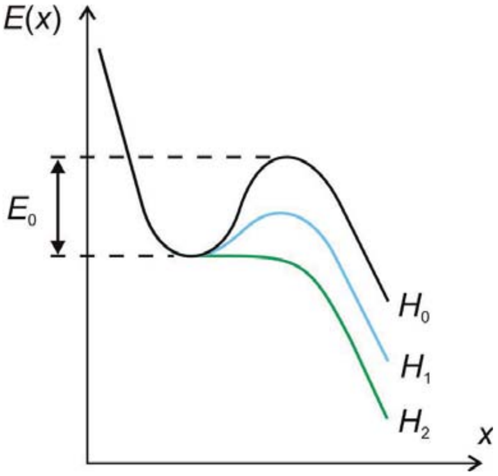

Figure 2.16: Schematic field-dependence of an energy barrier for domain-wall depinning or transmission. E_0 is the barrier height in zero applied field H_0, $H_2 > H_1 > H_0$ is the depinning field, all at zero temperature. After [Gar95].

todays domain-wall research are made in the displacement of domain walls by spin-polarized currents. The effect of spin-momentum transfer on the magnetic moments in a domain wall can be treated by expanding the Landau-Lifshitz-Gilbert equation by a torque term as indicated in Eq. 2.28 [Zha04, Thi05]. Since this aspect plays a minor role in this work, the reader may refer to the review of Boulle *et al.* [Bou11] for information about the underlying mechanisms. The critical currents to depin a domain wall are in the order of $10^{12}\frac{\mathrm{A}}{\mathrm{m}}$ and $10^{11}\frac{\mathrm{A}}{\mathrm{m}}$ for wires with in-plane and out-of-plane magnetization, respectively [Boc09, Bou11]. Cylindrical wires of soft-magnetic material are predicted to have a critical current of zero [Yan10]. Current flow in wires causes Joule heating. Thus, the aspect of thermally activated depinning always plays a crucial role in current-driven experiments [Bou08].

The often thermally activated hopping of domain walls from one defect to another is referred to as creep regime [Met07, Cay04]. Creeping is characteristic for wires with out-of-plane anisotropy where domain walls are typically very narrow, and their dynamic is more sensitive to local defects than in soft-magnetic wires. For low applied fields or currents, the domain-wall behavior of 180-degrees domain walls without pinning corresponds to viscous motion and the wall velocity increases linearly with the field strength [Sch74, Mou07]. For high applied fields or currents, typically at velocities of several 100 $\frac{m}{s}$, at the so-called Walker breakdown, the wall velocity is reduced due to periodic wall transformations. Only at very high fields the velocity increases again. The Walker limit imposes a fundamental obstacle on technological applications. Transverse domain walls in cylindrical nanowires however, are predicted to show a fundamentally different behavior [Yan10]. They can be considered as massless objects. Since they do not change their inner structure during motion, there is no Walker breakdown for this type of domain walls. The experimental confirmation of this is still due.

2.3 Magnetoresistive effects

Changes of the electrical conductivity due to a magnetic field are referred to as magnetoresistive effects. Section 2.3.1 gives an introduction to spin-dependent transport to equip the reader with the fundamental concepts for the understanding of magnetoresistive effects. In the following sections the major magnetoresistive effects occurring in bulk materials are reviewed. The Lorentz magnetoresistance, the negative magnetoresistance, and the anisotropic magnetoresistance (AMR) are present in all ferromagnets. This does not mean that they can always be observed since their contributions overlap with different orders of magnitude. Usually the AMR is dominant at small applied fields, while at higher fields one of the other two effects is responsible for the resistivity behavior. Domain walls in ferromagnetic metals are also known to be a source of resistance. The giant magnetoresistance (GMR) effect discovered in coupled multilayers [Bai88, Bin89] and related phenomena in magnetic/non-magnetic heterostructures are not addressed since they lie beyond the scope of this work.

2.3.1 Spin-dependent transport

From the Boltzmann theory of electronic transport we know that the electric current is carried by the electrons near the Fermi level with the Fermi energy E_F. In the Drude model for free electrons the electrical conductivity is given by [O'H00]

$$\sigma = \frac{1}{\rho} = \frac{ne^2\tau}{m^*}. \tag{2.31}$$

e is the elementary charge, m^* is the effective electron mass which is inversely proportional to the band curvature. The number of conduction electrons per unit volume n is proportional to the density of states at the Fermi level $D(E_\mathrm{F})$. The relaxation time $\tau = \frac{\Lambda}{v_\mathrm{F}}$ depends on the mean free path Λ between two scattering events and on the Fermi velocity v_F. At low temperatures ($T \to 0$), Λ is determined by defects and impurities embedded in the solid. For higher temperatures scattering at phonons and magnons appears.

In transition metals the current is mainly carried by delocalized s electrons. Since at the Fermi level s and d states overlap, there is a partial localization of the s electrons, while the localized d electrons become slightly delocalized. Due to this hybridization the usually parabolic s states become flatter what increases the effective mass and therewith decreases the mobility of the charge carriers in transition metals compared to other metals. An additional source of resistance is the so-called s-d scattering [Mot36, Mot64]. This mechanism is the main contribution to the resistivity of nickel and plays a crucial role for the understanding of the transport properties in ferromagnetic transition metals.

In addition to the electron charge, the magnetic moment related to the electron spin can play a role in electronic transport. Electrons with a spin orientation energetically favored with respect to an external or local magnetic field are referred to as majority electrons with spin down. Electrons with the opposite spin orientation are the minority electrons. Drude's formula Eq. 2.31 can be rewritten as

$$\sigma_{\mathrm{s}} = \frac{1}{\rho_{\mathrm{s}}} = \frac{n_{\mathrm{s}} e^2 \tau_{\mathrm{s}}}{m_{\mathrm{s}}^*} \tag{2.32}$$

with the electron spin s up ($\uparrow$) or down ($\downarrow$), and subband-dependent values for n_{s}, m_{s}^*, and τ_{s}. The relaxation time τ_{s} depends on the scattering potential V_{s} and on the spin-projected density of states at the Fermi level $D_{\mathrm{s}}(E_{\mathrm{F}})$ [O'H00]:

$$\tau_{\mathrm{s}}^{-1} \propto |V_{\mathrm{s}}|^2 \, D_s(E_{\mathrm{F}}). \tag{2.33}$$

The scattering potential V_{s} of impurities and defects can be different for majority and minority electrons. This is an extrinsic factor for the spin dependence of the conductivity σ_{s}. In solids the electronic configuration of an atom is controlled by its nearest neighbors.[6] If there is an asymmetry in the density of states for spin down and spin up electrons, $D_{\mathrm{s}}(E_{\mathrm{F}})$ and therewith n_{s} and m_{s}^* might be spin dependent. This intrinsic property is characteristic for ferromagnets.

The total current is the sum of the contributions of majority and minority electrons:

$$j = j_\downarrow + j_\uparrow = (\sigma_\downarrow + \sigma_\uparrow) E. \tag{2.34}$$

This is the basis of the '**two-current model**' where electronic transport is considered as a parallel connection of a channel for spin-down and a channel for spin-up electrons [Mot36, Cam82]. The channel with the higher conductivity acts like a short-circuit reducing the resistivity. If there is no spin-flip taking place, the resistivity is given by

$$\rho = \frac{1}{\sigma_\downarrow + \sigma_\uparrow} = \frac{\rho_\downarrow \rho_\uparrow}{\rho_\downarrow + \rho_\uparrow}. \tag{2.35}$$

Spin-flip means that the spin of a conducting electron changes from up to down or vice versa. This would constitute a short-circuit between the two channels. Campbell

---

[6] The electronic structure and therewith the conductivity is determined by the local environment, thus it is dependent on position. In inhomogeneous samples, such as layered structures, the density and nature of impurities is also strongly position dependent and the relaxation time is not isotropic. Consequently the resistivity of interface and bulk regions can be distinctly different and their contributions may have to be considered individually. Despite many experimental and theoretical studies, the influence of interfacial and bulk scattering is still controversial [Zah98].

and Fert proposed a two-current model including spin mixing [Fer69]. Spin-flip can happen through scattering events of electrons with magnons or electrons as well as through spin-orbit coupling [Stö06]. The importance of these three mechanisms is controversially discussed [Cam70, Ber11].

2.3.2 Lorentz magnetoresistance

If a metallic sample is exposed to a magnetic field, the conduction electrons move on circular paths due to the Lorentz force. This reduces the effective mean free path Λ between two scattering events and results in an increase of the resistivity ρ, since ρ is inversely proportional to Λ. This positive, also called 'ordinary' magnetoresistance, is usually a parabolic function of the applied field and occurs in all metals [Zim63]. Since it is often overruled by a much higher negative magnetoresistance, it is not always observable. Measurable effects are usually expected above 10 T at low temperatures [Raq02].

2.3.3 Negative magnetoresistance

Negative magnetoresistance is a linear function of the applied magnetic field and independent of the angle between current and magnetization direction [Raq02]. There are two mechanisms for its explanation. One contribution comes from the suppression of spin-disorder scattering by external fields. The same effect can be achieved by reducing the temperature. In the two-current model a decrease of the resistivity arises from a reduction of s-d scattering in one spin channel when the d band of the majority electrons is shifted or even falls below the Fermi level [Mot36, Mot64]. Both mechanisms account for the observation that the resistivity of ferromagnetic transition metals drops below the curve extrapolated for the resistivity behavior at higher temperatures once the temperature is reduced below the Curie point.

2.3.4 Anisotropic magnetoresistance

Anisotropic magnetoresistance (AMR) depends on the relative orientation of the magnetization and the current. The effects was discovered already in 1856 by William Thomson [Tho56]. Its microscopic origin, however, is not fully understood yet. Two aspects that play a major role are the spin-orbit interaction and the difference between spin-up and spin-down resistivities [Smi51, McG75, Jao77]. The resistance change due to AMR is usually in the order of a few percent. In bulk samples the AMR is proportional to $\cos^2(\theta)$, where θ is the angle between the current density $\vec{j}$ and the local magnetization $\vec{M}$ [Dör38]. The resistivity ρ is phenomenologically described by

$$\rho(\theta) = \rho_{\perp} + (\rho_{||} - \rho_{\perp}) \cos^2(\theta) \tag{2.36}$$

where $\rho_{\perp}$ and $\rho_{||}$ are the diagonal elements of the resistivity tensor for directions perpendicular and parallel to the magnetization, namely the resistivities for $\theta = 90°$ and $\theta = 0°$ [O'H00]. Due to boundary scattering there are deviations from Eq. 2.36 for magnetic nanostructures [Rij95].

AMR can be employed as a probe for the magnetic state of a nanowire, thus enables one to study magnetization reversal by an electrical measurement [Weg99]. In some ferromagnetic wires the AMR can be used to detect the presence of a domain wall. The precondition for this is that due to the rotation of the magnetization within the domain wall the magnetization components with respect to the current direction vary. This is the case for Bloch walls in wires with in-plane magnetization and Néel walls in wires with out-of-plane anisotropy. A Bloch wall in the latter kind of wire, however, does not contribute to the AMR.

2.3.5 Domain-wall resistance

In 1968 Taylor *et al.* observed that erasing the domains of an iron whisker by applying a magnetic field results in a reduction of the resistivity [Tay68]. Since then many experimental and theoretical studies on the contribution of domain walls to the electrical resistivity have been made [Ken01, Mar05]. The results are controversial in both experiments and theories. While in the quantummechanical model of Levy and Zhang [Lev97] as well as in the semi-classical model of Viret *et al.* [Vir96] spin-mistracking inside a domain wall results in a positive MR proportional to $(l_{DW})^{-2}$, Tatara and Fukuyama predict negative MR. They assume that impurity scattering reduces the weak localization what results in a dephasing of the conduction electrons in a domain wall at low temperatures [Tat97]. There are also theories, e.g. by van Gorkom *et al.*, that expect a positive or negative MR depending on the spin-dependent scattering times [Gor99]. An additional source of domain-wall resistance can be Joule heating due to eddy currents [Ber78]. The contribution of domain-wall resistance to the resistance of a structure is hard to isolate and often masked by other magnetoresistive effects, in particular the AMR. A condition for a measurably large signal is that the domain-wall width l_{DW} is smaller than the electron mean free path, thus that there is no possibility for adiabatic spin change. For a sufficiently large difference in the density of states at the Fermi level for majority and minority charge carriers, this means that there are no unoccupied states behind the DW to tunnel in, and the charge carriers are reflected from the DW what leads to a domain-wall resistance [Cab74].

2.4 X-ray magnetic circular dichroism

The asymmetry of the absorption cross-sections of atomic core levels for left and right circularly polarized x-ray photons is called x-ray magnetic circular dichroism (XMCD) [Sch87, Che90]. The XMCD effect is proportional to the projection of the photon spin $\vec{L}$ on the atomic moment and thereby on the magnetization $\vec{m}$ of a sample [Stö98]:

$$I_{\mathrm{XMCD}} \propto P_{\mathrm{circ}}\, \vec{m} \cdot \vec{L}. \tag{2.37}$$

P_{circ} is the degree of polarization of the x-ray photons. For a maximum dichroic effect the magnetization direction has to be in parallel to the photon wave vector.

Figure 2.17(a) illustrates the XMCD effect in a two-step model for resonant transitions of $2p$ core electrons into unoccupied $3d$ valence states in transition metals [Stö98]. Circularly polarized x-ray photons of positive (σ^+) or negative (σ^-) helicity carry the spin $+\hbar$ or $-\hbar$. In a first step this spin is transfered to a photoelectron via spin-orbit coupling. The spin-polarization of the photoelectrons is then probed by the spin asymmetry of the final $3d$ states. The conservation of spin momentum in

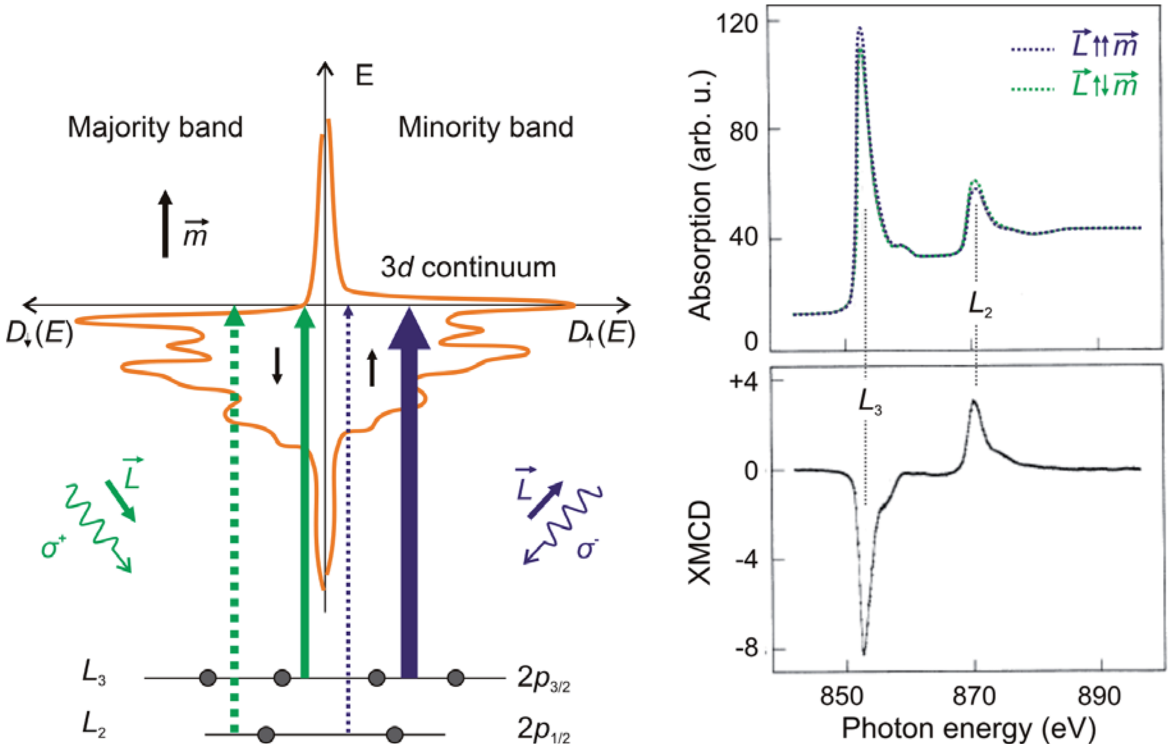

(a) (b)

Figure 2.17: (a) Illustration of the x-ray magnetic circular dichroism (XMCD) effect for the L-edge absorption in nickel. The density of states is sketched after Ref. [Mat01]. (b) X-ray absorption intensity (top) and XMCD signal (bottom) of nickel modified from Ref. [Che90].

this second step makes the excitation process spin sensitive. Due to spin-orbit coupling the p states are split, and transitions from the $2p_{3/2}$ (L_3) and $2p_{1/2}$ (L_2) levels occur at different photon energies. The transition probabilities from these levels for the two photon helicities are indicated by the thicknesses of the respective arrows in Fig. 2.17(a). They result in characteristic absorption spectra like the ones of nickel depicted in the top panel of Fig. 2.17(b). The offset between the two intensities is defined as the XMCD signal which is plotted below.

The XMCD contrast at the L_3 and L_2 edges is inverted. The reason for this is the spin-orbit coupling that leads to the parallel and antiparallel alignment of orbital and spin angular momentum $\vec{l}$ and $\vec{s}$ in the $2p_{3/2}$ (L_3) and $2p_{1/2}$ (L_2) levels, respectively. Excitations by circularly polarized x-ray photons from these levels can be associated with different spin polarizations [Stö98].

3 Micromagnetic simulations

3.1 Method

Micromagnetic simulations calculate the time evolution of micromagnetic systems by repeatedly solving a set of partial differential equations. To perform micromagnetic simulations the following steps are executed:

1. Spatial discretization of the system to be simulated by dividing space into cells.
2. Simulation of the magnetization dynamics by numerical integration of the Landau-Lifshitz-Gilbert (LLG) equation including the calculation of all energies involved.
3. Visualization and analysis of the results.

The individual steps are described below.

1. Discretization

The two common techniques for discretization are the finite difference method and the finite element method. Finite differences mean that space is discretized into small cuboids of constant dimensions. This approach is used for the simulations of magnetization reversal in Co/Pt multilayer wires presented in chapter 7. Finite elements subdivide space into small tetrahedra. While finite differences are well suited if the geometry to be simulated is of rectangular shape, curved geometries can be specified with a higher accuracy using the finite element method. This is illustrated in Fig. 3.1. Discretizing a sphere by finite differences leads to orthogonal edges (a). A sphere is described better by a mesh of finite elements that are tetrahedra of arbitrary shape (b). The micromagnetic simulations of cylindrical nanostructures presented in this work are done using the finite element method. Meshes are created using the software Gmesh. Figure 3.2 displays a typical mesh forming the ferromagnetic wire as well as the surrounding vacuum presented by the flat box. The diameter of the wire is $40 + 5$ nm, that means 40 nm at one side and 45 nm on the other. This symmetry breaking is necessary to define at which wire end the reversal process starts. The internal demagnetization field and the magnetic behavior of the wire are well-defined by the magnetic volume only. If one is interested in the external stray field, a mesh

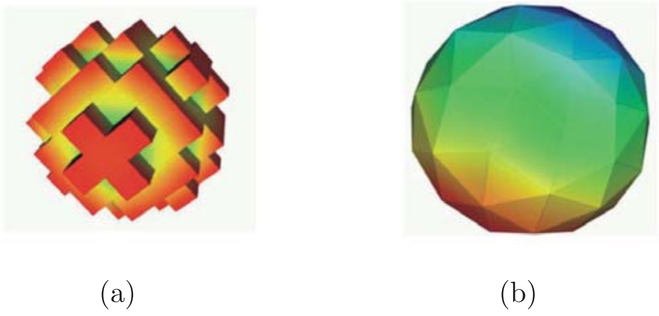

Figure 3.1: Discretization of a sphere using (a) finite differences and (b) finite elements. The images are taken from the nmag manual [Fan].

outside of the structure itself has to be created. The reason why the surrounding box is not a large cube but is designed flat becomes clear considering the second paragraph.

Typical parameters for the cell size of the mesh are 20 nm for the vacuum and $3 - 10$ nm for nickel nanostructures.[1] As can be inferred from Fig. 3.2 the mesh of the wire is finer at the end (3 nm) with a gradual transition to a wider cell size (10 nm) in the middle. It was confirmed by test simulations that this meshing leads to the same results for the switching fields, as would a meshing that is fine everywhere. The fields at which the magnetization of a 1 μm long wire with a diameter of $40 + 5$ nm reverses are 117 mT, 119 mT, and 119.5 mT for constant cell sizes of 10 nm, 5 nm, and 3 nm, respectively. These tests confirm that our mesh creation which aims at the saving of computation power (see below) is reasonable. When it comes to wires with diameter modulations, however, a constant cell size of 6 nm well below the exchange length of nickel is chosen for all regions where domain walls are propagating, since variations of the cell size can lead to unphysical variations of the calculated exchange energy when a domain wall passes transition regions.

2. Simulation

Before a simulation is started the initial magnetization configuration and the material parameters have to be set. As the initial configuration usually a parallel alignment of all magnetic moments along the wire's axis is chosen. To enforce a domain wall at a defined position in the wire a configuration as shown in Fig. 3.3 is set.

The actual micromagnetic simulation is the numerical integration of the LLG equation (Eq. 2.28), a set of coupled differential equations. Calculations are carried out by so-called micromagnetic packages. A famous package to handle finite differences is OOMMF standing for Object Oriented Micromagnetic Framework [Don99]. For the simulations presented in chapter 7 the micromagnetic simulation tool MicroMagnum

---

[1] To avoid wrong evaluations of the exchange energy, the cell size should be smaller than the exchange length which neglecting magnetocrystalline anisotropy is in the order of 10 nm for nickel.

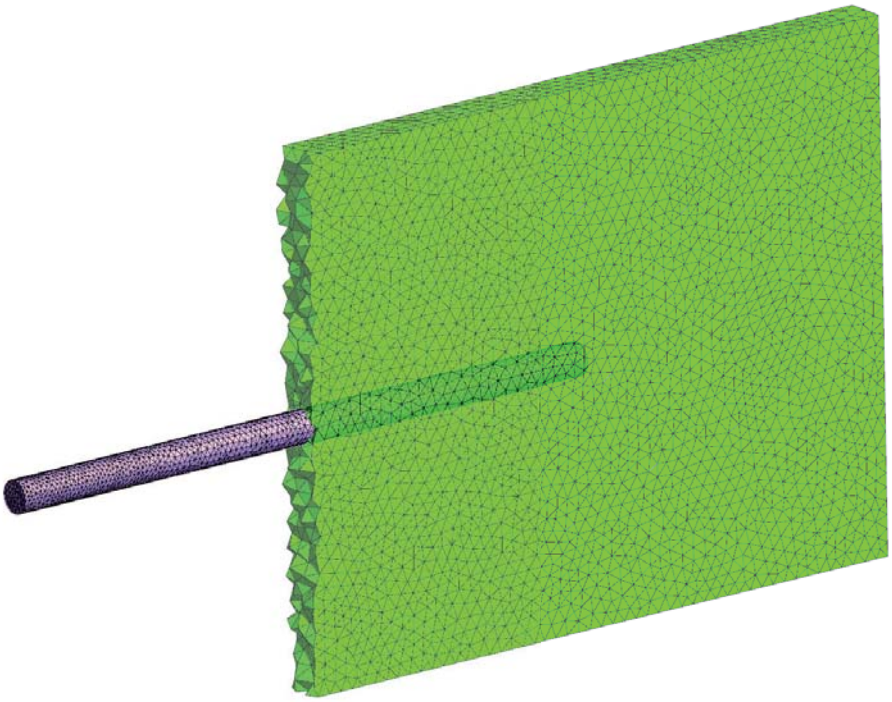

Figure 3.2: Mesh of finite elements created with Gmesh. The green box represents the vacuum around the cylindrical nanowire.

that runs on graphics-processing unites (CPUs) is used [MM]. The simulations of cylindrical nanostructures based on finite elements are performed using nmag [Fis07]. If not stated differently the parameters listed in Table 3.1 are used to simulate nickel nanostructures and the surrounding vacuum. The influence of magnetocrystalline anisotropy is neglected. The correctness of this when it comes to nickel nanowires is discussed in detail in chapter 5. The saturation magnetization M_s of the vacuum is set to a very small value instead of zero to avoid numerical problems due to division by zero. In this work we are mainly interested in static relaxed states rather than in magnetization dynamics. To faster relax the magnetization, the damping parameter

		Nickel	Vacuum
Anisotropy energy	$K(\mathrm{J/m^3})$	0	0
Exchange stiffness	$A(\mathrm{J/m})$	$10.5 \cdot 10^{-12}$	0
Saturation magnetization	$M_\mathrm{s}(\mathrm{A/m})$	$4.1 \cdot 10^5$	$1 \cdot 10^{-4}$
Damping parameter	α	$0.1 - 0.5$	0.5
Precession		false	false

Table 3.1: Standard parameters used for micromagnetic simulations. Note that the value for M_s differs from the one in Table 2.1 since here we use the same value as Hertel *et al.* [Her04].

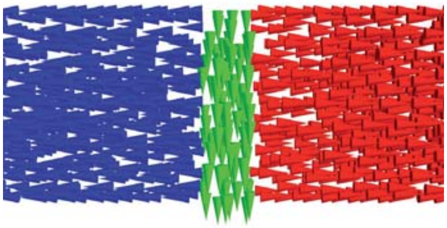

Figure 3.3: Initial magnetic configuration to place a domain wall at a certain position in a wire.

α is set to an unphysically high value of 0.5 and the precession term in the LLG equation is switched off (precession = false). For dynamic time evolutions, α is set to 0.01 and the precession term is switched on again (precession = true).

While the local terms as exchange, anisotropy, and Zeeman energies can be calculated at low cost, non-localized fields, such as the stray field, require extended computing power. MicroMagnum and OOMMF calculate the demagnetization term comparatively efficiently using Fast Fourier Transformation (FFT) techniques [Sto66, New93]. Nmag uses an approach based on the Fredkin and Koehler Hybrid Finite Element/Boundary Element method [Fre90] and usually requires much more computer memory. The expense of the computation grows proportionally to the square of surface points holding the boundary conditions. This is especially disadvantageous for the simulation of thin films. The high expense for the calculation of the stray field is the reason why the green box designed around the wire shown in Fig. 3.2 is flat. Since the cylindrical wire and therewith most of the observed magnetization configurations are rotationally symmetric the stray field in the green volume is representative. Of course this holds only if the symmetry is not broken by a domain wall. Since in this printed thesis we are limited to a two-dimensional visualization, the flat box is sufficient anyway. By tailoring the initial magnetic state it is enforced that the moments in the center of a transverse domain wall are aligned parallel or almost parallel to the large sides of the box for the magnetic states shown.

3. Visualization

After the requested set of data was calculated by the micromagnetic package the data has to be extracted and loaded by a software for three-dimensional visualization. The results on cylindrical nanostructures are presented using MayaVi2.

3.2 Examples

3.2.1 Magnetic states of a tube

This section demonstrates the influence of the individual energy terms on the magnetic states of a tube. We consider a 2 µm long nickel tube with a diameter of 100 nm and a wall thickness of 10 nm. The initial state is set so that the entire magnetization curls vortex-like around the wire axis as shown in the left inset in Fig. 3.4. The time integration of the LLG equation leads to minimization of the total energy until a local minimum in the energy landscape is reached. In the present case the magnetization aligns in parallel to the wire's axis. Only at the ends of the tube the vortex-like structure is preserved, compare right inset in Fig. 3.4. The time evolutions of the demagnetization energy E_{demag} and the exchange energy E_{ex} as well as their sum E_{tot} are plotted in Fig. 3.4. While E_{demag} slightly increases, E_{ex} is remarkably reduced. The latter can be understood considering that in the final state all magnetic moments are aligned in parallel, while in the initial state there was a small tilt between neighboring moments curling around the wire's axis on one circumference. The increase in E_{demag} can be attributed to the occurrence of magnetic charges at the end of the tube. Thus, the transition to the stable magnetic state taken at the

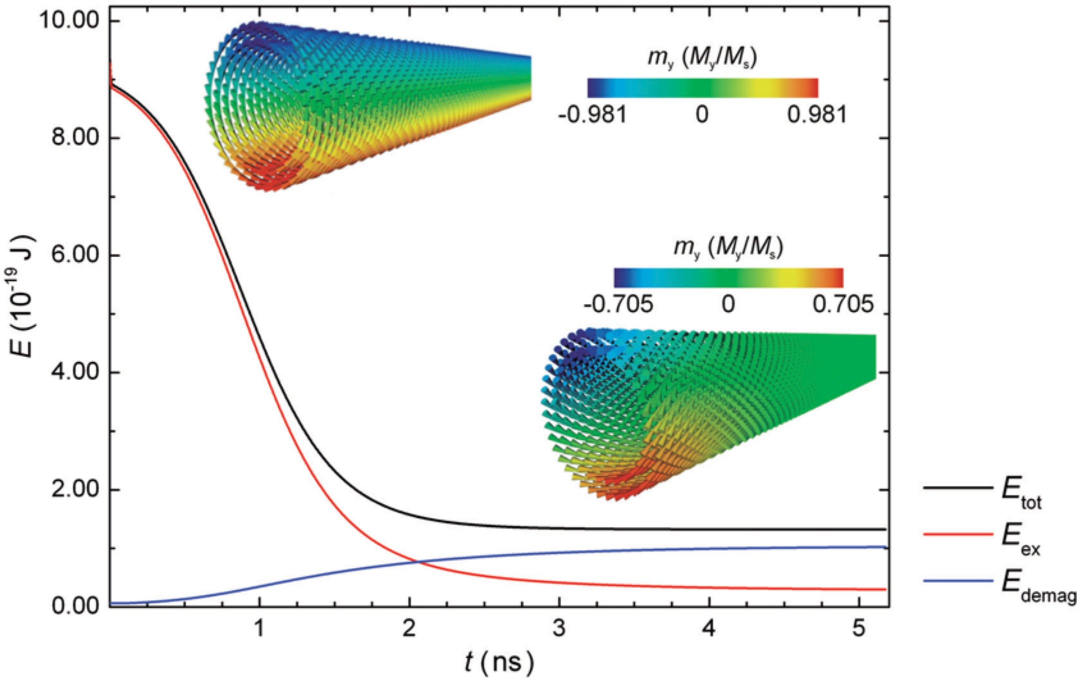

Figure 3.4: Time evolutions of the total energy E_{tot} (black), the exchange energy E_{ex} (red), and the demagnetizing energy E_{demag} (blue) of a nickel tube. The initial and final magnetic states are shown in the insets on the left and on the right, respectively. The tube is aligned in parallel to the x-axis.

end of the simulation is exchange governed. This means that we are looking at a rather untypical example here. As discussed in detail in Sec. 2.1, the equilibrium state of a sample is usually determined by the shape anisotropy associated with the urge to reduce the stray-field energy, which in this case is even increased. It has been shown analytically that the intrinsic anisotropy of a nanotube can be tailored by tuning the aspect ratios between radius, thickness, and length of the tube, and even be reduced to zero for soft-magnetic materials [Che10]. The remanent magnetic states of an iron-oxide tube enclosing a nickel core were studied experimentally in the frame of this work and are reported and discussed in publication [Kim11].

3.2.2 Demagnetization fields, nucleation, and reversal modes in cylindrical wires

Strong or inhomogeneous demagnetization fields H_{demag} can induce magnetization reversal by favoring the formation of domain walls. Figure 3.5 depicts H_{demag} simulated for the saturated states of different nickel nanostructures. In an ellipsoid (a) with a long axis of only 12 nm, which is in the order of the exchange length, the demagnetization field H_{demag} is homogeneous. There is no explicit point where a torque acts on the magnetization to initiate a nucleation process, and the magnetization reverses via coherent rotation according to the Stoner-Wohlfarth model, compare Sec. 2.1.5.

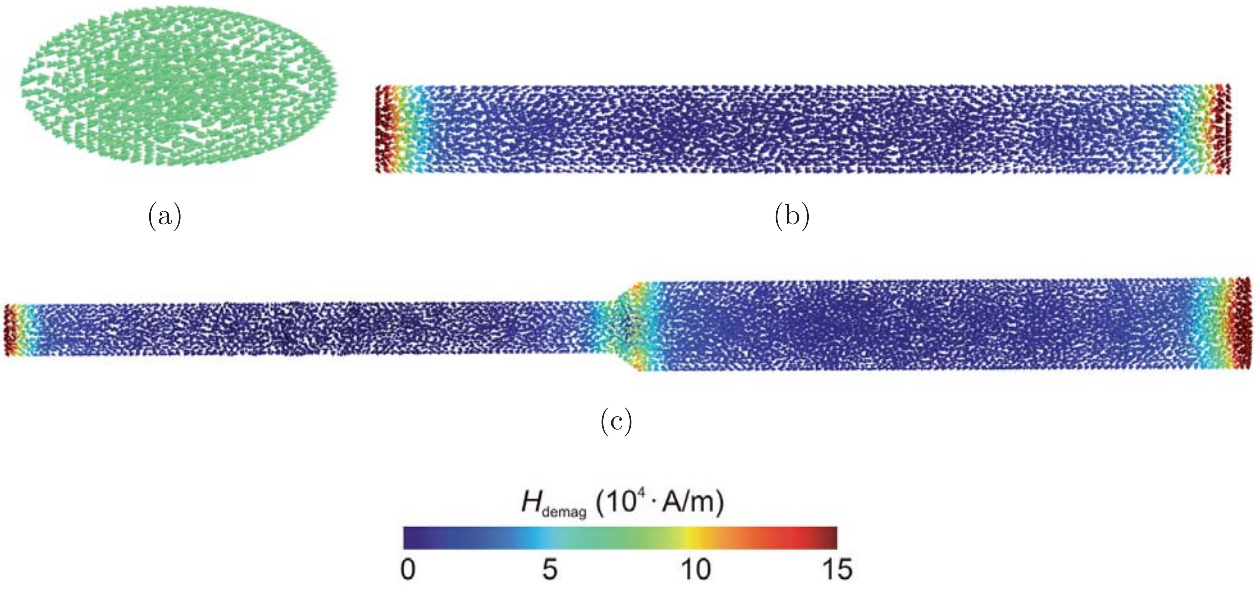

Figure 3.5: Demagnetizing fields H_{demag} simulated for (a) a 12 nm long ellipsoid, (b) a 500 nm long cylinder with a diameter of 40 nm, and (c) a 1000 nm long cylinder with one diameter modulation from 40 nm to 70 nm. The images depict saturated states.

Figure 3.5(b) depicts a 500 nm long cylindrical wire with a diameter of 40 nm. H_{demag} is strongest at the wire ends. This is were nucleation starts and a domain wall forms.

The dynamics of magnetization reversal in cylindrical nickel nanowires was studied by Hertel *et al.* using the finite element method [Her04]. Their results are comparable to ours. Depending on the diameter two reversal modes can be distinguished in cylindrical wires. For small radii a transverse domain wall nucleates at the end and propagates through the wire. The translation of the wall along the axis of the wire is superimposed with a precession. Since the magnetic moments in the wall point perpendicular to the applied field, a torque acts in radial direction and leads to a rotation of the wall, which gives the reversal type its characteristic name **'corkscrew' mode**. Without damping, the wall would not propagate at all but only precess. For larger diameters above about 42 nm the domain-wall structure is more complex. At the end of the wire the magnetization curls around the axis and a vortex is formed which propagates through the wire as a so-called Bloch point. To avoid confusion with vortex domain walls found in flat magnetic wires (compare Sec. 2.2.1), this reversal mechanism in cylindrical wires is named '**localized-curling**' **mode**.

Figure 3.5(c) depicts the demagnetization field H_{demag} of a 1 μm long cylindrical wire with one diameter modulation from 40 nm to 70 nm. In this case, an increased demagnetization field is visible not only at the ends of the wire but also at the modulation.

Magnetic charges can be considered as the sources and sinks of magnetic stray fields. The magnetization and the corresponding magnetic charges of a saturated and a relaxed straight wire are shown in Figs. 3.6 (a) through (d). Figure 3.6(e) depicts the magnetic stray field outside the wire for the relaxed case. Figure 3.7 displays the magnetization, magnetic charges, and stray field for a wire in which a transverse domain wall was prepared as described above.

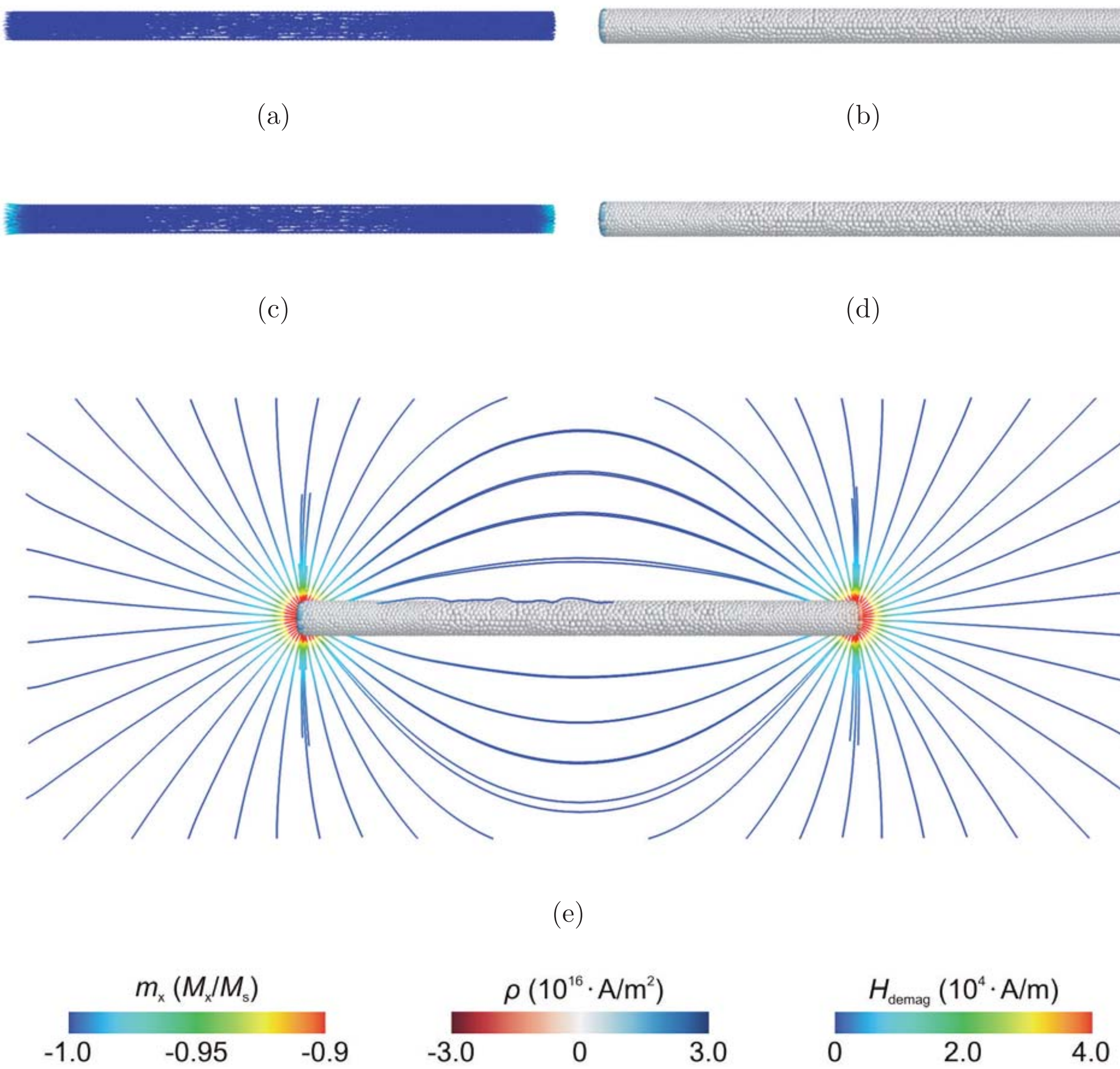

(a) (b)

(c) (d)

(e)

Figure 3.6: Simulated magnetization components m_x along the wire axis (left) and magnetic charge density ρ (right) for (a) and (b) a saturated and (c) and (d) a relaxed nickel wire with a diameter of 40 nm. The magnetic charge density for the relaxed state is also shown in (e) together with stream lines representing the resulting magnetic stray field H_demag.

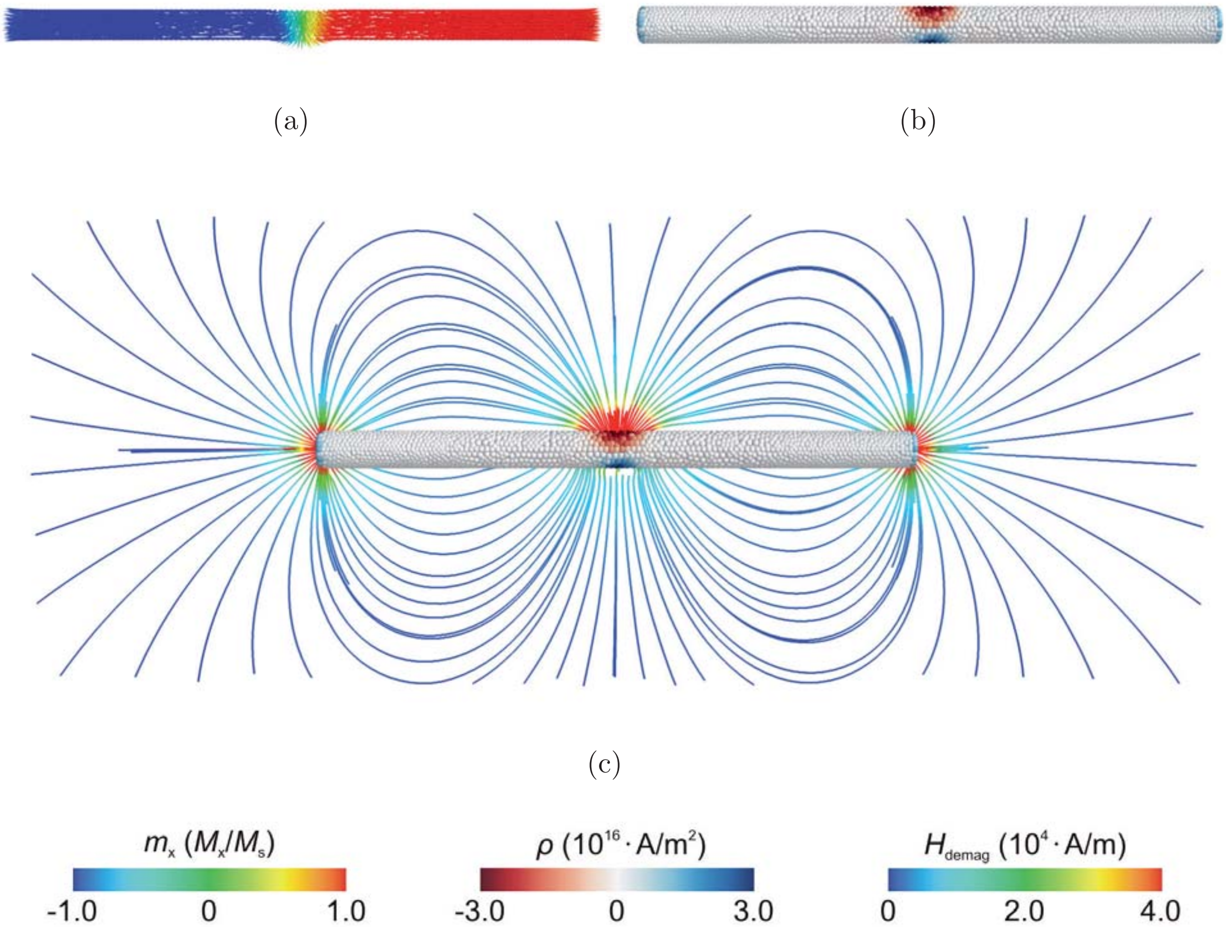

Figure 3.7: (a) Magnetization components m_x along the wire axis, (b) magnetic charge density ρ, and (c) magnetic charge density and associated stray field H_demag simulated for a straight nickel wire with a transverse domain wall. The wall was prepared as illustrated in Fig. 3.3. The images depict the relaxed state.

4 Methods

This chapter deals with the experimental methods used for the preparation and magnetic characterization of cylindrical nanowires. Section 4.1 gives an introduction to the synthesis of cylindrical nanowires. The focus lies on electrochemically synthesized nickel wires grown in alumina templates as they are investigated in this work. In the first section it is also described how the nanowires are arranged on substrates for experimental studies. The structural characterization of the wires is done by scanning electron microscopy, a standard method described elsewhere [Smi55, Nix69]. Section 4.2 describes the definition of contacts and the different setups used for magnetoresistance measurements. Magnetization reversal of the nanowires is imaged by magnetic force microscopy (MFM) as explicated in Sec. 4.3. Magnetic imaging by photoemission electron microscopy (PEEM) was proven to be a powerful tool for the study of cylindrical nanowires. Section 4.4 gives an introduction to PEEM as well as experimental details about the PEEM measurements performed. It includes a publication [Kim11] demonstrating the capability of the method. Cylindrical nickel wires with diameters between 80 nm and 300 nm were also studied by full-field transmission soft x-ray microscopy. A report of these measurements is given in the Appendix Sec. B.6.2.

4.1 Synthesis of cylindrical nanowires and sample preparation

Filling of porous templates with metal [Pos70] or conductive polymer [Mar94] facilitates the synthesis of functional nanowires with high aspect ratios. The template-based synthesis approach offers versatile options as concerns shape and material of the prepared particles. Releasing of the particles from a template provides a large amount of wires at low expense. The application fields of so-prepared nanostructures range from biomedicine over photonics to magnetism. Possible templates are track-etched polymer membranes. They are commercially available and offer a wide variety of pore sizes down to a few nanometers [Qui72]. Polymer fibrils with diameters of only 3 nm for example have high potential for nanometer-scaled electronic devices [Wu94]. The interpore distance in track-etched membranes can be high, such that magnetic nanowires in a template can be considered isolated from their neighbors as

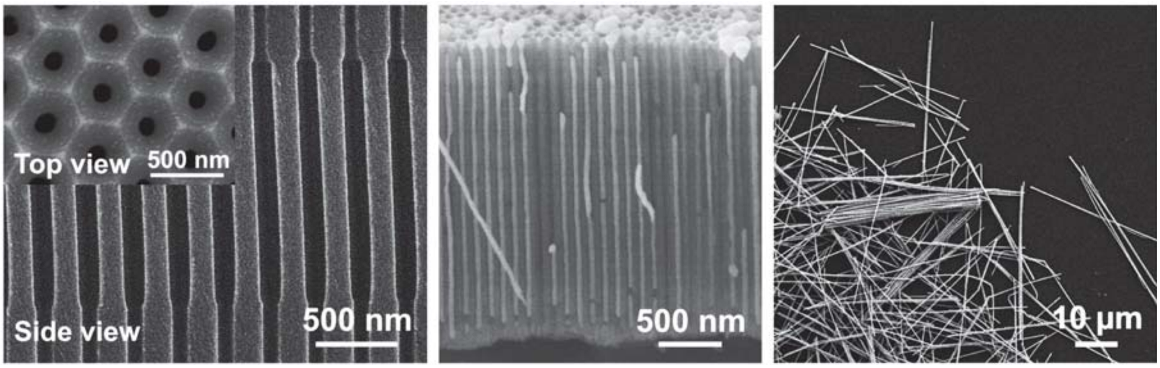

(a) (b) (c)

Figure 4.1: Scanning electron micrographs of (a) an empty membrane with diameter-modulated pores (from Ref. [Lee06]), (b) a membrane filled by electrochemical deposition (from Ref. [Sau02]), and (c) a bunch of individual wires on a substrate after the dissolution of the membrane.

concerns magnetic dipolar interaction [Weg98]. A disadvantage of track-etched membranes is that the pores are disordered, have a large distribution of diameters, and are not in parallel to one another [Mei96]. Alumina templates can provide highly ordered hexagonally arranged pores with discretized pore diameters [Jes98, Li98]. The perspective of mass production of monodisperse nanoparticles at low costs makes this method very attractive. The pore diameters of alumina templates can be widened by wet-chemical etching [Li98] or reduced by atomic layer deposition [Kne07, Lee09].

In this thesis the main focus lies on cylindrical nanowires synthesized by electrochemical deposition of nickel into self-organized pores of alumina templates. The nanostructures are provided by the group of Kornelius Nielsch at the Institute of Applied Physics, University of Hamburg. The individual steps of wire synthesis are exemplarily shown in Fig. 4.1. First, hexagonally ordered pores are etched into an aluminum foil by anodization. The diameter of the pores is determined by the anodization parameters and the acid used [Nie02b]. Typical pore diameters obtained are about 80 nm for so-called hard and 160 nm for mild anodization. Combining hard and mild anodization enables one to grow pores with diameter modulations as depicted in Fig. 4.1(a) [Lee06, Pit11, San11]. An alternative way to prepare diameter modulations is illustrated in Fig. 4.2. The anodization is stopped after a certain time and the pores grown so far are covered with a silica conformal coating by atomic layer deposition. Then a further anodization step is performed in the same anodization conditions as the first one. While the first grown segments are protected by the silica shell, the second segments can be widened by wet-chemical etching in phosphoric acid. The maximum pore diameter is limited by the interpore distance determined by the first anodization. Once pores of the desired shape are grown, the membrane

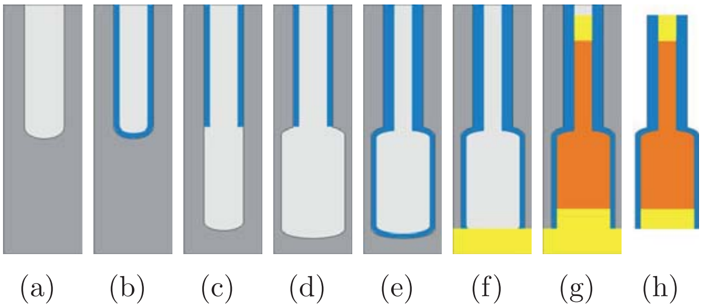

Figure 4.2: Schematic of the synthesis steps for the preparation of cylindrical wires with one diameter modulation created by means of pore widening. (a) First anodization step. (b) Atomic-layer deposition of silica shell (blue). (c) Second anodization step. (d) Widening of the non-protected pore segment in phosphoric acid. (e) Second atomic-layer deposition of silica. (f) Opening of the pore from the rear side and deposition of gold (yellow) as an anode for the next step. (g) Electrochemical deposition of gold, nickel (orange) and another gold segment. (h) Individual nanowire after the dissolution of the membrane.

can be conformally covered with different kinds of oxides using atomic-layer deposition to synthesize tubes [Bac07, Pit09] or layers protecting the material deposited in a possible next step: the synthesis of cylindrical nanowires. For this purpose, the membrane is opened from the rear side by reactive-ion etching and covered with a gold film serving as an anode. The so-created template is then filled by electrochemical deposition to grow solid cylinders [Nie00, Nav07]. Typical deposition parameters for nickel are given in Refs. [Nie02b] and [Pit11]. Details about the fabrication of the modulated nickel and nickel-iron wires studied are given in Refs. [Pit11] and [Sal12] as well as in the Appendix Sec. B.1. Most of the wires investigated were covered with a silica shell to prevent oxidation. Figure 4.1(b) shows a filled template. To obtain individual wires the alumina template is removed by selective chemical etching in a mixture of chromic and phosphoric acids. After filtration the wires are suspended in a solvent of choice, usually isopropanol or ethanol. For experimental studies the solution is dripped onto a silicon wafer substrate and left to dry in an applied magnetic field to align the wires in parallel. With a well chosen concentration of wires and a substrate wetted by the solvent, the method works quite well to prepare large areas with individual wires aligned along the same direction. However, capillary forces of the withdracting meniscus are strong, and accumulations of wires as shown in Fig. 4.1(c) are hard to avoid. If perturbing for the experiments to be performed, these accumulations can be removed by rinsing the sample or by wiping it with a Q-tip.

For magnetic imaging, the wires are applied on a marker substrate as shown in Fig. 4.3 prepared by electron-beam lithography. Every 400 μm there is a letter large enough to be visible in an optical microscope as the one included in the MFM setup.

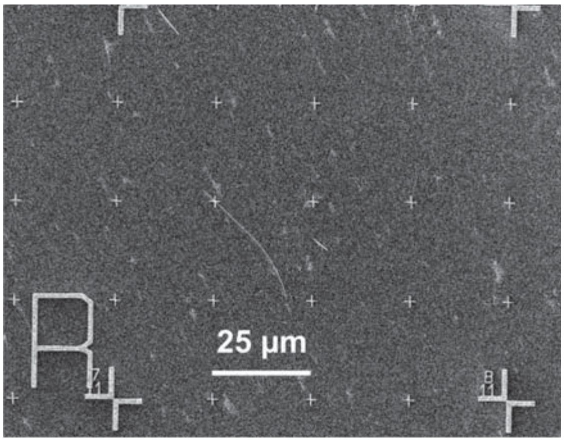

Figure 4.3: Scanning electron micrograph of a silicon wafer substrate with gold coordinates and markers defined by electron-beam lithography.

For PEEM imaging the field of view can be chosen between 70 µm and 3 µm, at the XM-1 microscope it is fixed to 10 µm. To relocate the wires designated for imaging with such a limited field of view, there are markers every 100 µm that can be identified by two numbers written next to them indicating the coordinates on the sample. Furthermore, there are small markers every 25 µm. These markers are required for the drift correction.

4.2 Magnetoresistance measurements

Changes in the magnetization configuration of ferromagnetic structures can lead to variations of their electrical resistivity. Due to these effects that are elucidated in Sec. 2.3 the magnetic behavior of nanowires can be studied by magnetoresistance (MR) measurements. This section describes how electrical contacts are defined on individual nanowires as well as the three different setups used for MR measurements. To demonstrate the potentials of MR measurements, some results are presented and discussed in this section.

Definition of contacts

For MR measurements, contacts are defined either by electron-beam lithography with a scanning electron microscope or by optical lithography. The individual steps of sample preparation are illustrated in Fig. 4.4. After the application of nanowires the substrate is covered with either an electron- or photon-sensitive positive resist. The thickness of the resist is chosen at least three times the diameter of the nanowire to facilitate the later lift-off step. For exposure by optical lithography a printed mask is inserted into the optical path of a conventional light microscope and projected onto the sample. The positioning of the mask is performed manually by eye while a filter in the optical path prevents the exposure of the resist. With this method that is

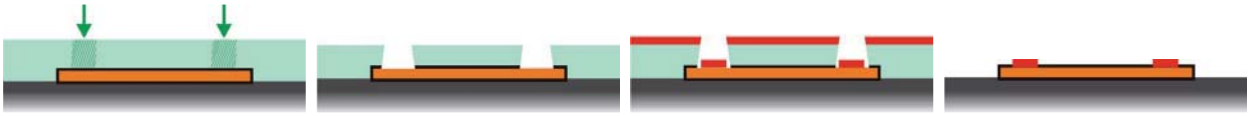
(a) Lithography (b) RF-plasma (c) Deposition (d) Lift-off

Figure 4.4: Steps of sample preparation during definition of contacts. (a) The sample is covered with resist (green) and exposed either by electron-beam lithography or optical projection lithography. (b) After development a radio-frequency (RF) plasma is applied to remove the oxide layer (black) on top of the nanowire (orange). (c) A metal film (red) is deposited in the same vacuum chamber. (d) The undesired metal film is removed by lift-off of the resist leaving the nanowire with ohmic contact pads.

described in detail in the diploma thesis of Tim Böhnert [Böh09] it is possible to define contacts on several nanowires within short time. Process parameters are given in the Appendix Sec. B.4. Samples prepared by optical lithography are displayed in Fig. 4.5. The round boundary of the individual exposures reflects the spot of the light microscope. The resolution of optical lithography is limited by the wavelength of the light used as well as by the properties of the resist, what leads to a minimum width and distance of the contact pads of about 1.5 μm. If a better resolution or high precision of the contact placement are required, electron-beam lithography is the method of choice. The method enables one to place contacts as thin as 150 nm with an accuracy of about 50 nm. A disadvantage is the complexity of sample processing. Since the resist is electron sensitive, the positioning of the contacts has to be done 'blind' making use of markers that have to be prepared in an antecedent lithography step. The position of every individual wire has to be determined relative to such markers before the sample is covered with resist, and the lithography design has to be adapted for every wire individually. A detailed description of the procedure, process parameters, as well as images of so-defined contacts on modulated nanowires are given in the Appendix Sec. B.3.

After exposure, the sample is developed to remove the resist in the exposed regions. Then the sample is transferred into a sputtering chamber in which a radio-frequency plasma can be applied. The plasma is needed to remove the silica shell or the native oxide layer of a nanowire, compare Fig. 4.4(b). This step is crucial to obtain ohmic contacts and has to be done in the same vacuum system as the deposition of the contact material to avoid reoxidation. The metal film deposited in the next step (Fig. 4.4(c)) consists of 2 nm aluminum serving as adhesive layer and a $120-200$ nm thick gold film.[1] Details about the etching and deposition parameters for the individual wires studied are listed in the Appendix Sec. B.5. The last step is the lift-off of

---

[1] The contacts on the wire called 3w were defined in a different sputtering chamber with comparable parameters and a metal film of titanium and platinum instead of aluminum and gold.

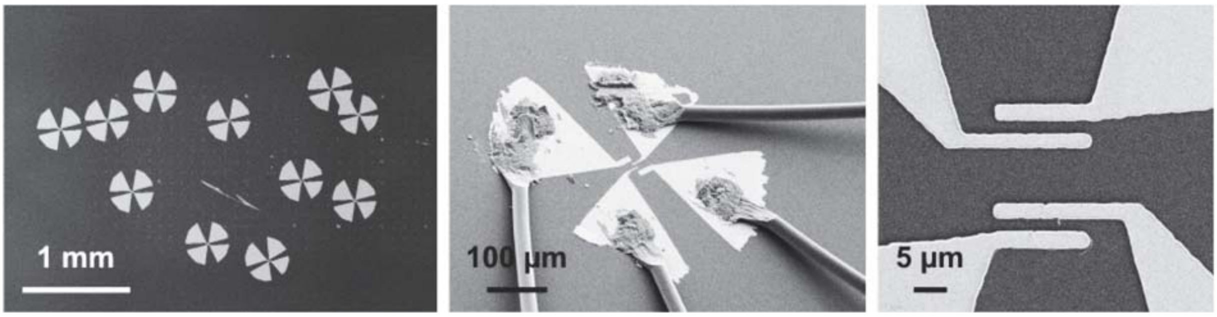

(a) (b) (c)

Figure 4.5: Scanning electron micrographs of gold contacts for magnetoresistance measurements. (a) Overview of a sample where contacts on several wires were defined by optical projection lithography. (b) Structure consisting of four bond and contact pads defined during one projection step. The bond pads are connected to a chip carrier (not shown) by wire bonding. (c) Close-up of optically defined contact pads.

the resist mask leaving an individual wire with several ohmic contacts as illustrated in Fig. 4.4(d).

Setups

For MR measurements on cylindrical nanowires three different setups are used. The contact pads of the wires are connected to the measuring instruments either by a probe station (setup 1 and setup 3) or by wire-bonding on a chip carrier as shown in Fig. 4.5(b) (setup 2).

Setup 1 is a probe station designed for high-frequency measurements [Boc11]. Two coil pairs on iron yokes allow for the application of an in-plane field up to 120 mT at varied angles (0° - 360°). The setup comes with a feedback circuit developed by Toru Matsuyama from the Institute of Applied Physics, University of Hamburg, which controls the applied magnetic field via Hall sensors. Figure 4.6 illustrates the absolute angle φ at that the external magnetic field is applied. $\varphi = 0°$ if the field points horizontally to the right. When it comes to the discussion of the results, the angle of interest is the angle θ between the applied magnetic field and the axis of a nanowire. This angle can be estimated from the way the sample is built into the setup. Using one's hands and an optical microscope (the resolution of which is not sufficient to see individual nanowires) the sample is adjusted such that the bottom edge of the substrate is aligned horizontally. The orientation of the wire is then inferred from scanning electron micrographs of the sample taken earlier. With this procedure the direction of a wire can be estimated with an accuracy of about ±2 degrees. Comparable procedures are applied at the other two setups.

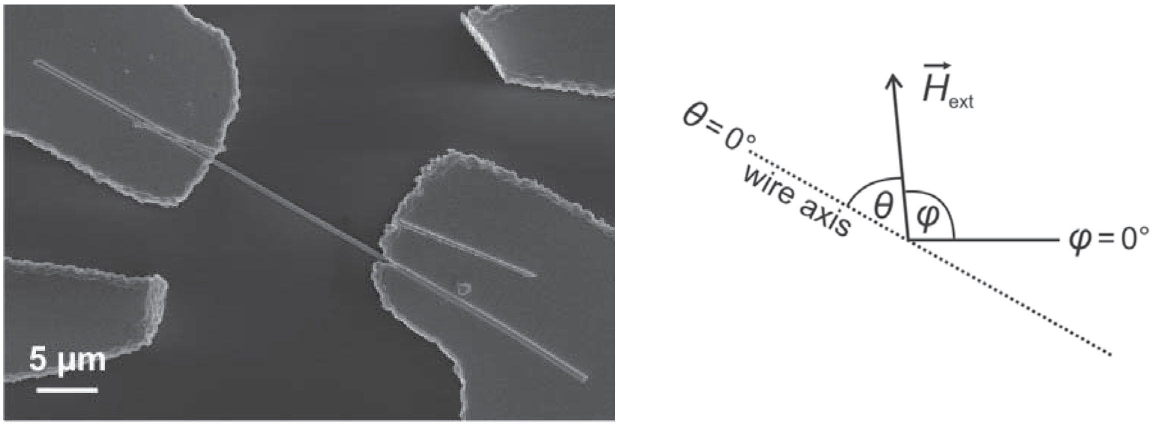

(a)

(b)

Figure 4.6: (a) Scanning electron micrograph of a wire called Jan5-01. (b) Illustration of the nomenclature for the angles describing the direction of the applied magnetic field.

MR measurements at setup 1 are done in two-point geometry with direct current (DC). The signal is read out with a multimeter (Keithley 2000) after amplification by a preamplifier (Stanford Research SR 560). There is no measurable thermal interaction between the coil currents and the resistivity of the sample, but the resistance measurements performed at setup 1 are often affected by the instability of the room temperature.

Setup 2 consists of a pair of Helmholtz coils (the same as used for MFM measurements) and a platform for a chip carrier to which the sample to be measured is connected by wire bonding. The maximum field value that can be applied using the Helmholtz coils is 100 mT. To change the direction of the uniaxial magnetic in-plane field relative to the wire axis the platform can be rotated manually. MR measurements at this setup are done in four-point and two-point geometry using alternating current (AC) and a lock-in amplifier (Stanford Research SR 830). Even though the coils are water cooled, the temperature increase caused by strong coil currents is visible in the resistance measurement. The sample can be thermally isolated from the environment by a copper shield with a built-in thermal element. While using this shield only two-point measurements are possible.

Setup 3 is a conventional probe station from Lakeshore (EMPX-HF) that allows for the application of a uniaxial in-plane field up to 550 mT. The sample can be rotated manually to vary the angle between the applied magnetic field and the wire's axis. During MR measurements the probe station is evacuated below 10^{-5} mbar to ensure thermal stability. Measurements are done with AC current in two-point and four-point geometry using a lock-in amplifier (Stanford Research SR 830).

All measurements are conducted at room temperature. The current applied during the measurements is chosen such that the resistance change indicating the magnetization reversal is at least five times as high as the noise. At setup 2 about 5 μA have to be applied for this purpose. At setup 3 an applied current of 10 μA is sufficient to obtain a resistance change 100 times larger than the noise. At setup 1 most measurements are done with 500 μA leading to a resistance change about 20 times larger than the noise. The maximum current density in the wires studied was about $1.5 \cdot 10^{10}\ \frac{\mathrm{A}}{\mathrm{m}^2}$. If not stated otherwise, measurements were done at setup 1.

Collection, illustration and significance of the data

Figure 4.7 depicts MR traces measured at setup 1 on the nickel wire shown in Fig. 4.6(a). The curves displayed in Fig. 4.7(a) are recorded in 10-degrees steps by sweeping the applied magnetic field symmetrically from +100 mT to −100 mT in a fixed direction for every curve shown. In Fig. 4.7(b) a different measuring mode, in the following referred to as saturation mode, is used. In this mode, the wire is first saturated by applying a field of +100 mT in a direction close to the wire axis (in this case 160 degrees and 340 degrees) before sweeping the reverse field from 0 mT to −100 mT at a certain angle in the opposite hemicircle ± 10 degrees, namely from 240 degrees to 80 degrees and 60 degrees to 260 degrees. The saturation mode has several advantages. First, the ferromagnetic wire studied is more likely to be in a defined, reproducible state if applying a strong field along the wire axis, whereas complex magnetic states can be prepared by applying a field at large angles. Second, the saturation mode is less time consuming, since only half of the data is recorded. At this point it has to be discussed which information can be extracted from the MR traces. For this purpose two MR traces of Fig. 4.7(a), namely the red ones recorded at $\varphi = 140°$ and $320°$ are plotted together in Fig. 4.8. The x-values of the 320-degrees curve are multiplied by −1 to obtain the conventional diagram of MR traces. The absolute resistance value in zero applied field is referred to as remanence R_0. It is used to calculate the MR-ratio $= \frac{R(\mu_0 H) - R_0}{R_0}$ which is plotted here. Possible magnetic configurations of the sample leading to the observed MR traces are sketched in the figure. There are two characteristic features of the curves. One of them is the curvature. Coming from saturation where the magnetic moments are aligned along the wire, the resistance continuously decreases in a certain manner. Assuming that the main contribution to the resistivity change originates from the anisotropic magnetoresistance (compare Sec. 2.3.4), this means that magnetic moments continuously rotate away from the wire's axis. The other, more prominent feature is a sudden jump of the resistivity at a distinct field value referred to as the switching field. While for the 140-degrees curve only one jump occurs, two jumps are observed when sweeping the field in the opposite direction. The latter indicates that the magnetization does not reverse at once what might be attributable to the pinning of a domain wall.

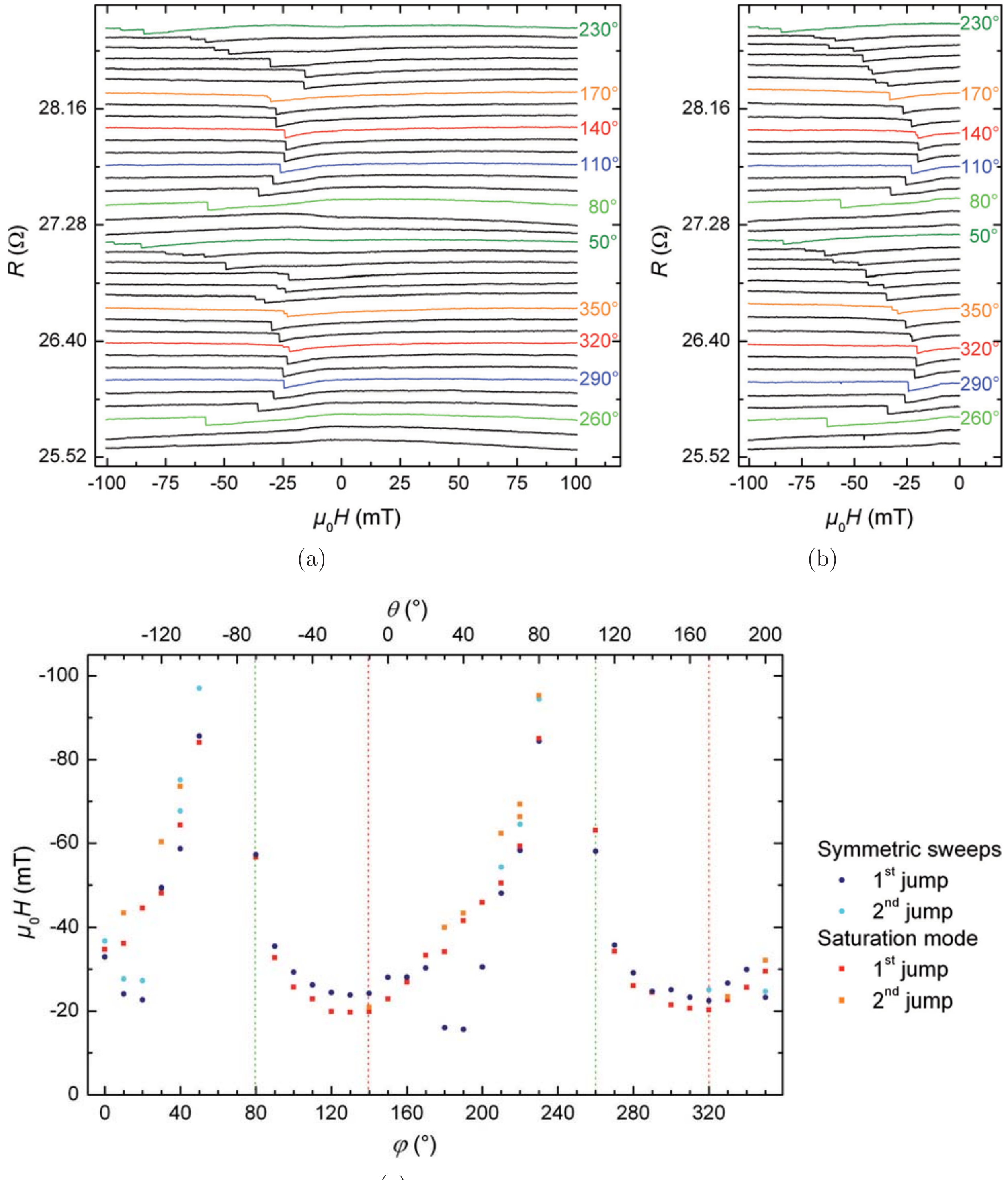

(a) (b)

(c)

Figure 4.7: Magnetoresistance traces of a nickel wire called Jan5-01 recorded at setup 1. For each curve in (a) the field was sweeped at a fixed absolute angle φ from +100 mT to −100 mT, while in (b) the wire was saturated by applying +100 mT along its axis ($\varphi = 160°$ or 340°) before sweeping a reverse field from 0 mT to −100 mT at a certain angle. Selected curves recorded at the same angle are shown in distinct colors in (a) and (b). Apart from the lowest curves the curves are shifted for clarity. (c) The blue circles and red squares are the switching fields indicated by the jumps in (a) and (b), respectively, plotted versus the absolute angle φ and the angle θ between the applied magnetic field and the wire's axis estimated from Fig. 4.6.

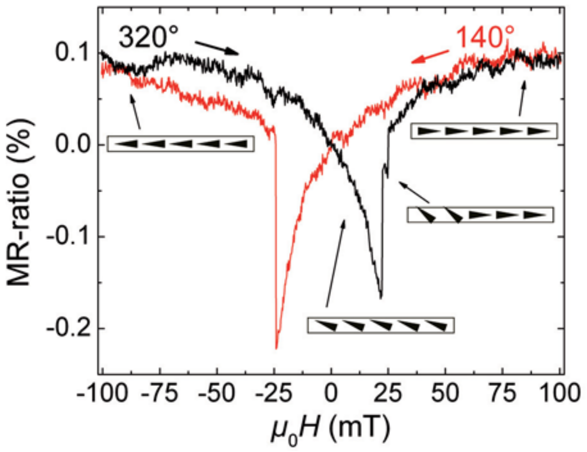

Figure 4.8: Magnetoresistance ratio of a cylindrical nickel nanowire (Jan5-01) and sketches of possible underlying micromagnetic configurations.

In order to facilitate the comparison and interpretation of the data, the switching fields are usually plotted as shown in Fig. 4.7(c). Each blue circle and red square represents a jump observed in Figs. 4.7(a) and (b), respectively. The darker symbols correspond to the first jump, while every additional jump is represented by a bright symbol. In this plot the difference of the two measuring modes used is clearly visible. While the data recorded in the saturation mode lies on a deformed but clearly deducible curve, there are some considerable outliers at around $\varphi = 10°$ and 190° if the field is sweeped symmetrically. A comparable behavior is observed for several other wires studied. If the applied magnetic field is sweeped symmetrically from +100 mT to −100 mT at a high angle between the field direction and the wire axis, the jump in the resistance versus field curve even happened to occur at positive fields, that is before a reverse field was applied. This can be attributed to complex magnetization patterns forming in the wire. When a strong field applied almost perpendicular to the wire's axis is slowly decreased, the magnetization might suddenly jump into the remanent state at one point instead of continuously rotating there.

Figure 4.7(c) has two x-scales. The bottom one depicts the absolute angles φ as measured, the upper one gives the estimated angles θ between the applied magnetic field and the wire's axis, compare Fig. 4.6(b). θ is an estimate both from the way the sample is positioned, and from the data measured. Reference points for the latter are the following two assumptions. First, the switching field is expected to be symmetric around zero (compare sections 2.1.5 and 2.1.6). Second, the switching field should have a minimum if the field is applied in parallel to the wire axis, assuming that the magnetization reverses via curling or domain-wall motion [Aha97a, Shi99]. For the present wire, none of this is the case, so it is hard to estimate the actual direction of the wire's axis. In chapter 5 only data of wires that show a more symmetric angular dependence of the switching field is presented.

For geometrical and technical reasons most of the MR measurements are conducted in two-point geometry. This means that the resistance of the measurement setup and the contacts (typically 10 Ω in total) contributes to the signal. The more voltage

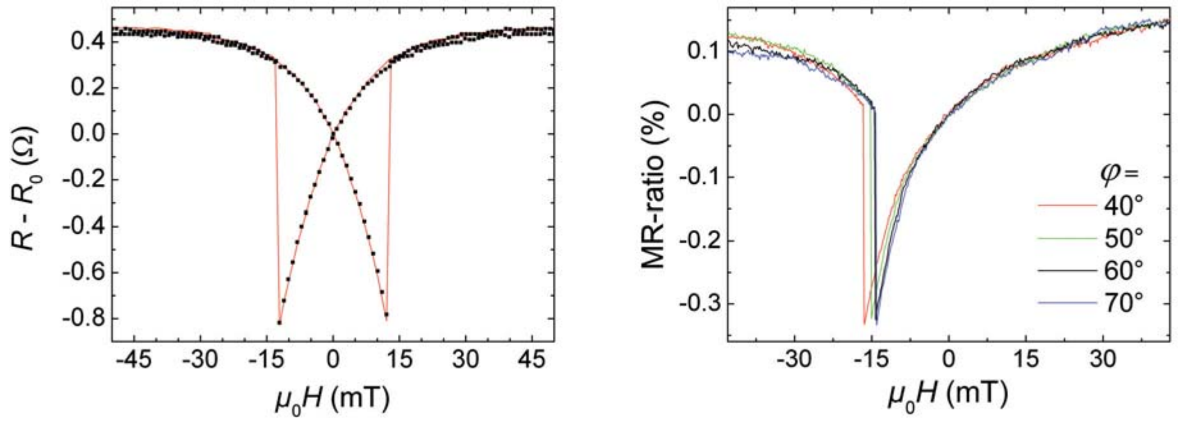

(a) (b)

Figure 4.9: (a) Comparison of the magnetoresistance traces measured in four-point geometry (red curve) and in two-point geometry between the inner contacts (black squares) on a wire called 3w at setup 3. (b) Magnetoresistance traces for four different angles φ between the applied magnetic field and the wire's axis. The axis is approximately aligned along the 55-degrees direction. The measurements were done at setup 1 between the outer two contacts o and u on wire T5-03 which is shown in Fig. 4.10(a).

drops at the contact area between the gold pads and the wire, the more sensitive is the measurement to this region. Figure 4.9(a) compares MR traces recorded in two-point and four-point geometry on a wire with comparably high contact resistance. If the resistances at remanence R_0 (194 Ω and 130 Ω, respectively) are subtracted, the curve progression is identical. This proofs that the meaningfulness of results obtained in two-point geometry is not reduced, even if the contact resistance is high. Figure 4.9(b) compares MR traces measured between the outer contacts (o and u) of the nickel nanowire shown in Fig. 4.10(a) for four directions of the external field, namely 40, 50, 60, and 70 degrees. From the way the sample was built in into the probe station and from the angular dependence of the switching field (not shown) it can be inferred that the wire axis approximately lies along the 55-degrees direction. Comparing the curvature of the MR traces one can conclude that the measured signal is not very sensitive to the angle between the applied field and the wire's axis, as long as the angle deviation from the wire axis is smaller than 15 degrees. This observation and the fact that a comparable behavior is found for other wires as well, justify that measurements are usually done in steps of 10 degrees, and that for the comparison of the curve progression of different wires presented in Fig. 5.17 of the results chapter, one of the curves of a wire is chosen which is close to zero degrees but possibly about 10 degrees away from the wire axis.

As can be inferred from the scanning electron micrograph of wire T5-03 (Fig. 4.10(a)) the MR traces shown in Fig. 4.9(b) are measured across two other contacts in the middle of the wire. The fact that only one jump is visible in the curves indicates that by the definition of contacts no artificial pinning sites are created. This cannot be taken for granted, since the sputter etching for the removal of the oxide shell of the wire is likely to take away some of the ferromagnetic material as well.

To further study the influence of the contacts and their positions on the MR traces, measurements were done between different combinations of contact pairs on wire T5-03. The nomenclature is illustrated in Fig. 4.10(a). Figures 4.10(b) through (d) depict resistance versus field curves recorded at an absolute angle φ of 60 degrees, which is close to the direction of the wire's axis. Each curve in a graph was measured using a different combination of contact pads as noted in the figure. Table 4.1 lists the distances z and the resistances at remanence R_0 between the individual combinations of contacts. In Fig. 4.10(b) the offsets between the resistances R measured at the respective field values and the resistances at remanence R_0 are plotted. The shapes of these curves differ strongly, especially as concerns the slope before the switching occurs. In Fig. 4.10(c) the offsets are normalized to the length z of the wire segments between the individual contacts and multiplied by the average area cross section $A = \pi \cdot (d/2)^2$, where the diameter is $d = 315$ nm. As expected, the curves look more similar now. The remaining differences might be attributable to the varying diameter of the wire and the unknown exact current paths. For example it can not be excluded that the wire segments underneath the contacts l and r are partially short-circuited by the deposited metal film. In Fig. 4.10(d) the resistance offsets are individually corrected by the factors z_{fit} and d_{fit} listed in Table 4.1. The curves look very similar now. The small variations left might be attributable to thermal fluctuations or locally varying magnetic properties. Figures 4.10(b) through (d) demonstrate that the curvature of MR traces can only be compared if normalized properly, especially when it comes to the comparison of different ferromagnetic wires.

Contacts	$R_0(\Omega)$	z (µm)	z_{fit}(µm)	d_{fit}(nm)
r and l	21.95	4.5	4.5	350
o and u	48.86	22	17	320
u and l	20.84	4.8	4.5	305
o and r	20.67	4.7	5.3	280
o and l	34.45	13.1	13.1	315

Table 4.1: Parameters of wire T5-03. R_0 are the resistances between the different combinations of contacts at remanence. z is the distance between two contact pads determined by scanning electron microscopy. z_{fit} and that d_{fit} are fitted distances between the contacts and fitted diameters of the nickel wire, respectively, that yield a good analogy of the magnetoresistance traces depicted in Fig. 4.10(d).

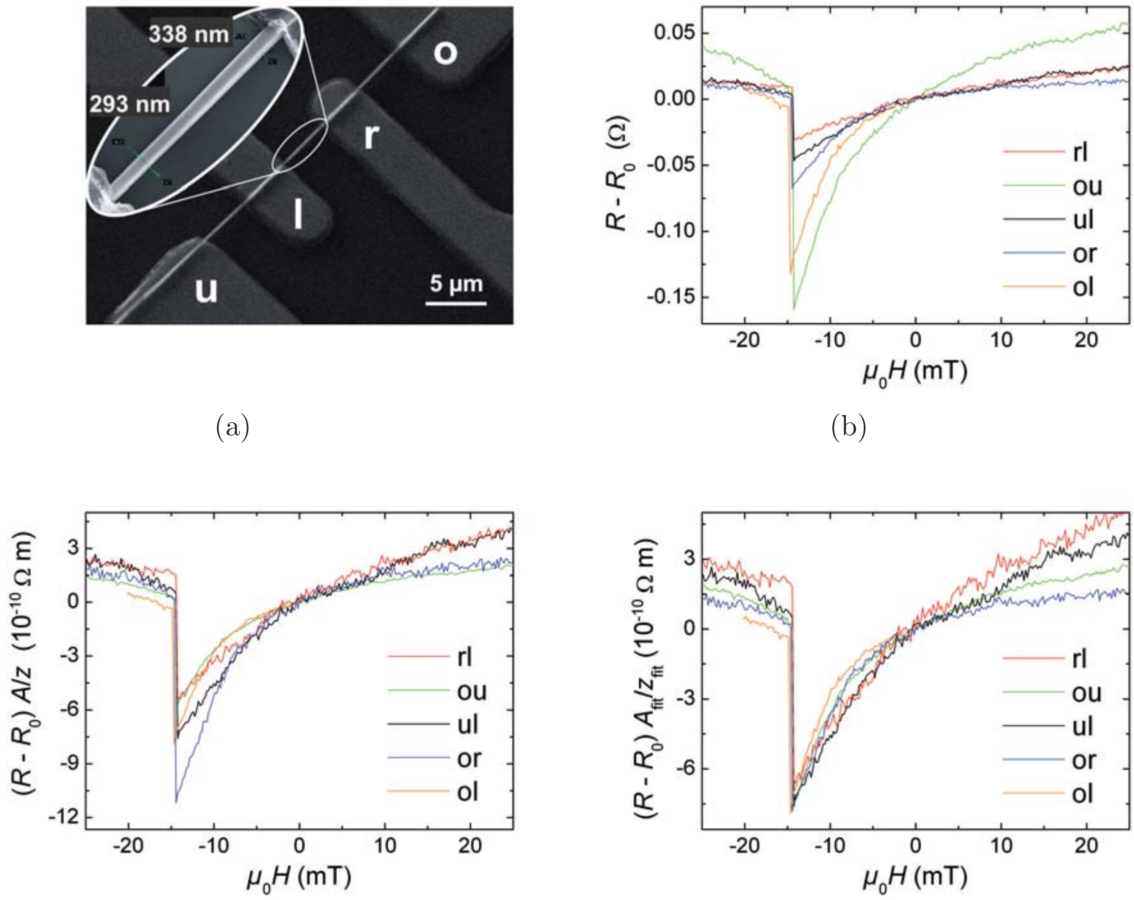

(a) (b)

(c) (d)

Figure 4.10: (a) Scanning electron micrograph of wire T5-03 with an average diameter d of 315 nm and a length of 37 µm. The lengths z of the wire's segments between the individual contact pads labeled u, l, r, and o are about 4.5 µm. (b) through (d): Magnetoresistance traces measured between different combinations of contacts. All curves are recorded applying the external field at an angle of $\varphi = 60°$, i.e. almost along the wire's axis. The curves in (b) are the offsets between the resistances R at the respective field values and the resistances at remanence R_0. In (c) the offsets are normalized to the lengths z of the wire segments and multiplied with the average area cross section $A = \pi \cdot (d/2)^2$. In (d) the offsets are individually corrected by the factors z_{fit} and d_{fit} listed in Table 4.1.

4.3 Magnetic force microscopy

Magnetic force microscopy (MFM) is a scanning probe microscopy method based on atomic force microscopy (AFM) and the stray-field interaction between a magnetic probe and the magnetic moments of a sample [Sar91]. MFM takes advantage of the different force-distance curves of atomic and magnetic interactions. To separate the magnetic information from the topography a two-pass method with a feedback loop is used [Mar87]. The first pass is equivalent to the one used in AFM. Depending on the sample the probe is scanned over the surface in contact or in non-contact mode. The interaction between the probe and the sample is given by chemical bonding, van-der-Waals forces, capillary forces, and others. In the contact mode this results in a bending of the cantilever on which the probe is fixed, whereas in the non-contact mode the resonance frequency of the cantilever is changed. To detect the deflection or frequency change a laser spot is reflected from the back of the cantilever into a four-quadrant diode. The signal is translated into a graph representing the topography of the sample. In a second pass along the same line the probe is scanned at a constant height above the sample surface where atomic forces are negligible to detect the stray-field gradient of the sample's magnetization. The magnetization of the probe is usually perpendicular to the sample surface, which means that it is mainly interacting with the stray-field components perpendicular to the sample plane [Loh99, Bar04]. The typical lateral resolution of an MFM scan is about 30 nm [Abe98], but never better than the scan height. Putting together the individual line scans yields topography and magnetic images as the ones shown in Fig. 4.11. Figure 4.11(a) reveals the topography of a 220 nm thick nickel wire with gold ends. The wire appears wider than it actually is, since the image is a convolution of the wire's topography and the shape of the probe [Bel98]. Figures 4.11(b) through (d) are the magnetic images of the wire recorded at different applied magnetic fields. As expected the gold ends are not visible in the magnetic images. Figure 4.11(b) is the remanent state after saturation at +64 mT. Due to the shape anisotropy the magnetization of the nickel wire is expected to align in parallel to the wire axis at remanence, and the magnetic stray field is strongest and of opposite direction at the wire ends, compare the simulated state shown in Fig. 3.6(e). The main signal[2], a dark and a bright spot, is obtained at the interfaces between the nickel wire and the gold ends. Thus, the magnetic image in Fig. 4.11(b) identifies the nickel wire in a single domain magnetic state.

To study the magnetization reversal of the nanowire MFM images were recorded at different applied magnetic fields. Figure 4.11(c) is the magnetic image of the nickel wire at −19 mT. Both wire ends show dark magnetic contrast. Of course, this does

---

[2] A weak magnetic contrast is also visible along the entire wire. The origin of this feature, which shall be disregarded here, is discussed in Sec. 5.2.

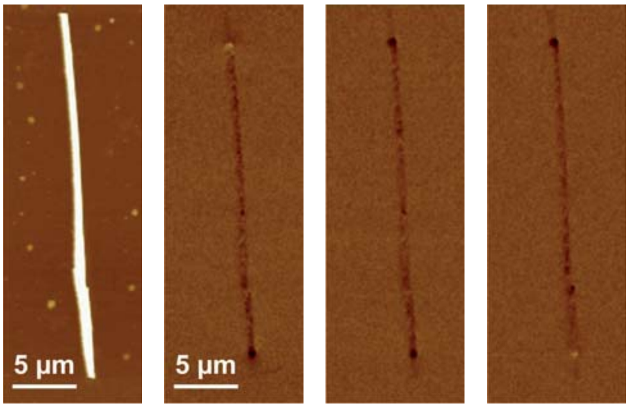

(a) (b) 0 mT (c) -19 mT (d) -20 mT

Figure 4.11: Magnetic force microscopy images revealing (a) the topography and (b) through (d) the magnetization reversal of an individual nickel nanowire with gold ends.

not mean that we are looking at a magnetic monopole. Depending on the size of the scanned area and the image resolution recording one MFM image takes between 10 and 45 minutes. If the applied field is close to the switching field, the probability of thermally activated magnetization reversal is high (compare Sec. 2.2.2). For the interpretation of the MFM images the slow scan direction, i.e. whether the image area is scanned top down or vice versa, can play a role. Figure 4.11(c) was scanned bottom up. When the scan was started the lower wire end showed the same dark magnetic contrast as in (b). During the scan the magnetization must have reversed, since when the upper wire end was scanned, its magnetic contrast had changed to dark. The switching is confirmed in Fig. 4.11(d), the subsequent MFM image recorded at −20 mT, where the magnetic contrast of the nickel wire is reversed compared to Fig. 4.11(b).

Besides the long time it takes to record an MFM image, the stray-field interaction between the magnetic probe and the sample magnetization is disadvantageous. To circumvent at least one or both of these problems two other modes of MFM measurements are performed in this work. To determine the switching field of a nanowire it is sufficient to monitor the magnetic stray field of one wire end. For this purpose the probe is continuously scanned along the same line across a wire end while driving the external magnetic field. The method is demonstrated in Fig. 4.12 by imaging the upper end of the nickel wire shown in Fig. 4.11. Figure 4.12(a) is a close-up of the topography at the interface between the nickel wire and the gold end, and (b) is the corresponding magnetic image. The red dotted lines mark the path along that the probe was scanned to record Figs. 4.12(c) and (d). The scan was done bottom up and started at an applied magnetic field of +32 mT. During the scan the field was swept to −31 mT and back to +31 mT. While the topography shown in Fig. 4.12(c) is constant, the magnetic contrast in (d) changes at −20 mT and at

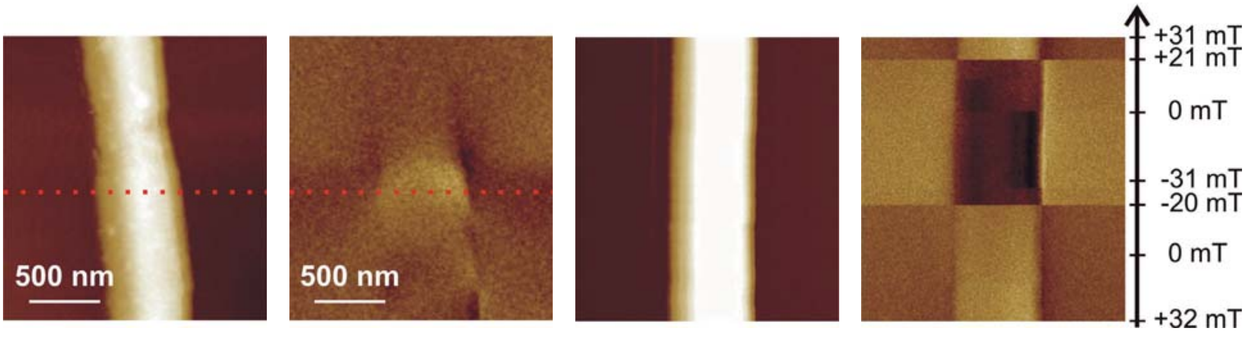

(a) (b) (c) (d)

Figure 4.12: (a) Topography and (b) magnetic contrast of the upper end of a nickel nanowire with gold ends. The red dotted line marks the path along that the probe was scanned to record subfigures (c) and (d) while sweeping the applied magnetic field. The scan was started at +32 mT from the bottom. Apart from small drifts the topography depicted in (c) remains the same, while the magnetic contrast in (d) changes at −20 mT and +21 mT indicating magnetization reversal.

+21 mT indicating the switching fields of the nickel wire. However, this value for the switching field is only representative if the wire's magnetization reverses all at once.

As can be inferred from the micromagnetic simulation depicted in Fig. 3.7(c), the presence of a domain wall in a wire changes the surrounding stray field. The perpendicular stray-field components caused by a domain wall are detectable by MFM. To observe possible domain boundaries in the middle of a nanowire, the probe can also be scanned along the wire while driving the external magnetic field. For this purpose it is required to adjust the fast scan direction to the wire's axis. This is challenging, especially when the wire is not perfectly straight what is sometimes the case. Figure 4.13 depicts an MFM scan along the axis of the nickel wire shown in Fig. 4.11. While the probe was continuously scanned along the same path on the nanowire (red dotted line), the magnetic field was sweeped from −64 mT to +64 mT and the magnetic image shown in the upper panel of Fig. 4.13 was recorded. The initial magnetic configuration of the wire is shown in the small MFM image at the bottom of the figure. The red dotted line marks the path along that the probe was scanned. The bright and dark contrast at the left and at the right end of the nickel wire is visible from the beginning of the scan at the bottom of the frame until an external field of +20 mT is reached. Then, both wire ends turn bright and a dark contrast appears in the middle of the wire. Two scan lines and accordingly 1 mT later the dark contrast is moved about 3 μm to the left. At +22 mT the contrast on the wire disappears and the left wire end turns dark. The contrast is now inverted compared to the initial state, and remains the same until the maximum field of +64 mT is reached. This kind of MFM scan provides the information that the magnetization of the nickel wire does not reverse at once, but via the formation of magnetic domains. Recording the

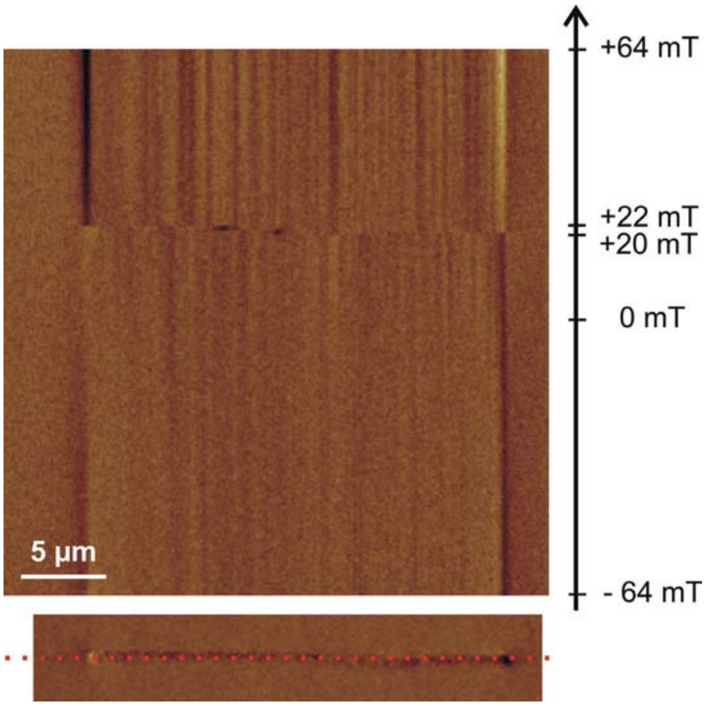

Figure 4.13: Continuous MFM scan along the axis of a nickel nanowire revealing its magnetization reversal. The scan was done bottom up while driving the external magnetic field from −64 mT to +64 mT. The initial magnetic state and the line along which the probe was continuously scanned are shown in the MFM image at the bottom. The bright and dark contrast at the wire ends to the right and to the left reveals a single domain magnetic state. Between +20 and +22 mT both wire ends appear bright, and a dark contrast indicating a domain wall is visible at two different positions on the wire, before the magnetization is completely reversed.

hysteresis of an individual nanowire with this method takes approximately 45 minutes and provides more or less the same information as completely imaging every individual state. This means a time saving of about 95 hours or accordingly of more than 99 percent.

The MFM measurements presented in this work are done with a MultiMode SPM from Digital Instruments in a non-contact mode, the so-called lift-mode. The scan height is usually set to about 50 nm, but sometimes up to 150 nm to obtain MFM images of reasonable quality. These comparably high values for the scan height are chosen since the cylindrical nanowires investigated are up to 300 nm thick. For the application of a uniaxial in-plane field the MFM is surrounded by a pair of Helmholtz coils. To change the angle between the applied magnetic field and the wire axis the sample has to be rotated manually. The maximum field value possible is 100 mT. Applying strong magnetic fields at the setup not only switches the sample magnetization but can also change the magnetization of the MFM probe. That is why for most of the measurements lower maximum fields in the order of 70 mT are applied to saturate the sample.[3] A disadvantage of MFM is that the interaction between the magnetic probe and the sample magnetization can manipulate the magnetic configuration of the sample [Gar01]. It has to be considered that the stray field of the probe triggers the magnetic switching of a nanowire, so the switching-field values recorded by MFM might be lower than the ones measured using a non-invasive method.

---

[3] It was found that for some nickel wires stronger fields are required to really saturate the magnetization. This is one aspect why the results obtained by MFM have to be handled with care. For a detailed discussion of this aspect the reader may refer to Sec. 5.2.

4.4 Photoemission electron microscopy

Photoemission electron microscopy (PEEM) is a photon-in/electron-out method that allows for magnetic imaging by making use of the asymmetry of the absorption cross-sections of atomic core levels for left and right circularly polarized x-ray photons, called x-ray magnetic circular dichroism (XMCD) [Stö93, Ima02]. The XMCD effect is explained in Sec. 2.4. A schematic of the PEEM setup and related components is shown in Fig. 4.14. Photons are supplied by the synchrotron light source BESSY II in Berlin, Germany. An undulator at the beginning of beamline UE49-PGMa accelerates electrons in the storage ring such that they emit x-ray photons, and allows for the selection of the photon helicity. The photon energy is set by a plane grating monochromator (PGM) with an energy resolution of $E/\Delta E = 10\,000$ at 700 eV. After the monochromator the x-ray beam is focused by a mirror such that the illuminated sample area matches the largest field of view.[4] The incident x-ray beam hits the sample at an angle of 16 degrees and excites secondary electrons the intensity of which is proportional to the x-ray absorption cross section of the sample [Stö93]. These electrons are accelerated towards the objective lens in an electrical field of 20 kV. The column transfers some of them to the energy analyzer before they are magnified onto a fluorescent screen by projective lenses.

Due to the resonant character of x-ray excitation PEEM provides element specificity [Bau90]. Furthermore, characteristic energy spectra like the one shown in Fig 2.17 can provide information about electronic structure and thereby about chemical states such as oxidation [Zaa86, Ton96, Dür09]. To obtain magnetic information from a sample, photoemission electron micrographs are recorded at an absorption edge for opposite photon helicities. While the magnetic information in the two types of images is inverted, other contrast mechanisms remain unaffected [Sch97]. Thus, non-magnetic contributions are eliminated by subtracting two images recorded at opposite photon helicities and dividing them by their sum. The resulting differential (XMCD) image reveals a magnetic contrast proportional to the magnetization components along the in-plane projection of the incident x-ray beam.

The spatial resolution of the images is determined by the electron optics of the PEEM [Stö98], and is in the order of 30 nm [Kro10]. In contrast to scanning electron microscopy, where images are acquired by scanning one pixel after the other with the incident electron beam, PEEM bases on parallel image acquisition. This means that the entire field of view is exposed to the incident x-ray beam and all secondary electrons that shall contribute to the image have to pass the complex system of electromagnetic lenses without losing the information about their origin. The paths of electrons depend on local magnetic fields. To compensate the deflection of the

---

[4] The microfocus increases the intensity in the region of interest, and it avoids that undesired electrons enter the column. The latter would lead to charging effects which reduce the image quality.

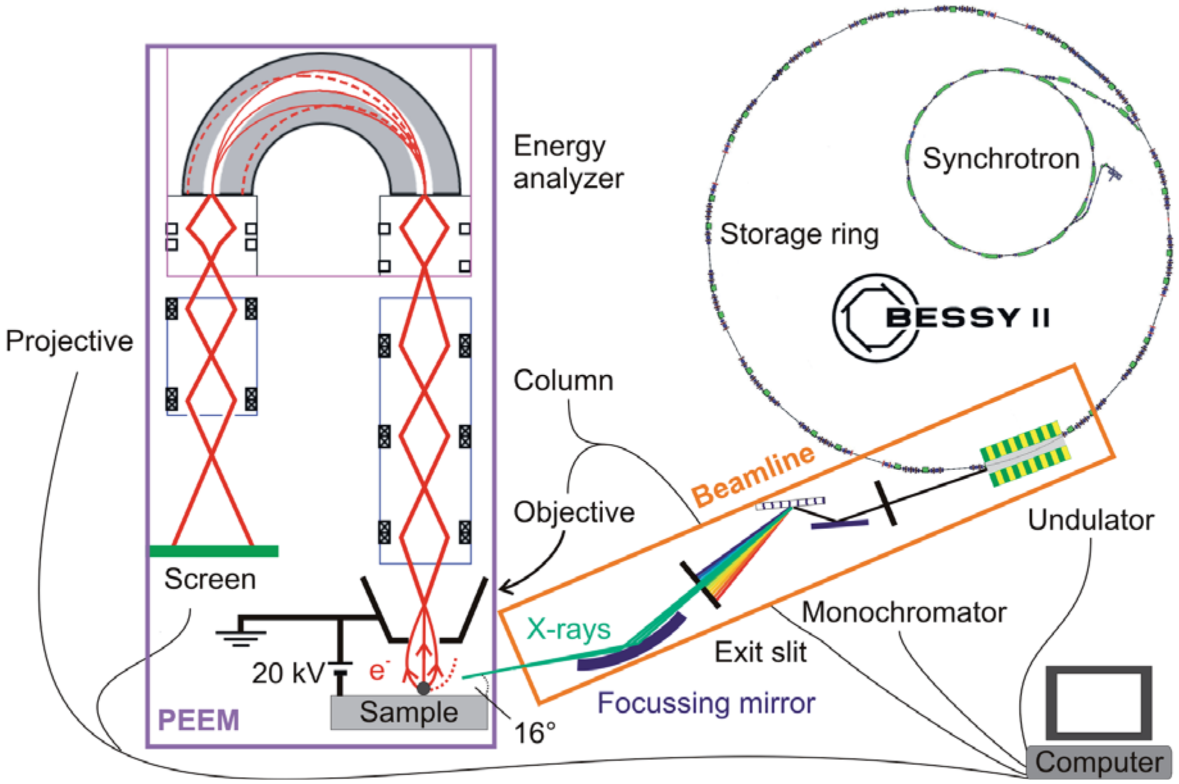

Figure 4.14: Schematic of the PEEM experiment including BESSYII and important beamline components. Based on [Kro10] and [BES]. Note that dimensions as well as the paths of the x-ray beam and the photoelectrons do not display the actual dimensions in the setup.

photoelectrons when applying a magnetic field at the sample, seven interdependent parameters of the PEEM optics settings have to be adjusted simultaneously to keep the image. To save time, the magnetic behavior of nanowires was sometimes studied by imaging the remanent states after applying certain field values.

A sample holder used for PEEM imaging in applied magnetic fields is shown in Fig. 4.15(a). It consists of two coils and yokes confining the magnetic field to the gap area. For our measurements we have sample holders with gap widths of 500 µm and 50 µm at our disposal. The field constants and maximum fields that can be applied without imaging and at which image acquisition is possible are listed in Table 4.2. The magnetic field experienced by a particular wire depends on the wire's position with respect to the yokes. Especially for the 50 µm gap sample holder the field strongly decreases with the distance from the center of the gap.[5] To place the substrate with the wires of choice at the right position on the yokes, the sample holder is fixed under a light microscope with a graticule pointing on the center of the gap. Then the substrate is positioned and fixed with silver glue before the cover

---

[5] Consequently, the magnetic field is not homogeneous. This plays a role particularly for the study of very long structures.

Gap size	Maximum field constant	Maximum field	Max. field during imaging
50 μm	0.25 mT/mA	225 mT	52 mT
500 μm	0.1 mT/mA	90 mT	35 mT

Table 4.2: Properties of the sample holders used for PEEM imaging. Calibration was done comparing the switching fields determined by PEEM to those determined by MOKE measurements.

plate is screwed onto the sample holder. During the entire procedure the position of the substrate is controlled via the light microscope.

The smaller the gap the stronger the decrease of the magnetic field not only laterally but also in vertical direction (compare Fig. 4 in Ref. [Kro10]). Thus, 50 μm thin silicon wafers that require sophisticated handling are used as substrates for the 50 μm gap sample holder, while wafers with a thickness of 500 μm can be used on the other one. The above disadvantages of handling samples on a 50 μm gap are compensated by the opportunity to image in strong applied fields up to about 50 mT.

Figure 4.15(b) shows an image of the PEEM end station of beamline UE49-PGMa at BESSY II, Berlin. After preparation, the sample holder is placed in a load lock and transferred into the preparation chamber where several samples can be stored. When a pressure below $1 \cdot 10^{-8}$ mbar is reached (this typically takes between five and ten hours), the sample can be transferred into the PEEM main chamber. As soon as the high voltage of 20 kV is turned on the parameters to monitor here are both the pressure (typically $1 \cdot 10^{-9}$ mbar) and the leakage current between sample and objective lens. The latter is caused by residuals or nanowires coming off from the sample. If the pressure or the leakage current are too high, the system either turns off the high voltage or there is a discharge (after which the system turns off as well). Even though the samples are rinsed and evacuated before putting them in the PEEM chamber, discharges are a regular challenge when studying cylindrical nanowires. Besides running the risk of polluting the entire PEEM, discharges are undesired since they are associated with heat development and strong magnetic fields, and sometimes change the magnetic behavior of the nanowires. The presence of tear-off edges of metallic contacts on the wires also increases the chance of discharges. This is the reason why it was not possible to study the same nanowire by PEEM and MR measurements. Some samples could not be imaged at all or had to be imaged at an acceleration voltage of 10 kV. The lower voltage not only decreases the chance of discharges but also reduces the resolution of the microscope by a factor of $\sqrt{2}$ [Flo].

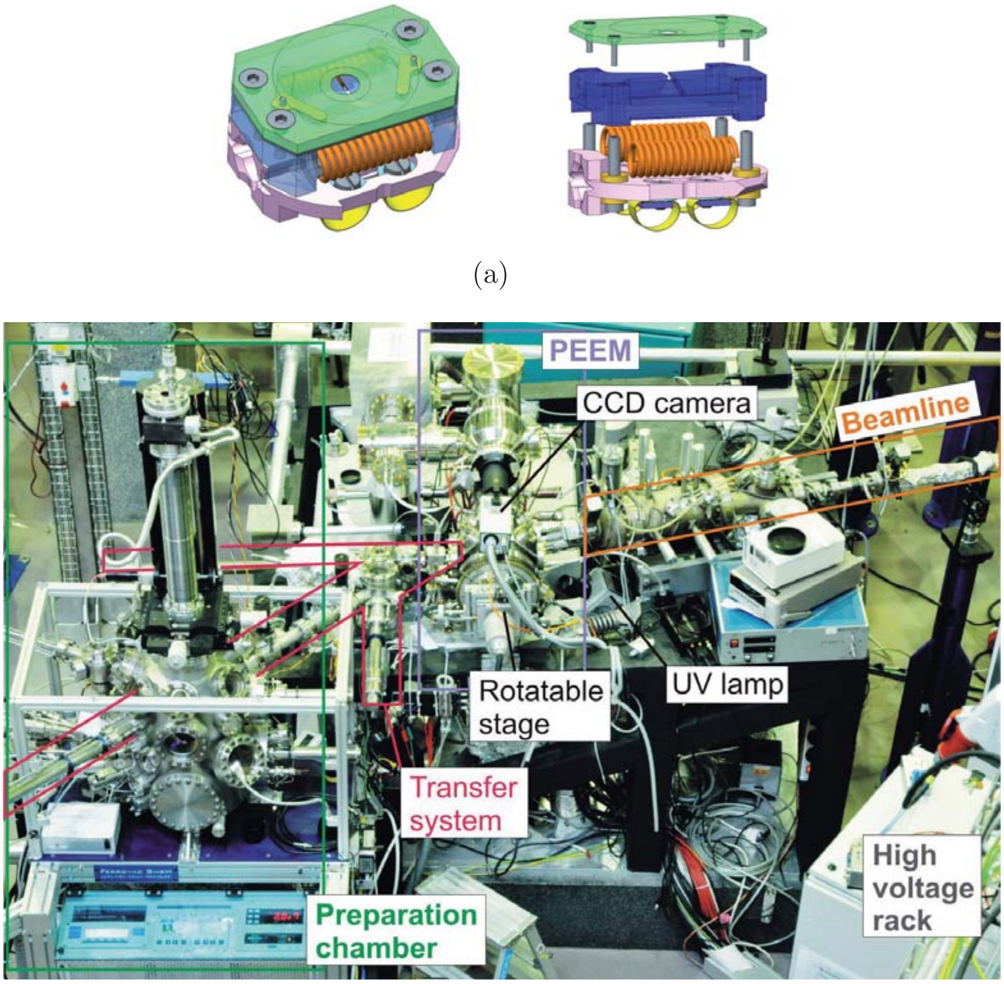

(a)

(b)

Figure 4.15: (a) Schematic top view (left) and side view (right) of a sample holder used for PEEM imaging in magnetic fields. Via the contact springs at the bottom (yellow) a current can be applied to the coils (orange) for the creation of a magnetic field which is confined to the sample area of interest by yokes (blue). The cover plate (green) can be equipped with metal contacts (yellow, only visible in the left panel) for in-situ magnetoresistance measurements. Schematics by courtesy of F. Kronast. (b) Photograph of the PEEM end station with preparation chamber.

Due to the limited mean-free path of photoelectrons PEEM is usually a surface sensitive technique. Recording both the electrons emitted directly from the surface of a nanoobject as well as the ones bounced out of the substrate by the transmitted x rays in the object's shadow, we can probe the surface and the bulk magnetization separately. The potential of the method is demonstrated in the following publication by imaging the individual magnetization patterns of composite nanomagnets, namely iron-oxide tubes and enclosed nickel cores. Simulated magnetic states of a tube are presented and discussed in Sec. 3.2.1.

Publication [Kim11]

PHOTOEMISSION ELECTRON MICROSCOPY OF THREE-DIMENSIONAL MAGNETIZATION CONFIGURATIONS IN CORE-SHELL NANOSTRUCTURES

by

Judith Kimling, Florian Kronast, Stephan Martens, Tim Böhnert,
Michael Martens, Julia Herrero-Albillos, Logane Tati-Bismaths,
Ulrich Merkt, Kornelius Nielsch, and Guido Meier

published in

Physical Review B **84**, 174406 (2011).

PHYSICAL REVIEW B **84**, 174406 (2011)

Photoemission electron microscopy of three-dimensional magnetization configurations in core-shell nanostructures

Judith Kimling,[1,*] Florian Kronast,[2,†] Stephan Martens,[1] Tim Böhnert,[1] Michael Martens,[1] Julia Herrero-Albillos,[2,‡]
Logane Tati-Bismaths,[2] Ulrich Merkt,[1] Kornelius Nielsch,[1] and Guido Meier[1]
[1]*Institut für Angewandte Physik und Zentrum für Mikrostrukturforschung Hamburg, Universität Hamburg, Jungiusstrasse 11, D-20355 Hamburg, Germany*
[2]*Helmholtz-Zentrum Berlin für Materialien und Energie GmbH, Albert-Einstein-Strasse 15, D-12489 Berlin, Germany*

(Received 5 April 2011; revised manuscript received 4 July 2011; published 9 November 2011)

We present a photoemission electron microscopy method that combines magnetic imaging of the surface and of the inner magnetization in three-dimensional core-shell nanostructures. The structure investigated consists of a cylindrical nickel core that is completely surrounded by a shell of iron oxide and silicon oxide layers. The method enables one to image the magnetization configuration of the nickel core even though the shell is thicker than the mean-free path of the photoelectrons. Characteristic L_3 and L_2 edges can be observed not only in the yield of the photoelectrons emitted from the surface of the nanostructure but also in its shadow. X-ray magnetic circular dichroism in the electron yield of the x rays absorbed and transmitted by the multilayered nanowire allows for the individual imaging of the magnetization configurations of the iron oxide tube and the nickel core. The method suggests novel approaches for the characterization of the magnetic and material properties of complex three-dimensional nanostructures.

DOI: 10.1103/PhysRevB.84.174406 PACS number(s): 75.75.−c, 68.37.Yz, 81.07.−b

I. INTRODUCTION

A large variety of techniques is available today to visualize the magnetization reversal of microstructures and nanostructures.[1] Which technique is best suited in a particular case depends on the considerations concerning spatial and temporal resolution as well as the complexity of the sample, to mention a few. When element specificity is required, the selection reduces to techniques based on x-ray absorption. Here, the magnetic contrast in ferromagnets and ferrimagnets arises from an asymmetry of the absorption cross sections of atomic core levels for left and right circularly polarized x-ray photons, called x-ray magnetic circular dichroism (XMCD).[2] X-ray magnetic linear dichroism even allows for the study of antiferromagnets.[3] In both cases a spatially resolved magnetic contrast can be obtained from the difference of two intensity measurements (one for each polarization) either of the transmitted x rays as in magnetic transmission x-ray microscopy[4] or of the electron yield as in photoemission electron microscopy (PEEM).[5,6] While transmission x-ray microscopy averages over the volume of the traversed sample, the sampling depth of PEEM is determined by the mean free path of the photoelectrons, making it a surface-sensitive technique.[2] Both methods are being improved constantly. Nowadays, they provide time resolution in the picosecond range[7–9] and a lateral resolution down to a few nanometers.[10,11] It has been shown recently that standing-wave excitation can add dimensionality to PEEM.[12,13] In particular, sampling interfaces or nanoobjects with standing waves can provide additional depth resolution down to a few Ångstroms. However, due to the period of the standing wave and the mean free path of the photoelectrons the sampling depth is limited to a few nanometers.

The resonant character of x-ray excitation opens unique possibilities for the study of core-shell nanoparticles, where one challenge lies in separating the magnetic contributions of the individual components.[14] In this work we present a method based on PEEM combining surface and bulk sensitive XMCD contrast. Extending the conventional PEEM imaging with a transmission experiment, it is possible to record magnetic information originating both from the surface and from the internal components of a nanostructure and to separate those two contributions. To prove that magnetic information can be obtained from regions below the sampling depth of photoelectrons, we employ cylindrical nickel nanowires surrounded by an approximately 27 nm thick shell of iron oxide and silicon dioxide. The individual magnetization states of the nickel core and the surrounding iron oxide tube are successfully imaged.

II. EXPERIMENTAL DETAILS

The multilayered core-shell nanowires studied in this work are synthesized by filling the hexagonally ordered pores of an alumina membrane with different materials and with different techniques.[15] In a first step, the pores are coated with $SiO_2(5\ nm)/Fe_2O_3(12\ nm)/SiO_2(10\ nm)$ by atomic layer deposition. Then the tubes are filled with nickel by electrochemical deposition. The nickel core has a diameter of about 100 nm that is determined by the pore diameter and the thickness of the shell layers. In the next step the template is removed by selective chemical etching in chromic acid. After filtration the individual core-shell wires are suspended in water. For PEEM imaging the solution is dripped onto a silicon wafer with a specific resistivity of about 10 Ωcm and left to dry in a magnetic field to align the wires in parallel. Before the experiment the Fe_2O_3 is reduced to Fe_3O_4 by annealing the sample in an argon-hydrogen atmosphere at 350 °C for 3 hours. The sample holder used for PEEM imaging allows for the application of a uniaxial in-plane field up to 200 mT (Ref. 16). PEEM imaging was performed at the undulator beamline UE49 PGM of the synchrotron light source BESSY II in Berlin, Germany. The beamline provides photons in the range from 100 to 1800 eV with an energy resolution $E/\Delta E = 10\,000$ at

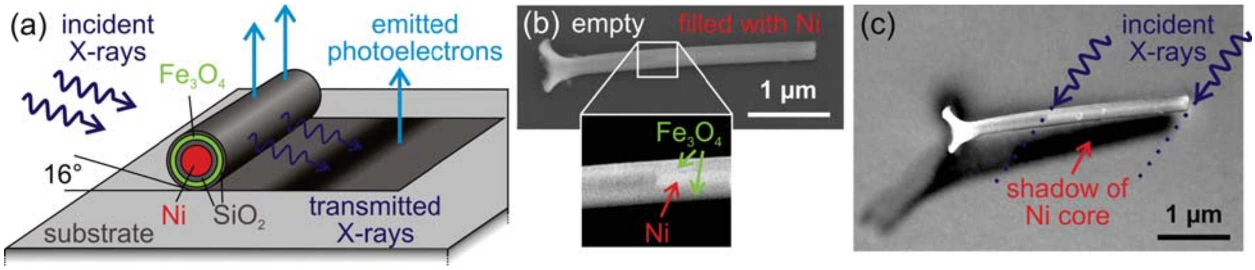

FIG. 1. (Color) (a) Schematic of a core-shell wire during PEEM imaging. (b) Scanning electron micrograph of an iron oxide tube partially filled with a nickel core. The blow up shows the transition from the empty tube (left) to the nickel core (right) that appears bright. (c) Cutout of a scanning electron micrograph combined with a PEEM image recorded at the nickel edge. The absorption of the nickel core can be distinguished in the shadow of the wire.

700 eV and full polarization control. The schematic of a core-shell wire on a silicon wafer exposed to an x-ray beam is shown in Fig. 1(a). The incident x rays hit the sample surface under an angle of 16°. Photoelectrons are emitted from the surface of the wire and the substrate. Details about the PEEM setup are described elsewhere.[16] A scanning electron micrograph of the core-shell nanowire that we have investigated is shown in Fig. 1(b). It reveals that the iron oxide tube is only partially filled with a nickel core. The nickel core appears bright due to the increased scattering of the secondary electrons. Figure 1(c) is the overlay of a scanning electron micrograph and a PEEM image recorded at the nickel edge. The nickel core can clearly be distinguished in the shadow of the structure. To observe both this shadow and the XMCD contrast caused by the magnetization components along the wire axis, an angle of about 45° between the in-plane projection of the incident x rays and the wire axis was chosen for imaging the magnetization reversal. At 90° the shadow would be larger, but only the magnetization components perpendicular to the wire axis could be mapped, while at 0° the XMCD contrast would be most sensitive to the magnetic moments aligned along the wire axis, but no shadow of the nickel core could be observed.

III. RESULTS AND DISCUSSION

Photoemission spectra from selected areas marked in the inserted PEEM image are shown in Fig. 2(a). The electron yield measured on the wire (curve A) gives a spectrum that is proportional to the x-ray absorption coefficient of the iron oxide. The absorbed x rays cause transitions into unoccupied 3*d* levels leading to iron-specific resonance peaks. The step-like background is caused by transitions into continuum states. For iron and nickel the electron sampling depth is about 5 nm (Ref. 17). Due to this surface sensitivity the nickel core does not contribute to the signal measured on the nanowire as it is evidenced by the blue curve (A) in Fig. 2(a). The x-ray absorption length is about one order of magnitude higher than the electron sampling depth. Some x-ray photons are transmitted through the nanostructure and excite photoelectrons in the substrate. The yield of these electrons emitted from the shadow area of the wire is also shown in Fig. 2(a). While the L_3 and L_2 edges of iron can be observed both on the wire (curve A) and in the entire shadow region (curves B and C), the nickel L_3 and L_2 edges are observed only in the shadow of the nickel core (curve C). The spectra recorded in the shadow are inverted with respect to the photoemission spectrum recorded on the wire since they are transmission spectra. Figure 2(b) illustrates the two areas in the shadow where the element-specific absorption lines and thereby the XMCD contrast of the respective materials can be observed.

Our experiment demonstrates that combining the conventional surface sensitive PEEM microspectroscopy with a transmission experiment, element-specific magnetic information of complex three-dimensional nanostructures can be obtained,

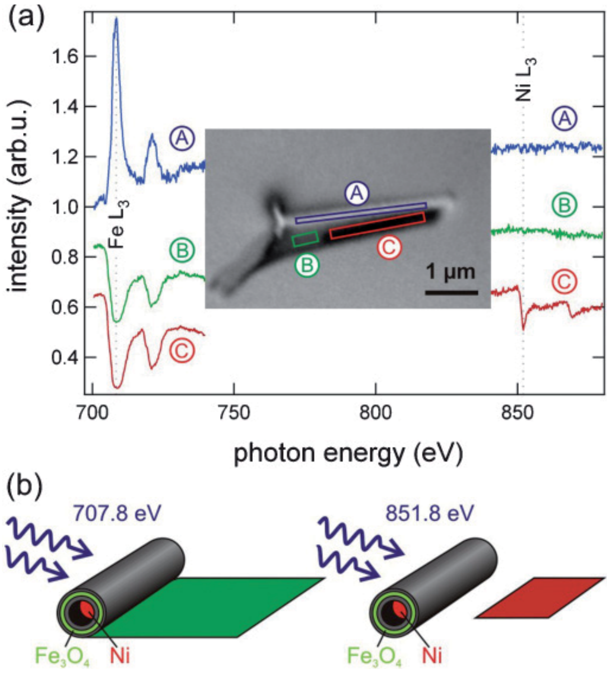

FIG. 2. (Color) (a) Photoemission spectra recorded on the wire (A, blue), in the shadow of the empty tube (B, green), and in the shadow of the nickel core (C, red). The respective regions are marked in the PEEM image shown in the middle. The red curves are shifted for clarity by −0.3. Note, that no absorption edges of the silicon substrate contribute in the energy range shown. (b) Schematic of a partially filled core-shell wire exposed to x rays of different photon energies. At 707.8 eV (Fe L_3 edge) XMCD contrast revealing the magnetic configuration of the iron oxide tube is obtained in the entire shadow region (green), while at 851.8 eV (Ni L_3 edge) magnetic contrast is only obtained in the shadow of the nickel core (red).

even though components are buried below the sampling depth of photoelectrons.

To image the magnetic configuration of the iron oxide tube and the nickel core, XMCD images are recorded at both the iron and the nickel L_3 edge. The XMCD images shown in the following figures represent the difference of two PEEM images recorded with circularly polarized x rays of opposite helicity, divided by their sum. Figure 3(a) shows PEEM images of the core-shell wire recorded at the iron L_3 and at the nickel L_3 edge after extraction of the background. The increased absorption by the nickel core is visible in the shadow only at the nickel edge. Figures 3(b) through 3(e) are pairs of differential XMCD images recorded at the respective absorption edges revealing the remanent magnetization configurations of the iron oxide shell (left) and the nickel core (right). The blue and red XMCD contrasts are proportional to the magnetization parallel and antiparallel to the direction of the in-plane projection of the incident x-ray beam, respectively. Thus, these contrasts indicate the magnetization components along the wire axis. The magnetization of the white areas is either zero or aligned normal to the photon wave vector. At the iron edge (707.8 eV) magnetic contrast can be obtained both on the surface of the wire and in its shadow. The contrast in the shadow is inverted as the electron yield from the substrate is proportional to the intensity of the transmitted x rays. At the nickel edge (851.8 eV) magnetic contrast can only be observed in a segment of the shadow. Comparing this area in Figs. 2 and 3 shows that this segment corresponds to the area where the nickel-specific absorption lines are observed in Fig. 2, namely the shadow of the nickel core.

The magnetic configurations shown in the image pairs in Figs. 3(b) through 3(e) are prepared as follows: first the structure is saturated along the wire axis in an external magnetic field. Then a reverse magnetic field is applied before the field is set to zero and XMCD images are taken in remanence.[18] This procedure is repeated for every image pair.[19] The magnitude of the reverse field for the individual image pairs is given in the figure. Figure 3(b) depicts the remanent state after saturation. The magnetizations of the two coaxial nanomagnets are aligned in parallel. In Fig. 3(c) the magnetic contrast of the nickel core remains the same compared to Fig. 3(b), while the XMCD contrast of the electrons emitted from the iron oxide tube increases. Given the direction of incidence of the x rays which is 45° to the wire axis, and given a constant magnetic moment, this means that the magnetization of the tube becomes tilted further away from the wire axis. At the same time the magnetic contrast in the shadow of the tube becomes more inhomogeneous and locally almost vanishes. This could be explained as follows: the x rays causing the XMCD contrast in the shadow probe the magnetization components of the two side walls of the tube. If the magnetization, for example, curls as described in the model of Chong *et al.*,[15] the contributions cancel and the contrast is lost. Figure 3(d) represents the remanent magnetization configurations after applying a magnetic field in the vicinity of the switching field. The feature of the vanishing shadow is observed again on the right end of the tube, where the magnetization has not switched yet. The nickel core also started to reverse its magnetization, and a domain wall can be observed. In Fig. 3(e) the reverse field applied is high enough to completely switch the magnetization of the iron oxide tube and the nickel core.

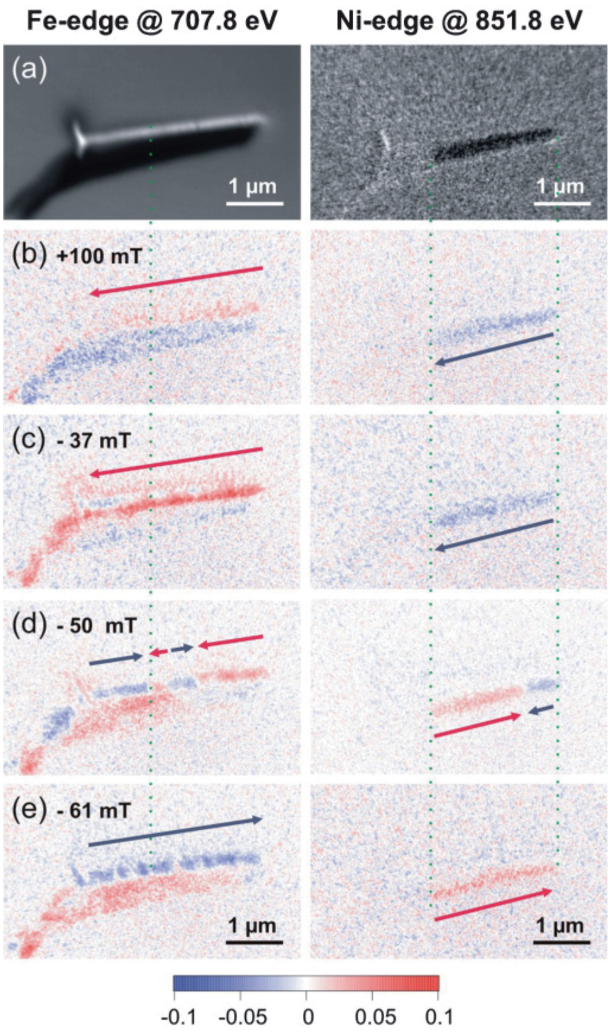

FIG. 3. (Color) (a) PEEM images of the core-shell wire recorded at the iron L_3 edge and the nickel L_3 edge (background extracted). (b)–(e) Differential XMCD images of the iron oxide tube (left) and the nickel core (right) recorded at the respective absorption edges. The color bar indicates the direction of the magnetic contrast in arbitrary units. The magnetic configurations are imaged in remanence after saturating at (b) -123 mT and (c)–(e) $+123$ mT and applying the displayed field values. (The values of the magnetic field are estimated from the position of the wire relative to the center of the pole shoes of the sample holder and the coil currents applied. Due to the remanence of the pole shoes we assume an error of approximately 1.4 mT in the displayed field values.) The arrows indicate the magnetization components along the wire axis. The green dotted lines mark the ends of the nickel core.

The remanent magnetization configurations provide a hint at the contrasting magnetic behavior of the iron oxide tube and the nickel core. In nickel the magnetocrystalline anisotropy is low (5 000 J/m^3). Thus, the magnetic easy axis of the core is given by its cylindrical shape and the high aspect ratio, and the magnetic moments remain aligned along the

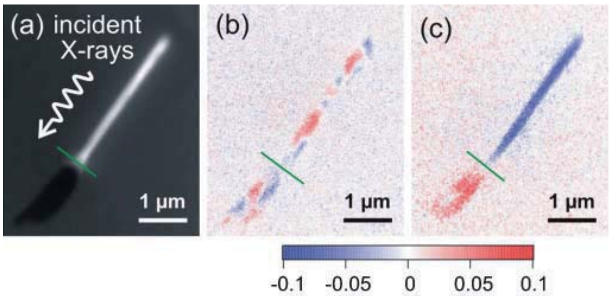

FIG. 4. (Color) (a) PEEM image of the core-shell wire taken at an angle of 0° between wire axis and incident x rays. (b) Differential XMCD image recorded at the iron L_3 edge in zero magnetic field after annealing (as-prepared) and (c) after the first field sweep 120 mT → −120 mT → 0 mT. The blue and red XMCD contrasts represent magnetizations along and antiparallel to the wire axis, respectively. The green lines mark the wire end.

wire axis even though the material is not single-crystalline. Apart from one abrupt contrast change, the magnetization of the nickel core appears homogeneous. This suggests magnetization reversal via domain-wall motion as predicted by micromagnetic simulations.[20] During propagation domain walls can be stopped by defects in the wire serving as pinning sites. The intrinsic anisotropy of the iron oxide tube is determined by an interplay of magnetostatic energy, exchange energy, and magnetocrystalline anisotropy. Since the walls of the tube are only 12 nm thick, the tube is expected to behave as a rolled-up thin film, in which the magnetization tends to align in the plane.[21] The magnetostatic energy associated with surface charges is minimized if the magnetization curls radially around the tube, while the exchange energy favors a parallel alignment of the magnetic moments along the wire axis. A typical magnetic state calculated for ferromagnetic tubes is a uniform magnetization along the axis in the middle part of the tube, and two vortices curling at the ends.[21,22] For the magnetization reversal the propagation of a vortex or a transverse domain wall from one end of the tube to the other is predicted.[21]

Figure 4 depicts PEEM images recorded at an angle of about 0° between the in-plane projection of the incident x-ray beam and wire axis. Figure 4(c) shows the remanent magnetization components along the wire axis after saturation at −120 mT. In agreement with the XMCD image of the comparable state recorded at 45° [Fig. 3(b)] the magnetization is not completely homogeneous, but predominantly aligned in the same direction along the wire axis. Both the images of the remanent states after saturation as well as the other magnetic states shown in Fig. 3 do not clearly evidence an increased rotation of the magnetization at the tube's end away from the wire axis (i.e., the theoretically predicted vortices).

In Figs. 3(c) through 3(e) the magnetization of the tube appears inhomogeneous. This might be attributable to the granularity of the iron oxide tube.[15,23] It has been shown analytically that the intrinsic anisotropy of a nanotube can be tailored by tuning the aspect ratio between radius, thickness, and length of the tube, and even be reduced to zero for soft magnetic materials.[22] In the present tube the contribution of the magnetocrystalline anisotropy of the iron oxide (11 000 $\mathrm{J/m^3}$) to the intrinsic anisotropy of the tube seems to be comparably high. The influence of the magnetocrystalline anisotropy and the random orientation of the grains in the iron oxide tube becomes apparent in the as-prepared magnetization configuration of the tube shown in Fig. 4(b). The term as-prepared refers to the state of the sample after reduction by annealing. Our data point to a discrepancy between theoretical predictions and the actual magnetization reversal process of the iron oxide tube. This indicates that the granular structure of the material should be implemented in the models.

IV. CONCLUSION

We have shown that separate PEEM imaging of the individual layers of core-shell nanostructures is possible, even if a layer is buried deeper than the sampling depth of the photoelectrons. Conventional surface sensitive PEEM is successfully combined with a transmission experiment probing the magnetization of inner components. The method enables one to image the individual magnetization configurations of two coaxial nanomagnets, an iron oxide tube, and an enclosed nickel core. Contributions originating from the surface and from the interior of a nanostructure can be separated, an interesting feature not only for magnetic characterizations but also for material analysis. Due to the limited x-ray transmission, the method is applicable to nanostructures with a maximum thickness of about 300 nm. In principle, it is possible to obtain full three-dimensional magnetic information by tomography.[24] Given the possibility to image in an applied magnetic field up to about 40 mT (Ref. 16), element specificity, a potential lateral resolution of a few nanometers and the option to implement time resolution in the picosecond range, the method opens new avenues for the study of magnetization reversal in complex three-dimensional nanostructures.

ACKNOWLEDGMENTS

The authors thank Yuen Tung Chong for providing the core-shell nanostructures, Peter Lendecke for help with the measurements, and Julien Bachmann and Detlef Görlitz for fruitful discussions. Financial support by the Deutsche Forschungsgemeinschaft via the Sonderforschungsbereich 668 and the Graduiertenkolleg 1286 as well as by the Forschungs- und Wissenschaftsstiftung Hamburg via the Cluster of Excellence Nanospintronics and by the Helmholtz-Zentrum Berlin is gratefully acknowledged.

---

[*] judith.kimling@physnet.uni-hamburg.de

[†] florian.kronast@helmholtz-berlin.de

[‡] Present addresses: Centro Universitario de la Defensa de Zaragoza, Carretera de Huesca s/n, E-50090 Zaragoza, Spain and Instituto de

Ciencia de Materiales de Aragón and Departamento de Física de la Materia Condensada, CSIC-Universidad de Zaragoza, E-50009 Zaragoza, Spain.

[1] M. R. Freeman and B. C. Choi, Science **294**, 1484 (2001).

[2] J. Stöhr, H. A. Padmore, S. Anders, T. Stammler, and M. R. Scheinfein, Surf. Rev. Lett. **5**, 1297 (1998).

[3] F. Nolting *et al.*, Nature (London) **405**, 767 (2000).

[4] P. Fischer, IEEE J. Quantum Electron. **42**, 36 (2006).

[5] A. Locatelli and E. Bauer, J. Phys.: Condens. Matter **20**, 093002 (2008).

[6] C. M. Schneider and G. Schönhense, Rep. Prog. Phys. **65**, R1785 (2002).

[7] T. Kamionka, M. Martens, K. W. Chou, M. Curcic, A. Drews, G. Schütz, T. Tyliszczak, H. Stoll, B. Van Waeyenberge, and G. Meier, Phys. Rev. Lett. **105**, 137204 (2010).

[8] J. Raabe, C. Quitmann, C. H. Back, F. Nolting, S. Johnson, and C. Buehler, Phys. Rev. Lett. **94**, 217204 (2005).

[9] B. Heitkamp, F. Kronast, L. Heyne, H. A. Dürr, W. Eberhardt, S. Landis, and B. Rodmacq, J. Phys. D: Appl. Phys. **41**, 164002 (2008).

[10] W. Chao, J. Kim, S. Rekawa, P. Fischer, and E. H. Anderson, Opt. Express **17**, 17669 (2009).

[11] R. Fink *et al.*, J. Electron Spectrosc. Relat. Phenom. **84**, 231 (1997).

[12] F. Kronast *et al.*, Appl. Phys. Lett. **93**, 243116 (2008).

[13] A. X. Gray *et al.*, Appl. Phys. Lett. **97**, 062503 (2010).

[14] H. A. Dürr *et al.*, IEEE Trans. Magn. **45**, 15 (2009).

[15] Y. T. Chong, D. Görlitz, S. Martens, M. Y. E. Yau, S. Allende, J. Bachmann, and K. Nielsch, Adv. Mater. **22**, 2435 (2010); Y. T. Chong (Private communication).

[16] F. Kronast, J. Schlichting, F. Radu, S. K. Mishra, T. Noll, and H. A. Dürr, Surf. Interface Anal. **42**, 1532 (2010).

[17] R. Nakajima, J. Stöhr, and Y. U. Idzerda, Phys. Rev. B **59**, 6421 (1999).

[18] The remanent magnetization configurations might differ from the ones prepared while an external magnetic field is applied. With our method it is possible to perform magnetic imaging in an applied magnetic field up to about 40 mT. This field is too low for imaging the magnetization reversal of the present nanostructure.

[19] In the image pair Fig. 3(d) the differential XMCD image obtained at the nickel edge was replaced by an image with better statistics. In the image shown the magnetic state of the nickel core is the same as in the image replaced. The images were taken during different field cycles with a reverse field of about 50 mT.

[20] R. Hertel and J. Kirschner, Physica B **343**, 206 (2004).

[21] J. Escrig, J. Bachmann, J. Jing, M. Daub, D. Altbir, and K. Nielsch, Phys. Rev. B **77**, 214421 (2008).

[22] A. P. Chen, K. Y. Guslienko, and J. Gonzalez, J. Appl. Phys. **108**, 083920 (2010).

[23] R. Zierold, Z. Wu, J. Biskupek, U. Kaiser, J. Bachmann, C. E. Krill, and K. Nielsch, Adv. Funct. Mater. **21**, 226 (2010).

[24] A. Fraile Rodriguez, A. Kleibert, J. Bansmann, A. Voitkans, L. J. Heyderman, and F. Nolting, Phys. Rev. Lett. **104**, 127201 (2010); By an azimuthal rotation of the sample the absolute value and direction of the magnetic moments can be determined. For this purpose it would be required to image the same magnetic state at several angles between the direction of the incident x rays and the wire axis.

5 Magnetization reversal in cylindrical nickel nanowires

Magnetization reversal in electrochemically synthesized nickel nanowires has been studied experimentally for more than 15 years. An overview of the results on wires embedded in the membrane they were grown in is given in the review of Sellmyer *et al.* [Sel01]. The interpretability of such ensemble measurements is limited since stray-field interaction and switching-field distributions blur the characteristics of the individual objects. A popular tool for the study of individual nickel nanowires are magnetoresistance measurements performed either on individual wires on a substrate [Rhe07b] or on single wires still embedded in the membrane they were grown in [Weg98, Weg99, Pig00].[1] Wernsdorfer *et al.* presented measurements on individual nanowires with a micro-SQUID (superconducting quantum interference device) magnetometer [Wer95, Wer96]. Magnetic force microscopy was also used for the study of individual nickel nanowires [Led95]. The first section of this chapter reviews some experimental results from other groups and the way the data was analyzed by the authors. Together with the results of the other groups, own results for the switching fields of nickel nanowires determined by magnetic force microscopy, magneto-optical Kerr-effect (MOKE) magnetometry, and magnetoresistance measurements are interpreted in the frame of the curling model. To date this model is the fundamental model for the description of the magnetization reversal in cylindrical nickel nanowires in the diameter range under consideration, namely from about 70 nm to 350 nm. The applicability of the curling model to the present system is discussed considering the experimental results and micromagnetic simulations. In Sec. 5.2 further experimental results are presented. They provide an insight into the actual magnetic behavior of nickel nanowires. The findings from magnetoresistance measurements and magnetic force microscopy underline the need for an additional experimental method allowing for the direct non-invasive magnetic imaging of the nanowires, which already emerges in Sec. 5.1. Photoemission electron microscopy (PEEM) is successfully proven to meet these demands.

---

[1] In track-etched membranes the distance between the individual wires is assumed to be large enough to neglect interactions via the magnetic stray field [Pir97, Fer97].

5.1 Magnetization reversal in straight nickel nanowires and the curling model

The external magnetic field where the main part of the magnetization in a wire reverses is called switching field. Both the value of this switching field and its dependence on the angle θ between the direction of the applied magnetic field and the wire's axis give a hint at the mechanisms underlying the reversal process. Figure 5.1 displays angular-dependent switching fields measured by other groups with different experimental techniques as stated in the inset. Besides the data points the figure depicts analytical curves drawn in the same color as the data they refer to. The stan-

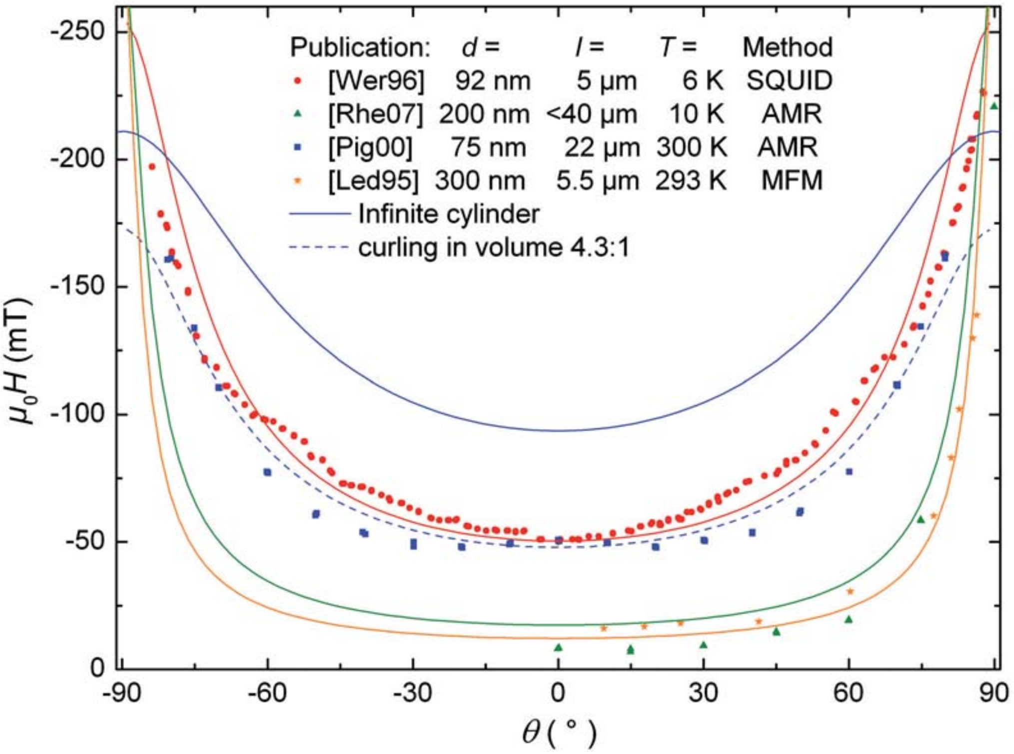

Figure 5.1: Dependence of the switching field on the angle θ between the applied magnetic field and the axis of nickel wires measured by other groups. The respective publications, the diameters d and the lengths l of the wires, as well as the temperature T at that the data was collected and the methods used (superconducting quantum interference device (SQUID), magnetoresistance measurements (AMR), and magnetic force microscopy (MFM)) are given in the figure's legend. The straight lines are drawn using Eq. 5.1 for magnetization reversal by curling in an infinite cylinder, $M_\mathrm{s} = 4.83 \cdot 10^5 \,\frac{\mathrm{A}}{\mathrm{m}}$, and inserting the diameters and critical radii from the respective publications. The dashed blue line assumes curling in a nucleation volume with an aspect ratio of 4.3:1 estimated to 1/65 of the entire volume of the wire (Eq. 5.2 with $N_\perp = 0.454$, $N_{||} = 0.092$, and $k = 1.2$ [Pig00].).

dard model for the fitting is magnetization reversal via curling in an infinite cylinder.[2] For an infinite cylinder the demagnetizing factors are $N_\perp = 0.5$ and $N_{||} = 0$ [Che91], and the geometrical factor is $k = 1.079$ [Aha97a]. Equation 2.25 reduces to [Wer96]

$$H_\mathrm{n}(\theta) = \frac{M_\mathrm{s}}{2} \frac{a\,(1+a)}{\sqrt{a^2 + (1+2a)\cos^2\theta}} \tag{5.1}$$

with $a = -1.079(2r_\mathrm{c}/d)^2$, where d is the diameter of the cylinder and r_c is the critical radius. The analytical curves in Fig. 5.1 are drawn using this formula, a saturation magnetization $M_\mathrm{s} = 4.83 \cdot 10^5 \frac{\mathrm{A}}{\mathrm{m}}$, as well as the parameters d and r_c from the respective publications. In the case of Rheem *et al.* and Pignard *et al.*, there is an offset of the fits compared to the ones shown in their papers the origin of which is unclear.[3] Nevertheless, some tendencies can be inferred from Fig. 5.1. While the theoretical curves fit the progression of the data points well for angles below about 60 degrees, there is a remarkable difference in the curvature for larger angles. To obtain a good fit to the data two requirements have to be met. First, the theoretical value of the switching field at an angle of zero degrees between the applied magnetic field and the wire axis has to match. Second, the theoretical slope of the angular-dependent switching fields has to be the same as the one of the experimental data. Both aspects will be discussed below.

The switching fields of the wires studied here as well as some values from the literature for an angle of zero degrees between the applied magnetic field and the wire axis are plotted in Fig. 5.2. Looking at the distribution of the switching fields, it is clear that a common analytical description fitting all data points cannot be found. Nevertheless, the data shall be compared to analytical models. If not stated differently the material parameters for bulk nickel at room temperature from Table 2.1 are used.

In the Stoner-Wohlfarth model the critical fields for coherent magnetization reversal are given by Eq. 2.21. Neglecting the influence of magnetocrystalline anisotropy one obtains the straight solid lines in Fig. 5.2 for an infinite cylinder (red), and cylinders with aspect ratios[4] of $n = 20$ (blue) and $n = 5$ (green). The red dashed line for an infinite cylinder includes the first term of Eq. 2.21 accounting for the magnetocrystalline anisotropy of nickel which leads to an offset of -18.6 mT.

---

[2] For details about the curling model the reader may refer to Sec. 2.1.6.

[3] One reason might be the use of different values for the saturation magnetizations M_s which are not stated in the respective publications. The material constant M_s is temperature dependent with a maximum value of $5.1 \cdot 10^5 \frac{A}{m}$ at zero Kelvin [Cra63]. Adapting the value used here for lower temperatures would even increase the offset in the case of Rheem *et al.*.

[4] The aspect ratio n of a cylinder with length l and diameter d is defined as $n = \frac{l}{d}$.

The nucleation field for a prolate spheroid based on the curling model is given by[5]

$$H_{\mathrm{n}}^{\mathrm{curl}} = -\frac{2|K_1|}{\mu_0 M_{\mathrm{s}}} + N_{||} M_{\mathrm{s}} - \frac{M_{\mathrm{s}}}{2}\frac{k}{d^2}(2r_{\mathrm{c}})^2. \tag{5.2}$$

Assuming magnetization reversal by curling in the three cylinders with aspect ratios $n = \infty$, $n = 20$, and $n = 5$ we obtain the red, the blue, and the green curves in Fig. 5.2, respectively, showing a dependence of the nucleation fields on the diameter of the wires. For the calculation of these curves, the magnetocrystalline anisotropy is neglected and the critical radius is set to 20.7 nm since this is the value usually referred to in the related literature. The orange curves represent the nucleation field of an infinite cylinder for a critical radius of 8.3 nm.

The first summand of Eq. 5.2 accounts for the contribution of magnetocrystalline anisotropy. With the material parameters of nickel it leads to a maximum offset of -18.6 mT as indicated by the dashed lines for infinite cylinders in Fig. 5.2. This maximum offset is only achieved for uniaxial anisotropy with an anisotropy axis in parallel to the long axis of the spheroid. Due to the high aspect ratio and the polycrystalline structure of the nickel wires this magnetocrystalline contribution is often argued to be of minor importance and neglected [Pig00, Wer96, Led95]. Nickel, however, has a cubic anisotropy, so at remanence the magnetic moments in bulk nickel tend to align along one of the <111> directions. This means that even if all grains had the same orientation with respect to the wire axis, this would not necessarily be the case for the magnetization within these grains, if the coupling is weak.

The second summand of Eq. 5.2 accounts for the influence of the demagnetization field created by the magnetic charges at the long ends of the spheroid. For an infinite cylinder, where $N_{||} = 0$, this contribution is omitted (compare Eq. 5.1). The aspect ratios of the wires studied in the frame of this work range from 28 to 380. According to Eq. 2.22 the corresponding demagnetizing factors for cylinders are 0.005 and about $4.5 \cdot 10^{-5}$. The maximum contribution of the second summand based on these values is +3 mT. The smallest aspect ratio of the wires studied in the literature under discussion is $n = 18$ [Led95], what results in $N_{||} = 0.01$ and therewith in an offset of +6 mT. The effect of adding uniaxial magnetocrystalline anisotropy to the curling model (first summand) has essentially the same effect as changing the shape anisotropy (second summand) by adapting the geometrical parameters [Aha97a].

Due to the large parameter space, the focus of the following quantitative discussion shall be on the third summand of Eq. 5.2. It is a linear function of the geometrical parameter k plotted in Fig. 5.3. In the range of the aspect ratios of the wires under consideration k varies about 3 percent. If we assume that the nucleation volume

---

[5] This equation for $H_{\mathrm{n}}^{\mathrm{curl}}$ differs from Eq. 2.24 since we stick to the convention of Aharoni who considers $|K_1|$ in the first summand.

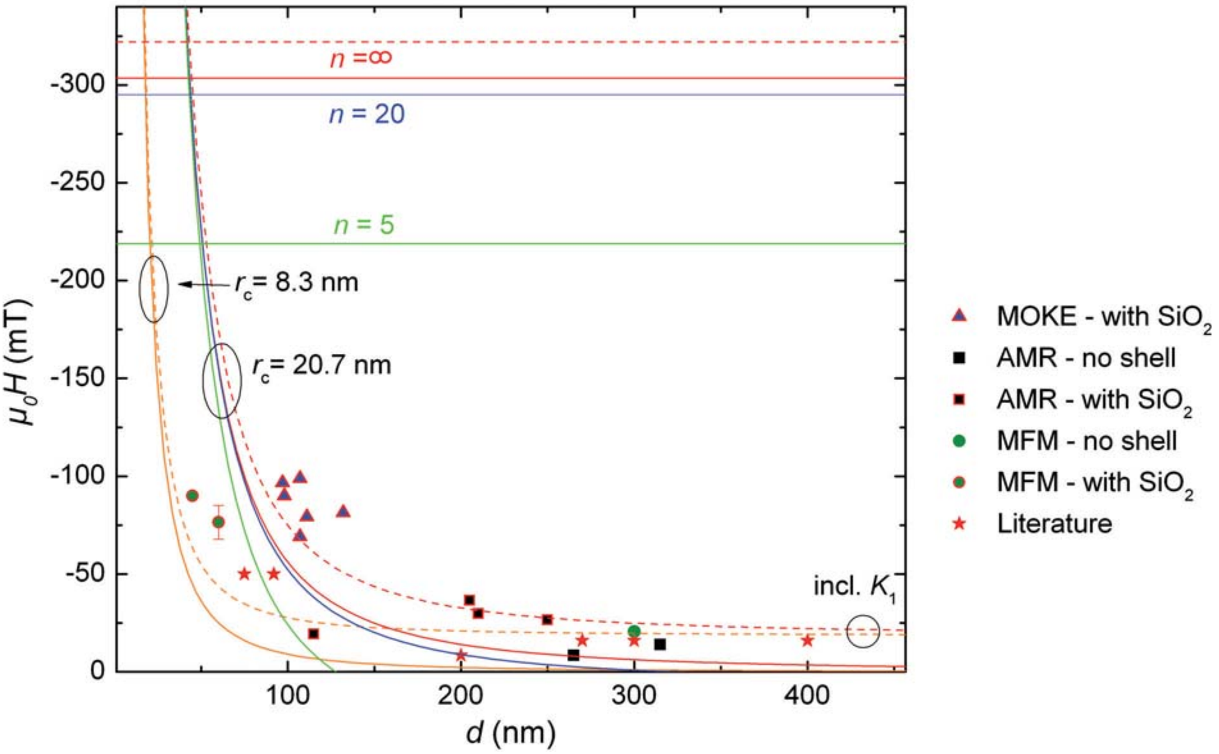

Figure 5.2: Switching fields of cylindrical nickel nanowires versus the diameter d of the wires. Own data was recorded by magnetoresistance measurements (AMR), magnetic force microscopy (MFM), and magneto-optical Kerr-effect (MOKE) magnetometry [Pit11, Kri] at room temperature. The MOKE data points are averages of at least 500 sweeps, the AMR data contains statistics since it is a fit parameter to angular-dependent switching fields. The MFM value at 45 nm has no error bar, for the one at 300 nm the error is smaller than the size of the data point. A red edge around the data points indicates that the respective wires are surrounded by a silica shell. The stars represent values obtained by other groups at different temperatures [Led95, Rhe07b, Wer96, Pig00]. To our knowledge these wires do not have a silica shell. The straight lines and the curves are the critical fields calculated according to the Stoner-Wohlfarth model of coherent rotation (Eq. 2.21) and assuming magnetization reversal by curling (Eq. 5.2), respectively, for an infinite cylinder ($n = \infty$, red), a cylinder with aspect ratio[4] $n = 20$ (blue), and $n = 5$ (green). The orange curves are calculated for a critical radius $r_c = 8.3$ nm, the other curves based on the curling model using $r_c = 20.7$ nm. For the continuous curves the influence of magnetocrystalline anisotropy is neglected. The dashed curves include the first summand (≈ -18.6 mT) accounting for the influence of magnetocrystalline anisotropy (K_1).

corresponds to the volume of the entire wire, the small variation of the parameter k can be neglected facing the huge variation of the switching fields. Using $k = 1.079$ for an infinite cylinder [Aha97a] the nucleation field is then given by

$$\tilde{H}_{\mathrm{n}}^{\mathrm{curl}} = -2.158\ M_{\mathrm{s}} \frac{1}{d^2} (r_{\mathrm{c}})^2. \tag{5.3}$$

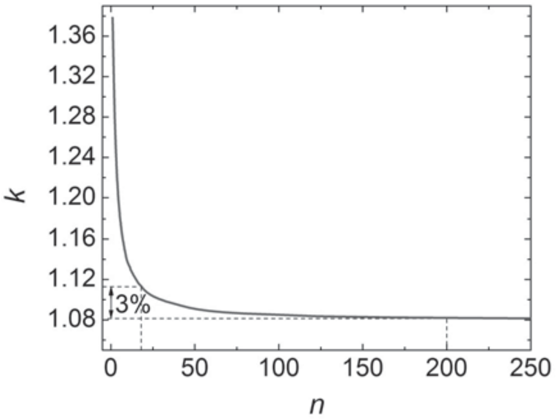

Figure 5.3: Geometrical parameter k plotted versus the aspect ratio $n = l/d$ of an ellipsoid with length l and diameter d. The data is taken from Fig. 1 of Ref. [Aha86].

With this equation the critical radius r_c can be calculated from the experimental values for the switching field displayed in Fig. 5.2. The results are plotted in Fig. 5.4 in dependence of the wire diameter d and of the aspect ratio n both for own measurements and for the values from literature. The critical radius is often used as a fitted parameter. Apart from the value reported by Wernsdorfer *et al.*, the critical radii in the literature differ from the ones plotted in Fig. 5.4. The reason for this is the application of the cgs-units system and different prefactors.

Studying the magnetization reversal in individual nickel nanowires of diameters between 75 and 100 nm with a micro-SQUID [Wer95] at temperatures of 6 K and below, Wernsdorfer *et al.* found a critical radius of 17 ± 2 nm by fitting measurements with Eq. 5.1 [Wer96]. As an example, the angular dependence of the switching field of a nickel nanowire with a diameter of 92 nm and the corresponding fit are plotted in Fig. 5.1(red).

Lederman *et al.* studied individual nickel wires with diameters ranging from 270 nm to 450 nm by magnetic force microscopy. They found that all nickel cylinders show the same angular dependence of the switching field independent of their radius and length and can be fitted by Eq. 5.1 for an infinite cylinder using $S = 5.2$ even though $S = \frac{d}{2r_\mathrm{c}}$ actually ranges from 6.5 to 10.9. This means that the critical radius varies between 26 nm and 38.5 nm for wires with diameters between 270 nm and 400 nm, respectively. Lederman *et al.* conclude that "in finite cylinders, curling may play an important role in the magnetization reversal, and the finite size, i.e., the existence of poles may lead to nucleation by a common factor independent of radius" [Led95].

Rheem *et al.* obtained a value of $r_\mathrm{c} = 23$ nm for nickel wires with a diameter of 200 nm using magnetoresistance measurements and Eq. 5.1. For a 30 nm thin wire they found $r_\mathrm{c} = 4.72$ nm. As possible reason for the difference in the critical radius they assume stress-induced anisotropy in the 30 nm diameter nanowire due to the low temperature of 10 K at which the measurement was done as well as structural differences such as surface morphology and grain size. Rheem *et al.* conclude that

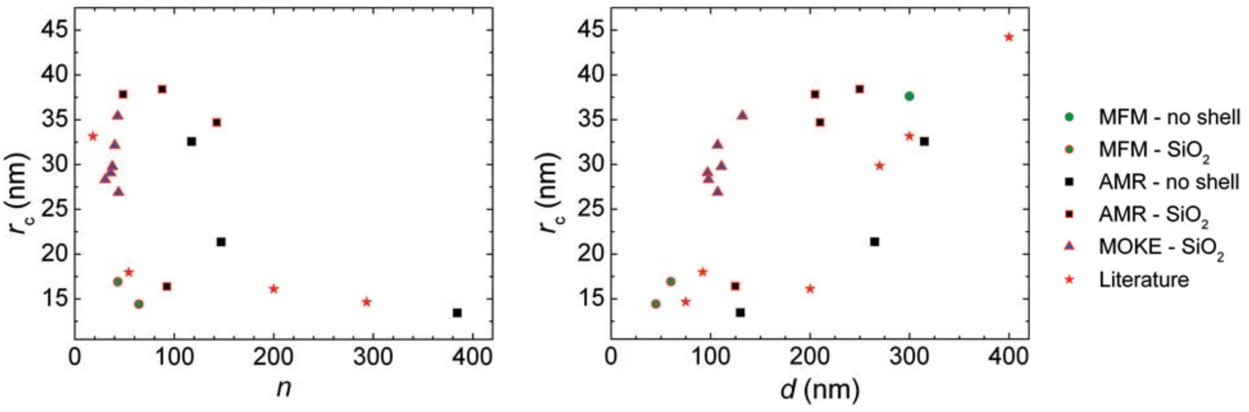

(a) (b)

Figure 5.4: Critical radii r_{c} versus (a) the aspect ratio n and (b) the diameter d of nickel wires calculated for the data shown in Fig. 5.2 and assuming magnetization reversal via curling in a homogeneous infinite cylinder without magnetocrystalline anisotropy (Eq. 5.3). The coloring of the data points indicates the technique by which they were acquired. A red frame around a data point symbolizes that the respective wire was surrounded by a silica shell. Some data points only occur in (b) since the lengths of the respective wires and thus the aspect ratios n are unknown. Note that some values from the literature base on measurements at low temperatures. Own measurements were done at room temperature.

their “results strongly imply that local curling or the size of the curling magnetization exists at a value smaller than the diameter of the nanowire” [Rhe07b].

Figure 5.4 reveals that our experimental results are in good agreement with the values from literature. In summary, there is no obvious dependence of the critical radius r_{c} on the aspect ratio n, but r_{c} tends to increase with increasing diameter d of the nanowires. To interpret this observation, it is required to deal with the meaning of the critical radius.

The critical radius is often related to the exchange length l_{ex}. A variety of definitions for the exchange length in literature can lead to confusion at this point. Many papers about the magnetization reversal in cylindrical nickel nanowires refer to the value of $\tilde{l}_{\mathrm{ex}} = 20.7$ nm calculated by Schabes using the equation $\tilde{l}_{\mathrm{ex}} = \sqrt{A}/M_{\mathrm{s}}$ and the material parameters exchange constant $A = 10^{-6}\frac{\mathrm{erg}}{\mathrm{cm}}$ and saturation magnetization $M_{\mathrm{s}} = 483\frac{\mathrm{emu}}{\mathrm{cm}^3}$ [Sch91]. The fact that the formula used by Schabes does not deliver a length in units of meters is never discussed. However, the value of 20.7 nm is used when calculating one possible curve for the dependence of the switching field on the diameter of the wires in Fig. 5.2, since it is often referred to in the literature and since it is a median value for r_{c} facing Fig. 5.4.

Using the SI system the exchange length is given by $l_{\mathrm{ex}} = \sqrt{A/K}$ (Eq. 2.19). With the material parameters listed in Table 2.1 this yields $l_{\mathrm{ex}} = 8.3$ nm for nickel if the shape anisotropy given by $K_\mathrm{d} = \mu_0 M_\mathrm{s}^2/2 = 1.47 \cdot 10^5 \frac{\mathrm{J}}{\mathrm{m}^3}$ is considered as the leading anisotropy term. This result is a factor of $\sqrt{2\pi}$ smaller than the value calculated by Schabes. Considering only the magnetocrystalline anisotropy $|K_1| = 0.45 \cdot 10^4 \frac{\mathrm{J}}{\mathrm{m}^3}$ yields $l_\mathrm{ex} = 47$ nm. Regarding Fig. 5.4 one could have the idea that these two values are the lower and upper limits for the critical radius.

There are also other definitions of the critical radius for the transition from coherent rotation to magnetization reversal via curling. Since the mode by which a particle reverses its magnetization will always be the one with the lowest critical field [O'H00], one approach for the calculation of the critical radius is equating the critical fields for coherent rotation and curling given by Eqs. 2.21 and 5.2, respectively [Hub09]. This yields a critical radius of

$$\tilde{r}_\mathrm{c} = \sqrt{\frac{r_\mathrm{c}^2 k}{2N_\perp}} = \sqrt{\frac{kA}{N_\perp \mu_0 M_\mathrm{s}^2}}. \tag{5.4}$$

The expression still includes a critical radius which at this point shall be the exchange length $l_\mathrm{ex} = \sqrt{A/K}$ with $K = K_\mathrm{d} = \mu_0 M_\mathrm{s}^2/2$.

Another approach is to consider the following energy balance: The stray-field energy that has to be overcome during uniform magnetization reversal is given by $N_\perp \mu_0 M_\mathrm{s}^2$. This energy can be saved by magnetization reversal via curling which avoids most of the stray field. Equating this energy with the cost of exchange energy due to curling of the magnetization in a prolate ellipsoid as calculated by Frei *et al.* [Fre57] yields a critical radius of

$$r_\mathrm{c} = \sqrt{\frac{3A}{N_\perp \mu_0 M_\mathrm{s}^2}\left[ln(\frac{4r_\mathrm{c}}{a}) - 1\right]}. \tag{5.5}$$

Here, a is the radius of the core singularity which is usually chosen to be the lattice constant [Fre57, O'H00]. For nickel it is given by $a_\mathrm{nickel} = 0.352$ nm [Wik]. Equation 5.5 can only be solved numerically.

The above expressions for the critical radius are reminiscent of an exchange length corrected by additional factors accounting for the geometry of the nucleation volume. Thus, the critical radius can be interpreted as a function of an effective anisotropy K_eff:

$$r_\mathrm{c} = \sqrt{\frac{A}{K_\mathrm{eff}}}. \tag{5.6}$$

Figure 5.5 shows the effective anisotropy resulting from the data presented in Fig. 5.2 using Eqs. 5.3 and 5.6.[6] The maximum value of $K_\mathrm{eff} \approx 7 \cdot 10^4 \frac{\mathrm{J}}{\mathrm{m}^3}$ is smaller than the anisotropy contribution expected due to the demagnetizing energy that is given by

---

[6] Equation 5.3 considers only the third term of Eq. 5.2. Thus, a systematic error might be made in this consideration. The other two summands of Eq. 5.2 also account for the influence of an effective

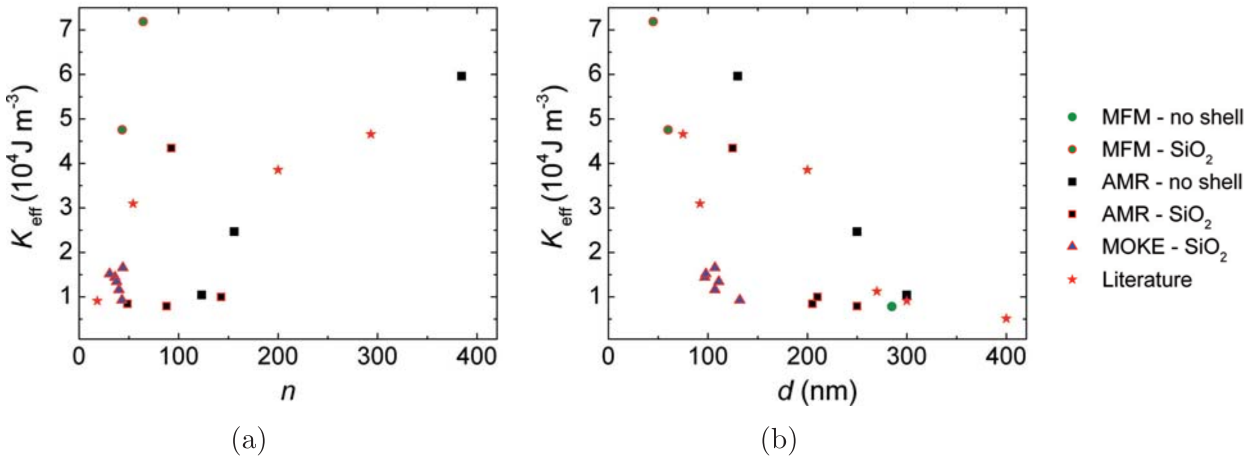

(a) (b)

Figure 5.5: Effective anisotropy of nickel nanowires versus (a) the aspect ratio n and (b) the diameter d of the wires. The data was calculated from the switching fields shown in Fig. 5.2 using Eqs. 5.3 and 5.6. Some data points only occur in (b) since the lengths of the respective wires and thus the aspect ratios n are unknown.

$K_\mathrm{d} = \mu_0 M_\mathrm{s}^2/2 = 1.47 \cdot 10^5\ \frac{\mathrm{J}}{\mathrm{m}^3}$. Thus, in none of the wires the effective anisotropy originates from the shape anisotropy of the whole cylinder volume alone.

A source of error is the limited accuracy when measuring the diameter of the wires with a scanning electron microscope (SEM). Usually the diameter was measured in the middle of the wire. The measured value is not necessarily the one that should be considered when applying analytical models. The thickness of the nickel-oxide layer was not subtracted from the total diameter of the nickel wires, since their exact value is unknown. Furthermore, it is often observed that the wires are cone-shaped. Variations of the diameter of more than 20 percent from one end to the other are not a rarity. It is also possible that the pores of the membranes the wires were grown in were not round but elliptical, compare Fig. 5.6(a). As a consequence the wires are not of perfect cylindrical shape either. Whether this is the case for a particular wire is hard to tell from SEM images. Sometimes the pores do not grow straight but there is so-called branching and two pores grow into one. A moderate form of this effect leads to bumps on one side of a wire as the one shown in the close-up of Fig. 4.10(a). In this case the cross-section of the wire is not elliptical anymore. These geometrical aspects do not only affect the effective diameter of the wires, which's wrong determination can not solely be responsible for the large scattering of the switching fields and thus K_eff anyway. The demagnetizing fields and thus the shape anisotropy are highly sensitive to surface irregularities. Strictly speaking

---

anisotropy. As emphasized by Aharoni the effect of adding uniaxial magnetocrystalline anisotropy to the curling model has essentially the same effect as changing the shape anisotropy by adapting the geometrical parameters [Aha97a].

the analytical models only describe magnetically homogeneous particles of ellipsoidal shape including the limit of an infinite cylinder with elliptical cross-section, and the anisotropy axes have to coincide with the sample axes [Hub09]. Figures 5.6(b) and (c) are transmission electron micrographs of nickel nanowires comparable to the ones studied in this work. The wires do not appear homogeneous, a granular structure of the material is clearly visible. As discussed above the shape of the wires often differs from ellipsoidal shape. Regarding our experimental results, the last condition, namely a single anisotropy axis in parallel to the wire axis, is not met as well. The variation of the effective anisotropy is only one example. Another indication for the presence of multiple anisotropy axes is the sometimes observed asymmetry of the angular-dependent switching fields as shown in Fig. 4.7(c).[7]

While the aspect ratio n of the nickel wires does not seem to have an impact, the effective anisotropy plotted in Fig. 5.5 remarkably decreases with increasing diameter d of the wires. An explanation for this could be a change of the crystalline structure of the wires with varying diameter. It is well known that the 'softness' of a ferromagnetic structure is grain-size dependent [Her90]. Unfortunately, there is only little information about the orientation and size distribution of the grains in the wires under discussion. Rheem *et al.* report a grain size of 22 nm and 30 nm in wires with a diameter of 30 nm and 200 nm, respectively. In the thinner wires the preferred orientation of the grains with respect to the wire axis is the <220> direction, while in the 200 nm wires it is random [Rhe07b]. In his Ph. D. thesis Kornelius Nielsch reports grain sizes up to 100 nm and a preferred <220> orientation in nickel wires with a diameter of 55 nm [Nie02a]. A <220> oriented crystal growth in electrodeposited nickel wires is reported by other groups as well [Pan05, Che10]. These groups also claim that under certain growth conditions single-crystalline wires can be synthesized. In electrodeposited nickel wires with diameters between 30 and 200 nm grown in track-etched polycarbonate membranes, Whitney *et al.* found a polycrystalline structure with grains generally extending the full width of the wire. The preferred growth direction was <111>. From the examination of many wires, however, a number of other orientations were observed, particularly for wires with smaller diameters [Whi93]. With the information available, we can only speculate that regarding our data a change of the crystalline structure of the wires is responsible for a varying contribution of magnetocrystalline anisotropy to the effective anisotropy of the nickel nanowires.

It seems as if the presence of a silica shell leads to an additional reduction of the effective anisotropy. This might be attributable to different surface anisotropies.

---

[7] The axis of wire Jan5-01 was approximately aligned into the $\varphi = 150°$ direction. A minimum value of the switching field is measured at $\varphi = 130°$ what corresponds to an angle of $\theta = -20°$ between the applied magnetic field an the wire's axis. It appears as if the angular dependence of the switching field is an overlay of a curve symmetric around $\varphi = 130°$ and a curve with a minimum at about $\varphi = 180°$, and thus the consequence of at least two anisotropy axes.

Without silica shell the surface of the nickel wires oxidizes during the dissolution of the alumina membrane by phosphoric acid. The thickness of the native nickel-oxide layer usually varies between 5 nm and 10 nm [Kor]. If the wires are protected by a silica shell the nickel is not expected to oxidize. The difference between the two types of surface layers could account for a difference of the magnetic properties at the surface. If for example the oxidation of the nickel occurred grainwise, the pure nickel core in wires without a silica shell would have a rougher surface. The thickness of the native nickel oxide layers was not subtracted from the total diameter of the nickel wires in the above evaluation. This would lead to a systematic shift of the values for wires with and without silica shell and even increase the offset between the effective anisotropies. An other aspect is magnetostriction which is known to have a large impact on the anisotropy in nickel wires [Mei96]. Since our own measurements were conducted at room temperature, the mechanism possibly causing stress is not as clear as in the publication of Meier *et al.* where it is caused by the different thermal expansion coefficients of the nickel wires and the surrounding polycarbonate membrane. The presence of a silica shell might also affect the electrochemical deposition, therewith the crystal growth, and thus vary the 'softness' of the wires as discussed already in the previous paragraph.

Besides varying contributions to the effective anisotropy, variations of the saturation magnetization could be a reason for the scattering of switching fields. The theoretical value for M_s can be calculated considering the magnetic moment per atom which is about 0.6 μ_B, the amount of atoms in a unit cell that is four for a face-centered cubic lattice, and a lattice constant of $a_\mathrm{nickel} = 0.352$ nm: $M_\mathrm{s} = \frac{0.6\,\mu_\mathrm{B}\cdot 4}{a_\mathrm{nickel}} \approx 5.1 \cdot 10^5 \frac{\mathrm{A}}{\mathrm{m}}$. This value corresponds to the experimental value at zero Kelvin. The material constant M_s

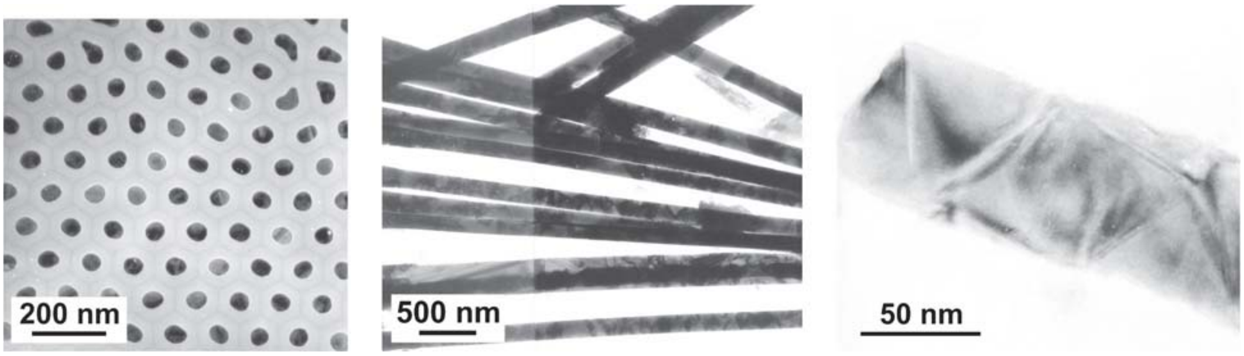

(a) (b) (c)

Figure 5.6: Transmission electron micrographs of nickel nanowires. (a) Cross-section of an array in an alumina membrane. (b) Several wires after dissolution of the membrane. (c) Close-up of an individual wire. Images by courtesy of K. Nielsch.

is known to decrease for increasing temperatures following a Curie-Weiss law.[8] Since all our measurements are conducted at room temperature where $M_\mathrm{s} = 4.83 \cdot 10^5 \frac{\mathrm{A}}{\mathrm{m}}$ for bulk nickel, this reason for a fluctuation of M_s can be excluded. Probably the predicted value for M_s only exists on a microscopic scale. For an inhomogeneous material as the nickel wires under consideration, the direction of the spontaneous magnetization varies from one point to another, so that the macroscopic average is smaller than the theoretical value [Bro45]. Furthermore, deviations of the saturation magnetization compared to the bulk value are sometimes observed in nanostructured materials. Possible explanations are intrinsic stress due to lattice defects and surface effects resulting in a reduction or enhancement of the lattice constant [Qin99, Sal12]. The above aspects can account for a variation of M_s from wire to wire.

So far we have assumed that the nucleation by curling takes place in the entire volume of a wire which was approximated by an infinite cylinder. It is clear that the magnetic behavior in a finite geometry differs fundamentally from that of an infinite cylinder [Ehl88]. An infinite cylinder has no poles, and thus no demagnetizing fields at the wire ends. The presence of magnetic poles leads to an additional energy contribution that can be reduced by the rotation of the magnetic moments at the wire ends. The demagnetizing field at a wire end adds to the effective field, so the switching fields decrease if poles are considered. It was already assumed by other authors that the nucleation only takes place in a small fraction of the wire's volume [Weg99, Pig00]. This is in agreement with our micromagnetic simulations presented below and the ones of Hertel *et al.* [Her02, Her04] in which during nucleation the magnetization curls only at the wire ends, compare Fig. 5.8. The aspect ratio n of the nucleation volume in which the magnetization curls at the wire end is small compared to that of the entire cylinder.[9] Hence, the contribution of the shape anisotropy to the effective anisotropy reduces compared to a long or even infinite cylinder. As a consequence the influence of other anisotropy contributions such as magnetocrystalline anisotropy and magnetostriction increases. According to Eqs. 5.4 and 5.5, the critical radius is proportional to $\sqrt{\frac{1}{N_\perp}}$. Calculating the demagnetizing factor $N_\perp$ using Eq. 2.23 a reduction of the aspect ratio of the nucleation volume from $n = 200$ to $n = 2$ leads to an increase of the critical radius by 28 percent. If the reversal process is dominated by nucleation in a small volume, the local magnetic properties of this volume play a crucial role, and the presence of defects in this region will have a large impact. This, however, cannot be accounted for in an analytical model.

---

[8] At low temperatures $M_\mathrm{s}(T)$ for nickel actually decreases at a higher rate than the Brillouin function for $S = \frac{1}{2}$ due to spin waves [O'H00].

[9] The volume on the opposite wire end where the magnetization curls as well is not added to the nucleation volume for the following reason: to break the symmetry the wire in the micromagnetic simulation was chosen to be 5 nm thicker on one end. This ensures that the reversal always starts from the same side, namely the thicker end. Thus we will only consider the nucleation process there.

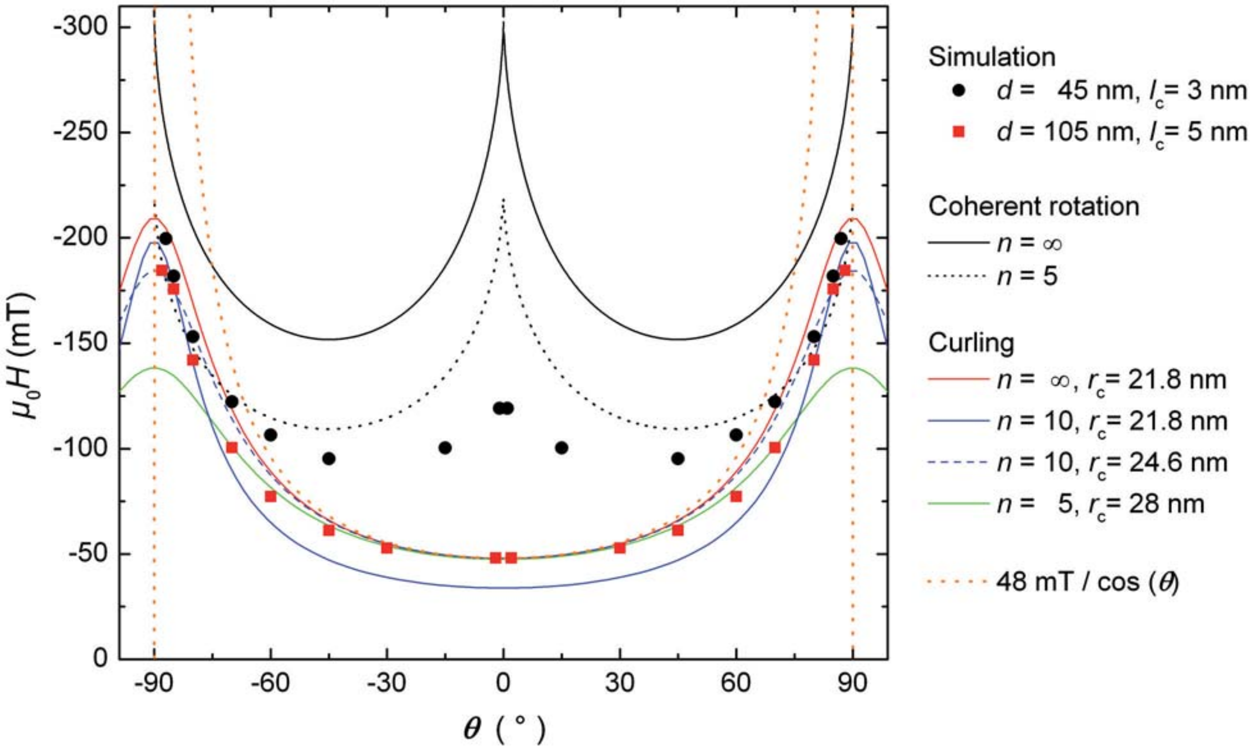

Figure 5.7: Angular dependence of the switching field simulated for 1 μm long nickel nanowires with diameters of $40 + 5$ nm (black circles) and $100 + 5$ nm (red squares). The average mesh sizes l_c at the wire ends used for the simulation with the software nmag are given in the legend together with the parameters of the analytical curves, which are plotted for comparison. The curves are calculated using Eqs. 2.20-2.23 and Eq. 2.25 without considering the magnetocrystalline anisotropy K_1. Since the saturation magnetization used for the simulations is $M_s = 4.1 \cdot 10^5 \frac{\mathrm{A}}{\mathrm{m}}$ (according to Hertel *et al.* [Her04]) the same value is used for the analytical curves here.

As discussed above, the approximation of an infinite cylinder for the description of nickel nanowires has to be used with caution. The assumption of a small nucleation volume at the wire ends seems to be more reasonable. Considering a nucleation volume smaller than the volume of the entire wire by applying the curling model includes two errors: First, only one side of this volume experiences the demagnetizing field, while the other one is not a real end but connected to the rest of the wire's volume. Second, if this nucleation volume reverses, it is separated from the rest of the wire by a domain boundary, the energy of which cannot be neglected [Aha99]. The large scattering of the experimental values shows that even if an appropriate model considering these two aspects was found, reality would still not be described. The magnetic behavior seems to be dominated not by the geometry but by structural and magnetic inhomogeneities.

Given the doubts about the applicability of the curling model discussed above, micromagnetic simulations are advisable. Figure 5.7 depicts the angular dependence of the switching field simulated with nmag[10] for 1 μm long nickel cylinders with diameters of $40 + 5$ nm and $100 + 5$ nm.[11] For comparison the critical fields resulting from the Stoner-Wohlfarth model of coherent rotation and from the curling model for nickel cylinders of different aspect ratios are plotted in the figure as well. The angular-dependent switching field of the $40 + 5$ nm thin wire looks like a mixture of both reversal mechanisms. This argues for the diameter of the wire being in the vicinity of the critical radius which marks the transition from coherent rotation to curling. The curve progression of the switching field simulated for the $100 + 5$ nm thick wire has a minimum if the external magnetic field is applied along the wire's axis. For small angles up to 30 degrees it is well described by analytical curves based on the curling model. The appropriate value for the minimum of the switching field can be obtained using different combinations of parameters as listed in the legend of Fig. 5.7. For an infinite cylinder and a critical radius of 21.8 nm the curling model predicts the red curve. Using the same critical radius and the actual aspect ratio $n = 10$ of the simulated wire reduces the minimum of the switching field from -48 mT to -34 mT (blue curve). A variation of the critical diameter of only 2.8 nm shifts the minimum back to -48 mT (dashed blue curve). Choosing even smaller aspect ratios of the nucleation volume and larger critical radii r_c the curve progression can be changed to better fit the simulated values at angles between 30 and 70 degrees (green curve). However, there is still a discrepancy that cannot be overlooked.

Figure 5.8 depicts the simulated magnetic states right before the magnetization reverses. For small angles θ between the applied magnetic field and the wire axis the core around which the magnetization curls is clearly visible at the end of the wire. At $\theta = 45°$ the core has reached the edge, and for larger angles it has moved to the side wall of the cylindrical wire. The magnetic configuration looks very different now. A rotational symmetry as it is characteristic for the curling mode is not even rudimentarily given anymore. The magnetic structure at the front side of the wire is rather reminiscent of the reversal in wires thinner than the critical radius in which transverse domain walls, nucleating via coherent rotation, are observed. It might thus be an option to assume that for large angles the angular dependence of the switching field can be described by the Stoner-Wohlfarth model. As can be inferred from Fig. 5.7, it is possible that the curves for coherent rotation and curling cross each other. Since the reversal will always take place via the mode with the smaller critical field, a transition from curling to coherent rotation at large angles is possible. This idea was

---

[10] The basics on micromagnetic simulations and the software package nmag as well as the reversal modes found in soft magnetic cylindrical nanowires are presented in chapter 3. Like the analytical models our micromagnetic simulations are done for idealized particles. Nowadays granularity and imperfections such as surface roughness, magnetic inhomogeneities, and defects can be implemented into the micromagnetic models [Nma, For02]. The complexity of such simulations as concerns modeling and computational power lies beyond the scope of this work. Furthermore, the grain size and distribution of the nickel nanowires studied are unknown.

[11] +5 indicates that one wire end was chosen to be 5 nm thicker to create a directed reversal process.

pursued by Pignard *et al.* and Rheem *et al.* when interpreting their data on 35 nm thin nickel nanowires and cobalt-nickel wires, respectively [Pig00, Rhe07a]. With respect to our simulation it contradicts the truncating progression of the switching fields for angles above 80 degrees, which is not given in the Stoner-Wohlfarth model. Even for large angles, the magnetic configurations right before switching are never uniform as it is characteristic for coherent rotation.

A point which was not addressed yet is that the curling model yields a nucleation field that is not necessarily equal to the switching field. Only in the case of the external

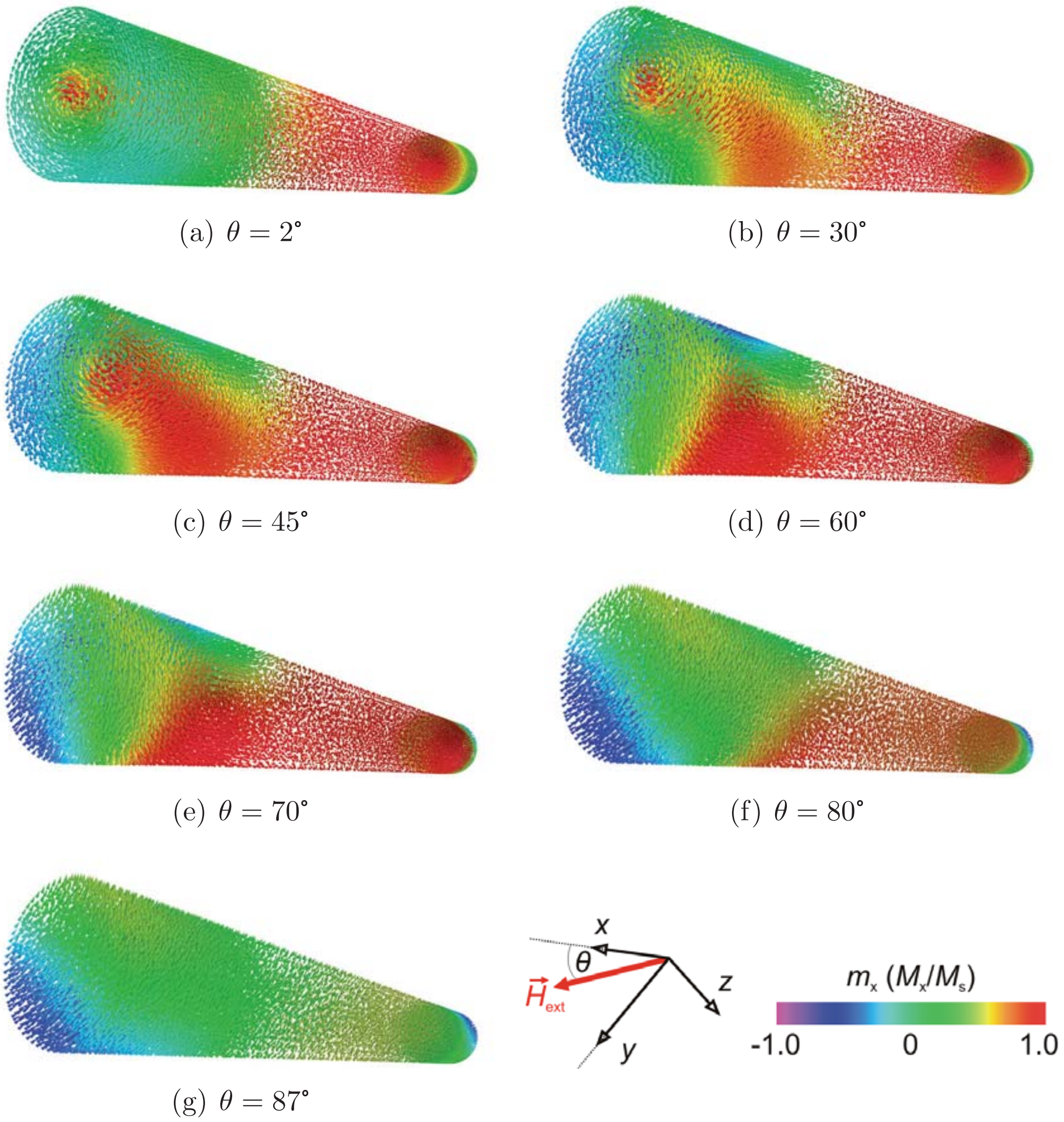

(a) $\theta = 2°$

(b) $\theta = 30°$

(c) $\theta = 45°$

(d) $\theta = 60°$

(e) $\theta = 70°$

(f) $\theta = 80°$

(g) $\theta = 87°$

Figure 5.8: Magnetic states of a 100+5 nm thick nickel wire right before the magnetization reverses simulated for several angles θ between the applied magnetic field $\vec{H}_{\mathrm{ext}}$ and the wire's axis (x-axis).

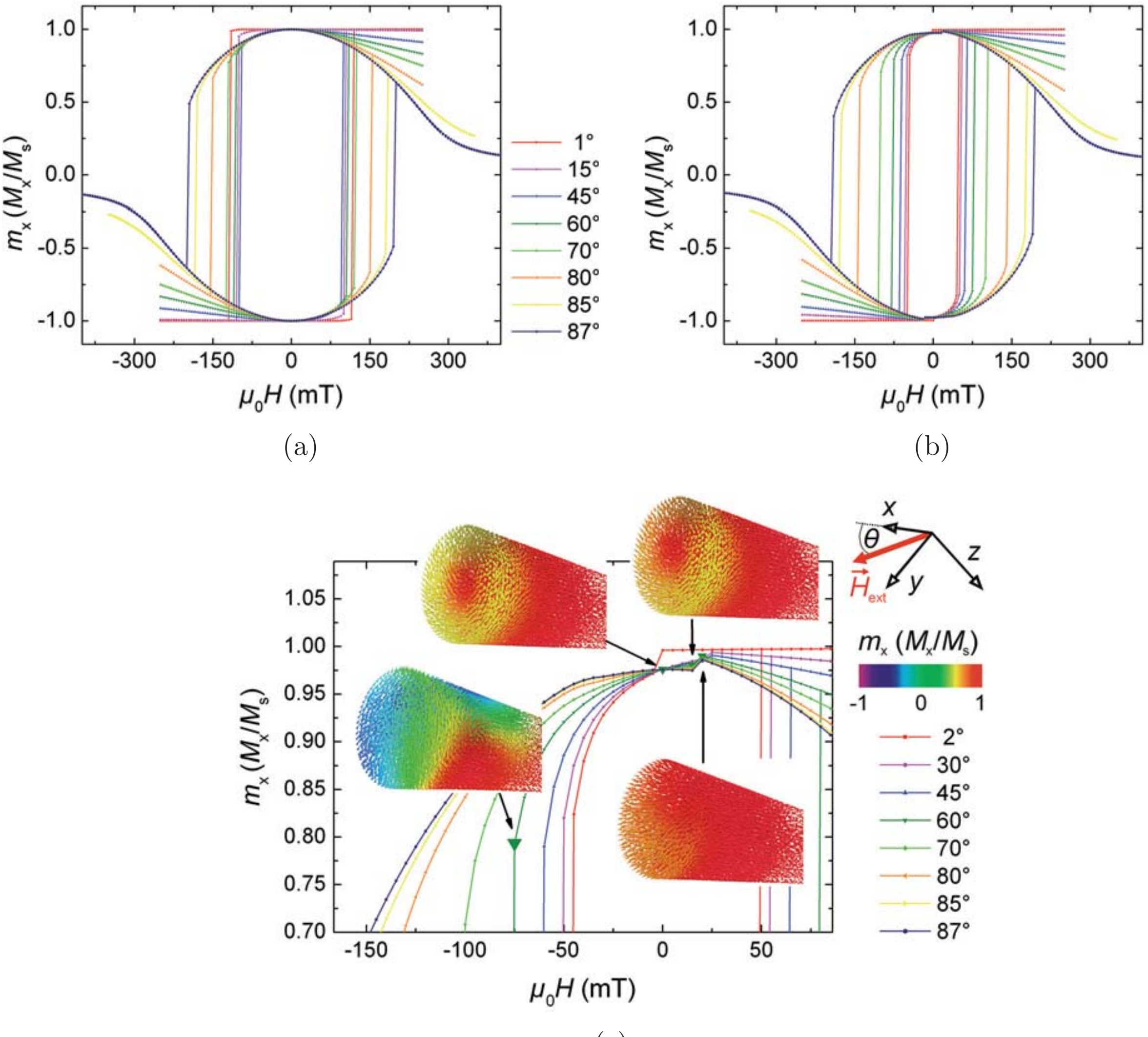

(a) (b)

(c)

Figure 5.9: Magnetization versus field curves simulated for nickel nanowires with a diameter of (a) $40+5$ nm and (b) $100+5$ nm. Plotted are the projections of the total magnetization on the wire axis m_x for several angles θ between the applied magnetic field $\vec{H}_{\text{ext}}$ and the wire axis (x-axis). (c) is a blow-up of (b) revealing the nucleation process in the wire with a diameter of $100+5$ nm. The insets show the magnetic states simulated for a field direction of 60 degrees (green curve).

field being applied in parallel to an infinite cylinder the magnetization reversal occurs right at the nucleation field [Aha58]. Figure 5.9 shows the magnetization versus field curves of the $40 + 5$ nm and of the $100 + 5$ nm thin wires simulated for different angles between the applied magnetic field and the wire axis. The huge jumps indicate the respective fields at which most of the wires' magnetization reverses, namely the switching fields.[12] In the curves for the $100 + 5$ nm wire (Fig. 5.9(b)) there is an additional small jump. It occurs a few field steps before the applied field is reduced to zero.[13] Figure 5.9(c) is a close-up of these jumps which can be observed when coming from positive saturation. The insets depict the magnetic states at the characteristic points (enlarged green symbols) right before and after the jump, at remanence, and before switching simulated for an angle of 60 degrees between the applied magnetic field and the wire axis. At the other angles the magnetic states look similar or are rather shown in Fig. 5.8. The small jumps are caused by the nucleation of the vortex-like magnetic structure at the wire end. Since in the respective field range the step size was large, the exact values of the nucleation fields are unknown. In view of the stray-field energy it is not surprising that in the remanent state the magnetization at the wire ends is already curled. Solely from this consideration the equality of the nucleation field yielded by the curling model for long cylinders and the switching field of nickel nanowires is disputable. The critical fields plotted in Fig. 5.2 for cylinders with an aspect ratio of $n = 20$ (blue curve) and $n = 5$ (green curve) cross the x-axis for diameters of 300 nm and 125 nm, respectively. This illustrates that the critical fields obtained from the curling model are not switching but nucleation fields. It is well known that the Stoner-Wohlfarth model overestimates the experimental values of the critical fields by more than 100 percent [Kro87, Kro07]. This is called Brown's paradox. Since the curling model used to analyze the data is derived from the Stoner-Wohlfarth model, it is to some extend surprising that it matches the experimental results comparably well. It can not be excluded that this is just a coincidence.

To conclude, the applicability of analytical models to cylindrical nickel nanowires has to be called into question. Nevertheless, the curling model was applied in this section to evaluate data. For isotropic prolate spheroids with aspect ratios below $n = 500$, there exist no other modes for magnetization reversal than the ones considered [Aha97b]. Furthermore, the systematic study using micromagnetic simulations is rather time consuming, and dependencies as the one of an effective anisotropy on the switching field are not as obvious. The application of the curling model, especially when assuming an infinite cylinder, certainly leads to wrong results as concerns absolute values. Nevertheless, important insights concerning the magnetic properties of cylindrical nanowires and their influence on the magnetization reversal were obtained. The distribution of the experimental values for the switching field of cylindrical nickel nanowires can be attributed to the influence of defects and variations of the saturation magnetization as well as to varying anisotropy contributions in the

---

[12] To find the switching fields plotted in Fig. 5.7 additional simulations with finer field steps in a smaller field range were performed to save computation time.

[13] The jump in the magnetization curve simulated for an angle of two degrees between the applied magnetic field and the wire's axis occurs not before a small reverse field is applied. This result is physically unlikely and can be attributed to the fact that thermal effects and other fluctuations mediating magnetic states with similar energy are not considered in the simulations.

individual wires. The nucleation volume is unlikely to correspond to the entire volume of a wire. Micromagnetic simulations suggest nucleation at the wire end. The smaller the aspect ratio of the nucleation volume, the weaker is the influence of the shape anisotropy which has to compete with other anisotropy contributions, in particular with the magnetocrystalline anisotropy. The above evaluation also revealed that the nickel wires studied in this work are comparable to the ones investigated by other groups. The following section discusses further experimental results obtained by magnetoresistance measurements, magnetic force microscopy, and photoemission electron microscopy. The latter two methods provide a direct insight into the magnetic behavior of nanostructures since they allow for magnetic imaging, and thus throw a brighter light on the reversal process in nickel nanowires.

5.2 Experimental results

In the last section the magnetization reversal in electrochemically synthesized nickel nanowires was analyzed by comparing absolute values of the switching field to analytical models and micromagnetic simulations. Besides the absolute values, the statistic scattering of switching fields provides information about the reversal process. The first part of this section deals with the shape of magnetoresistance traces as well as with statistics obtained by magnetoresistance measurements and magnetic force microscopy (MFM). Then, magnetic images acquired by MFM and photoemission electron microscopy (PEEM) are presented. Based on the direct insight into the magnetic behavior of nickel nanowires, a model on how the magnetization reversal takes place is suggested.

Magnetoresistance measurements were performed on about 15 straight nickel wires. Details about the definition of contacts and the experimental setups used are given in Sec. 4.2. Figure 5.10 depicts typical magnetoresistance traces. The black and red curves in (a) were recorded while the external magnetic field was sweeped in parallel to the wire's axis and perpendicular to it, respectively.[14] Magnetoresistive effects such as the anisotropic magnetoresistance (AMR, see Sec. 2.3.4) result in a curve progression that gives a footprint of the magnetic behavior of the sample [Weg98, Weg99]. At the maximum applied fields of ±550 mT the red curves are almost saturated at a minimum value. This means that most of the magnetization in the wire is aligned perpendicular to the current direction which is along the wire's axis. If the field is reduced the resistance increases until a maximum is reached at remanence. Applying a field in the opposite direction, the resistance decreases again. The red curve is almost symmetric around zero field. In the center and around

---

[14] For technical reasons an accuracy of ±2 degrees in the specification of the angle between the applied magnetic field and the wire's axis has to be assumed.

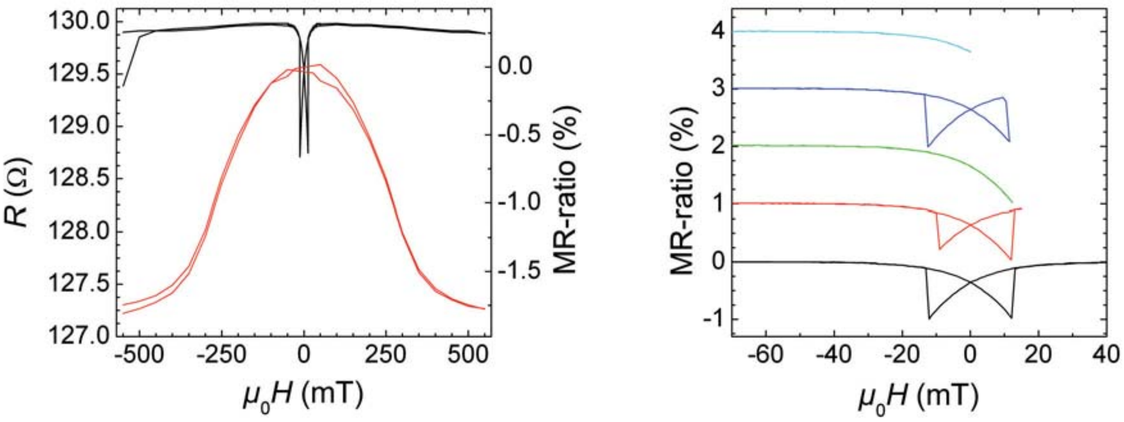

(a) (b)

Figure 5.10: Magnetoresistance traces recorded on a nickel nanowire called 3w with an average diameter of 155 nm. (a) The red and black curves were recorded in two-point geometry sweeping the field between ±550 mT perpendicular and in parallel to the wire's axis, respectively. (b) Minor loops with the magnetic field applied along the wire's axis. Apart from the bottom curve, which is a close-up of the black curve shown in (a), the curves are shifted for clarity. The measurements were done in four-point geometry at setup 3.

−500 mT the back and forth sweeps do not overlap. Monitoring of the temperature during the measurement shows that thermal drifts can be excluded as a cause for this at around zero field. Thus the offset of the curves has to be attributed to different micromagnetic configurations. Since no full saturation can be reached to 'reset' the structure, this is not unlikely. If the external field is applied in parallel to the wire (black curve), hysteretic magnetic behavior is observed. Saturation is reached at about ±50 mT. For larger fields the resistance is dominated by the negative magnetoresistance (see Sec. 2.3.3). The bottom curve in Fig. 5.10(b) is a close up of the center part of the black curve in (a). The minor loops also shown in (b) reveal that the magnetoresistance traces are characterized by two main features providing insight into the magnetic behavior of nickel nanowires: an irreversible jump and a gradual reversible contribution. The hysteretic jumps indicate the switching fields in positive and negative field direction. The average values of these fields for wires of different diameters were discussed on the basis of the curling model in the previous section of this chapter. The statistic scattering of the switching fields in an individual wire also provides information about the reversal mechanism. This will be analyzed in the following. The other feature is revisited later.

Figure 5.11 illustrates the switching-field distribution of a nickel nanowire with a diameter of 155 nm. The top and bottom panels depict the statistics of the switching events for sweeps into positive and negative field directions, respectively. In Fig. 5.11(a) the external magnetic field was applied along the axis of the wire. For

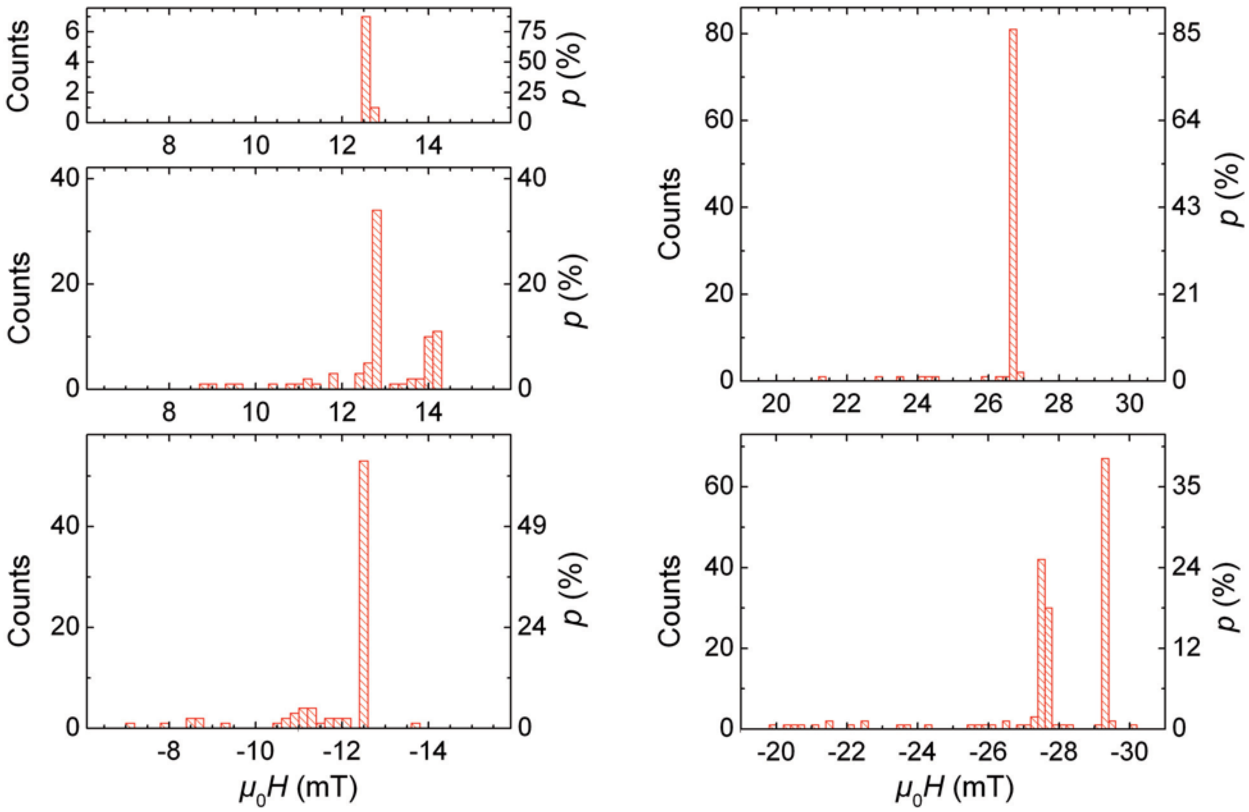

(a) 0 degrees (b) 67 degrees

Figure 5.11: Statistic of the switching fields of a nickel nanowire called 3w with an average diameter of 155 nm measured at setup 3 with the external field applied (a) in parallel to the wire axis and (b) at an angle of about 67 degrees. p are the probabilities for magnetization reversal at a certain value of the applied field. Due to the influence of thermal drift on the switching fields measured at 67 degrees, the values were corrected as explicated in the Appendix Sec. B.7. The two lower panels in (a) were recorded in four-point geometry. Then the wire got destroyed by a discharge between one pair of outer contacts and the experimental studies were continued by two-point measurements. To confirm that no fundamental changes of the magnetic behavior of the wire were caused by its partial destruction, the statistic shown in the upper panel of (a) was recorded. It is in line with the previous results shown below.

negative reverse fields there is one sharp peak at -12.5 mT at which 53 percent of the counts occur and a wide Gaussian shaped distribution around -11.3 mT (in total 25 percent of the counts). In the positive field direction the sharp peak is shifted to 12.7 mT (51 percent), and there is an additional accumulation of events around 14 mT that make up about 30 percent of the total counts. In both field directions there are several individual counts at comparably small fields down to 7 mT. A striking point is that instead of a stochastic distribution around the peak values a distinct scattering towards lower fields is observed. Only the rather symmetric accumulation of events around −11.3 mT is an exception here. In negative field direction there is a single count in the vicinity of 14 mT. These results imply that the magnetization reversal does not always take place via the same mechanism associated with a characteristic field value, but that there are competing processes. Each process has its characteristic probability and switching-field distribution. Figure 5.11(b) displays the scattering of the switching fields for an angle of about 67 degrees between the applied magnetic field and the wire's axis. The overall behavior is the same as in (a). Interestingly, the characteristic probabilities for the individual reversal processes have changed. In negative field direction there are still two accumulation values, namely at −27.5 mT and −29.3 mT. The associated probabilities are 50 and 42 percent, respectively. At positive fields, however, there is only one sharp peak. At angles of 22 degrees (6 sweeps) and 45 degrees (4 sweeps) between the applied magnetic field and the wire's axis the switching fields were measured as well. The average values and standard deviations are plotted in Fig. 5.12 (blue and black symbols). The figure also shows the angular-dependent switching field of a straight nickel wire with gold ends determined by magnetic force microscopy (MFM) (green and orange symbols). An MFM image of the wire is shown in Fig. 4.11 of Sec. 4.3 where the method is explained.

No difference in switching field was found if the MFM probe was scanned across the end of the wire or along the wire's axis. In the latter case it was possible to observe that the magnetization does not always reverse at once. In the cases where this so-called pinning is observed, the field at that the first wire segment reverses is taken as switching field. The orange triangles in Fig. 5.12 indicate the average field values H_{fin} at that the wire completely reverses its magnetization.[15] For both wires treated in Fig. 5.12 the standard deviations as a measure for the scattering of the switching fields do not vary remarkably for the different angles between the applied magnetic field and the wires' axes.

It was found that the chance to observe pinning in the 300 nm thick nickel wire studied by MFM can be increased by increasing the angle between the wire's axis and the applied magnetic field. This is illustrated in Fig. 5.13. If the field is applied in a direction close to the wire's axis, the probability of magnetization reversal without the detection of a domain boundary is 50 percent. For an angle of 63 degrees between the applied magnetic field and the wire's axis increased magnetic contrast in the middle of the wire indicating pinning is observed during all reversal processes recorded.[16]

---

[15] It was also observed once that for large angles the maximum field of 100 mT was not sufficient to erase all domain walls.

[16] At such a large angle between the applied magnetic field and the wire's axis the interpretation of data recorded by doing line scans along the wire is challenging. Four out of seven sweeps are not included into the evaluation, since both wire ends appeared with the same color contrast.

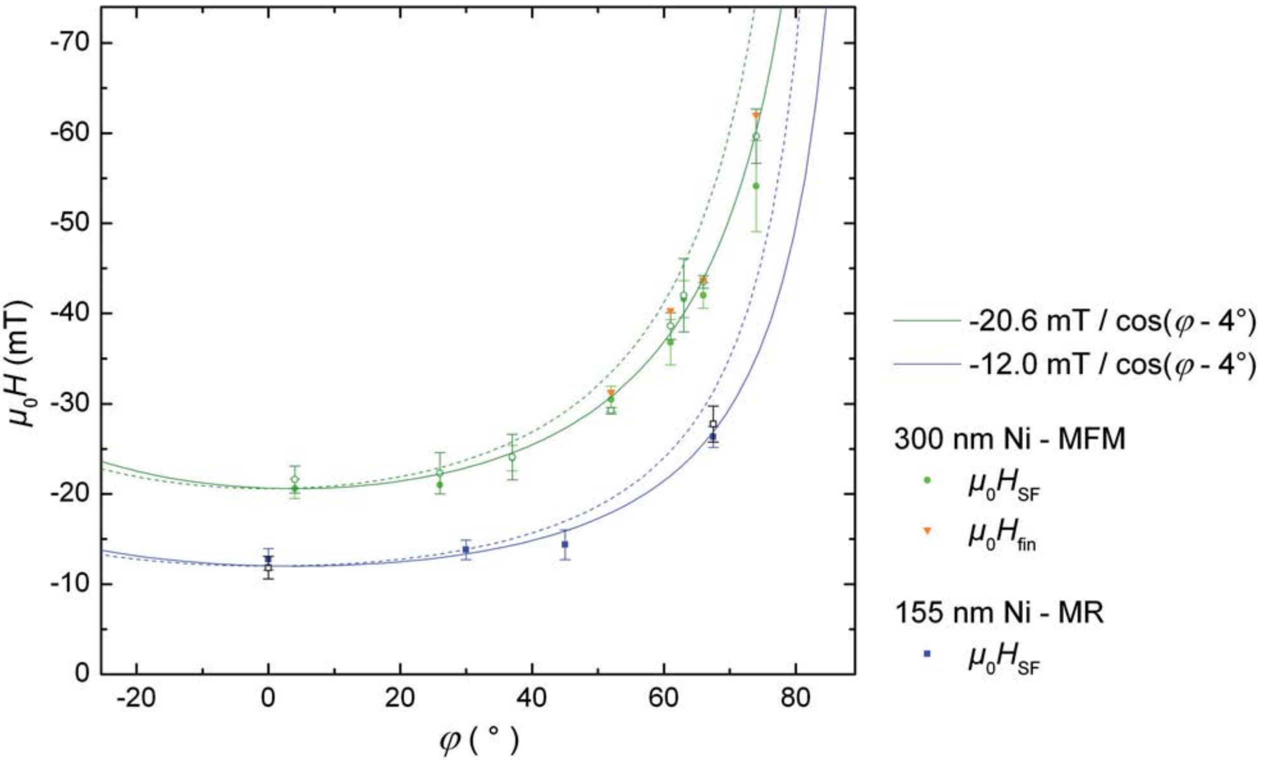

Figure 5.12: Angular dependence of the switching fields H_{SF} of cylindrical nickel nanowires. The green data points were measured by magnetic force microscopy (MFM) on a wire with gold ends and a diameter of about 300 nm. The orange triangles mark the maximum field values H_{fin} up to which a domain wall could be observed in the wire. The blue data points were obtained by magnetoresistance (MR) measurements at setup 3 on a wire called 3w with a diameter of 155 nm. Both wires are not surrounded by a silica shell. The open symbols are the switching fields measured in the opposite field direction. φ is the angle between the applied magnetic field and the wire axis estimated from the experimental layout. The dashed and straight curves are proportional to $1/\cos\varphi$ and $1/\cos\varphi - 4°$, respectively. The latter curves fit the data better what hints at an offset of 4 ± 2 degrees between the actual and the estimated anisotropy axis.

Different pinning probabilities can be associated with different domain-wall types. Thus, the different pinning probabilities for different angles between the applied magnetic field and the wire axis indicate that the magnetization reversal can take place based on miscellaneous nucleation processes, the probability of which depends on the direction of the external field. This is one aspect of magnetization reversal via various competing paths [Bri11]. The idea of miscellaneous paths is supported by the observation that the magnetic patterns differ from reversal to reversal. Figure 5.13(b) depicts two typical processes. In the upper scan recorded at an angle of four degrees between the external magnetic field and the wire's axis the magnetic contrast on the left end of the wire changes from dark to bright at an applied field of −20 mT. At the same time a dark contrast arises in the middle of the wire. The right end turns dark

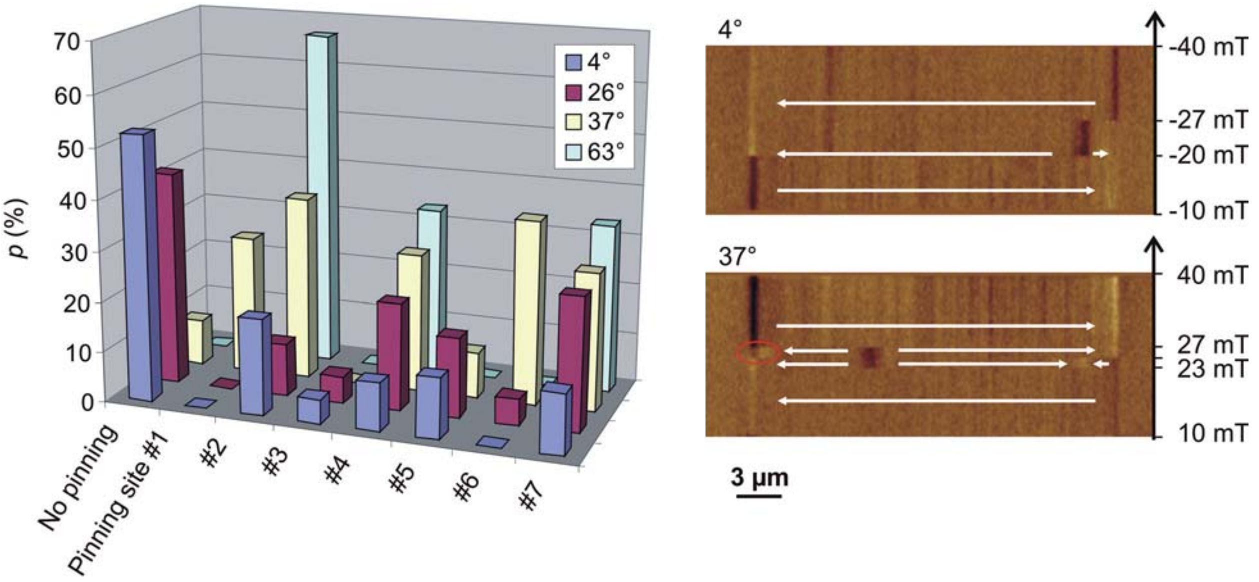

(a) (b)

Figure 5.13: (a) Probability p of domain-wall pinning at defects in a straight nickel nanowire with a diameter of 300 nm, gold ends, and no silica shell. The statistics were measured by magnetic force microscopy scanning the probe along the wire's axis while the external magnetic field is sweeped. Underlying data is exemplarily shown in (b).

at −27 mT. At the same time, the dark contrast in the middle vanishes. This can be interpreted as a magnetization reversal via the propagation, pinning, and depinning of a domain wall. Considering all cases where a domain boundary is observed in the middle of the wire the distribution of reversals starting from the left and from the right side of the wire is 50 : 50. The MFM scan shown in the bottom panel of Fig. 5.13(b) reveals a reversal process during that an inner segment of the wire switches first at about 23 mT, while the magnetic contrast at the wire ends stays unchanged. Such a behavior is never observed at four degrees but in two out of 19 and six out of 11 sweeps at 26 degrees and 37 degrees, respectively. The red oval in the figure marks the nucleation of a fourth domain on the left wire end at about 25 mT.

Summarized, the reversal process in nickel nanowires is of highly stochastic nature. There are several accumulation values for the switching fields which scatter statistically. Such a behavior is characteristic for magnetization reversal via domain-wall motion [Im09]. Furthermore, MFM images reveal that magnetization reversal does not always commence at the same place. Thus, there is not only a competition between different nucleation processes in one volume, but there are also several competing nucleation volumes. This leads to a variety of paths via that the reversal process can take place, each of which is associated with its characteristic switching field and switching-field distribution.

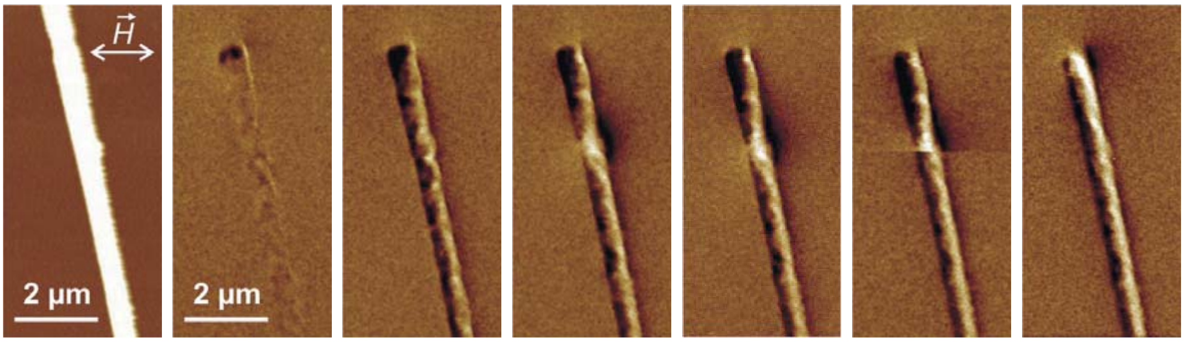

(a) AFM (b) 0 mT (c) 50 mT (d) 58 mT (e) 62 mT (f) 72 mT (g) 80 mT

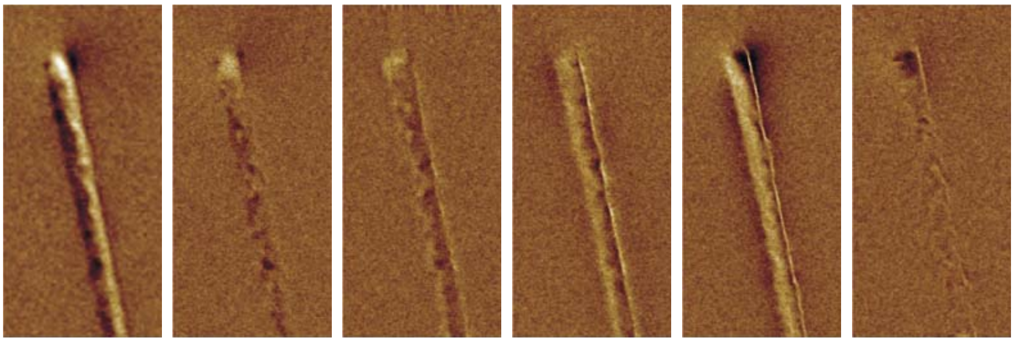

(h) 50 mT (i) 0 mT (j) -25 mT (k) -50 mT (l) -70 mT (m) 0 mT

Figure 5.14: (a) Topography and (b) through (m) hysteresis of a cylindrical nickel nanowire with a diameter of 300 nm imaged by magnetic force microscopy. The external magnetic field is applied horizontally at an angle of about 74 degrees to the wire's axis.

To address the physics behind the second characteristic feature of the MR traces in Fig. 5.10, namely the reversible continuous decrease of the resistivity before the switching of a wire, we will have a closer look at the magnetization between the ends of nickel nanowires. The magnetic contrast between the two wire ends in Fig. 5.13(b) is not always homogeneous, even if there is no domain boundary present in the wire. This means that there are other sources of magnetic stray fields. To obtain a better insight into the magnetic behavior of the wire, the MFM images depicted in Fig. 5.14 were recorded at different external fields applied at an angle of 74 degrees with respect to the wire's axis. Figure 5.14(a) displays the topography of the right end of the 300 nm nickel wire with gold segments at the ends. The corresponding magnetic image Fig. 5.14(b) depicts the remanent state after saturation at -100 mT. Besides a dark contrast at the transition from the nickel wire to the gold segment a weak magnetic pattern is visible throughout the entire nickel wire. Comparable patterns are observed in the remanent states shown in Figs. 5.14(i) and (m), as well as for weak applied fields (j). They originate from stray fields caused by locally varying orientations of the magnetic moments in the wire. For strong applied fields the magnetization is aligned along the (horizontal) field direction and the wire appears divided into a dark and a bright half along its axis. In Figs. 5.14(d) through (f) a bright contrast indicating a domain boundary is present. It is erased while the magnetic probe scans across it at an applied field of 72 mT. Comparable observations indicating that the depinning is triggered by the stray field of the magnetic probe were sometimes made on other wires as well. The switching-field values determined by MFM, however, did not depend on whether the probe was scanned along the wire or across its end only. This rather argues against a strong interaction between the magnetic probe and the sample's magnetization. Anyway, non-invasive imaging is advantageous. Thus, the magnetization reversal of cylindrical nanowires was also studied by PEEM, a method that uncovers the magnetization configurations underlying the inhomogeneities of the stray field detected by MFM.

Figure 5.15 displays PEEM images of a nickel nanowire with gold ends revealing the magnetization components along the wire's axis. If the effective anisotropy of the nickel wire was dominated by its cylindrical shape, the remanent magnetization after saturation should be homogeneous and mainly parallel to the wire's axis. The x-ray magnetic circular dichroism (XMCD) image in Fig. 5.15(c), however, depicts a rather inhomogeneous magnetic state. In a reverse field the inhomogeneity further increases, as can be seen from Fig. 5.15(d). Figures 5.15(e) and (f) are close-ups of the left wire end in an applied field of −27 mT before and after magnetization reversal, respectively. In the absolute PEEM images (top) an intensity variation on the wire reveals the granular structure of the nickel. In the XMCD images (bottom) the influence of the grains on the magnetic pattern is clearly visible. Local energy scans around the nickel L_3 edge in the marked areas A and B show a small difference in the characteristic of the satellite peaks emerging at 854.2 eV and 858.2 eV in area A. This might indicate different chemical states of the nickel, for example due to oxidation. After applying −41 mT to switch the wire the magnetic state imaged in an applied field of −27 mT (Fig. 5.15(f)) still does not appear homogeneous. This inhomogeneity of the magnetic contrast might partially be attributable to locally varying maxima of the XMCD contrast caused by material irregularities. Reasons for these can be local variations of the saturation magnetization or oxidation. The SEM image in Fig. 5.15(a) and the corresponding PEEM image in (b) reveal that a sole gold segment and an empty silica shell lie next to and on top of the wire under consideration. An empty shell is also visible in the central panel of Fig. 5.16(a). It is hard to say if the shells were peeled off of the wires imaged or if they come from unfilled pores. It cannot be excluded that the wires imaged have broken shells, and the nickel is at least partially oxidized at the wire's surface, as it is indicated by the PEEM spectra in Fig. 5.15(e).

Figure 5.16 displays the remanent magnetic state of an other nickel wire from the same batch. The top panels depict a scanning electron micrograph and PEEM images. The bottom panels in subfigures (a) and (b) are an overview and a close-up of the magnetization components in parallel to the axis of the wire. By changing the

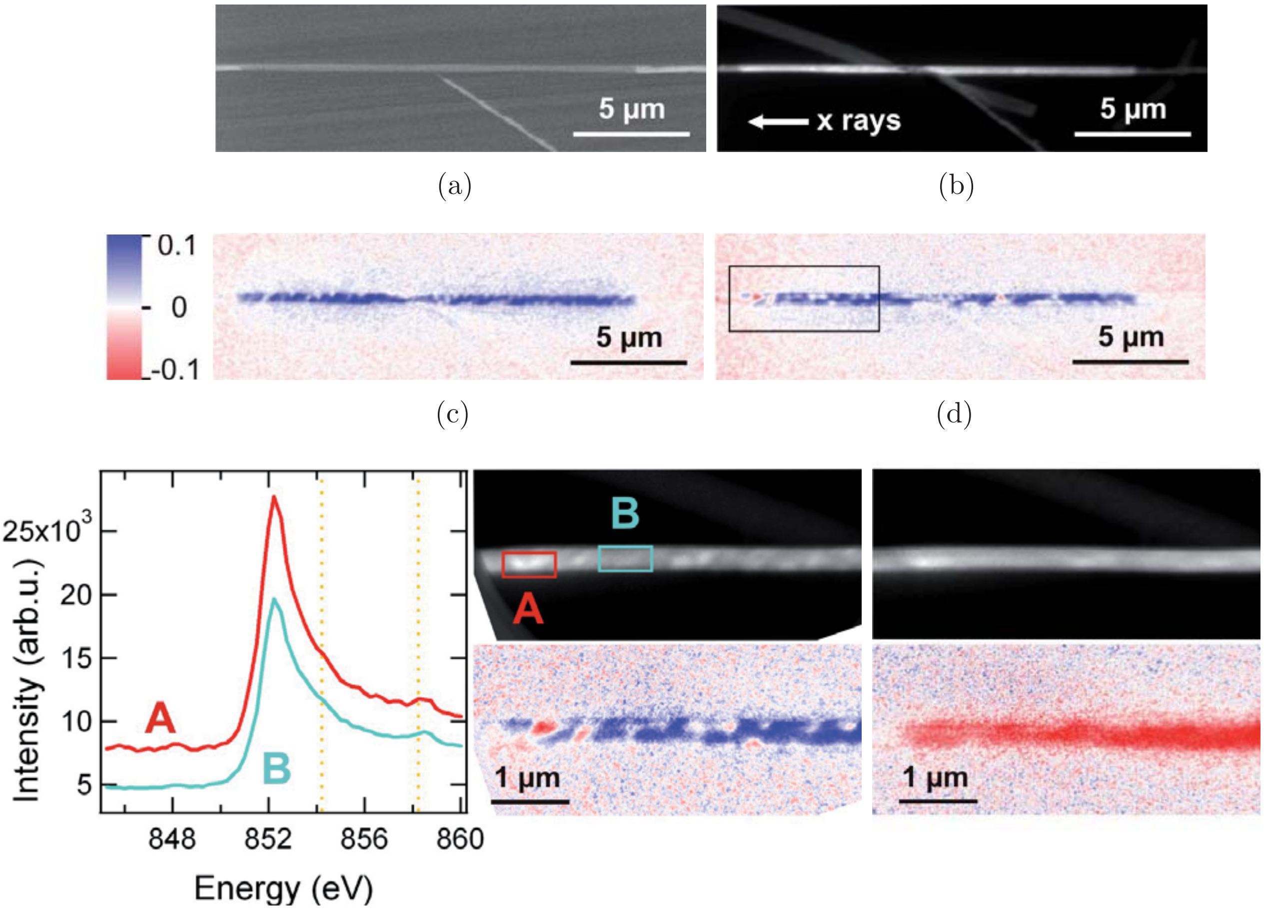

(a) (b) (c) (d) (e) (f)

Figure 5.15: (a) Scanning electron microscopy (SEM) image and (b) absolute photoemission electron microscopy (PEEM) image of an electrochemically synthesized nickel nanowire with gold ends. The nickel wire with a diameter of 310 ± 10 nm was surrounded by a 10 nm thick silica shell. The gold ends appear bright in the SEM image due to increased electron scattering, while they are hardly visible in the PEEM images recorded at the nickel L_3 edge (852 eV). In (b) something is visible that is not detected by SEM. This might be an empty or peeled-off silica shell. (c) and (d) are x-ray magnetic circular dichroism (XMCD) images revealing the magnetization components along the wire's axis at remanence and in a reverse field of −27 mT before switching, respectively. (e) Close-up of (d) and local PEEM spectra taken in the marked regions A and B. (f) Same wire end imaged at −27 mT after reversing the magnetization by applying −41 mT. Estimated field constant: $0.09\frac{\mathrm{mT}}{\mathrm{mA}}$.

angle between the in-plane projection of the incident x-ray beam and the wire's axis from zero to 90 degrees the magnetization components perpendicular to the axis of the wire can be imaged as well. Figure 5.16(c) depicts the same magnetic state as in (b) after the rotation of the sample. On the surface of the wire a complex magnetic pattern is visible. It consists of alternating red and blue segments with a periodicity

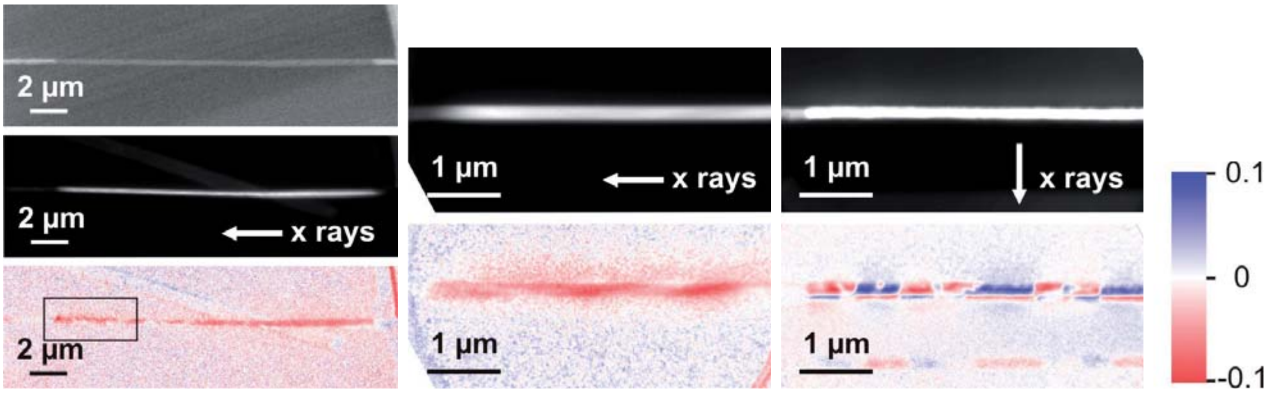

(a) (b) (c)

Figure 5.16: (a) Scanning electron micrograph (top), photoemission electron microscopy (PEEM) image (middle), and XMCD contrast (bottom) of a nickel nanowire with gold ends. The nickel wire with a diameter of about 310 ± 10 nm was surrounded by a 10 nm thick silica shell. (b) and (c) are close-ups of the left wire end (black frame in (a)). (a) and (b) reveal the magnetization components along the wire's axis. In (c) the incident x-rays hit the wire at an angle of 90 degrees to probe the magnetization components perpendicular to the wire's axis. All XMCD images (bottom row) recorded at the nickel L_3 edge reveal the same remanent magnetic state after saturation. The gold ends of the wire appear bright in the SEM image in (a) due to increased electron scattering, while they are hardly visible in the PEEM images that are displayed above the XMCD images in (a) through (c).

of about 700 nm. In the center of some segments a small region of opposite contrast is visible. The inverse alternating pattern is visible at the upper and the lower edge of the nanowire's shadow area, while no clear XMCD contrast is visible in the center of the shadow region. A possible explanation for the magnetic pattern observed is that the magnetization curls around the wire axis. The varying XMCD contrast indicates that the sense of rotation changes along the wire several times. The x rays causing the XMCD contrast in the middle of the shadow area probe magnetic moments on both sides of the nickel wire and in the center. If the magnetization curls, the contribution from opposite sides cancel out, and no XMCD contrast is visible in the wire's shadow. Another explanation for the comparably weak XMCD contrast in the center of the shadow is that in the inner volume of the nickel wire the magnetization is mainly aligned along the wire's axis. There might be a general difference in the magnetic behavior of the surface and of the bulk of the nickel wire.

All magnetic PEEM images recorded at the nickel L_3 edge are shown with the same scale of XMCD contrast of ±10 percent. The average XMCD contrast along the axes of nickel nanowires at remanence after saturation is about 6.7 percent. If the magnetic moments are aligned in an applied field, a contrast of almost 9 percent can be measured. This maximum is in agreement with values reported in the literature [Che90].

In a reverse field the XMCD contrast indicating the magnetization components along the wire axis always gets weaker. The magnitude of the magnetic contrast caused by the perpendicular magnetization components is comparable to the one along the wire's axis, and in some wires locally even stronger. This implies that the magnetization locally rotates more than 45 degrees away from the axis.[17] The XMCD contrast revealing the magnetization components perpendicular to the wire axis was not that strong and complexly patterned for all nickel wires studied. A tendency is observed that the XMCD contrast in thinner wires appears more homogeneous, and that the perpendicular magnetization components are reduced.

The orientation of the magnetic moments relative to the wire axis determines the resistivity due to the anisotropic magnetoresistance. Thus, magnetoresistance traces as the ones shown in Fig. 5.10 can also be used to estimate the angle between the current direction and the average magnetization direction in a wire. Using Eq. 2.36 and the two resistance curves in Fig. 5.10(a) yields an angle of about 22 degrees between the average magnetization direction and the wire's axis at remanence. This does not contradict with the 45 degrees estimated from the PEEM measurements. First, the wire studied in Fig. 5.10 is comparably thin. Second, only the XMCD contrast arising from the surface of the nickel wires was considered. Third, strictly speaking Eq. 2.36 only holds if surface effects are negligible [Rij95], which is not necessarily given for the wires under consideration.

Figure 5.17 displays magnetoresistance traces of six different nickel nanowires in the diameter range from 155 nm to 315 nm. The curves were recorded while the external magnetic field was sweeped along the axes of the wires. They describe the specific resistivity offsets $\Delta\rho = \frac{(R-R_0)\,A}{z}$, where A is the area cross-section, l is the length of the wire segment on which the resistance R is measured, and R_0 is the resistance at remanence.[18] The parameters of the individual wires, the names of which are given in the legend of the figure, are listed in Table 5.1. Scanning electron micrographs of them are shown in Fig. 5.21. Apart from the switching fields which are not a point of interest here, the magnetoresistance traces vary both in the field value at which the curves are saturated and in the drop of resistivity at remanence compared to the saturation value.[19] The difference in the latter might partially be explicable by incorrect normalization of the curves due to unknown current paths. One half of the curves in Fig. 5.17 are the magnetoresistance traces of wires without a silica

---

[17] This discussion delivers just an estimate. To obtain the exact values of XMCD contrast, local XMCD spectra would be required. By an azimuthal rotation of the sample the absolute value and direction of the magnetic moments can be determined [FR10]. For this purpose, it would be required to image the same magnetic state for at least four angles between the direction of the incident x-ray beam and the wire axis. Due to the limited time available during the PEEM measurements, this was not possible.

[18] This normalization procedure is exemplified in Sec. 4.2 on the basis of Fig. 4.10.

[19] For the 250 nm wire called Jan4-01 the curve is not completely saturated even at 100 mT.

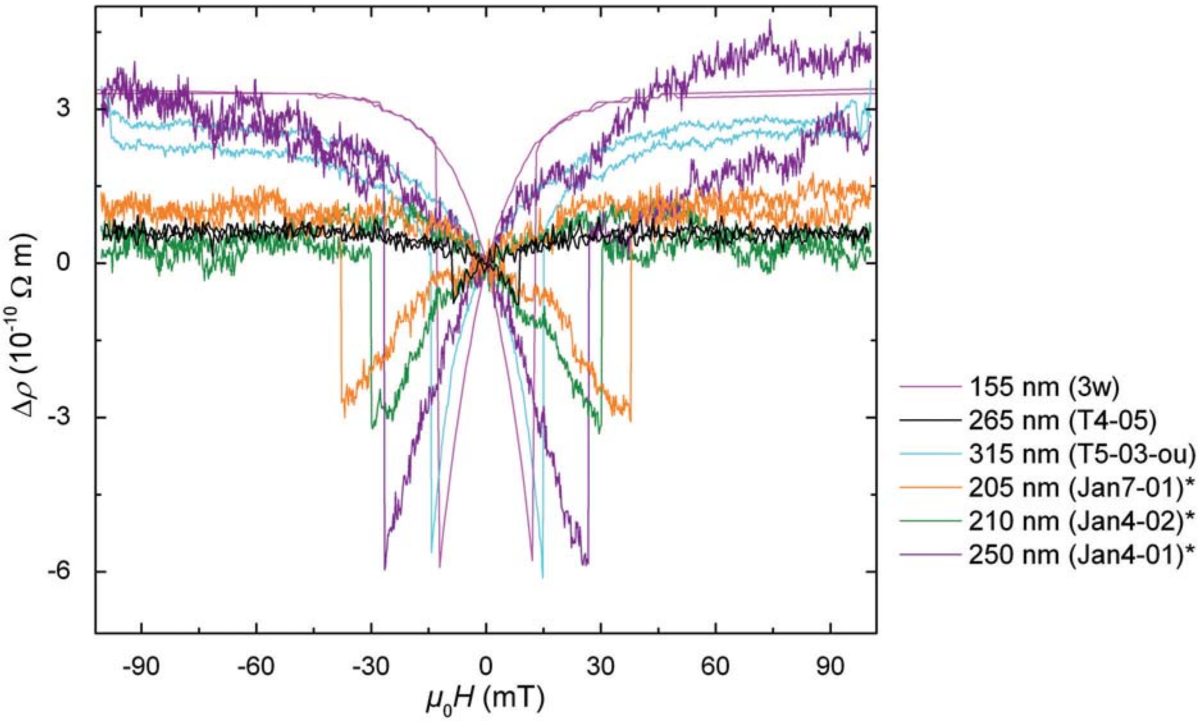

Figure 5.17: Magnetoresistance traces of several straight nickel nanowires recorded in two-point geometry. $\Delta\rho$ is the difference of the resistance measured at the respective field values and the resistance at remanence times the area cross-section and divided by the length of the wire segment on that the magnetoresistance was measured. The diameters and names of the wires are given in the legend, * means that the respective wire is surrounded by a silica shell. More details about the wires are listed in Table 5.1, scanning electron micrographs are shown in Fig. 5.21.

shell, where a native nickel oxide layer is present at the surface. This oxide layer does not seem to affect the features of the curves. It is plausible to assume that the influence of the shape anisotropy increases with decreasing wire thickness. This implies that in thinner wires the rotation of the magnetization away from the wire's axis at remanence is generally weaker, and that saturation is reached at lower fields. However, none of the above seems to be the case. Neither the drop of resistivity at remanence compared to the saturation value nor the fields at which the resistivity is saturated can be correlated with the diameter of the wires. There are several possible explanations for this. Since in the cylindrical wires most of the volume lies under the surface, the magnetoresistance measurements are highly sensitive to surface effects. Our PEEM images imply that the magnetic behavior at the surface differs from the one of the wire's core (see below). Different diameters lead to different contributions of surface effects. This may affect both the influence of diffusive surface scattering on the anisotropic magnetoresistance and the micromagnetic behavior. Possible mechanisms for the latter are varying contributions of defects and of the surface anisotropy on the effective anisotropy of the wires. Furthermore, most of the wires were synthesized in different batches. This could mean that they have different granular structures due to a variation of synthesis parameters, the influence of which is unknown. Unfortunately, no structural investigations were performed to confirm this. It also has to be taken into consideration, that there is still a contribution of the contact resistances. Since about 1/4 of the total resistance drops there, the behavior of the magnetization in the contact areas, where the oxide-shell was removed by a radio-frequency plasma, might remarkably distort the magnetoresistance traces. This aspect is however rather unlikely, since the influence of the contacts was checked, compare Sec. 4.2. Even though the curves in Fig. 5.17 look different, they have in common that the resistance at remanence clearly drops compared to the saturation value. Since the resistances are probed at inner segments of the wires they only reflect the orientation of the magnetic moments in that region. It can be concluded that in nickel nanowires the magnetization at remanence is not homogeneously aligned along the wire axis.

The difference in magnetic behavior of the wires studied by magnetoresistance measurements underlines the influence of the granular structure which is likely to vary from wire to wire. This is in line with the observations on individual nickel nanowires by PEEM, and already became apparent in the first section of this chapter dealing with the values of the switching fields. Our experimental results show that neither the analytical models nor the idealized micromagnetic simulations performed provide a good description of the system. In contrast to the micromagnetic simulations, where the magnetization only curls at the extremities of the wires, we observe a tilt of the magnetization away from the axis, that is rather reminiscent of curling along the entire wire. An increased rotation of the magnetization at the wire ends where the demagnetization fields are strong, as seen in the simulations, was not found to be a characteristic feature of the nickel wires. It could rather be imaged by PEEM and MFM that at least in some wires the nucleation and accordingly the magnetization reversal commences in the middle of a wire.

Figure 5.18 displays the PEEM images of a domain wall at an intrinsic pinning site of a nickel nanowire at remanence. (a) reveals the magnetization components along the wire's axis imaged at the nickel L_3 edge, and (b) depicts the XMCD contrast at the L_2 edge caused by the perpendicular magnetic moments.[20] The position of the domain wall is clearly visible in both XMCD images. The left part of the wire (red contrast in Fig. 5.18(a)) reversed its magnetization when a magnetic field was applied to prepare the domain wall. On the left side of Fig. 5.18(b), more than 1 μm away from the domain wall, the magnetic contrast at the surface of the wire

---

[20] Since the x-ray absorption at the nickel L_3 edge is higher than at the L_2 edge [Che90], PEEM images are sometimes acquired at the L_2 edge where the higher intensity of the signal caused by transmitted x-rays compensates the reduced XMCD contrast in the shadow area.

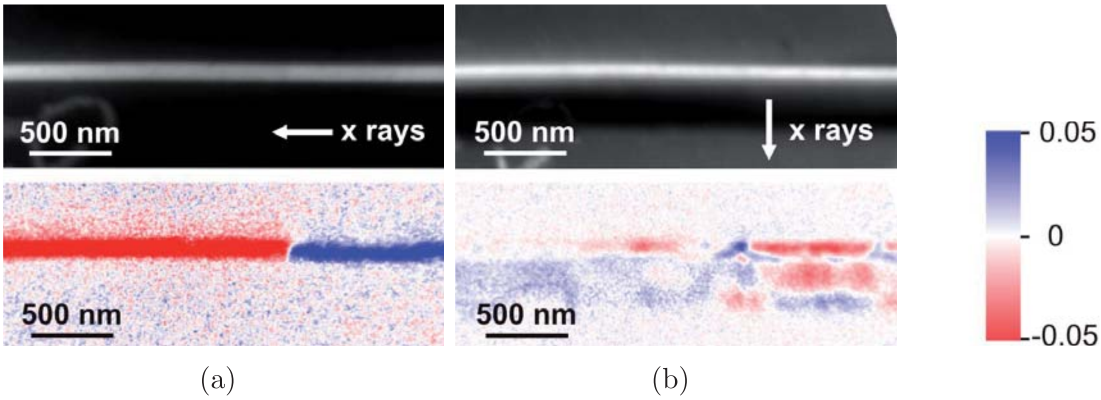

Figure 5.18: Photoemission electron micrographs of a domain wall in a nickel nanowire with a diameter of 130 nm imaged at an angle of (a) zero degrees and (b) 90 degrees between the in-plane projection of the incident x-ray beam and the wire's axis. The images are acquired at remanence at the nickel L_3 and L_2 edges (852.0 eV and 869.3 eV), respectively.

almost vanishes. In the shadow, however, there is a weak but clearly visible blue contrast indicating that in the bulk of the wire magnetic moments are tilted away from the wire axis. Closer to the domain wall the contrast on the wire's surface increases, and gets more inhomogeneous in the shadow. As expected the XMCD contrast indicating the perpendicular magnetization components is strongest at the position of the domain wall, while the corresponding XMCD contrast revealing the magnetization components parallel to the wire axis is zero. The magnetic structure of the domain wall appears very complex, hence a simple transverse or vortex-like domain wall structure can be excluded. In the right segment of the wire, where the magnetization is not reversed yet, the perpendicular components on the surface are strong as well, while the components along the wire axis are weaker as on the reversed segment. Interestingly, the shadow of the right segment is split into red XMCD contrast in the center and blue XMCD contrast at the edge. This underlines that the magnetic behavior at the surface of the nanowire can differ from the one of the bulk magnetization. Furthermore, the possibility of domain formation in radial direction has to be taken into account.

Figure 5.19 depicts PEEM images of domain walls in a 240 nm thin wire recorded at remanence at an angle of 45 degrees between the in-plane projection of the incident x-ray beam and the wire axis at the nickel L_2 edge. Figure 5.19(a) is the absolute PEEM image, (b) and (c) are the corresponding XMCD images. The domain walls in (b) and (c) were prepared by applying ±7.3 mT, respectively, after saturating the wire in the opposite direction. The magnetic patterns of the two domain walls are different. Given the occurrence of more than one accumulation value of the switching field and facing the complexity of domain walls observed in cylindrical nickel nanowires, it is not surprising to find various domain-wall structures in one

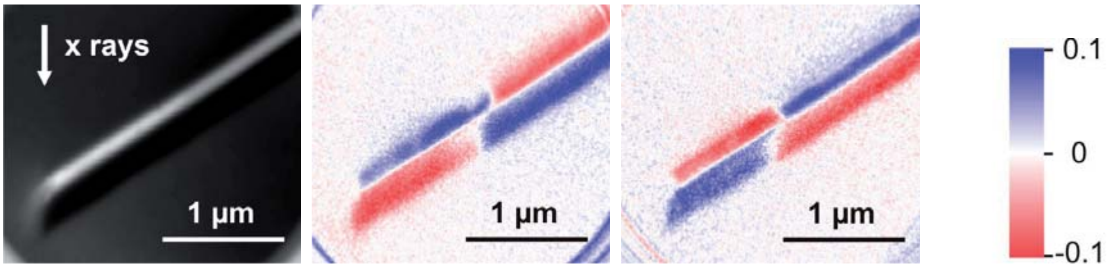

(a) (b) (c)

Figure 5.19: (a) Photoemission electron micrograph of the end of a nickel nanowire with a diameter of 240 nm acquired at the nickel L_2 edge (869.3 eV) and an angle of 45 degrees between the in-plane projection of the incident x-ray beam and the wire's axis. (b) and (c) are the corresponding differential XMCD images revealing domain walls at remanence. The walls were prepared by applying reverse fields of +7.3 mT and −7.3 mT after saturation at ∓36 mT, respectively. Estimated field constant: $0.09\frac{\mathrm{mT}}{\mathrm{mA}}$.

wire. The experiment reported in Fig. 5.19 was not repeated often enough to tell, whether the difference in the domain-wall pattern is a characteristic of the direction of the field applied to prepare the domain wall. If the latter was the case, this would explain the finding that the switching fields of nickel nanowires are often not symmetric around zero. Since there is no specified direction in space for magnetic fields, this is rather untypical for ferromagnets. A possible explanation is exchange bias due to the presence of antiferromagnetic nickel oxide at the surface of the wires.

Based on the above observations it can be devised how the magnetization reversal in nickel nanowires takes place. The reversible part, where the magnetization rotates away from the wire axis, is attributable to the comparably strong influence of additional anisotropy contributions competing with the shape anisotropy. Most likely these contributions are surface effects and the granularity of the wires combined with a non-negligible magnetocrystalline anisotropy. Those factors also play a crucial role in the nucleation process. Somewhere in the wire, in a volume determined by the interplay of anisotropy contributions, demagnetizing fields, and defects, nucleation starts and domain walls form. At a certain value of the external field, namely the switching field, a domain wall is depinned and propagates through the wire while the magnetization reverses. Due to competing nucleation processes, a variety of individual, possibly very complex, domain-wall structures can be formed. Each domain-wall structure is associated with a characteristic switching field and the corresponding switching-field distribution. This model of magnetization reversal contradicts analytical models of defined nucleation and switching fields with equal values.

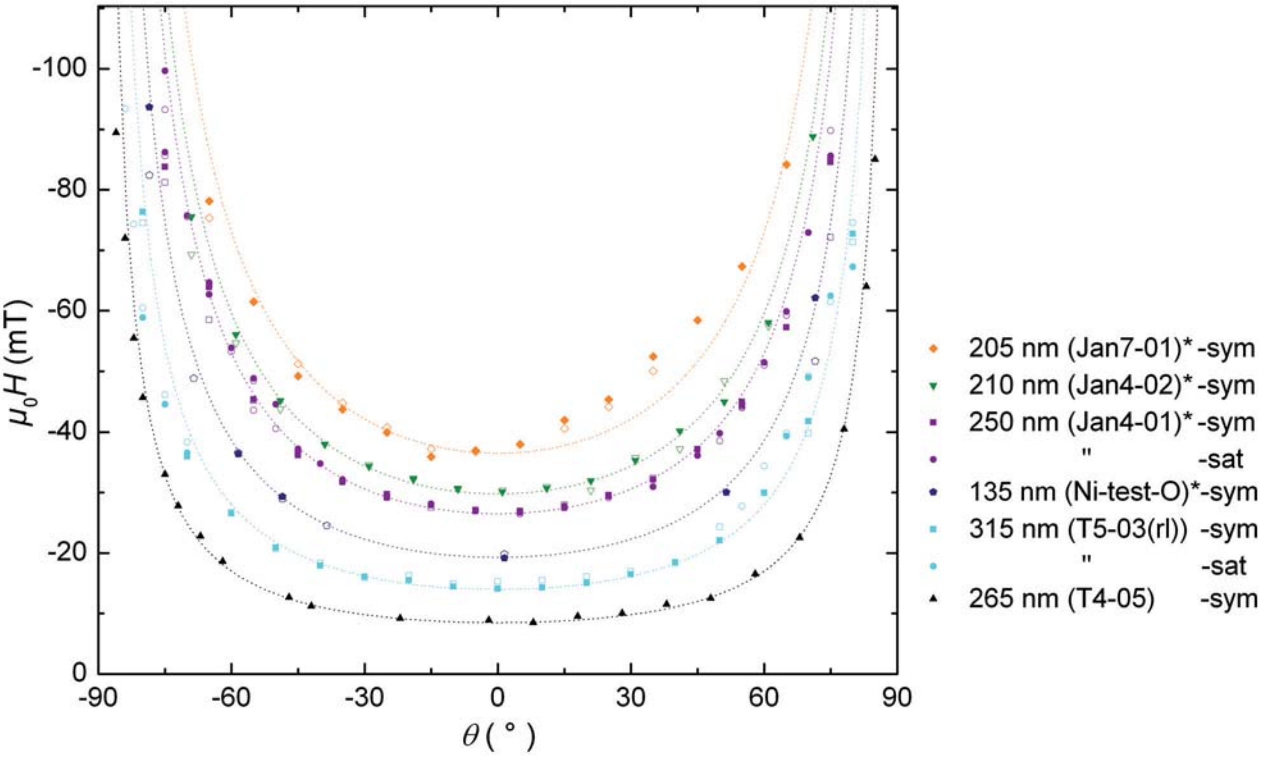

Figure 5.20: Angular dependence of the switching fields of several straight nickel nanowires. The diameters and names of the wires are given in the legend, * indicates that the respective wire is surrounded by a silica shell. -sym and -sat means that the switching fields were determined by sweeping the applied magnetic field symmetrically from -100 mT to $+100$ mT at a fixed angle or by using the saturation mode (compare Sec. 4.2), respectively. The dotted lines are fits to the data proportional to $1/\cos\theta$. The prefactors $\mu_0 H_0$ as well as the parameters of the wires are listed in Table 5.1. Scanning electron micrographs of the wires are shown in Fig. 5.21.

The angular dependence of the switching fields that can be associated with a magnetization reversal via domain-wall motion is proportional to $1/\cos\theta$ [Shi99]. Figure 5.20 depicts the angular dependences of the switching fields determined for six different nickel nanowires by magnetoresistance measurements. The dotted functions fitting the data are given by $f = \mu_0 H_0/\cos\theta$ where H_0 is chosen to fit the smallest value of the switching fields measured for a particular wire. Compared to the analytical curves based on the curling model drawn in Figs. 5.1 and 5.7, these functions describe the progression of the data very well. Instead of arbitrarily choosing parameters for the critical radius r_c and the aspect ratio n of the nucleation volume, a procedure by which more or less any curve progression can be created, only one fit parameter, namely H_0, has to be found. Knowing about the actual, very complex magnetic microstructure of the nickel nanowires the applicability of an analytical model has to be called into question anyway, as it was discussed in detail in Sec. 5.1.

Wire name	d (nm)	l (µm)	z (µm)	SiO_2	$\mu_0 H_0$(mT)	δ (°)
3w	155	55	26.4	-	12.0	-4
T4-05	265	39	4.6	-	8.5	n.a.
T5-03 rl / ou	315	37	4.5 / 22	-	14	-5
Ni-test-O	135	11.6	3.3	5 nm	19.3	0.5
Jan7-01	205	10	3	10 nm	36.5	5
Jan4-02	210	30	3.5	10 nm	29.8	-1
Jan4-01	250	22	3.4	10 nm	26.5	6

Table 5.1: Parameters of the wires studied by magnetoresistance measurements. d is the diameter of a nickel wire without the silica shell. The wires called 3w and T4-05 were studied at setup 3 and setup 2, respectively. All other wires were measured at setup 1.

Not all of the angular dependences of the switching fields shown in Fig. 5.20 are symmetric around $\theta = 0°$. One reason for this is a stochastic scattering of the switching-field values which leads to deviations from the $1/\cos\theta$ progression. For the strong asymmetry of the switching fields of wire Jan7-01 which looks rather systematic, there must be another reason. There are even more deformed progressions, for example the one of Jan5-01 shown in Fig. 4.7, which are not plotted here. In those cases it appears as if the angular dependence of the switching field is an overlay of at least two $1/\cos\theta$ curves, and thus the consequence of multiple anisotropy axes.

Due to experimental uncertainties it is not sure if what is considered as $\theta = 0°$ here really corresponds to an angle of zero degrees between the applied magnetic field and the wire axis. The offsets δ between the orientation of the wires as estimated from scanning electron micrographs and the way the switching fields are plotted in Fig. 5.20 are given in Table 5.1. These offsets are up to six degrees in magnitude. The $1/\cos\theta$ curves plotted as fits in Fig. 5.12 imply that for both wires under consideration the offsets δ are about four degrees. While deviations in the order of ± 2 degrees can be attributed to a natural uncertainty in the experimental procedure described in Sec. 4.2, larger offsets indicate the tilting of the effective anisotropy axis away from the wire's axis. This is a further indication for additional anisotropy contributions competing with the shape anisotropy.

To clarify the influence of magnetocrystalline anisotropy on the magnetic behavior of electrochemically synthesized nanowires, the magnetization reversal in cobalt-nickel wires was imaged by PEEM. Results on a $Co_{71}Ni_{29}$ nanowire, which has a higher magnetocrystalline anisotropy than nickel wires, are presented in the Appendix Sec. B.8. As expected, the magnetization patterns observed reflect the granularity of the wire even stronger.

The influence of the crystalline structure on the magnetic properties of nanowires was studied by several groups [Bie07, Zou08, Che10]. Our results show that the magnetic properties vary strongly even between wires that are nominally identical as concerns dimensions and synthesis parameters.

In the literature on the magnetization reversal in electrochemically synthesized nickel nanowires it is often assumed that due to the polycrystalline structure of the wires randomly oriented grains average out the contribution of magnetocrystalline anisotropy [Wer96, Fer97] or that the latter can be neglected since the effective anisotropy is dominated by the shape anisotropy [Pig00, Led95]. Our experiments clearly contradict these assumptions. Zheng *et al.* consider the magnetocrystalline anisotropy as a weak perturbation [Zhe00]. Tian *et al.* found that in an ensemble of polycrystalline nickel nanowires with a radius of only 20 nm the crystal structure and interaction of the grains influences the magnetic behavior [Tia08]. By the application of an external magnetic field during the growth of the wires they change the size

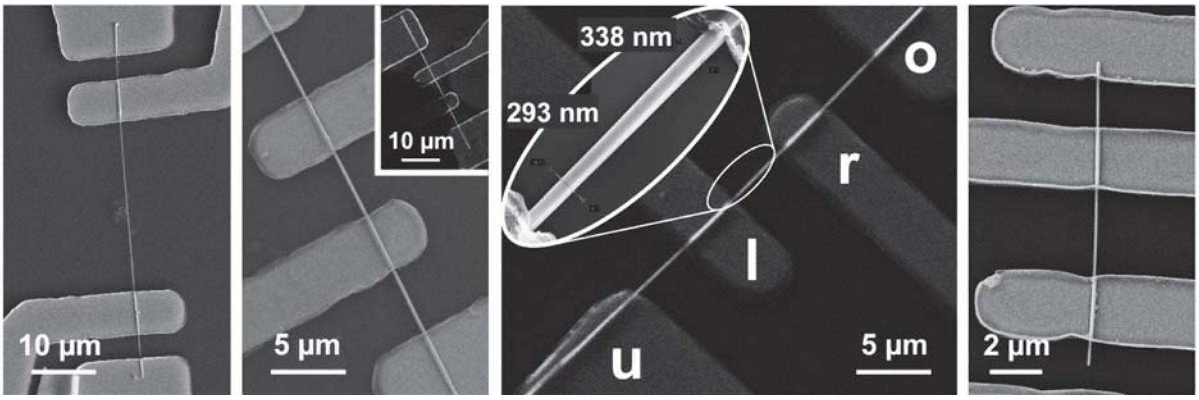

(a) 3w (b) T4-05 (c) T5-03 (d) Ni-test-O

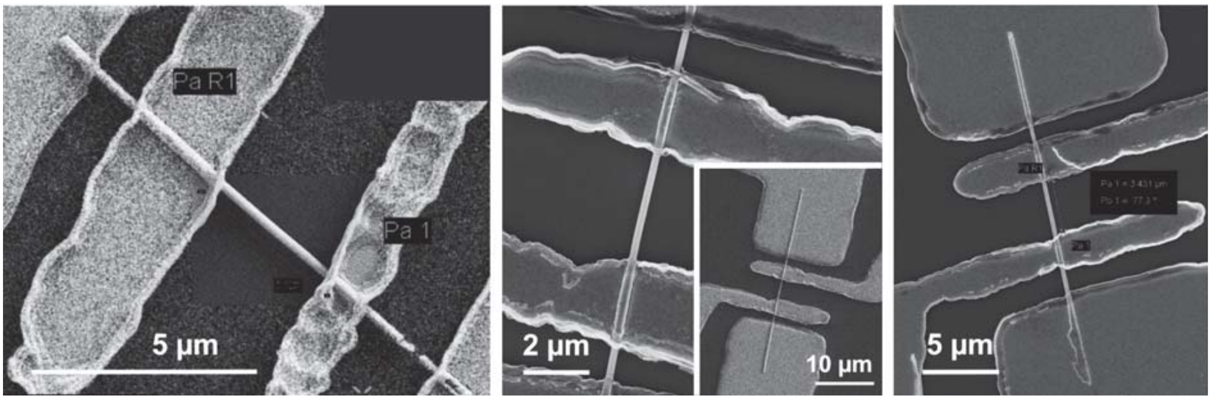

(e) Jan7-01 (f) Jan4-02 (g) Jan4-01

Figure 5.21: Scanning electron micrographs of straight nickel nanowires studied by magnetoresistance measurements.

distribution of the grains. Comparing the shape of the magnetization curves measured by vibrating sample magnetometer to the results of micromagnetic simulations, they conclude that the difference at remanence of the curves can be attributed to different exchange constants. They assume that the remanent magnetization states of the wires are multidomain states. In their simulation they implement the granular structure of the wires by choosing cylindrical segments of about 15 nm with a size distribution according to the actual grain structure revealed by transmission electron micrographs as micromagnetic cells. Every cell is then treated as a single domain. The result of such a simulation has to be handled with care, since a mesh size corresponding to the grain size and the exchange length of a structure can lead to domain-wall collapse [Don98], nevertheless, it points into the right direction.

To summarize, our experiments show that the magnetization reversal in electrochemically synthesized nickel nanowires is very complex. This can be attributed to the granular structure of the material and a non-negligible magnetocrystalline anisotropy. In particular the PEEM images reveal a strong influence of the granular structure on the magnetic behavior. The shape of magnetoresistance traces and the angular dependence of the switching field imply that additional anisotropy contributions overlap the shape anisotropy and cannot be neglected. Thus, the applicability of analytical models and simplifying micromagnetic simulations for the description of the system is limited. It can be assumed that magnetization reversal takes place via the nucleation, depinning, and propagation of domain walls.

Domain-wall pinning is mainly observed in wires without silica shell. A reason for this might be intrinsic pinning sites induced by the larger roughness of the interface between nickel and nickel oxide in these wires compared to wires protected by a silica shell. It is also plausible that the strength of the intrinsic pinning sites does not vary between the different types of wires, but that the pinning is observed more often in wires without silica shell since the switching fields of these wires are comparably low (compare Fig. 5.2). The latter increases the chance to observe pinning also at weak pinning sites. The following chapter deals with the feasibility of controlled domain-wall preparation.

6 Preparation of domain walls in cylindrical nanowires

This chapter deals with the preparation of domain walls in electrochemically synthesized nanowires. Section 6.1 summarized experiments on nickel wires that have been manipulated with a focused ion beam. Section 6.2 presents results obtained on bent wires, and the last section, Sec. 6.3, discusses the magnetization reversal in cylindrical nickel and nickel-iron wires with one or more diameter modulations.

6.1 Ion irradiation

The magnetic behavior of cylindrical nickel nanowires can be manipulated by means of ion irradiation. For this purpose, wires were locally irradiated with a 30 kV Ga^+ focused ion beam (FIB). This was done using the Raith software Elphy and a CrossBeam 1540 XB from Zeiss with the support of Dipl. Phys. Matthias Hagner in the Nanostructure Laboratory of the University of Konstanz, Germany. To study the influence of FIB irradiation the wires were characterized by magnetoresistance (MR) measurements before and after the manipulation. In total five wires have been manipulated with different ion doses, irradiating either an area or a line only. In the following the results obtained on two of these wires are presented. The wires are called Jan4-01 and Jan3-01. Both wires are coated with an approximately 10 nm thick shell of silica and have total diameters of 270 nm and 250 nm, respectively. Jan4-01 was milled along a single line with a dose of 3.5 $\frac{\mathrm{nAs}}{\mathrm{cm}}$. Figure 6.1(a) depicts constrictions comparable to the one created on wire Jan4-01. A scanning electron micrograph of Jan3-01 after milling on a 500 nm wide area with an ion dose of 0.5 $\frac{\mathrm{nAs}}{\mathrm{cm}^2}$ is shown in Fig. 6.1(b). Both milling procedures were done with a current of 1 pA and a step size of 1.6 nm. To ensure a homogeneous irradiation the dose was not deposited at once but distributed during ten loops. However, an inhomogeneous removal of the material is observed, compare Fig. 6.1(b). This can be attributed to the granularity of the material.

Figure 6.2(a) depicts typical MR traces recorded on wire Jan4-01 before (black) and after (red) the manipulation with a FIB. The curves are the plain resistance offsets without normalization. They differ strongly as concerns both the curvature and the

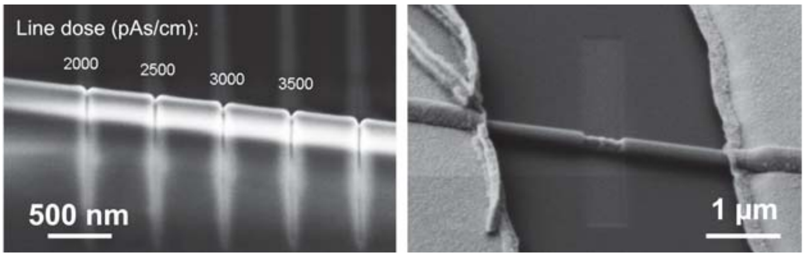

(a) (b)

Figure 6.1: Scanning electron micrographs of (a) a wire with several constrictions comparable to the single cut with a focused ion beam on wire Jan4-01 and (b) wire Jan3-01 after ion milling.

jumps indicating the irreversible parts of magnetization reversal. After FIB manipulation, the curve progression is a lot steeper and while the black curve recorded earlier is almost saturated at 100 mT, the red curve is not close to saturation even at strong applied fields. Assuming the anisotropic magnetoresistance (see Sec. 2.3.4) to be responsible for the resistivity change, this means that not all magnetic moments in the wire are aligned in parallel to the sensing current yet. Unfortunately, there is no SEM image of the single FIB cut on wire Jan4-01, but only Fig. 6.1(a) showing a comparable sample with several cuts. As can be inferred from the image, material is not only removed on the top of the wire but also on the sides. While usually the average behavior of all grains in a wire is monitored, the present measurement is likely dominated by the few grains or the single grain at the constriction only. The strong curvature and high saturation fields of the red MR curve in Fig. 6.2 indicate that this region obviously favors a magnetization rotated away from the wire's axis, either due to intrinsic material properties, namely magnetocrystalline anisotropy, or due to the manipulation by FIB. Possible mechanisms for the latter are stray fields caused by the geometry created, or material variations by the exposure to gallium ions. Ion exposure can change both the structural and the magnetic material properties. A reduction of the saturation magnetization is often reported for comparable experiments [Par02, Fas08]. The effect is usually attributed to ion implantation. Structural variations caused by non-implanted ions are also a possible mechanism to vary magnetic properties such as the magnetocrystalline anisotropy. Another aspect that could change the magnetic behavior in the constriction region is that after the ablation of material the silica shell is removed and the nickel partially oxidizes. Increased demagnetizing fields, added defects, or the local variation of material properties could be responsible for a decreased switching field as it is indicated by the position of the first jump in the MR traces after FIB manipulation.

The creation of defects not only facilitates nucleation but also induces pinning sites [Fas08, Vog10]. In principle it is possible that both nucleation and pinning occur in the irradiated areas. Figure 6.2(b) displays a model of the wire with the single FIB cut in the center and two gold contacts (red) used to probe the resistance. Due to the halo of the ion beam that is indicated by the blue shaded area in the schematic at the top of Fig. 6.2(b), the irradiated volume is most likely not limited

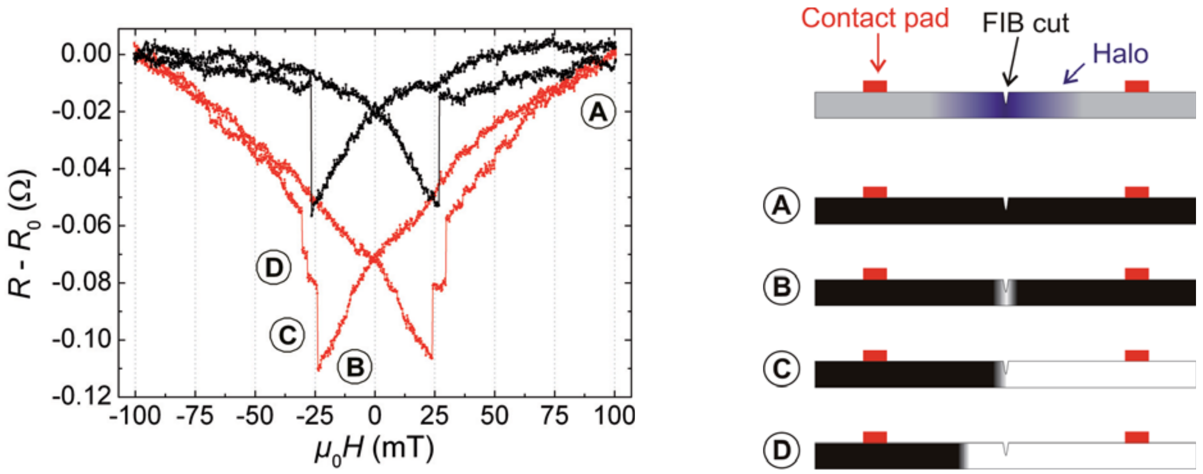

(a) (b)

Figure 6.2: (a) Resistance versus field curves of wire Jan4-01 recorded before (black) and after (red) ion milling ($R_0 \approx 18.5\ \Omega$). (b) Model to explain the occurrence of three jumps in the resistance curve after FIB irradiation. The upper image is a schematic of the nickel wire with two contacts, the cut created with the FIB, and the halo of the FIB that induces pinning sites. (A) through (D) depict the magnetic states. Black and white contrasts indicate a magnetization in parallel and antiparallel to the wire's axis, respectively.

to the region where material was ablated [Kub87]. The lower schematics (A) - (D) display magnetic states that could account for the shape of the MR curves based on anisotropic magnetoresistance. Black and white contrast indicates a magnetization along and antiparallel to the wire's axis, respectively. (A) depicts a saturated wire for which the resistance is high since the magnetic moments are predominantly aligned in parallel to the current direction. The continuous steep decrease of the MR trace after FIB manipulation indicates a gradual nucleation rather than the sudden occurrence of two domain boundaries.[1] The heights of the jumps give a hint at the length of the wire segment reversing. In the case of two jumps both jumps have about the same height (compare red curve in Fig. 6.2(a) for sweep in positive field direction). This supports the idea of nucleation in the middle of the wire where the FIB hit, and two domain walls propagating from there into opposite directions. The jumps in the MR traces mark the depinning fields of the two domain walls, which in the following are referred to as switching fields. The magnetic state right before the depinning and propagation of one of the domain walls is sketched in (B). In (C) one domain wall is depinned and the right segment of the wire reversed its magnetization. This process can be associated with the first jump in the MR traces the height of which is independent of the following switching events. If only one additional jump occurs,

---

[1] As discussed in detail in Sec. 5.2 a certain, weaker decrease of the resistance is characteristic for the magnetic behavior of cylindrical nickel nanowires also without FIB manipulation, compare the black curve in Fig. 6.2(a).

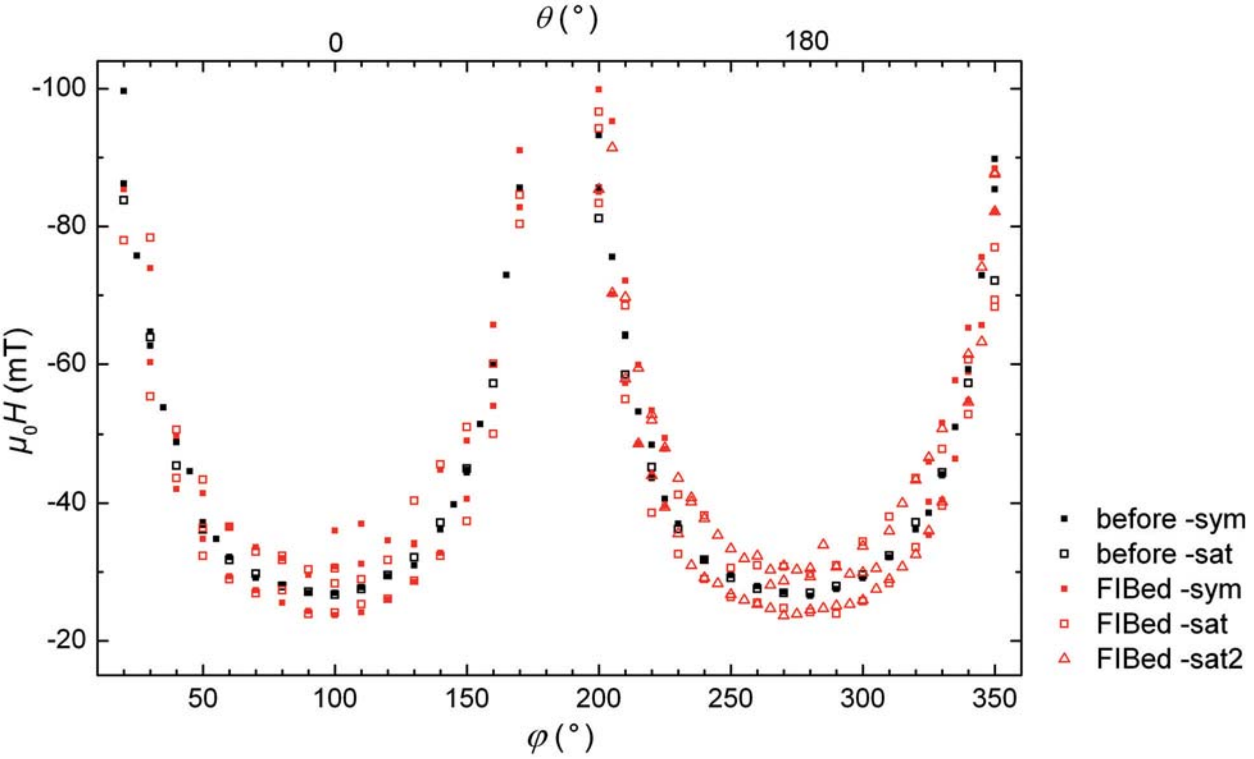

Figure 6.3: Angular-dependent switching fields of wire Jan4-01 before (black) and after (red) ion milling. φ is the absolute angle in the setup, θ is the estimated angle between the applied magnetic field and the axis of the wire. Open and full symbols indicate that data was recorded while sweeping the field symmetrically (-sym) or in the so-called saturation mode (-sat) as explained in the text. The squared and triangular symbols were recorded during different batches.

the other domain wall gets depinned at the respective field value and propagates to the left end of the wire. In the case of two more jumps, the first of which is about half as high as the last one, it is likely to assume that the domain wall on the left side of the nucleation volume gets pinned at a defect created by the halo close to the FIB cut as modeled in (D), before the reversal process is completed.

The black and red data points in Fig. 6.3 are the angular-dependent switching fields before and after wire Jan4-01 was manipulated with a FIB. The filled symbols are data recorded in symmetric field sweeps from +100 mT to −100 mT at a fixed angle between the applied magnetic field and the wire axis. The open symbols are the switching fields measured at the respective angles after the wire was saturated by applying a reverse field almost in parallel to the wire's axis, i.e. along the $\varphi = 100°$ and the $\varphi = 280°$ direction (saturation mode, compare Sec. 4.2). For this particular wire, the choice of the measuring mode does not lead to different magnetic behavior. As reported earlier, this was not always the case, compare for example Fig. 4.7. The angular dependence of the switching field for wire Jan4-01 before FIB manipulation is also plotted in Fig. 5.20. It is well described by a $1/\cos(\theta)$ curve. Apart from a few

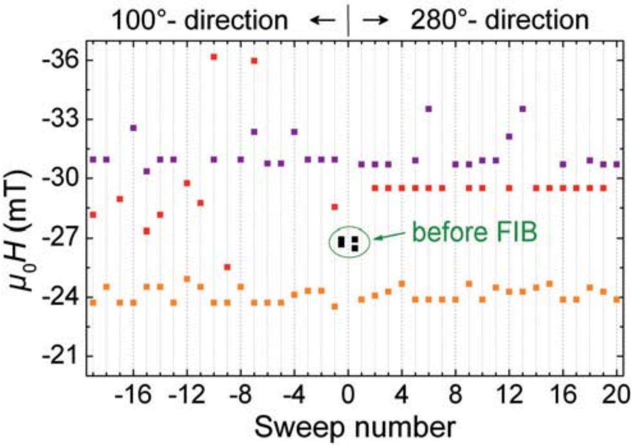

Figure 6.4: Distribution of switching fields of wire Jan4-01 before (black) and after (other colors) manipulation with a focused ion beam (FIB). The color coding shall associate the individual events with characteristic accumulation values of the switching fields.

outliers the angular-dependent switching field after ion milling displayed in Fig. 6.3 follows the same $1/\cos(\theta)$ dependence. This supports the above idea of magnetization reversal through the depinning and propagation of domain walls [Shi99].

The statistics of the switching fields for the external field sweeped along the wire's axis was studied in more detail. Figure 6.4 illustrates the distribution of the irreversible jumps for wire Jan4-01 before and after the FIB manipulation. The black data points in the center of the graph are the switching fields observed before ion milling during field sweeps in $\varphi = 100°$ direction (left) and in 280-degrees direction (right). For each of the opposite field directions two values of the switching field were recorded. They are symmetric around zero with an average value of $-(26.8 \pm 0.22)$ mT. After the sample was manipulated with a FIB, the switching behavior of the nanowire changed as already described above on the basis of Fig. 6.2. Instead of one single jump in the resistance curve two or three jumps occurred. The first of these jumps (orange points in Fig. 6.4) occurs at $-(24.1 \pm 0.37)$ mT which is about 10 percent less than the original switching field. This event associated with the depinning of one of the two domain walls around the nucleation volume takes place reliably.

Additional jumps occur at fields in the order of or higher than the original switching field. The few events in the vicinity of the original switching field could be associable with the 'old' nucleation volume. Most of the additional switching fields accumulate around two field values, namely -29.5 mT and -31.0 mT.[2] These fields, that are interpreted as the depinning fields of the other domain wall from the nucleation volume and later from a defect in the volume irradiated by the halo of the FIB, scatter strongly. In 60 percent of the cases only one of the two additional jumps occurs. The events presented in Fig. 6.4 were started with sweep number -1 in

---

[2] It is somehow surprising to observe switching at fields that are much higher than the original switching field, at which the entire magnetization reversed before. If the 'old' nucleation volume was still active, domain walls originating from there should be able to complete the reversal process at lower fields already. A possible explanation is that the 'old' nucleation volume lies in that segment of the wire that reverses first at about 24 mT.

100-degrees direction after ion irradiation. Here, at the beginning, only two jumps occurred as it is also observed in the angular-dependence measurements for most angles, compare Fig. 6.3. All sweeps were performed by increasing the magnitude of the absolute angle φ. As illustrated in Figs. 6.4 and 6.3, the probability to observe three jumps increases when the field has been sweeped in a direction close to the wire's axis several times. We might look at a kind of magnetic training effect here. For the sweeps along the 280-degrees direction (positive sweep numbers in Fig. 6.4) performed subsequently to the sweeps along the 100-degrees direction the scattering of the switching fields is remarkably decreased, in particular for the second jump. Obviously there exist multiple paths via which the reversal process takes place. It is likely to assume that a variety of domain-wall structures can form, each of which has its characteristic pinning and depinning behavior. This makes the magnetic behavior of wire Jan4-01 after ion irradiation highly stochastic.

Figure 6.5 depicts MR traces of wire Jan3-01 before and after ion milling. A scanning electron micrograph of the constriction created by FIB is shown in Fig. 6.1(b). During measurements the wire is approximately aligned along the 130-degrees direction. From the angular dependences of the switching fields (not shown) and the measuring procedure it can be excluded that the tilt of the sample between the measurements before and after ion milling is more than five degrees. To ensure that the changes in the MR traces are not due to a rotation of the sample, MR traces recorded after FIB manipulation at an absolute angle of $\varphi = 130°$ are compared to curves recorded before at $\varphi = 120$, 130, and 140 degrees in Fig. 6.5. The green and black curves recorded prior to the ion milling show a single jump that occurs at around -33.5 mT

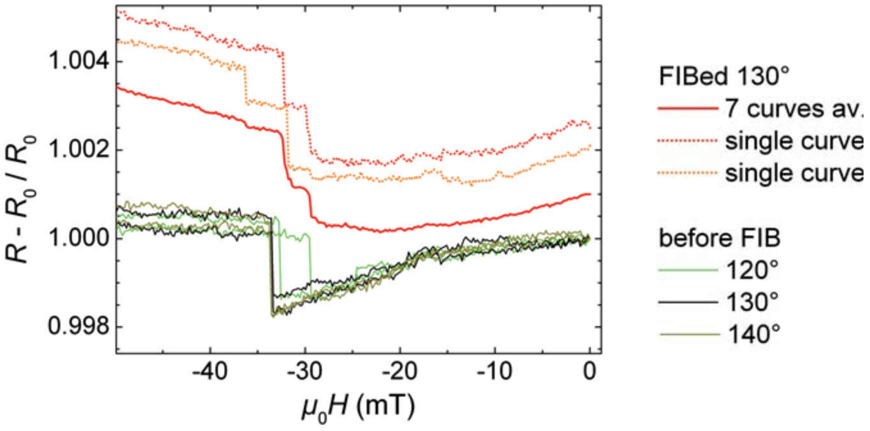

Figure 6.5: Magnetoresistance traces of wire Jan3-01 before (black and green curves) and after (red dotted curves) manipulation with a focused ion beam (FIB). The wire is approximately oriented into the 130-degrees direction. The red line is an average of seven curves recorded after ion milling. $R_0 \approx 20.5\ \Omega$.

with one exception, namely −29.5 mT for a curve recorded at 120 degrees. Looking back at the statistics in Fig. 5.11 such outliers are rare but characteristic for the stochastic behavior of nickel nanowires. The reddish dotted curves in Fig. 6.5 are two out of seven MR traces recorded after ion milling. All curves recorded have two distinct jumps and sometimes an antecedent small step. The red curve is the average of all seven curves recorded. Besides information about the average positions of the jumps it includes statistics about the probabilities that a jump occurs at a certain field value. The last step in the orange dotted line is hardly visible, what reveals that this event is rather unlikely. In most cases switching occurred at about −29.5 mT and −32 mT. The fact that the first jump appears at the same field value as did once the switching before ion milling is probably just a coincidence. The behavior of wire Jan3-01 is comparable to the one of wire Jan4-01 described above. Again it can be assumed that two domain walls are formed during nucleation in the volume manipulated by ion irradiation. The nucleation field is decreased by 12 percent. The small steps that occur in some of the MR traces after ion milling can be interpreted as the displacement of a domain wall within the manipulated area.

We performed photoemission electron microscopy (PEEM) experiments on comparable FIB-manipulated wires as well as on wires irradiated without material ablation. The XMCD contrast indicating the magnetization components along the wire axis in the irradiated and milled areas is reduced compared to the contrast within the rest of the wires at remanence. This means that in the areas where the FIB hit a wire the saturation magnetization is reduced or the magnetization is rotated further away from the axis, or both. These two, possibly related, aspects are likely to favor nucleation in the irradiated regions. Pinning, however, could never be observed by PEEM.

In summary, manipulation with a FIB is not suited to tailor pinning sites for the controlled preparation of domain walls in cylindrical nickel nanowires. Ion milling decreases the nucleation field by about 10 percent. The halo of the ion beam creates defects that can act as pinning sites.

6.2 Bent wires

An established method for the preparation of a domain wall is the application of an external magnetic field on a bent wire as described in Sec. 2.2.1. To obtain bent cylindrical wires two options were tried. One of them is the centrifugation of the wires while they are in solution. The amount of bent wires that was found on a substrate after the application of the centrifuged solution was small, and the wires were usually fractured at the kink as shown in Fig. 6.6(a). Another possibility is to bend the wires manually once they are on the substrate. Different tools, for example tweezers and cannulas, were tested. It was found that to bend a wire without breaking it thin elastic tools such as vibrissae are suited best. Figures 6.6(b) and (c) display nickel nanowires bent with a hair. With this method the breaking of the wires could be avoided, but usually the silica shell burst at the kink, compare Fig. 6.6(c). As can be inferred from subfigure (b), the curvature created differs from wire to wire. No reproducible method for the preparation of bent nanowires was found that would have allowed for a systematic study of domain-wall behavior in this geometry.

However, the concept of domain-wall preparation in a bent wire was tested on a cylindrical nickel nanowire with a diameter of about 225 nm from a centrifuged solution that was not fractured at the kink. Figure 6.7(a) displays the topography of the wire. The direction of the external magnetic field is indicated by the arrow. Figure 6.7(b) reveals the magnetic configuration of the wire after saturation at +80 mT. The bright MFM contrast at both wire ends indicates that the magnetization points towards the wire ends. Consequently, there is a tail-to-tail domain wall in the wire which causes the opposite magnetic contrast, as it is clearly visible right at the kink. After the application of a reverse field of −39 mT the dark contrast, indicating the position of the domain wall, is moved out of the kink into the upper wire segment.

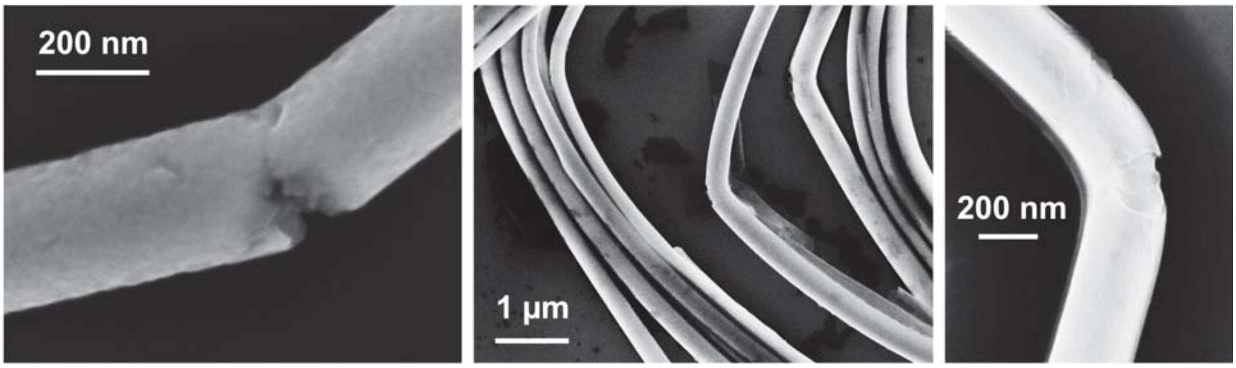

(a) (b) (c)

Figure 6.6: Scanning electron micrographs of nickel nanowires bent (a) by centrifugation of the solution, and (b), (c) manually. In (c) the burst silica shell is clearly visible.

Figure 6.7: Topography (a) and magnetic force micrographs of a bent nickel nanowire with a diameter of 225 nm after saturation at +80 mT (b) and after the application of a reverse field of −39 mT (c). The images are acquired at remanence. The bright magnetic contrast is caused by the stray fields at the wire ends. The dark contrast indicates the position of a domain wall.

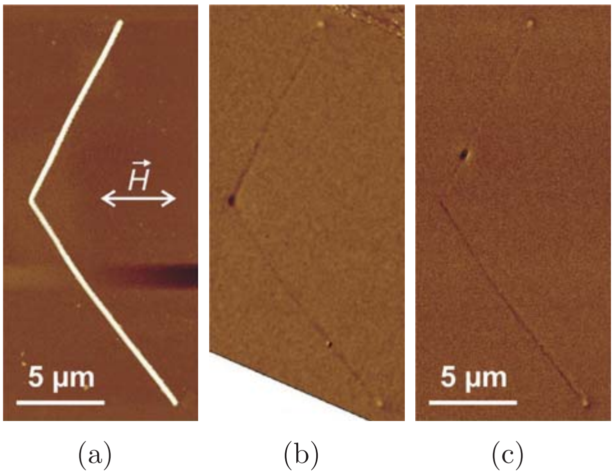

(a) (b) (c)

The depinning behavior of so-prepared domain walls was studied in more detail. The external fields required to depin a domain wall from the kink scatter between 30 mT and 45 mT. This comparably large field range suggests that we are not only looking at the stochastic distribution of depinning fields due to thermal activation over a single energy barrier. Since a variety of spin structures may be formed during the preparation of the domain wall, different energy barriers can be expected [Kim11b, Hay06b]. The spatial resolution of magnetic force microscopy lies between 50 nm and 100 nm, so different domain-wall structures formed would not necessarily be detectable.

Figure 6.8 displays two sequences of magnetic force micrographs revealing different depinning processes for head-to-head domain walls that were prepared by applying a field of −80 mT. Figures 6.8(a) through (c) depict a depinning process where the domain wall is first slightly displaced between 35 mT and 40 mT before it completely depins and leaves the kink at about 45 mT. A possible explanation for the comparably high switching field is that the domain wall is not only translated but that its spin structure is transformed. The energy landscape for the transformed domain wall can look completely different, what results in a change of depinning fields. Such complex depinning processes are also observed in planar permalloy wires with more simple spin structures [Bri11, Ake10].

Figures 6.8(d) through (g) depict a depinning process where the domain wall is depinned from the kink between 30 mT and 35 mT without antecedent visible transformations. Figure 6.8(e) is scanned bottom-up. The domain wall leaves the kink while the magnetic probe scans right across it. That is why the bright magnetic contrast disappears abruptly. The domain wall is detected again about 1.5 µm away from the kink. From there it depins at 40 mT during the scan displayed in Fig. 6.8(f) which is done top down. Figure 6.8(g) shows the subsequent magnetic force micrograph recorded at 45 mT. Again, the domain wall, which has moved about 1 µm

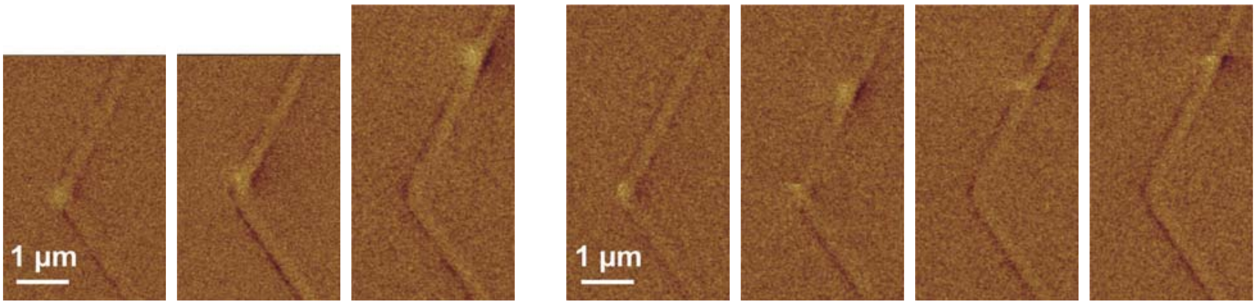

(a) 25 mT (b) 40 mT (c) 45 mT (d) 25 mT (e) 30 mT (f) 40 mT (g) 45 mT

Figure 6.8: Magnetic force micrographs revealing two possible depinning processes of a domain wall prepared in a bent nickel nanowire. The magnitudes of the horizontal magnetic fields applied during the scans are written below the images. (a) through (c) depict the behavior of a domain wall prepared in the kink by applying a magnetic field of −80 mT. (d) through (g) show the depinning of the domain wall after it was pushed back into the kink by applying −40 mT.

further up, depins while the probe scans across it. These observations suggest that the depinning process can be triggered by the stray field of the magnetic probe.

Figure 6.9 is a close-up of the domain wall shown in Fig. 6.7(c). The scan is done top down while the external magnetic field is increased from 0 mT to 45 mT at a variable rate. At 29 mT the domain wall, which at that time is pinned at the upper edge of the MFM image, gets slightly displaced before it depins and the magnetic contrast at that position is lost. The domain wall is detected again about 1.5 µm further down where it stays pinned up to a field of at least 35 mT. By the time the scan is finished at the bottom of the frame, the applied field is 45 mT, but the domain wall has not moved back to the kink yet. This experiment demonstrates that a domain wall can be moved back and forth from one pinning site to another by applying an external magnetic field.

The domain wall displayed in Fig. 6.9 moved from the kink where it was prepared to the upper pinning site at −39 mT. From there it depinned at a reverse field of only 29 mT. The wall is then pinned at the lower pinning site up to 45 mT, even though it passed that pinning site on its way up at −39 mT without remarkable influence on its propagation. This behavior either indicates a strong asymmetry of the individual pinning potentials or it has to be attributed to a transformation of the spin structure of the domain wall during the depinning process or during propagation. Our MFM data, which is not completely shown here, indicates a change of the domain-wall structure before depinning in some cases. Since only static states can be imaged, and since no detailed studies on the depinning fields were made, no unambiguous statement about the origin of the asymmetric pinning behavior can be made at this point.

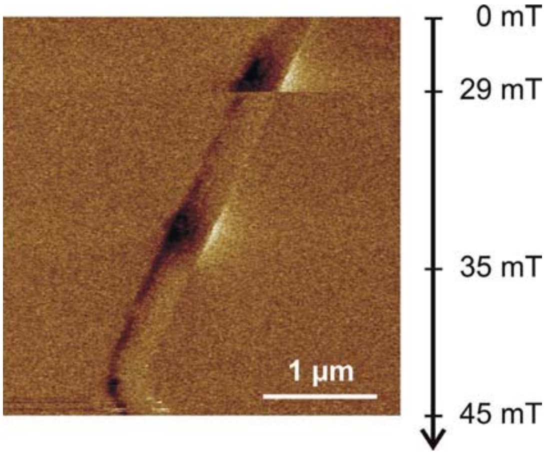

Figure 6.9: Magnetic force micrograph of a bent nickel nanowire. The dark contrast on the wire is caused by the magnetic stray field of a domain wall. During the scan, which was done top down, the applied magnetic field was sweeped from 0 mT to 45 mT at a non-constant rate. Details are given in the text.

The stray field caused by the domain wall is reminiscent of a transverse domain wall. For comparison the reader may turn back to the micromagnetic simulation depicted in Fig. 3.7. The presence of a transverse domain wall is surprising in this 225 nm thick nickel wire, since in the simulations transverse domain walls only occur in wires with diameters below 42 nm. It could however be explicated by the way the domain wall is prepared. An additional fact that at first glance conflicts with the assumption of a transverse domain wall propagating through the wire is that the stray field of the domain wall looks similar at all positions. From the micromagnetic simulations we know that such transverse domain walls are expected to screw through a wire instead of just translating. This means we could expect to see the transverse domain wall from different sides, what would lead to distinguishable stray-field patterns. Those, however, cannot be observed. The reason for this could be that the MFM images do not display dynamics but a static energy minimum in which the Zeeman energy leads to an alignment of the domain wall along the external field direction. If the field applied during the propagation of the domain wall would be responsible for the orientation of the wall, the patterns should be different for head-to-head and tail-to-tail domain walls, since they are depinned from the kink by applying fields into opposite directions. Comparing the magnetic contrasts caused by the head-to-head domain wall in Fig. 6.8(c) and the one caused by the tail-to-tail domain wall in Fig. 6.9 shows that for the two domain walls the magnetic contrast is simply inverted. This indicates that the chirality of the two domain-wall types is the same. Considering the fields applied while the two images were recorded (+45 mT +35 mT) implies that the chirality of the domain walls is not determined by the present external field but through their preparation in the kink.

6.3 Diameter-modulated wires

Geometric constrictions like the one shown in Fig. 2.13 can be employed for the controlled preparation of domain walls in planar soft-magnetic wires. The applicability of a comparable concept for three-dimensional wires was investigated by magneto-optical Kerr-effect (MOKE) magnetometry, magnetic imaging using magnetic force microscopy (MFM) and photoemission electron microscopy (PEEM), as well as through micromagnetic simulations. Parts of this work, namely the results obtained by MOKE magnetometry on nickel wires with diameter modulations from (80 ± 10) nm to (160 ± 10) nm created by combining mild and hard anodization, have been published in [Pit11]. The paper, which also includes results obtained by superconducting quantum interference device (SQUID) magnetometry on ensembles of wires with one or two modulations, is appended to this thesis in Sec. A.1. Due to the limited spatial resolution of MOKE magnetometry, and due to the averaging over several hundred reversal events, no unambiguous hint at domain-wall pinning at a modulation could be found in the studies presented in publication [Pit11]. Thus, further experiments on various types of modulated wires have been done by MFM and PEEM providing higher spatial resolution. Figures 6.10(a) through (d) are scanning electron micrographs of diameter modulations created by pore-widening as described in Sec. 4.1. The images depict close-ups of nickel wires with one modulation. Studying the magnetization reversal in these nanowires by PEEM, no pinning in the vicinity of a modulation could be observed. In total we studied five wires of geometry (a), one wire of geometry (b), three wires of geometry (c), and two wires of geometry (d). Subfigure (e) depicts a modulation deformed due to branching during pore growth. For this geometry no pinning could be observed at the modulation either.

As reported in Sec. 5.2 the magnetization reversal in nickel wires with diameters in the range of 100 nm to 300 nm is rather complex. To increase the chance of domain-wall pinning at a diameter modulation, nanowires with smaller radii were synthesized of nickel-iron alloys. Permalloy, an alloy of 80 percent nickel and 20 percent iron, provides a magnetocrystalline anisotropy that is one order of magnitude smaller than the one of nickel (compare Table 2.1). Realizing exactly this concentration during electrochemical deposition into the pores of alumina membranes is challenging. Amongst others the deposition parameters depend on the diameter of the pores. Thus, a variation of the alloy's concentration at diameter modulations is hard to avoid [Víc]. It can lead to a variation of magnetic properties such as the saturation magnetization at the modulation [Sal12]. Consequently, the influence of the modulation on the magnetic behavior of the wires cannot unambiguously be attributed to geometric aspects only.[3] Energy-dispersive x-ray spectroscopy on ensembles of wires reveals an atomic

---

[3] To check if the concentration varies along a particular wire, local XMCD spectra would be required. Recording sufficient data takes about 10 hours and was not done for these wires due to the limitation of beam time available.

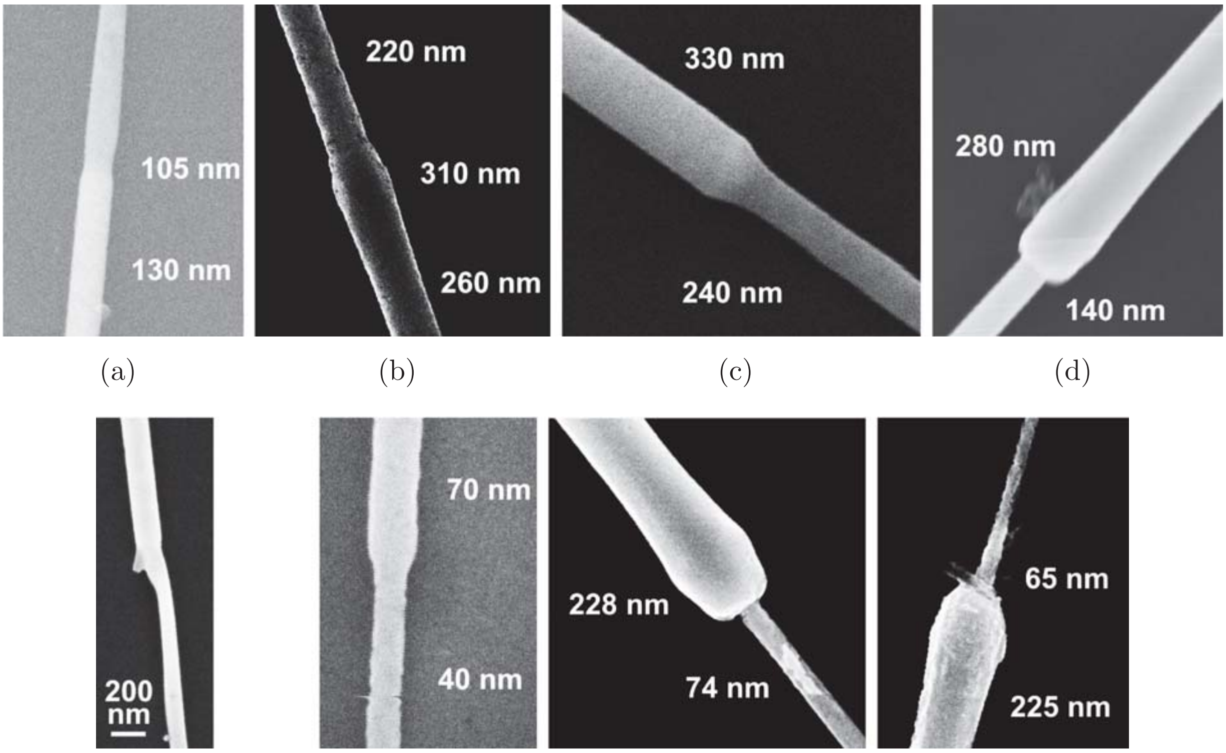

(a) (b) (c) (d)

(e) (f) (g) (h)

Figure 6.10: Scanning electron micrographs of (a) through (e) nickel wires and (f) through (h) nickel-iron wires with one diameter modulation. The radii of the thin and the thick segments are given in each image. In (e) the modulation is deformed due to branching during the growth of the pores in the alumina membrane. Only at the modulation shown in (h) a domain wall could be pinned successfully.

compositions of 80 ± 2 percent and 83 ± 2 percent nickel for the wires depicted in Fig. 6.10(f) and Figs. 6.10(g) and (h), respectively.

Figure 6.10(f) depicts a permalloy wire from a batch of wires with one diameter modulation from (42 ± 4) nm to (70 ± 7) nm.[4] The modulation was created using the pore-widening method. Deposition parameters are given in the paper of Salem *et al.* [Sal12]. The size of the crystallites in these permalloy wires is about 8 nm. We studied five wires of this type by PEEM. In up to eleven trials of applying a reverse field in the vicinity of the switching field, no pinning could be observed. This behavior contrasts with the observation in pure nickel wires, where pinning at intrinsic pinning sites could regularly be observed, mainly in the thin wire segment.

---

[4] Note that in this chapter the notation $(x \pm y)$ nm refers to the average variation of the diameters of wires synthesized in one batch, and does not indicate a gradual change in the diameter of one wire as when it comes to micromagnetic simulations.

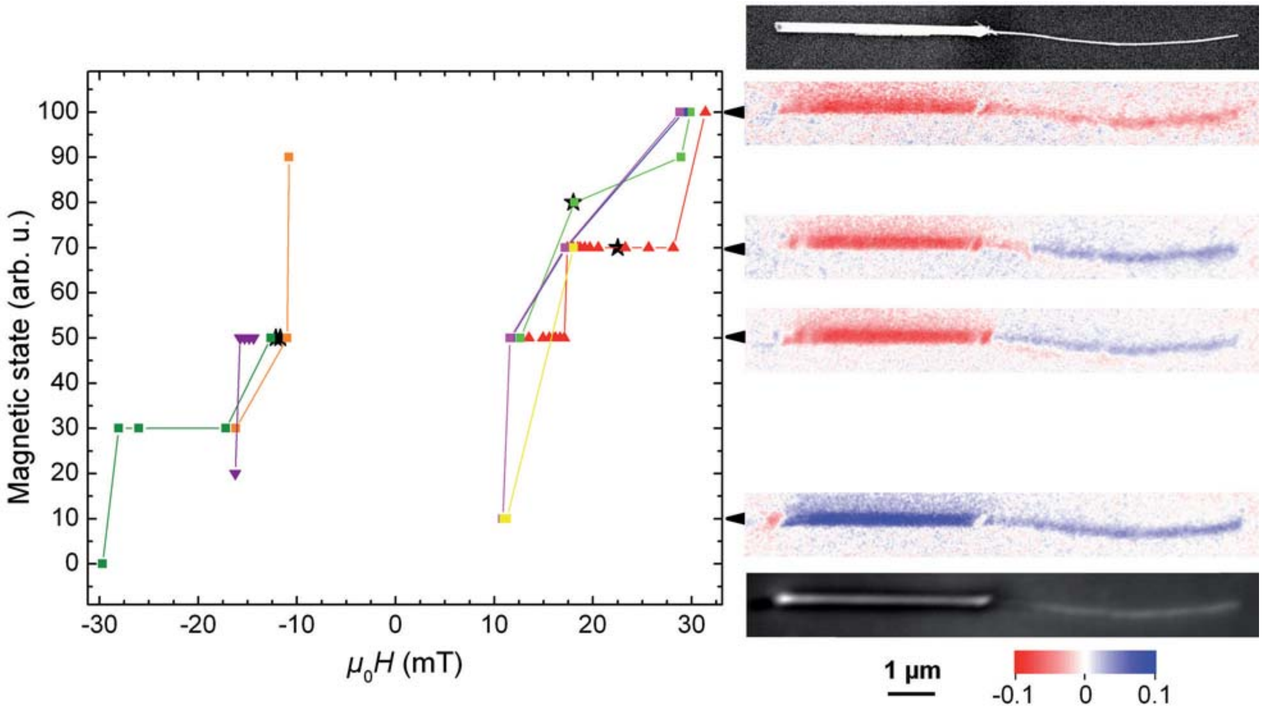

Figure 6.11: Hysteresis of a nickel-iron nanowire with a diameter modulation from 65 nm to 225 nm (see Fig. 6.10(h)). The PEEM images on the right recorded at 851.8 eV (Ni L_3 edge) depict some of the typical magnetic states observed in the wire. The states are connected to numbers that approximately correspond to the percentage of magnetization reversed as indicated by the arrows for positive reverse fields. 50 denotes domain-wall pinning at the modulation. The data points in the graph illustrate after the application of which field values the respective magnetic states are observed at remanence. The bottom and top images on the right are an absolute PEEM image and an SEM image, respectively. Estimated field constant: $0.09\frac{\text{mT}}{\text{mA}}$.

The strongest modulations that could be prepared using the pore-widening method are from (70 ± 5) nm to (225 ± 10) nm.[5] In one out of four wires of this type shown in Figs. 6.10(g) and (h) pinning at a modulation could be found. The magnetic behavior of the respective wire is illustrated in Fig. 6.11. The data points in the graph illustrate the different magnetic states observed. The states were prepared by applying the field values given in the horizontal axis and probed by acquiring PEEM images at remanence.[6] Data points shown in the same color are connected. They represent a sequence of states observed without saturating the sample by applying a reverse field of ±45 mT in between. The black stars represent states probed individually. Representative magnetic states are displayed in the PEEM images on the right of Fig. 6.11. Arrows next to the images associate them with numbers representing

---

[5] The synthesis parameters are given in the Appendix Sec. B.1.2.

[6] To compensate hysteretic behavior of the PEEM setup some images were acquired in small applied fields that are not expected to influence the magnetic state.

the magnetic state. The nomenclatures approximately correspond to the amount of magnetization reversed. 0 and 100 depict the states after saturation into negative and positive field direction, where the main part of the magnetization is aligned in parallel (blue XMCD contrast) or antiparallel (red XMCD contrast) to the wire's axis, respectively. A reverse field in the order of 11 mT is not sufficient to reverse the magnetization of the thick wire segment. However, at the thick end of the wire parts of the magnetization irreversibly switched already (state 10). At the thick end's transition towards the thin end the magnetic contrast is decreased, as it is also observed in the other XMCD images. This gives a hint at where the nucleation takes place, namely at both extremities of the thick wire segment. Regarding the demagnetizing field of a modulated nickel wire depicted in Fig. 3.5(c) this is not surprising. The overlay of local magnetic fields and local magnetic properties in a wire decides about where nucleation occurs. Nucleation at the modulation, where the effective field is high due to an increased demagnetizing field, is observed in the majority of wires studied. If a reverse field above 11.2 mT is applied, the thick segment switches and a domain wall is pinned in the vicinity of the modulation. This state is represented by the value 50 in the graph of Fig. 6.11. The chance to observe pinning at the modulation by applying a reverse field between 11.5 mT and 15.8 mT is 100 percent. Upon further increasing the reverse field, domain-wall pinning is observed at three other pinning sites in the thin segment of the wire (states 70, 80, and 90 after negative saturation and states 30 and 20 after positive saturation). The surface of the thin segment of this wire is rather rough, compare Fig. 6.10(h), what might be one reason for the occurrence of these intrinsic pinning sites.

As discussed in Sec. 5.1 the switching field of cylindrical nanowires decreases with increasing diameter. Thus, in modulated wires thick wire segments take over the function of injection pads in planar soft-magnetic wires (compare Fig. 2.13). Intrinsic pinning sites in the thin segment can be employed for the controlled preparation of several domain walls as illustrated in Fig. 6.12. Subfigure (a) is a scanning electron micrograph of the upper wire end with the modulation from 230 nm to 70 nm, (b) depicts the absolute PEEM image of the entire wire. Figures 6.12(c) through (g) reveal the individual magnetic states prepared during the minor field sweeps for the preparation of three domain walls. The remanent state after saturation at −21 mT (c) shows a rather homogeneous magnetization. After the application of a reverse field of +15 mT a domain wall is pinned in the thin wire segment (d). It can be pushed to propagate further by applying +24 mT (e). Another domain wall is then injected into the wire by applying a field of −21 mT (f). By applying +15 mT once more (g), a third domain wall is injected and pinned at the same position as the one in (d). This and comparable procedures could successfully be executed several times.

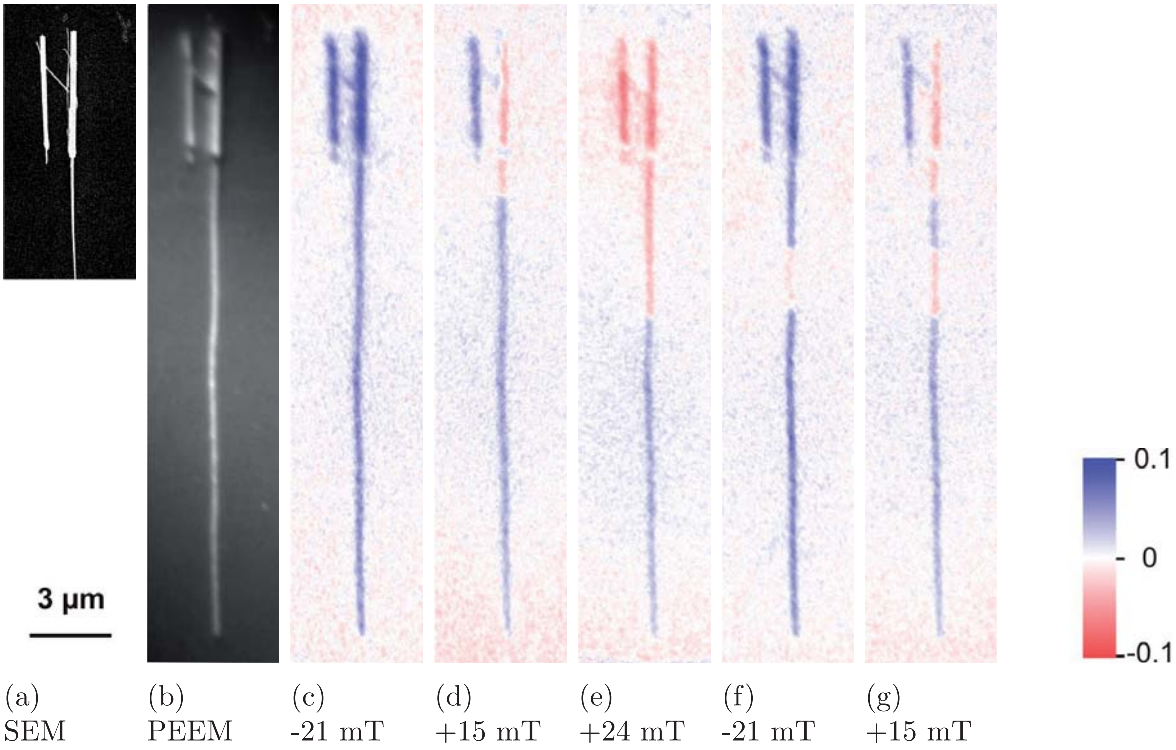

Figure 6.12: Photoemission electron micrographs illustrating the preparation of several domain walls in a nickel-iron nanowire with one diameter modulation by driving minor field sweeps. The thick segment with a length of 4.7 µm and an average diameter of 230 nm acts as an injection pad for domain walls. The walls are pinned at several intrinsic pinning sites in the thin segment with a diameter of 70 nm. The images were recorded at remanence after applying the field values given below the panels at a photon energy of 851.8 eV (Ni L_3 edge). Estimated field constant: $0.03\frac{\mathrm{mT}}{\mathrm{mA}}$

Magnetization reversal in cylindrical wires with diameter modulations was also investigated by micromagnetic simulations. In a wire with one modulation from 40 nm to 70 nm as shown in Fig. 6.13 a domain wall with a vortex-like structure nucleates at the thick wire end and starts to propagate through the wire at the switching field. The system does not relax until the wall has passed through the wire and is annihilated at its thin end. When entering the thin wire segment the domain wall is transformed into a transverse wall characteristic for wires with diameters below about 42 nm [Her04]. A comparable behavior is observed if a transverse wall is prepared in the thick wire segment as described in Sec. 3.1 and the system relaxes. The same observation is made by Allende *et al.* solving the LLG equation for a one-dimensional model [All11]. They find that a transverse wall approaching the modulation from the thick towards the thin segment is even accelerated, a result that we would obtain as well if we studied dynamics. There are two energy contributions accounting for this behavior, namely the stray field and the exchange energies. In the following they are discussed separately.

By solely considering the exchange energy the behavior of domain walls in modulated wires can be intuitively understood. A domain wall is represented by the gradual rotation of magnetic moments between antiparallel aligned domains. The exchange energy associated with the wall is proportional to the area cross section of the wall. It is reduced if the wall is in the thin wire segment due to the reduced expansion of the wall which is proportional to the square of the wire's radius. Thus, one can expect a domain wall to propagate from a thick into a thin segment of a wire to reduce its exchange energy, while the wall rather stops before passing from a thin into a thick segment.

The magnetic stray field can be associated with magnetic charges. These charges were simulated for a relaxed modulated wire. Figure 6.13(b) depicts the surface charges which are present wherever magnetization components are not in parallel to the surface of the wire. The thick wire end appears red symbolizing negative magnetic charges, the modulation and the thin wire end carry positive charges that appear blue. In total all magnetic charges sum up to zero. Figure 6.14 presents a model based on magnetic charges for the intuitive explanation of in which case the propagation of a domain wall can be stopped by the diameter modulation. The charge

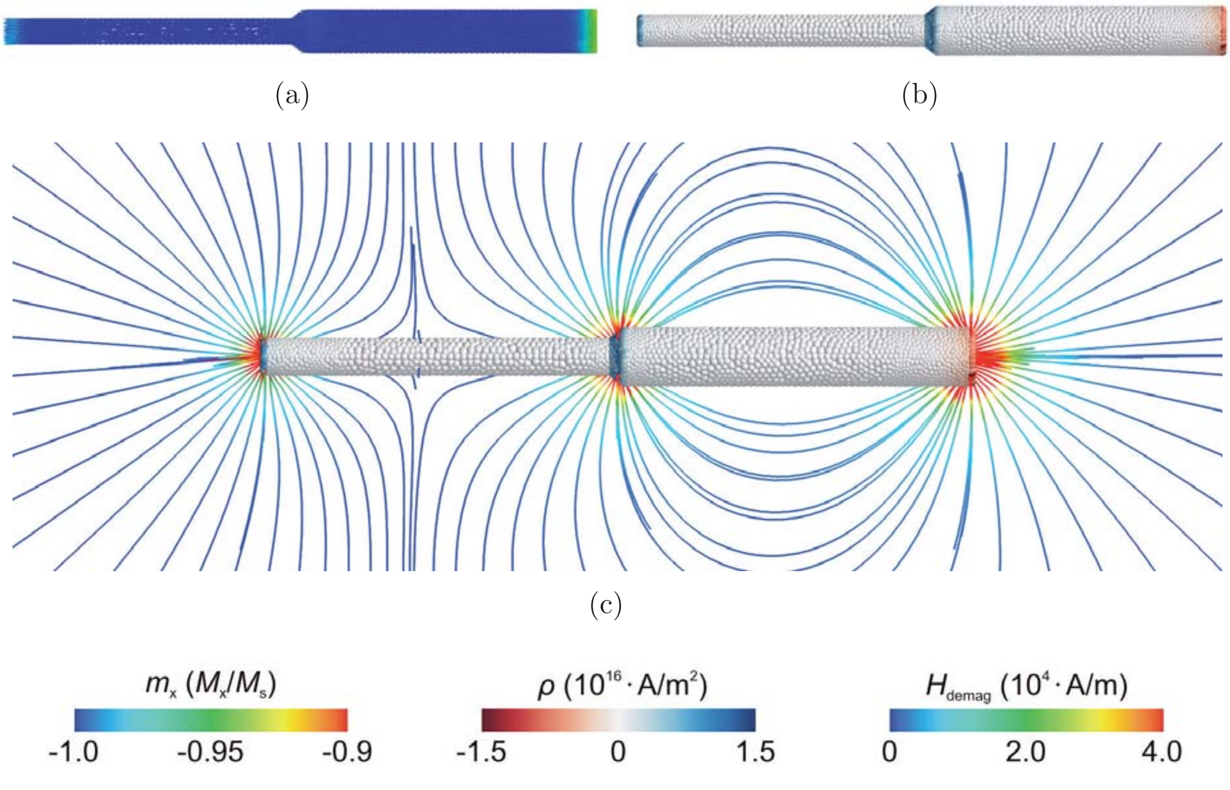

Figure 6.13: (a) Magnetization component m_x, (b) magnetic charge density ρ, and (c) stray field H_demag together with its sources ρ of a relaxed modulated nickel wire after saturation in $-x$ direction which is in parallel to the wire's axis.

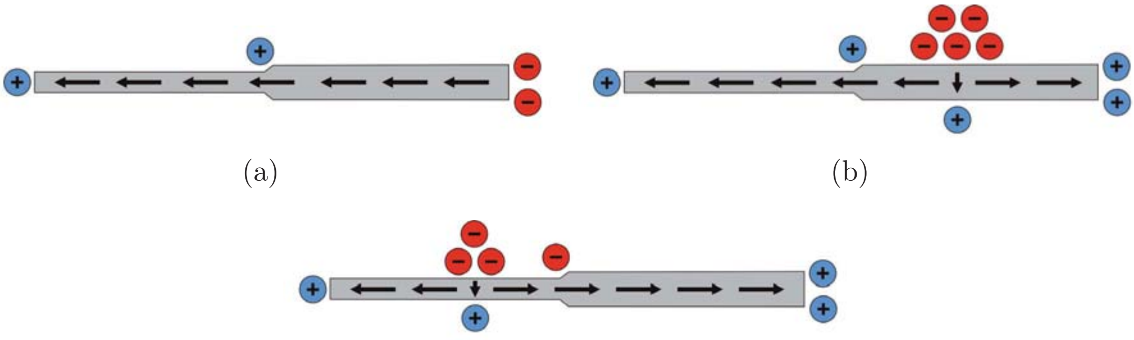

(a)

(b)

(c)

Figure 6.14: Qualitative model based on magnetic charges for (a) a uniformly magnetized wire, (b) a domain wall in the thick segment, and (c) a domain wall in the thin segment of the wire. Note that this model does not distinguish between surface and volume charges.

distribution of the simulated relaxed state in Fig. 6.13(b) is sketched in Fig. 6.14(a). Fig. 6.14(b) qualitatively illustrates the magnetic charges for a domain wall present in the thick segment of the wire.[7] Apart from the sign the charge distributions at the extremities of the wire and at the modulation are independent of whether a domain wall is present in one of the wire segments or not. The image depicts a transverse wall effectively carrying fourfold negative charge. Since the charge distribution in the rest of the wire is independent of the domain-wall type, a vortex-like wall would carry the same amount of magnetic charges. Comparing the effective charges of the modulation and the domain wall, it is clear that the negatively charged wall is attracted by the positive charge at the modulation to reduce the stray-field energy and eventually the total charge of the system domain wall - modulation.

Contrasting behavior is observed if a domain wall is present in the thin segment of the wire as in the simulation depicted in Fig. 6.15. Based on Fig. 6.15(b) the distribution of magnetic charges is sketched in Fig. 6.14(c). In this case the domain wall effectively carries a double negative charge. It is repelled by the negative charge at the modulation. This behavior is in agreement with the micromagnetic simulations presented below as well as with the ones by Allende *et al.*.

The effective charges and the resulting energy between a domain wall and a modulation can be calculated analytically.[8] We consider a wire with one modulation from a thin segment with diameter d_1 to a thicker segment with diameter d_2. The domain

---

[7] The model does not distinguish between surface and volume charges. Strictly speaking, the surface charges of the domain wall cancel out, and the effective charge is made up of volume charges which are not visible in the simulations shown. For more details the reader may refer to Ref. [Krü12].

[8] The following expressions are inspired by Ref. [Krü12] and based on calculations by M. Martens. To be published as J. Kimling, M. Martens, *et al.*.

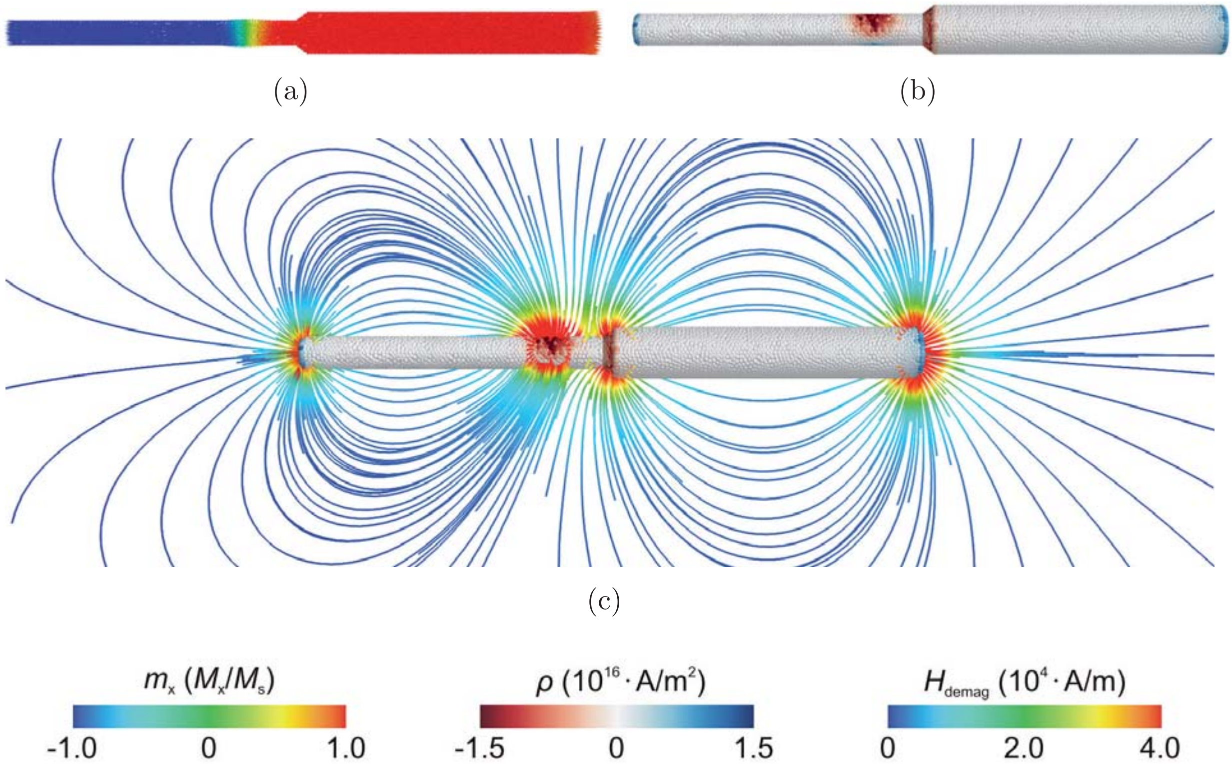

(a) (b)

(c)

Figure 6.15: (a) Magnetization component m_x, (b) magnetic charge density ρ, and (c) stray field H_demag together with its sources ρ of a modulated nickel wire with a domain wall prepared in the thin segment. Note that the magnetic volume charges of the domain wall are not visible here.

wall is in the thin segment of the wire at the position $-x$ as illustrated in Fig. 6.16(a). The effective charge q_w carried by the domain wall is given by

$$q_\mathrm{w} = 2\, a\, M_\mathrm{s}\, \pi \left(\frac{d_1}{2}\right)^2 \tag{6.1}$$

where $a = +1$ for a head-to-head and $a = -1$ for a tail-to-tail domain wall. The effective charge q_m of the modulation is given by its surface charge. Using Eq. 2.12 to calculate the total surface charge of the modulation yields

$$q_\mathrm{m} = a\, M_\mathrm{s}\, \pi \left[\left(\frac{d_2}{2}\right)^2 - \left(\frac{d_1}{2}\right)^2\right]. \tag{6.2}$$

In first order the magnetic charge of the modulation can be modeled as a point charge monopole due to the symmetry of the modulation. The same holds for the charge carried by a vortex-type domain wall. For transverse domain walls, however, the asymmetry of the wall leads to dipole contributions. While the monopole-monopole contribution to the interaction between domain wall and modulation is proportional to x^{-1}, monopole-dipole interaction drops with x^{-2} and is thus negligible as long as the domain wall is not too close to the modulation. Since in our simulations (see below) the domain wall stops in a certain distance from the modulation, it seems likely that the domain-wall type, vortex or transverse, is of minor importance.

Considering only monopole-monopole interaction, the energy between domain wall and modulation simply depends on the effective charges:

$$E_{\mathrm{qq}} = \frac{\mu_0}{4\,\pi} \cdot \frac{q_{\mathrm{m}}\,q_{\mathrm{w}}}{|x|} = \frac{\pi}{2}\,\mu_0\,M_{\mathrm{s}}^2 \left(\frac{d_1}{2}\right)^2 \left[\left(\frac{d_2}{2}\right)^2 - \left(\frac{d_1}{2}\right)^2\right] \cdot \frac{1}{|x|}\,. \tag{6.3}$$

The distance $|x|$ is measured from the center of the modulation to the center of the domain wall.

Figure 6.16 illustrates the simulation of a domain wall that was prepared in the thin segment of a wire and pushed towards the modulation by an increasing background field H_{ext}. Figures 6.16(a) through (d) depict selected relaxed states of the magnetization at various applied fields. The position x of the domain wall is negative as long as the wall is in the thin segment on the left hand side of the modulation. The distance $|x|$ from the modulation at which the domain wall stops its propagation decreases with increasing H_{ext} until the applied field is strong enough to push the wall into the modulation. There, the wall is pinned ($x \geq 0$) for some more field steps before it leaves the modulation and the entire magnetization of the wire is reversed. While the external field in the micromagnetic simulation is increased step wise, not only the position x of the domain wall but also the rest of the wire's magnetization changes. To separate the energy contribution responsible for the observed behavior, two parallel simulations were performed. In one of them the domain wall was 'pinned' after the first simulation step (-2 mT). The exchange energy and the demagnetizing energy of this simulation were subtracted from the other one to remove contributions not caused by the domain-wall motion. The result is plotted in Fig. 6.16(e). Both energies increase when the domain wall approaches the modulation and are thus responsible for the micromagnetic behavior. As expected, the exchange energy stays almost constant until the domain wall is close to the modulation ($x \approx -75$ nm) and gets deformed. The non-local stray-field energy influences the propagation of the domain wall already at a large distance, namely more than 200 nm away from the modulation. The green curve plotted in Fig. 6.16(e) is a fit to the simulated data in the interval $-220\text{ nm} \leq x \leq -75$ nm and given by $E_{\mathrm{demag}}^{\mathrm{fit}} = E_0 + 0.95 \cdot 10^{-25}\ \mathrm{Jm} \cdot x^{-1}$. Inserting the values $d_1 = 40$ nm and $d_2 = 70$ nm in Eq. 6.3 yields $E_{\mathrm{qq}} = 1.12 \cdot 10^{-25}$ Jm $\cdot x^{-1}$. The good agreement between this analytical result and the fit $E_{\mathrm{demag}}^{\mathrm{fit}}$ to the simulated data justifies the above approach to consider monopole-monopole interaction as the leading energy contribution.

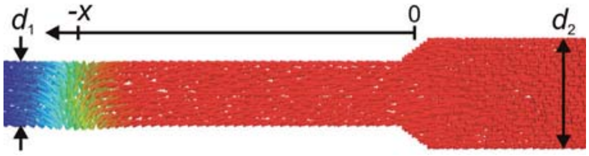

(a) -2 mT, ($x = -233$ nm)

(b) -23 mT, ($x = -59$ nm)

(c) -48 mT, ($x = -34$ nm)

(d) -49 mT, ($x = +3$ nm)

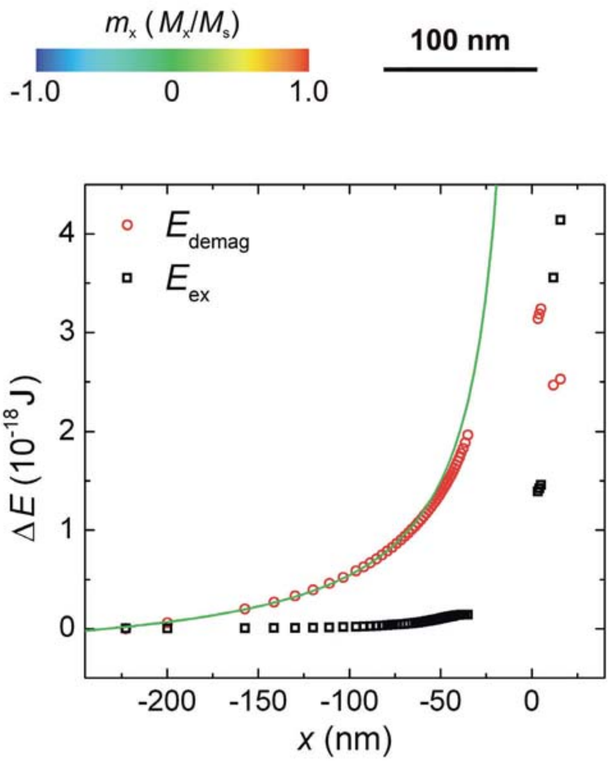

(e)

Figure 6.16: Micromagnetic simulation of a domain wall prepared in the thin segment of a 3 μm long wire with a diameter modulation from $d_1 = 40$ nm to $d_2 = 70$ nm. The wall is pushed towards the modulation by an increasing external field. (a) through (d) are relaxed magnetic states at the field values given below each panel. $|x|$ is the distance between domain wall and modulation. Negative x values indicate that the wall is in the thin segment of the wire on the left hand side of the modulation. The graph in (e) depicts the increases of the exchange and demagnetizing energies, ΔE_{ex} and ΔE_{demag}, that can be attributed to the displacement of the domain wall as a function of x.

The effective magnetic charge carried by the modulation is independent of the modulation's shape. It only depends on the diameters of the two wire segments, compare Eq. 6.2. Consequently, the repulsion[9] experienced by a domain wall can be tuned by varying the aspect ratio $n = \frac{d_2}{d_1}$ of the modulation. This is demonstrated by the micromagnetic simulations presented in Fig. 6.17(a). The diameter d_1 of the thin segment is kept fixed at 40 nm, while d_2 is varied between 55 nm and 160 nm. The length l of the modulation is 20 nm. The graph depicts the distances $|x|$ from a modulation at that domain walls stop their propagation in applied fields of -5 mT

---

[9] Note that in the quasi-particle model based on the Landau-Lifshitz-Gilbert equation [Tho07] $\frac{\partial E}{\partial x}$ rather yields a velocity than an acceleration like it is known from classical mechanics. Nevertheless, $\frac{\partial E}{\partial x}$ is referred to as a 'force' here.

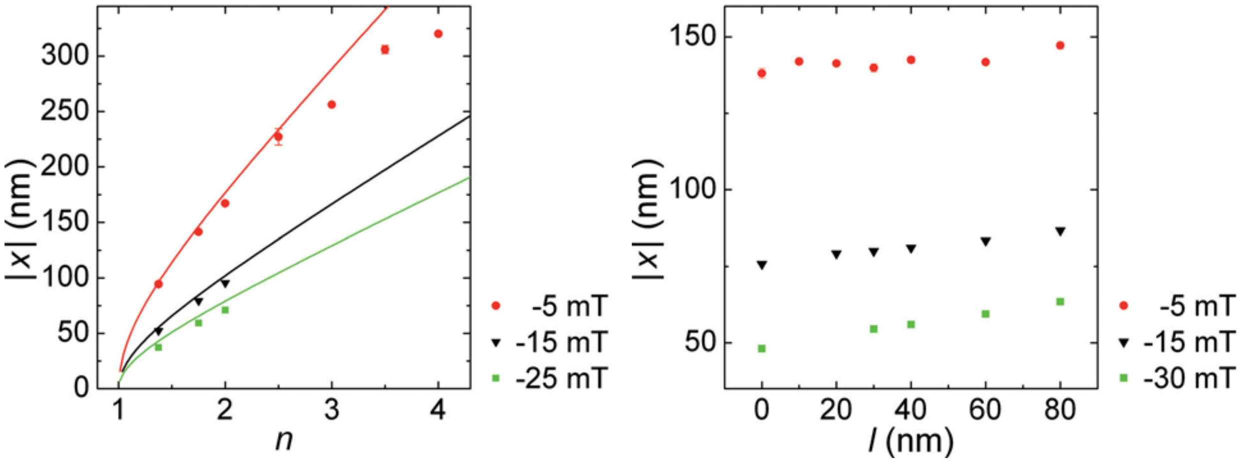

(a) (b)

Figure 6.17: Distance $|x|$ from a modulation at that a domain wall relaxes in applied fields of -5 mT (red), -15 mT (black), and $-25(30)$ mT (green) in dependence of (a) the aspect ratio $n = \frac{d_2}{d_1}$ of a modulation (for $l = 20$ nm) and (b) the length l of a modulation (for $n = 1.75$). The curves in (a) are the analytical results given by Eq. 6.5 and the parameters from the simulations.

(red), -15 mT (black), and -25 mT (green) in dependence of the aspect ratio n.[10] As can be inferred from the graph, $|x|$ increases with increasing aspect ratio n as expected. The equilibrium position of the domain wall is determined by the interplay between the stray-field energy E_{qq} (Eq. 6.3) of the modulation and the wall and the Zeeman energy due to the external field pushing the wall towards the modulation. The Zeeman energy E_{Zeeman} is given by

$$E_{\mathrm{Zeeman}} = 2\,\pi \left(\frac{d_1}{2}\right)^2 a\,\mu_0\,M_{\mathrm{s}} \cdot H_{\mathrm{ext}} \cdot |x| \ . \tag{6.4}$$

Solving $\partial(E_{\mathrm{Zeeman}} + E_{\mathrm{qq}})/\partial\,|x| = 0$ yields the following equilibrium position $|x|_{\mathrm{e}}$ of the domain wall:

$$|x|_{\mathrm{e}} = \sqrt{\frac{M_{\mathrm{s}}}{4\,a\,H_{\mathrm{ext}}}\left[\left(\frac{d_2}{2}\right)^2 - \left(\frac{d_1}{2}\right)^2\right]} = \frac{1}{4}\sqrt{\frac{M_{\mathrm{s}}}{a\,H_{\mathrm{ext}}}} \cdot d_1 \cdot \sqrt{n-1} \ . \tag{6.5}$$

---

[10] The error bars for the data at -5 mT originate from a dependence of x on the propagation direction of the domain wall. Each simulation step was considered as relaxed when the torque experience by the magnetic moments in the domain wall fell below a critical value. The final relaxation of the wall, however, would have occurred only if the wall had propagated some more nanometers. Due to numerical problems it was not possible to use a lower critical value for the torque. No errors were determined for the other data points, since the error is usually smaller than the size of a data point.

This analytical result is plotted in Fig. 6.17(a) for the same parameters used to obtain the simulated results. Again, there is an excellent agreement between micromagnetic simulations and the predictions of our charge model, even though only monopole-monopole interaction is considered. It is thus shown that the repulsion a domain wall experiences can be tuned by varying the aspect ratio n of a modulation.

The exact shape of the modulation, however, does not make much difference. The influence of the length l of a modulation from 40 nm to 70 nm ($n = 1.75$) on the behavior of a domain wall was also studied by micromagnetic simulations. Fig. 6.17(b) depicts the distance $|x|$ from a modulation at that a transverse domain wall relaxes in applied fields of -5 mT (red), -15 mT (black), and -30 mT (green). As expected, $|x|$ and therewith the repulsion is almost independent of the modulation's shape. Of course this does not hold anymore when the domain wall is too close to or inside the modulation. In particular for long modulations a domain wall enters the modulation already at larger distances $|x|$. This deforms the domain wall and its geometrical center based on which x is determined does not coincide with the center of its charge distribution anymore. Furthermore, it has to be considered that higher multipole orders become more important when the domain wall is close to the modulation. Thus, the position of the domain wall varies strongest (15 nm difference) with changing l when the wall is only about 55 nm away from the modulation, compare green data points in Fig. 6.17(b). At distances of 80 nm and 140 nm from the modulation the variation of $|x|$ is only about 10 nm.

The above findings are of interest from a synthesis point of view. While it is obviously worth putting effort in obtaining high aspect ratios n of modulations, the 'sharpness' of the transition can be considered as being a minor issue. Unfortunately, the maximum diameter of the pores in alumina templates and thereby n is limited by the interpore distance. The strongest modulations that could be prepared in the frame of this work have an aspect ratio n of about four.

Based on the above discussion it is clear why no domain-wall pinning could experimentally be observed in wires with only one diameter modulation: the reliable localization of a domain wall by means of a diameter modulation in a cylindrical nanowire requires that the wall approaches the modulation from the thin towards the thick segment of the wire. Figure 6.18(a) depicts a nickel wire with a modulation from about 240 nm to 340 nm with a bent wire lying on top of it. Studying the magnetization reversal of this wire by PEEM it was found that a segment in the middle of the wire reverses first, and a domain wall could reliably be pinned in the vicinity of the modulation. This, however, is a rare case, since the reversal usually commences in the thick segment. Nucleation of a domain wall in the thin wire segment on purpose could for example be realized by local ion irradiation. As demonstrated in Sec. 6.1 manipulation with a focused ion beam decreases the nucleation field.

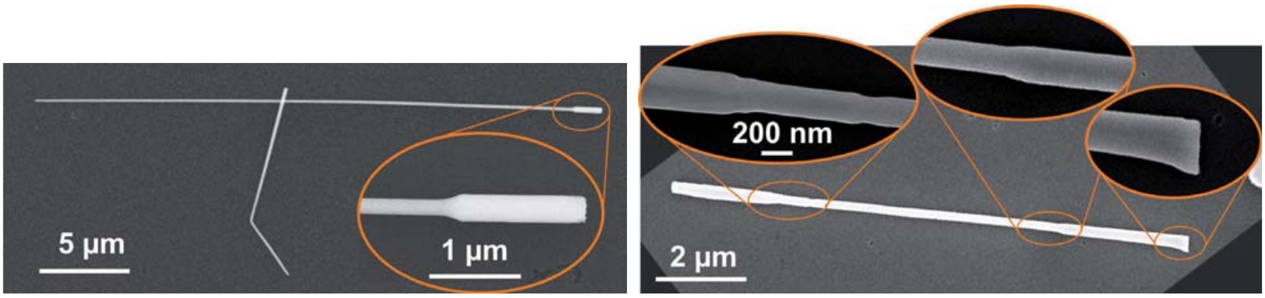

(a) (b)

Figure 6.18: Scanning electron micrographs of nickel nanowires in which a domain wall approaching a modulation from the thin towards the thick wire segment could be pinned in the vicinity of the modulation. All insets in (b) are shown with the same scale.

Another approach to enforce that a domain wall has to pass from a thin into a thick wire segment is changing the geometry of a wire. The synthesis method based on alumina templates allows for the creation of more than one diameter modulation per wire. Dumbbell-shaped wires like the one depicted in Fig. 6.18(b) were prepared by a combination of mild and hard anodization to create three segments with diameters of 220 nm, 170 nm, and 220 nm. Then the template was protected by a silica layer before the anodization was continued. To break the symmetry for a directed reversal process, the last grown segments were then widened to about 300 nm using the pore-widening method. The so-created template was covered with another silica layer by atomic-layer deposition before it was filled with nickel by electrochemical deposition.[11] The length of the individual segments typically is about 2 µm for the outer two thick segments, and 1 µm for the inner thick segment. The wires have a total length of (10 ± 2) µm.

Figure 6.19 illustrates the magnetization reversal of the wire shown in Fig. 6.18(b). Figure 6.19(a) depicts an absolute PEEM image (left) and several differential PEEM images revealing the magnetization components along the wire's axis. The field values at which the images were recorded are stated in milli Tesla below each panel. If not marked, the images were acquired in a row. $^+$ or * indicates that an image was recorded at the respective applied field after positive or negative saturation, respectively. Each magnetic state observed is associated with a number between 0 and 100 estimating the percentage of magnetization reversed. These numbers are noted at the top of each image. To provide an overview of the magnetic behavior of the wire, hysteresis curves are shown in Fig. 6.19(b). The curves are reconstructed from the PEEM data. Symbols of the same color are connected by a line to imply that the states were recorded during one field sweep. If the line is interrupted the sample was saturated in between. Coming from saturation the magnetization of the

---

[11] A detailed description of the synthesis is given in the Appendix Sec. B.1.3.

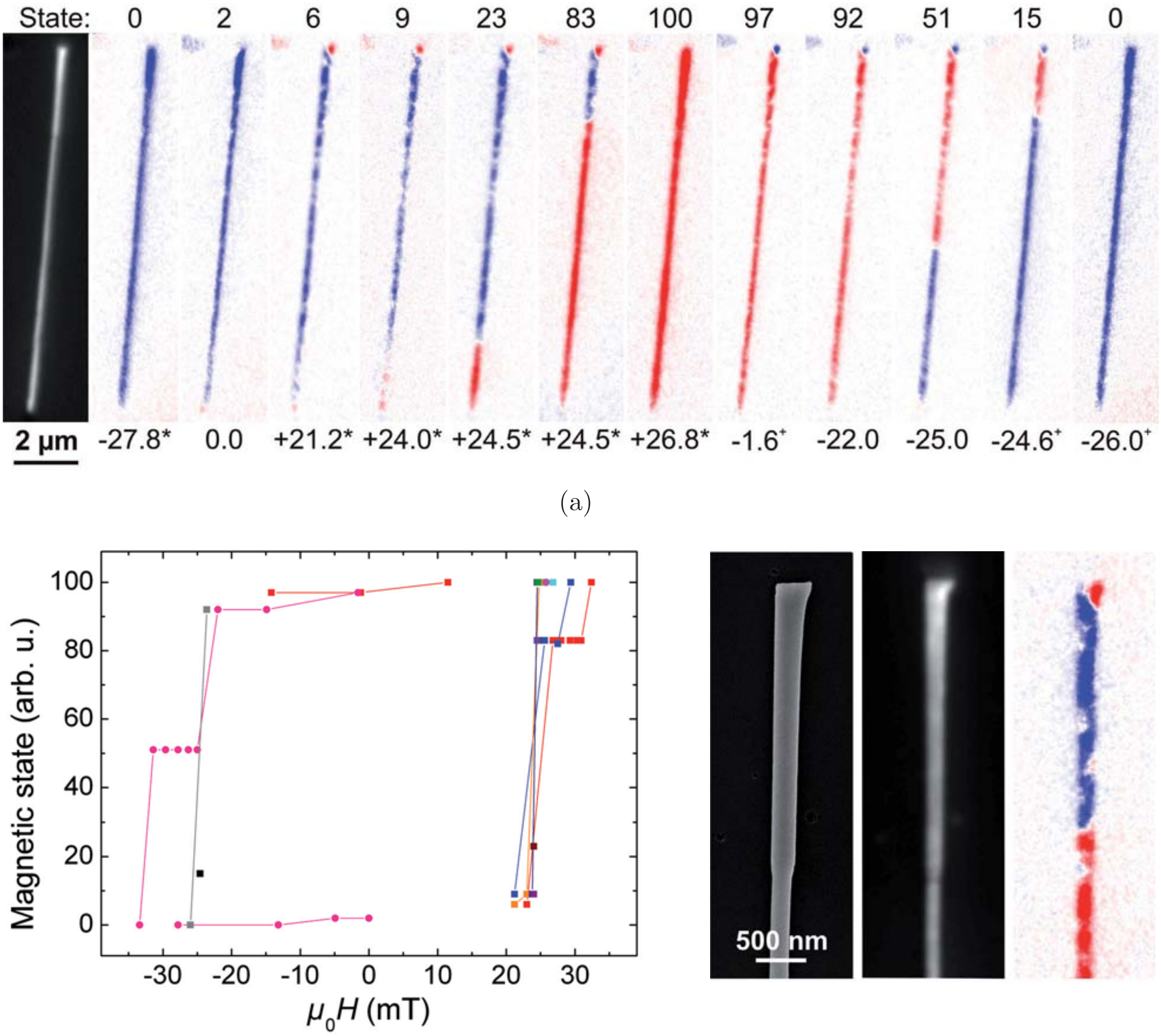

(a)

(b)

(c)

Figure 6.19: Magnetization reversal of a nickel nanowire with three diameter modulations (compare Fig. 6.18(b)). (a) Absolute PEEM image (left) and differential PEEM images revealing the magnetization components along the wire's axis. If not marked, the images were acquired in a row at the field values stated below the panels (values in mT). $^+$ or * indicates that an image was recorded in the respective applied field after positive or negative saturation, respectively. The numbers at the top of the panels label the individual magnetic states. The hysteretic behavior of the wire is illustrated in (b) where these states are plotted versus the applied magnetic field at which they were observed. (c) Scanning electron micrograph (left) and PEEM images of the upper modulation. The magnetic contrast (right) depicts a domain wall at remanence. All PEEM images were recorded at 849.6 eV (Ni L_3 edge). The magnetic contrast is not normalized to the sum of the intensities for both helicities as usual. Estimated field constant: $0.1\frac{\text{mT}}{\text{mA}}$.

wire is uniform down to an applied field of about ±10 mT. When the applied field is further decreased, the magnetic contrast decreases, in particular at the two wire ends. This indicates the beginning of magnetization reversal. Around zero field some grains at the wire ends already reversed their magnetization. In a reverse field the magnetic contrast along the entire wire decreases further. While the inhomogeneous magnetic pattern in the upper part of the wire remains about the same, the thickest segment of the wire at the bottom of the images displays a completely different magnetic behavior. We will get back to this later. In reverse fields of about ±24.5 mT a domain wall can be detected. The propagation of the wall likely starts at the lower end of the wire. During most of the sweeps the wall is pinned at one position in the wire. There is one exception during a field sweep into negative field direction where no domain wall was detected. For the other two sweeps in this direction a domain wall is once pinned at a defect in the middle of the wire up to −31.5 mT, and a domain wall could be detected in the vicinity of the upper diameter modulation. In positive reverse fields pinning is once observed at the lowest modulation in a field of +24 mT. Applying a reverse field between +24.5 mT and +26.8 mT the probability to observe pinning in the vicinity of the upper modulation makes up 40 percent. The right PEEM image in Fig. 6.19(c) is a close up of the domain wall at the upper modulation. Comparison to the SEM image and the absolute PEEM image on the left reveals that the wall is not pinned in the thin segment of the wire as expected from micromagnetic simulations, but about 300 nm away from the modulation in the thick segment. In this case it has to be taken into consideration that the pinning potential is not created by the modulation but by a defect. However there is a clear correlation between the locations of domain-wall pinning and the modulations in the wire under consideration.

The magnetization reversal of another wire in that a domain wall has to pass from a thin into a thick segment based on the geometry is illustrated in Fig. 6.20. Subfigure (a) reveals the topography, (b) through (n) depict the magnetic states observed by MFM, and (o) is the transmission electron micrograph of a comparable wire from the same batch production.[12] The wire consisted of two segments with diameters of about 80 nm separated by a 160 nm thick segment with a length of 1.3 μm. It was electrically connected and got destroyed by a discharge. During the discharge the upper segment broke and a bump formed where the upper end of the wire is now. This bump promotes the injection of a domain wall. The interpretation of the MFM data is not as straight forward as the interpretation of PEEM images, in particular since no MFM signal could be detected from the lower wire end buried underneath the contact pad, and every change in diameter causes a magnetic stray field, compare Fig. 6.13(c). The presence of a domain wall at a modulation does not necessarily change the sign of magnetic contrast there. It is always the combination of magnetic contrasts at the upper wire end and at the two modulations that is used

---

[12] The synthesis parameters are given in publication [Pit11].

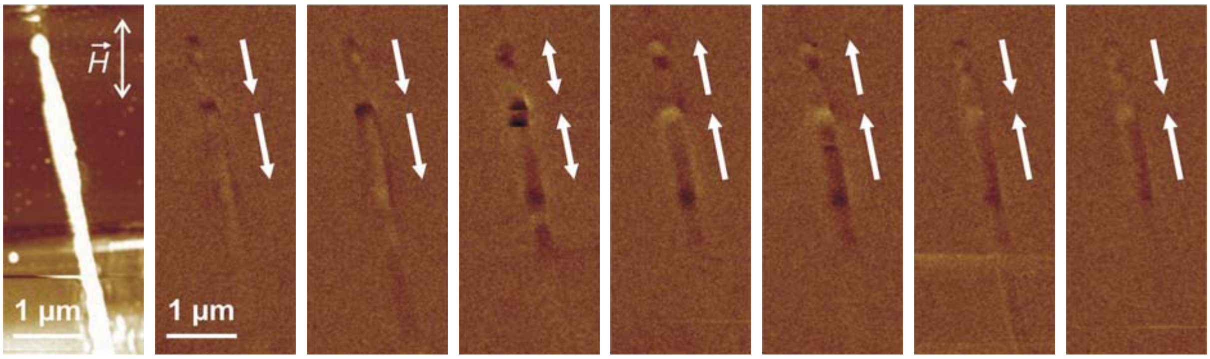

(a) AFM (b) -60 mT (c) 0 mT (d) 35 mT (e) 38 mT (f) -3 mT (g) -43 mT (h) -50 mT

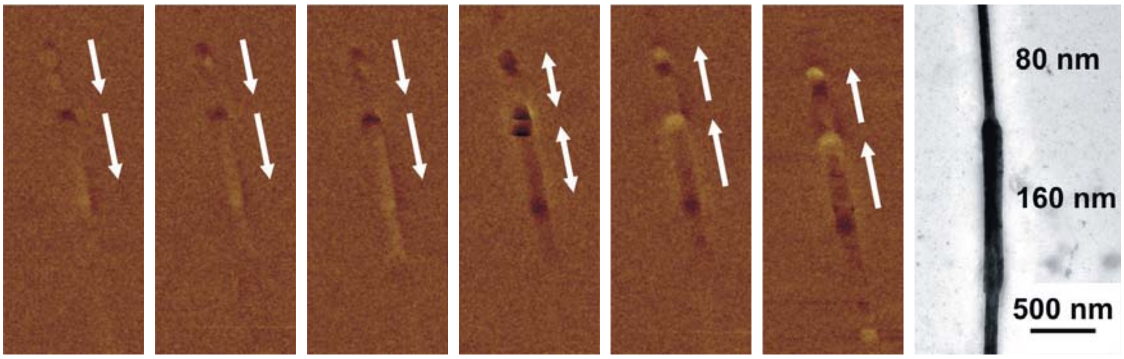

(i) -53 mT (j) -60 mT (k) 0 mT (l) 35 mT (m) 38 mT (n) 0 mT (o) TEM

Figure 6.20: (a) Topography and (b) through (n) magnetic force micrographs revealing the magnetization reversal of a nickel wire with two modulations. The external magnetic field $\vec{H}$ was applied at an angle of about 12 degrees to the wire's axis. The lower end of the wire lies under a gold contact, the upper end is a thick bump that was formed when the wire got destroyed by a discharge. The arrows indicate the magnetization direction of the upper thin and the thick segment. (o) Transmission electron micrograph of a comparable nickel nanowire.

to reconstruct the magnetic states of the upper thin and the thick segment. These states are indicated by the white arrows. The states of the lower segment and thus the presence of a domain wall at the lower modulation cannot be inferred from the MFM images.

In a strong applied field of -60 mT (Fig. 6.20(b)) a single domain state can be assumed. At remanence (c) the magnetic contrast remains mainly the same, while during the scan at 35 mT (d), which was done top down, several changes occur. A domain wall seems to move from the bump through the wire, is pinned at the modulation and again a bit below it in the thick segment before the reversal is completed and at 38 mT (e) the entire contrast is reversed compared to (c). When a weak reverse field of -3 mT is applied (f), no remarkable changes can be observed. At -43 mT (g) the contrast at the upper wire end is inverted, while the contrast at the extremities of the thick segment does not change much. This indicates that a domain wall is pinned at the upper modulation, what is still the case at −50 mT (h). At −53 mT the contrast at the extremities of the thick segment changes, meaning that the domain wall got depinned or annihilated and the entire magnetization is reversed. The magnetic state in Fig. 6.20(j) recorded at −60 mT is the same as in (i) and also as in (b). Subfigures (k) through (n) were recorded at the same applied fields as subfigures (c) through (f), and the same magnetic behavior is observed. This demonstrates the reproducibility of pinning at the upper modulation from 80 nm to 160 nm.

As mentioned above the magnetization reversal of the wire shown in Fig. 6.18(a) starts in the thin wire segment.[13] Thus, a domain wall propagating through the wire approaches the modulation from the thin towards the thick segment of the wire. The magnetization reversal of the wire is illustrated in Fig. 6.21. Differential PEEM images of the individual magnetic states observed are depicted on the right side of the figure. As can be inferred from the shadows in the absolute PEEM image at the bottom the angle between the in-plane projection of the incident x-ray beam and the wire's axis is of about zero degrees. Consequently, the magnetic contrast represents the magnetization components in parallel to the axis of the wire. Arrows next to the XMCD images link them to a certain value representing the magnetic state in the graph on the left. The states 70 and 80 distinguish themselves not in the position of the domain wall but in the magnetic pattern of the domain wall. This is indicated by the arrows next to XMCD images in the center of the figure displaying the two different domain-wall types observed in the vicinity of the modulation. All states are plotted versus the fields applied for their preparation before the images were acquired at remanence. The black and green symbols mark the data for positive and negative reverse fields, respectively. A strikingly different magnetic behavior is observed for the two sweep directions. For negative reverse fields no domain-wall pinning is observed and the switching field is at least two percent smaller than the one for the other field direction. Such an asymmetry of the switching field is often observed in the nickel wires studied and was discussed already in chapter 5. For positive reverse fields the chance to observe domain-wall pinning is almost 100 percent. At reverse fields above +29 mT domain walls are pinned twice at an intrinsic pinning site located about 2 μm before the modulation in the thin segment of the wire (state 40). Applying a reverse field between +28.8 mT and +29.0 mT a domain wall is pinned at the modulation from 240 nm to 340 nm in four out of five cases (states 60, 70, and 80).

To obtain a deeper insight into the magnetic behavior at the modulation, PEEM images were acquired in a smaller field of view at three different angles between the in-plane projection of the incident x-ray beam and the wire's axis. These images are presented in Fig. 6.22. In the absolute photoemission electron micrographs on

---

[13] A detailed description of the synthesis if this wire is given in the Appendix Sec. B.1.1.

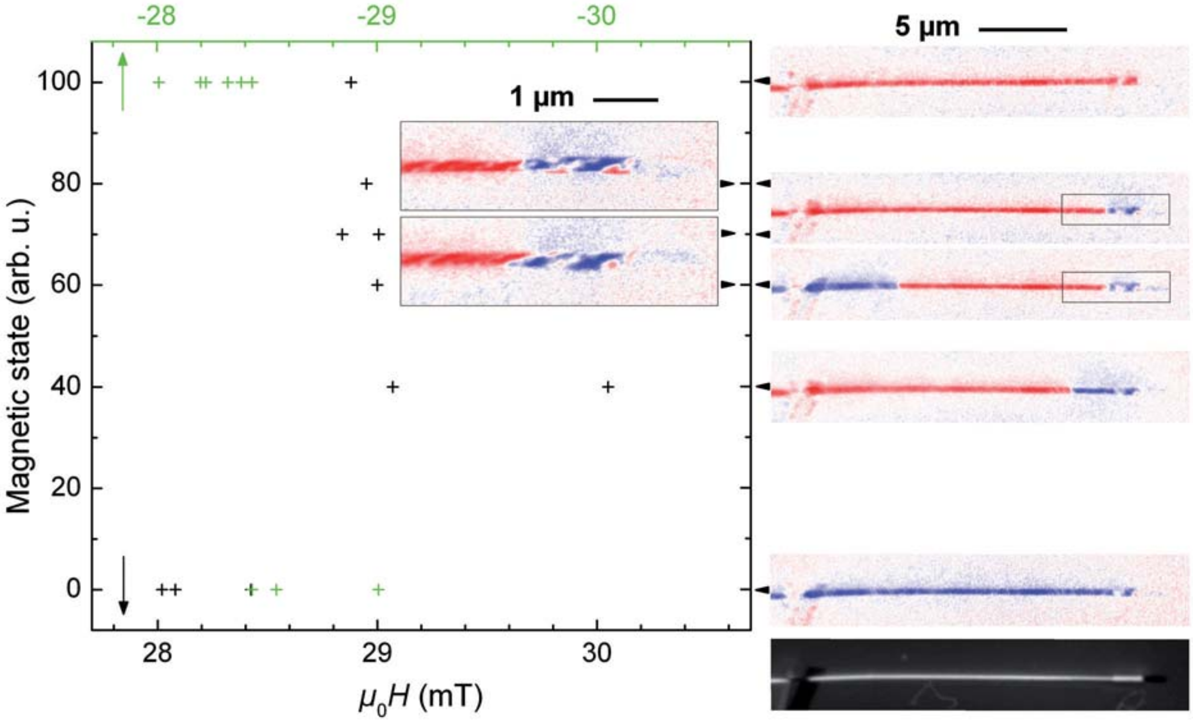

Figure 6.21: Magnetization reversal of a nickel nanowire with a diameter modulation from about 240 nm to 340 nm. The differential PEEM images recorded at 852 eV (Ni L_3 edge) depict the magnetization components along the wire's axis. The arrows next to the images point at the values representing the individual magnetic states in the graph on the left hand side. It is illustrated which fields were applied before these magnetic states were imaged at remanence. Estimated field constant: $0.1\frac{\mathrm{mT}}{\mathrm{mA}}$.

the left the direction of the incident x-ray beam is indicated by white arrows. The subsequent XMCD images reveal the corresponding magnetization components. Figures 6.22 (b) and (c) depict the domain wall described by the magnetic state 40 in Fig. 6.21 at remanence and in a reverse field of +30.2 mT, respectively. At remanence the magnetization on both sides of the domain wall shows the typical inhomogeneity reflecting the granularity of the wire. In an applied field the red magnetic contrast in the part of the wire that is reversed already turns stronger and more homogeneous since the magnetic moments get further aligned into the field direction. The blue magnetic contrast in the right part of the wire gets weaker. This means that more magnetization components are rotated away from the wire's axis. At the extremities of the thick segment several grains reversed their magnetization, a process which already commenced at remanence. A comparable behavior is observed in other more than 300 nm thick segments of modulated nickel wires if the thick segment is not longer than about 2 µm, compare for example the bottom end of the wire shown in Fig. 6.19. Besides the larger diameter, likely associable with a different crystalline structure as discussed in Sec. 5.2, the influence of demagnetizing fields can be responsible for this behavior. In micromagnetic simulations we see that in a 120 nm thick and only 1 µm long segment the magnetization curls along the entire segment instead of at the end only. The reversal occurs in a different mode, rather reminiscent of curling than propagation of a Bloch point. Figure 6.22(d) was recorded in a reverse field of +33.2 mT after switching of the wire's magnetization. However, there are still inhomogeneities. This implies that the applied field is not strong enough to completely saturate the structure. For technical reasons it was not possible to image in stronger applied fields.

Comparable images revealing the magnetization components at 45 degrees with respect to the wire's axis are shown in Figs. 6.22(f) through (h) without a domain wall and in subfigures (i) and (j) with a domain wall pinned at the modulation. The overall signal recorded on the wire, that is limited to XMCD contrast arising from the surface, is again inhomogeneous. Besides surface information the 45-degrees configuration provides an insight into the behavior of the bulk magnetization via the wire's shadow.[14] The XMCD contrast in the shadow of the thin segment is comparably homogeneous. In the single domain remanent state (f) the magnetic contrast caused by the x rays traversing the thick segment is weaker what partially might be due to the reduced transmission. In a reverse field of +27.5 mT (g), however, this contrast is even reduced to zero in the center region of the shadow. This means either that there are no magnetization components along the incidence direction of the x-ray beam or that magnetization components of opposite orientations cancel out the intensity contrast. A possible explanation for the latter could be a curling-like rotation of the magnetization. It is eye catching that in this subfigure (g) as well as in the subfigures (i) and (j) the magnetic contrast at the edge of the thick segment's shadow is drawn like a frame around the shadow area. The x rays causing this contrast pass the top and the very end of the wire. At least the ones going through the top have less material to pass, what might be one reason for the stronger contrast. The pattern of the frame's XMCD contrast is partially different than the one representing inner components. This is another strong indication for a difference in the magnetic behavior of the wire's surface and the bulk. In Fig. 6.22(h) the magnetic contrast in the shadow area is almost homogeneous again. Only at the very end of the wire it is nearly zero or even inverted, another indication for the influence of demagnetizing fields.

In the following we have a closer look at a domain wall pinned at the modulation. The magnetization components along the wire's axis are shown in the middle insets of Fig. 6.21 for the two different domain-wall structures observed. From the XMCD image Fig. 6.22(i) it cannot be inferred at which one of the two spin structures we are looking here. Figures 6.22(i), (j), (l), and (m) depict the same wall[15] that

---

[14] For details on the method see publication [Kim11] in chapter 4.

[15] To ensure that the same domain-wall structure is imaged at different angles both at remanence and in an applied field it was confirmed that the magnetic pattern does not change by turning the field

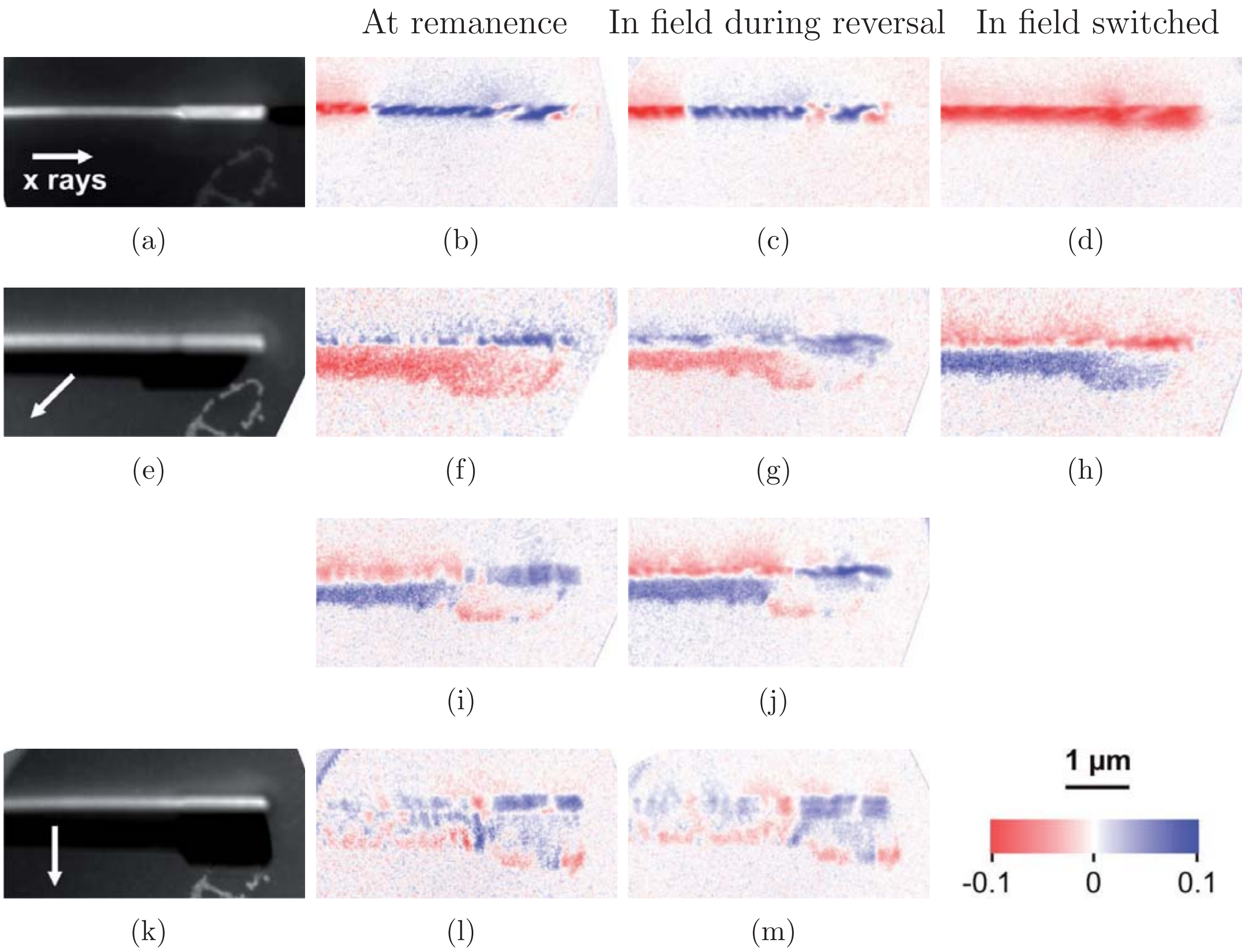

Figure 6.22: PEEM images of a nickel nanowire with a diameter modulation from about 240 nm to 340 nm. The white arrows in the absolute PEEM images (left) indicate the direction of incidence of the x-ray beam. The corresponding XMCD images reveal the magnetization components in parallel to the wire ((b) through (d)) imaged at the nickel L_3 edge (852 eV), as well as the magnetization components at 45 degrees ((f) through (j)), and perpendicular ((l) and (m)) to the wire's axis imaged at the nickel L_2 edge (869.3 eV).

was prepared during a field sweep different from the ones illustrated in Fig. 6.21. The domain wall is pinned right before the transition towards the thick segment of the wire as it is also observed in the micromagnetic simulations. At remanence (Fig. 6.22(i)) its structure appears complex. While in the center region of the shadow there is one transition form blue to red contrast, at the surface and in the respective shadow region an alternating pattern of blue and red is visible. In an applied field of +28.0 mT (j) the transition from red to blue contrast can clearly be distinguished at the surface of the wire and inverted in the entire shadow region. Figures 6.22(l) and (m) depict the same domain wall imaged at remanence and at an applied field

---

on and off or vice versa. Among others this testing was necessary because the sample could not be rotated without turning off the applied field.

of +28.0 mT, respectively, at an angle of almost 90 degrees between the in-plane projection of the incident x-ray beam and the wire's axis. These images provide no information about the magnetization components along the axis of the wire, but reveal the perpendicular components. Nevertheless, the position of the domain wall is clearly visible. Where the magnetic moments gradually rotate from a parallel to an antiparallel alignment with respect to the wire's axis, they give rise to perpendicular components and thereby to an increase in magnetic contrast. The images recorded in the 90-degrees configuration show a strong red contrast on the wire where the wall is pinned before entering the thick segment. In the shadow this contrast is inverted. While at remanence (l) it is extended perpendicularly to the wire's axis through the entire shadow, there is a distortion when a field is applied (m). The components at the wire surface and the corresponding ones at the edge of the shadow do not change much, but the center of the wall seems to be dragged towards the thick segment into the modulation. At the position of the domain wall as well as in the shadow area of the thin segment the XMCD contrast is stronger at remanence (Fig. 6.22(l)). When the reverse field of +28.0 mT is applied (m), the magnetization in the thin segment, which is already in parallel to the external field, gets further aligned. Consequently, both the intensity of the magnetic contrast and the complexity of its pattern are reduced. There is not much change observable in the thick segment at 90 degrees when an external field is applied. The curling-like rotation of the magnetization in the thick segment that was already indicated in the images recorded in the 45-degrees configuration is confirmed by the contrast being comparably strong at the surface of the wire at 90 degrees, while only weak contrast is visible on the thin segment. For the XMCD images recorded at 45 degrees it was discussed above that there is a difference in the shadow's magnetic contrast representing the bulk magnetization and at the edge associated with the surface magnetization. Comparable observations are made at 90 degrees. The edge of the shadow and the center region even show opposite XMCD contrast along almost the entire wire. This underlines once more the difference in the magnetic behavior of the surface and of the bulk magnetization as well as the possibility of domain formation in radial direction.

From the PEEM images presented in this work it can be inferred that the length of a domain wall typically corresponds to approximately half of the wire's width.[16] For efficient spin-torque induced domain-wall displacement, as it is of interest for possible applications, such wide domain walls are not desirable. The complex domain-wall structures observed likely provide intrinsic degrees of freedom which also lower the efficiency of domain-wall displacement and impose a highly stochastic nature on domain-wall dynamics. One approach to obtain simpler spin structures is to fabricate either single-crystalline wires or wires of a material with negligible magnetocrystalline anisotropy such as nickel-iron or nickel-cobalt alloys of appropriate

---

[16] For this approximation the distance between the maxima of opposite XMCD contrasts revealing the magnetization components along the wire axis are considered.

composition stoichiometry [Veg12]. A challenge will be the homogeneous concentration of the alloys across modulations. Another option to obtain more simple domain patterns is the use of thinner wires or of wires that do not enforce a singularity of the magnetization, namely tubes.

In this section it was demonstrated both experimentally and by micromagnetic simulations that the reliable preparation of a domain wall by means of a diameter modulation in a cylindrical nanowire can be realized, if a domain wall has to pass from a thin into a thick segment. To enforce the latter, a dumbbell-like structure was suggested. The feasibility of such a structure based on electrochemical deposition into anodic alumina templates was demonstrated, and a correlation between domain-wall pinning and the position of the modulations was shown. A model based on magnetic charges was proposed to explain the magnetic behavior observed. The model explains why the repulsion or attraction that a domain wall experiences when approaching a modulation depends on the aspect ratio but not on the exact shape of the modulation.

7 Magnetization reversal in Co/Pt wires with perpendicular magnetic anisotropy

The previous chapters were dedicated to electrochemically synthesized nickel and nickel-iron wires of cylindrical shape. This chapter deals with a completely different system, namely flat wires with perpendicular magnetic anisotropy that were lithographically patterned from Co/Pt multilayers. Details on electron-beam lithography are given in the Appendix Sec. B.3.1. Co/Pt multilayers were sputtered by André Kobs in the group of Hans Peter Oepen at the Institute of Applied Physics, University of Hamburg. Magnetization reversal was imaged by transmission x-ray microscopy at the Advanced Light Source in Berkeley, CA, USA. Details on the experimental setup are given in the Appendix Sec. B.6.1. The following publication [Kim13] focuses on the tuning of the nucleation field in Co/Pt wires by designing triangular-pointed wire ends. To improve the understanding of the magnetic behavior observed, micromagnetic simulations were performed by Theo Gerhardt from the Arbeitsbereich Technische Informatik Systeme of the Department of Informatics, University of Hamburg. Experimental aspects concerning the creation of pinning sites for domain walls are also addressed.

Publication [Kim13]

TUNING OF THE NUCLEATION FIELD IN NANOWIRES WITH PERPENDICULAR MAGNETIC ANISOTROPY

by

Judith Kimling, Theo Gerhardt, André Kobs, Andreas Vogel,
Sebastian Wintz, Mi-Young Im, Peter Fischer, Hans Peter Oepen,
Ulrich Merkt, and Guido Meier

published in

Journal of Applied Physics **113**, 163902 (2013).

JOURNAL OF APPLIED PHYSICS **113**, 163902 (2013)

Tuning of the nucleation field in nanowires with perpendicular magnetic anisotropy

Judith Kimling,[1] Theo Gerhardt,[1] André Kobs,[1] Andreas Vogel,[1] Sebastian Wintz,[2]
Mi-Young Im,[3] Peter Fischer,[3] Hans Peter Oepen,[1] Ulrich Merkt,[1] and Guido Meier[1]
[1]*Institut für Angewandte Physik und Zentrum für Mikrostrukturforschung Hamburg, Universität Hamburg, Jungiusstr. 11, 20355 Hamburg, Germany*
[2]*Institut für Ionenstrahlphysik und Materialforschung, Helmholtz-Zentrum Dresden-Rossendorf, 01314 Dresden, Germany*
[3]*Center for X-ray Optics, Lawrence Berkeley National Laboratory, Berkeley, California 94720, USA*

(Received 28 February 2013; accepted 8 April 2013; published online 23 April 2013)

We report on domain nucleation in nanowires consisting of Co/Pt multilayers with perpendicular magnetic anisotropy that are patterned by electron-beam lithography, sputter deposition, and lift-off processing. It is found that the nucleation field can be tuned by changing the geometry of the wire ends. A reduction of the nucleation field by up to 60% is achieved when the wire ends are designed as tips. This contrasts with the behavior of wires with in-plane anisotropy where the nucleation field increases when triangular-pointed ends are used. In order to clarify the origin of the reduction of the nucleation field, micromagnetic simulations are employed. The effect cannot be explained by the lateral geometrical variation but is attributable to a local reduction of the perpendicular anisotropy caused by shadowing effects due to the resist mask during sputter deposition of the multilayer. © *2013 AIP Publishing LLC* [http://dx.doi.org/10.1063/1.4802687]

I. INTRODUCTION

Magnetization reversal in ferromagnetic nanowires is governed by three processes: domain nucleation, domain-wall motion, and pinning. If the nucleation field exceeds any propagation or depinning field, no domain walls can be statically observed. Thus, the nucleation field determines the minimum potential depth of pinning sites to reliably trap domain walls. Weak pinning sites and therefore small nucleation fields are of interest in connection with current-driven depinning of domain walls, since high current densities, which are otherwise required, can modify or even destroy a sample.[1] It was experimentally found that the critical current density for magnetization reversal in systems with perpendicular magnetic anisotropy can be orders of magnitude smaller than in soft-magnetic materials.[2] The high efficiency of the underlying non-adiabatic spin-transfer torque arises from relatively narrow domain-wall widths.[3,4] In nanowires with perpendicular anisotropy, a reduced inversion symmetry can significantly support the magnetization reversal via spin-orbit torque[5] and a recently discovered spin Hall effect based phenomenon.[6] Another advantage of systems with perpendicular anisotropy is that generally Bloch walls appear,[2] whereas in soft-magnetic wires complex two-dimensional spin structures with intrinsic degrees of freedom occur.[7,8] All in all, wires with perpendicular anisotropy, in particular Co/Pt wires, are promising candidates for possible applications based on the displacement of domain walls by spin-polarized currents like in the race-track memory[9] as demonstrated in various studies (see, e.g., Refs. 10–12). Furthermore, Co/Pt layered structures are preferably used to investigate domain-wall resistance.[13–15] Recently, a new kind of effect, i.e., the anisotropic interface magnetoresistance, was found in these materials.[16–18]

In the case of soft-magnetic wires, for example, patterned from permalloy ($Ni_{80}Fe_{20}$), a common strategy to control domain nucleation for studying field- and current-induced domain-wall dynamics is the usage of laterally extended pads of continuous film attached to one of the wire ends. The magnetization reversal commences in this so-called nucleation pad due to its smaller shape anisotropy compared to the wire region.[19] A domain wall is injected from the pad into the wire and propagates until it pins at a defect or at an intentionally created pinning site, for example, a notch[20] or a magnetically softened region.[21] For wires with triangular-pointed ends, the formation of flux-closure domains is suppressed. This leads to an increase of the switching fields compared to wires with flat ends[22,23] or nucleation pads.

In wires with perpendicular anisotropy, nucleation pads do not work as for in-plane magnetized samples since demagnetizing effects play only a minor role. In systems with few defects acting as nucleation sites, the size of the pad has to be in the order of several $100\,\mu$m to observe any effect.[24,25] Nevertheless, smaller nucleation pads were recently used for perpendicularly magnetized wires. Since no systematic studies on the pad design were made, and the samples were usually studied by methods based on transport measurements providing only little spatial resolution such as extraordinary Hall effect[10] or giant magnetoresistance,[26] a proof of concept is still missing. A well known route to decrease the nucleation field is lowering the perpendicular anisotropy or inducing defects acting as nucleation sites by means of local ion irradiation.[27] For instance, Alvarez *et al.* demonstrated the functionality of Ga^+-irradiated nucleation pads by imaging the magnetization reversal of Co/Pt multilayer wires with a Kerr microscope.[28] Another approach for the nucleation of domains in wires with perpendicular anisotropy is to exploit the Oersted field that accompanies a current pulse flowing through a strip line attached to the wire.[29]

In this study, we demonstrate that in contrast to in-plane magnetized wires, where triangular-pointed ends suppress the nucleation of domains, the nucleation field in Co/Pt wires with perpendicular anisotropy can be decreased by almost 60% by designing tip-shaped wire ends. It is further shown that the nucleation field can be intentionally tuned by varying the opening angle of the tip. Details about sample preparation and magnetic imaging are given in Section II. Section III presents the experimental results and addresses aspects concerning the creation of pinning sites. The experimental results are further discussed in Section IV along with supporting micromagnetic simulations. Section V concludes our study.

II. METHODS

Samples were prepared by electron-beam lithography, sputter deposition of the Co/Pt multilayer, and lift-off processing of the resist as illustrated in Fig. 1(a). As substrate a silicon-nitride membrane with a thickness of 150 nm was used.[30] The resist[31] was spin-coated with 8000 rpm, baked out at 170 °C for 30 min, and exposed with a scanning electron microscope at 10 kV. After development, the sample was treated by reactive-ion etching to remove residuals of the resist in the exposed areas. Then, the thin-film stack $\mathrm{Pt}(5.0\,\mathrm{nm})/[\mathrm{Co}(0.7\,\mathrm{nm})/\mathrm{Pt}(2.0\,\mathrm{nm})] \times 4$ was deposited at room temperature at a base pressure below 2×10^{-9} mbar: First, a 4 nm thick Pt seed layer was grown via ion-beam sputtering utilizing an electron cyclotron resonance source. Subsequently, dc magnetron sputtering was employed to deposit both a 1 nm thick Pt layer and right afterwards the Co/Pt multilayer.[32] The lift-off was done by dissolving the resist in acetone. In a last step, the sample was rinsed with isopropanol and blow-dried with nitrogen.

Magnetization reversal was imaged by transmission soft x-ray microscopy at the XM-1 full field microscope at beamline 6.1.2 of the Advanced Light Source in Berkeley, CA, USA.[33] The setup allows for the application of a magnetic field perpendicular to the sample plane. Magnetic contrast is based on the x-ray magnetic circular dichroism (XMCD) effect.[34] It is proportional to the magnetization components along the projection of the x-ray beam. The perpendicularly magnetized sample was inserted into the microscope setup such that the surface normal was in parallel to the beam direction.

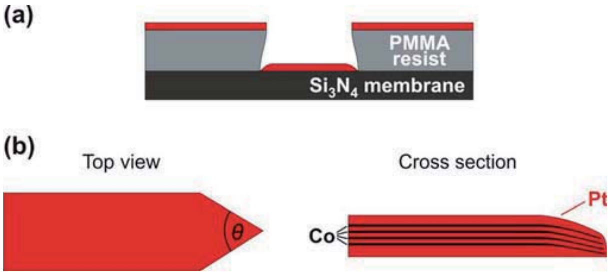

FIG. 1. (a) Illustration of sample preparation. (b) Wire geometry: due to shadowing by the resist mask during sputter deposition of the metal film, less material is deposited at the triangular-pointed wire end with tip-opening angle θ.

Micromagnetic simulations were performed with the MicroMagnum code.[35] The external magnetic field was applied at an angle of 3° to the surface normal. This symmetry breaking is required to enable domain nucleation since our simulations were performed for zero temperature and other fluctuations are neglected. In case fluctuations and imperfections are not considered, there is usually an offset between the simulated values for the critical fields and the experimental results. This effect is known as Brown's paradox.[36,37] The thickness of the simulated wires was 0.7 nm according to the thickness of one Co layer in the actual sample, and the multilayer structure of the Co/Pt film was not taken into account. Discretization was done using finite differences.

III. EXPERIMENTAL RESULTS

Figure 2(a) depicts a transmission x-ray micrograph of a Co/Pt wire with a triangular-pointed end located at its top, a straight segment with a notch, and a nucleation pad at its bottom end which is not completely visible. The structure was saturated by applying a field of about -200 mT before increasing the reverse field in steps of $+0.1$ mT. Figures 2(b) through 2(d) are differential images revealing the magnetization change between two field steps. Magnetization reversal does not start in the nucleation pad but at the upper end of the wire at an applied field of $+11.8$ mT, i.e., the nucleation field. More precisely, the reversal process commences with the nucleation of an oppositely oriented domain within the triangular-pointed end. A domain wall propagating top-down is pinned twice before the entire magnetization is reversed at $+12.1$ mT. The presence of the notch (see arrow in Fig. 2(a)) has no influence on the mobility of the domain wall.

We attribute the observed nucleation behavior to a variation of the local anisotropy constant due to shadowing effects during multilayer growth. The Co/Pt multilayer was sputter-deposited onto the resist mask ($\approx$160 nm thick) created by

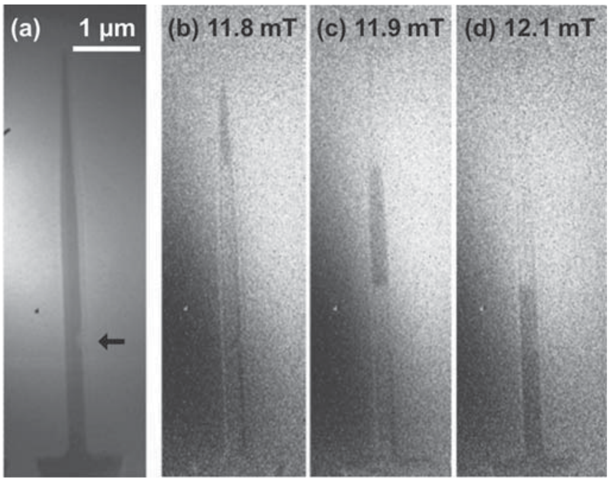

FIG. 2. (a) Transmission x-ray micrograph and (b) through (d) corresponding differential images (the respective previous image serves as reference) of a $\mathrm{Pt}(5.0\,\mathrm{nm})/[\mathrm{Co}(0.7\,\mathrm{nm})/\mathrm{Pt}(2.0\,\mathrm{nm})] \times 4$ wire with a nucleation pad (bottom, not completely visible), a notch marked by the arrow in (a), and a triangular-pointed end (top) recorded at the given field values after saturation at -200 mT.

electron-beam lithography. Since for magnetron sputtering the diameter of the source is comparable to its distance to the sample, shadowing by the sample morphology has to be taken into account. In case of the bottom-up approach used, the amount of deposited material locally varies and depends on the lateral distance to the edges of the resist mask. In particular, at the triangular-pointed end, less material reaches the substrate compared to the straight wire segment. The same holds true for geometrical constrictions such as notches. A schematic representation of a straight wire with a triangular-pointed end is shown in Fig. 1(b). The left hand side of the figure depicts the lateral geometry, while the wire's cross-section is sketched on the right. Since Co and Pt are deposited at the same angle towards the sample surface and from the same distance under the same conditions, the ratio of Co and Pt thicknesses in the multilayer stack is unaffected by the reduction of film thickness towards the triangular-pointed wire end. It can be assumed that the saturation magnetization M_s remains basically constant down to very thin layer thicknesses.[38,39] What is left as a changing property is the magnetocrystalline anisotropy constant $K_1 = K_{1,eff} + \mu_0 M_s^2/2$ which for the present system mainly originates from interface contributions. We consider a continuous reduction of the anisotropy constant K_1 towards the triangular-pointed end of a tip, as well as in other regions where less material is deposited, to be the origin for the reduction of the nucleation field.[40] There are two reasons for the reduction of the anisotropy of the Co/Pt multilayer due to shadowing effects. The first reason is the gradual reduction of the thickness of the Co layer as below $t_{Co} \lesssim 0.5\,\text{nm}$ the first order anisotropy constant $K_{1,eff}$ decreases with decreasing t_{Co}.[41] This behavior is in accordance with other studies, see, e.g., Refs. 42 and 43. The second reason for the gradual reduction of the anisotropy constant is connected with the thickness of the Pt interlayer. When it falls below $t_{Pt} \approx 2\,\text{nm}$, we observe a decrease of the anisotropy for our multilayer system.[32] This is in agreement with previous results.[44,45] Consequently, a gradual reduction in perpendicular magnetic anisotropy occurs in the regions where the Co- and Pt-layer thicknesses are gradually reduced due to shadowing effects. As discussed in Section IV it is confirmed by micromagnetic simulations that the reduction of the nucleation field for wires with triangular-pointed ends can indeed be caused by such a reduced anisotropy.

Shadowing effects not only change the anisotropy but also induce defects. Thus, they do not only affect domain nucleation but also the pinning of domain walls. We observe that in wires with periodic lateral modulations domain walls get pinned both at the transitions from wide to narrow and from narrow to wide regions (not shown). Here, the mechanism responsible for pinning is presumably not an increase in domain-wall energy when entering a wider segment, but connected with defects and gradients of the anisotropy in the multilayer due to variations in the layer thicknesses caused by shadowing of the resist mask. Consequently, it has to be cross-checked whether lateral geometrical variations, such as notches or anti-notches, or above mentioned effects caused by shadowing are responsible for pinning. In the latter case, the preparation has to be performed with particular care. The aspect of domain-wall pinning remains a major issue in the field of perpendicularly magnetized media, which shall not be addressed further in this paper, where the focus lies on the nucleation of domain walls.

The dependence of the nucleation field on the wire geometry was studied in detail for three different widths of nanowires, namely, 320 nm, 430 nm, and 570 nm. For increasing tip-opening angles, the total length of a wire decreases from 28 μm to 20 μm. The reason for this is that the volume of the wires was kept constant for the different geometries in order to exclude a variation of the switching fields due to a change of the number of volume defects.[46,47] Figure 3(a) exemplarily depicts scanning electron micrographs of wire ends with different tip-opening angles. Switching fields were determined by transmission x-ray microscopy. After saturation at an out-of-plane field of about -200 mT, a reverse field was applied and increased in steps of $+1.1$ mT. In the field of view of the microscope, which has a diameter of 10 μm, about half of the total length of the wires could be imaged. Pinning of domain walls was never observed. Thus, it can be assumed that nucleation field and switching field are the same or close within the uncertainty of a field step of 1.1 mT.

Figure 3(b) depicts the average switching field as a function of the tip-opening angle θ determined from nine field sweeps for each data point. For all three wire widths, the same behavior is observed. The switching fields of wires with a flat end scatter around $(+18.5 \pm 0.5)$ mT. For decreasing angle θ, the switching field decreases to a value of $(+7.9 \pm 0.6)$ mT for $\theta = 2.5°$. This corresponds to a reduction of the nucleation field by (57 ± 5)%. The fact that there is no influence of the wire width on the switching field

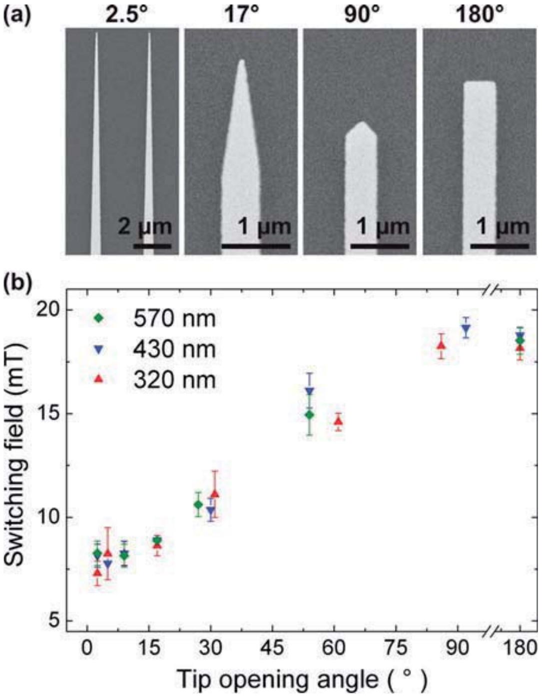

FIG. 3. (a) Scanning electron micrographs of wires with various opening angles of the tip's end. (b) Switching field versus tip-opening angle determined by transmission x-ray microscopy for three different widths of nanowires.

indicates that nucleation takes place in a volume of the tip end that is provided independently of the tip's length, which increases with increasing width of the wires. That the nucleation takes place in the tip area is in complete agreement with the XMCD images presented in Fig. 2. As stated above, the reduction of the nucleation field is assumed to originate from a decrease of the local anisotropy constant in the tip area due to shadowing during sputter deposition of the multilayer.

Before presenting the results of micromagnetic simulations that support this hypothesis, the impact of the experimental results shall be discussed. The possibility to reliably control the nucleation field shows that the bottom-up microfabrication approach used is worth being pursued. One further advantage of this preparation method is that it is based on a single lithography step. This distinguishes it from other methods that require a second preparation step to diminish the nucleation field, for example, local ion irradiation. A possible disadvantage of the bottom-up approach used is that shadowing effects do not only cause a modulation of the multilayer stack along the axis of a wire due to triangular-pointed ends. At all edges of a wire, the multilayer does not end abruptly but the thickness gradually decreases on the way to the edge according to the scheme of Fig. 1(a). The alternative patterning approach is to deposit the magnetic film first, to employ lithography with a negative resist, and to pattern the nanowires top-down by etching. Besides the disadvantage of more steps of sample preparation in the top-down approach, also the problem of edge damage cannot be excluded with this method. It has been shown by Shaw *et al.* that even small variations in the edge properties can completely change the reversal behavior of perpendicularly magnetized nanostructures.[48] Furthermore, possible damage of the entire multilayer system[24] can occur during etching if the film is only protected by a resist mask and not, for example, by a titanium layer.[25] Anyway, with the bottom-up approach pursued in this work we can be sure that the multilayer stack is not significantly modified in the center of the wires compared to the pristine film, which can be concluded from the fact that rectangular wires with flat wire ends of arbitrary width exhibit the same switching field.

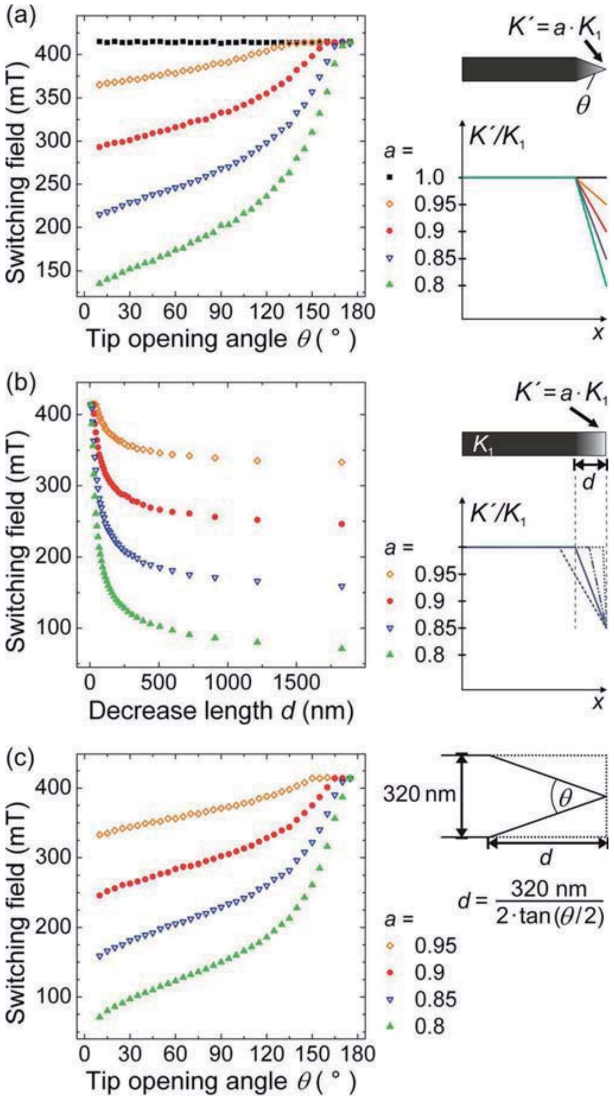

FIG. 4. (a) Dependences of the switching field on the opening angle θ of the tip simulated for a wire with homogeneous anisotropy (black squares) as well as for wires with a linear reduction of the local anisotropy constant in the tip area from K_1 to $K' = a \cdot K_1$ (other color) as sketched on the right hand side. (b) Dependence of the switching fields on the total reduction of the anisotropy constant K' along the decrease length d simulated for rectangular-shaped wires. (c) Same data as in (b) plotted versus tip-opening angle θ that corresponds to a certain decrease length d as illustrated on the right hand side.

IV. MICROMAGNETIC SIMULATIONS

To study the influence of both the anisotropy variation and the tip geometry on the switching field, micromagnetic simulations were performed. The width of the wires in the simulations was taken as 320 nm in accordance with one type of wires studied in the experiment. The local anisotropy constant was reduced linearly in the tip area from the maximum value K_1 to $K' = a \cdot K_1$ at the very end as sketched on the right hand side of Fig. 4(a). The total reduction of the local anisotropy constant was varied between zero ($a = 1.0$, $K'_{1,\mathit{eff}} = 350\,\mathrm{kJ/m^3}$) and 20% ($a = 0.8$, $K'_{1,\mathit{eff}} = 34\,\mathrm{kJ/m^3}$). At an anisotropy reduction of $a = 0.78$, the spin-reorientation transition to in-plane anisotropy occurs. Figure 4(a) depicts the switching field simulated for wires with tip-opening angles θ between 10° and 175°. For a homogeneous anisotropy constant ($a = 1.0$, black squares), the geometry does not influence the switching field. Besides a reduction of the switching field, the same behavior is found for lower values of a homogeneous anisotropy constant down to $0.8\,K_1$ (not shown). This demonstrates that the reduction of the nucleation field reported above cannot be explained via the different opening angles of the tips. If we assume that the anisotropy constant is locally reduced in the range of the tips, we obtain a reduction of the switching field with decreasing tip-opening angle θ. This dependence is most pronounced for the highest reduction of K'. It is thus the amount of material with reduced anisotropy that determines the switching field. For an angle $\theta = 10°$, the maximum value of the switching field (that is $H_{\max} = 415\,\mathrm{mT}$ for flat wire ends) is reduced by 12%, 29%, 48%, and 67% for anisotropy reductions of 5%, 10%, 15%, and 20%, respectively. The simulated curves vary not only in the absolute reduction of the switching fields but also in the critical tip-opening angle at which the reduction sets in. While for $a = 0.95$ the switching field stays constant down to $\theta = 130^\circ$, it drops below the maximum value already at $\theta = 155^\circ$ for $a = 0.9$. The experimental values depicted in Fig. 3(b) stay constant for large angles as well and start to decrease somewhere between $\theta = 85^\circ$ and $\theta = 75^\circ$. While this behavior corresponds to a reduction of the local anisotropy constant at the wire end of less than 5%, the relative decrease of the nucleation field in our sample rather implies a reduction of about 18%.

The experimental data show a nearly perfect linear dependence on the tip-opening angle θ up to 90° in accordance with the simulations. For higher angles, the experimental nucleation field remains constant, while a strengthened increase is found in the simulations. A possible explanation for this discrepancy is that shadowing effects during sputter deposition lead to a continuous reduction of the film thickness at all edges of the wires, while in the simulation abrupt edges are assumed. The gradual decay of the film thickness at the wire edges means that there is a gradual reduction of the anisotropy constant for all wires independent of the tip-opening angle. At sharp tips, the regions of both edges where the anisotropy decreases can overlap causing an anisotropy reduction in the whole tip area. For blunt tips, this effect is strongly reduced and the influence on the switching field is fading away. The experimental results therefore indicate that the reduction of the anisotropy constant is localized at the edges in contrast to the simulations where the anisotropy is taken as reduced in the whole tip region. This probably leads to a “saturation” of the increase of the nucleation field at $\theta \approx 90^\circ$ in the experiment, since the gradual reduction of the film thickness at all edges has the same effect as the gradual reduction of the film thickness in the triangular-pointed ends when the tip-opening angle exceeds a critical value.

To further investigate the influence of the wire’s geometry on the nucleation field, additional simulations have been performed. Instead of having one triangular-pointed end, nanowires were designed with two flat ends. Nevertheless, the anisotropy constant was reduced linearly at one end of the wire. Thereby the distance d over which the anisotropy decreases, corresponds to the length of a tip with a certain opening angle as sketched on the right hand side of Fig. 4(c). Figures 4(b) and 4(c) reveal that the switching fields show the same dependences but are stronger reduced in comparison to the switching fields of nanowires with triangular-pointed ends (compare Fig. 4(a)). This finding qualitatively shows that nucleation depends on the total area with reduced anisotropy constant, as in nanowires with flat ends this area is much larger than in nanowires with triangular-pointed ends. In particular, the region at the wire end, where the anisotropy constant is lowest, is significantly reduced in nanowires with triangular-pointed ends, compare sketch in Fig. 4(c). Rectangular wires with a comparable linear reduction of the local anisotropy constant over the same decrease length d (and the corresponding tip-opening angle θ) thus provide a larger area for a certain nucleation volume to reverse and consequently have lower switching fields. With the same arguments, it can be explained why the switching field depends on the opening angle θ in wires with triangular-pointed ends: the smaller θ, the larger is the tip area available for nucleation.

V. CONCLUSION

We have shown that the critical field for the nucleation and injection of domain walls in Co/Pt nanowires can be tuned and reduced by up to about 60% compared to the switching field of rectangular-shaped wires by designing triangularly pointed wire ends. The reasoning is based on the reduction of the perpendicular magnetic anisotropy within the tip region that is caused by shadowing effects during sputter deposition of the multilayer. As confirmed by micromagnetic simulations the reduction of the local anisotropy constant accompanied by an increase of the nucleation area in sharper tips accounts for the effect observed. A low nucleation field is a necessary prerequisite for the preparation of domain walls at comparably weak pinning sites as it is of interest for fundamental studies and applications.

ACKNOWLEDGMENTS

The authors gratefully acknowledge financial support by the Deutsche Forschungsgemeinschaft via the Graduiertenkolleg 1286 and the Sonderforschungsbereich 668. The operation of the x-ray microscope is supported by the Director, Office of Science, Office of Basic Energy Sciences, of the U.S. Department of Energy under Contract No. DE-AC02-05-CH11231.

[1] P. S. Ho and T. Kwok, Rep. Prog. Phys. **52**, 301 (1989).
[2] O. Boulle, G. Malinowski, and M. Kläui, Mater. Sci. Eng. R **72**, 159 (2011).
[3] G. Tatara and H. Kohno, Phys. Rev. Lett. **92**, 086601 (2004).
[4] J. Xiao, A. Zangwill, and M. D. Stiles, Phys. Rev. B **73**, 054428 (2006).
[5] P. Gambardella and I. M. Miron, Philos. Trans. R. Soc. London, Ser. A **369**, 3175 (2011).
[6] P. P. J. Haazen, E. Murè, J. H. Franken, R. Lavrijsen, H. J. M. Swagten, and B. Koopmans, Nature Mater. **12**, 299, (2013).
[7] M. Hayashi, L. Thomas, C. Rettner, R. Moriya, X. Jiang, and S. S. P. Parkin, Phys. Rev. Lett. **97**, 207205 (2006).
[8] S. Hankemeier, A. Kobs, R. Frömter, and H. P. Oepen, Phys. Rev. B **82**, 064414 (2010).
[9] S. S. P. Parkin, M. Hayashi, and L. Thomas, Science **320**, 190 (2008).
[10] O. Boulle, J. Kimling, P. Warnicke, M. Kläui, U. Rüdiger, G. Malinowski, H. J. M. Swagten, B. Koopmans, C. Ulysse, and G. Faini, Phys. Rev. Lett. **101**, 216601 (2008).
[11] L. S. E. Alvarez, K. Y. Wang, S. Lepadatu, S. Landi, S. J. Bending, and C. H. Marrows, Phys. Rev. Lett. **104**, 137205 (2010).
[12] M. Cormier, A. Mougin, J. Ferré, A. Thiaville, N. Charpentier, F. Piechon, R. Weil, V. Baltz, and B. Rodmacq, Phys. Rev. B **81**, 024407 (2010).
[13] C. Hassel, M. Brands, F. Y. Lo, A. D. Wieck, and G. Dumpich, Phys. Rev. Lett. **97**, 226805 (2006).
[14] A. Aziz, S. J. Bending, H. G. Roberts, S. Crampin, P. J. Heard, and C. H. Marrows, Phys. Rev. Lett. **97**, 206602 (2006).
[15] J. H. Franken, M. Hoeijmakers, H. J. M. Swagten, and B. Koopmans, Phys. Rev. Lett. **108**, 037205 (2012).
[16] A. Kobs, S. Hesse, W. Kreuzpaintner, G. Winkler, D. Lott, P. Weinberger, A. Schreyer, and H. P. Oepen, Phys. Rev. Lett. **106**, 217207 (2011).
[17] A. Kobs, S. Hesse, H. P. Oepen, and P. Weinberger, Philos. Mag. **92**, 2835 (2012).
[18] J.-C. Lee, C.-H. Hsieh, C.-C. Chang, L.-W. Huang, L.-K. Lin, and S.-F. Lee, J. Appl. Phys. **113**, 17C714 (2013).

[19] R. P. Cowburn, D. A. Allwood, G. Xiong, and M. D. Cooke, J. Appl. Phys. **91**, 6949 (2002).

[20] M.-Y. Im, L. Bocklage, P. Fischer, and G. Meier, Phys. Rev. Lett. **102**, 147204 (2009).

[21] A. Vogel, S. Wintz, J. Kimling, M. Bolte, T. Strache, M. Fritzsche, M.-Y. Im, P. Fischer, G. Meier, and J. Fassbender, IEEE Trans. Magn. **46**, 1708 (2010).

[22] K. J. Kirk, J. N. Chapman, and C. D. W. Wilkinson, Appl. Phys. Lett. **71**, 539 (1997).

[23] T. Schrefl, J. Fidler, K. J. Kirk, and J. N. Chapman, J. Magn. Magn. Mater. **175**, 193 (1997).

[24] N. Bardou, B. Bartenlian, C. Chappert, R. Mégy, P. Veillet, J. P. Renard, F. Rousseaux, M. F. Ravet, J. P. Jamet, and P. Meyer, J. Appl. Phys. **79**, 5848 (1996).

[25] F. Fournel, Y. Chen, F. Carcenac, N. Essaidi, H. Launois, V. Kottler, and C. Chappert, IEEE Trans. Magn. **34**, 1027 (1998).

[26] T. Ono, H. Miyajima, K. Shigeto, K. Mibu, N. Hosoito, and T. Shinjo, J. Appl. Phys. **85**, 6181 (1999).

[27] J. Fassbender, D. Ravelosona, and Y. Samson, J. Phys. D: Appl. Phys. **37**, R179 (2004).

[28] L. S. E. Alvarez, G. Burnell, C. H. Marrows, K.-Y. Wang, A. M. Blackburn, and D. A. Williams, J. Appl. Phys. **101**, 09F508 (2007).

[29] D. Chiba, G. Yamada, T. Koyama, K. Ueda, H. Tanigawa, S. Fukami, T. Suzuki, N. Ohshima, N. Ishiwata, Y. Nakatani, and T. Ono, Appl. Phys. Express **3**, 073004 (2010).

[30] Silicon-nitride membranes were purchased from Silson Ltd., UK.

[31] As resist PMMA A4 from MicroChem was used.

[32] H. Stillrich, C. Menk, R. Frömter, and H. P. Oepen, J. Appl. Phys. **105**, 07C308 (2009).

[33] P. Fischer, Mater. Today **13**, 14 (2010).

[34] C. T. Chen, F. Sette, Y. Ma, and S. Modesti, Phys. Rev. B **42**, 7262 (1990).

[35] See http://micromagnum.informatik.uni-hamburg.de; The simulation parameters are $K_1 = 1.58 \times 10^6\,\mathrm{J/m^3}$, $M_s = 1.4 \times 10^6\,\mathrm{A/m}$, and exchange constant $A = 30 \times 10^{-12}\,\mathrm{J/m}$. The magnetic anisotropy K_1 of the Co/Pt multilayer was determined experimentally from a hard-axis remagnetization curve probed with magneto-optical Kerr-effect[32] using $K_{1,\mathrm{eff}} = (350 \pm 30)\,\mathrm{kJ/m^3} = K_1 - \frac{\mu_0 M_s^2}{2}$. A high Gilbert damping parameter of $\alpha = 0.1$ was chosen in order to avoid unrealistic dynamic effects as the field in the experiment is reduced slowly compared to the micromagnetic time-scale.

[36] H. Kronmüller, Phys. Status Solidi B **144**, 385 (1987).

[37] H. Kronmüller and S. S. P. Parkin, *Handbook of Magnetism and Advanced Magnetic Materials* (John Wiley & Sons, 2007).

[38] Z. S. Shan, J. X. Shen, R. D. Kirby, D. J. Sellmyr, and Y. J. Wang, J. Appl. Phys. **75**, 6418 (1994).

[39] G. Schütz, R. Wienke, W. Wilhelm, W. B. Zeper, H. Ebert, and K. Spörl, J. Appl. Phys. **67**, 4456 (1990).

[40] T. Gerhardt, A. Drews, and G. Meier, J. Phys.: Condens. Matter **24**, 024208 (2012).

[41] H. Stillrich, C. Menk, R. Frömter, and H. P. Oepen, J. Magn. Magn. Mater. **322**, 1353 (2010).

[42] W. B. Zeper, F. J. A. M. Greidanus, P. F. Carcia, and C. R. Fincher, J. Appl. Phys. **65**, 4971 (1989).

[43] M. Kisielewski, A. Maziewski, M. Tekielak, J. Ferré, S. Lemerle, V. Mathet, and C. Chappert, J. Magn. Magn. Mater. **260**, 231 (2003).

[44] C.-J. Lin, G. L. Gorman, C. H. Lee, R. F. C. Farrow, E. E. Marinero, H. V. Do, H. Notarys, and C. J. Chien, J. Magn. Magn. Mater. **93**, 194 (1991).

[45] R. L. Stamps, L. Louail, M. Hehn, M. Gester, and K. Ounadjela, J. Appl. Phys. **81**, 4751 (1997).

[46] T. Thomson, G. Hu, and B. D. Terris, Phys. Rev. Lett. **96**, 257204 (2006).

[47] J. W. Lau, R. D. McMichael, S. H. Chung, J. O. Rantschler, V. Parekh, and D. Litvinov, Appl. Phys. Lett. **92**, 012506 (2008).

[48] J. M. Shaw, S. E. Russek, T. Thomson, M. J. Donahue, B. D. Terris, O. Hellwig, E. Dobisz, and M. L. Schneider, Phys. Rev. B **78**, 024414 (2008).

8 Conclusion

Magnetization reversal in cylindrical nickel nanowires has been studied both experimentally and by micromagnetic simulations. Switching fields determined by magnetoresistance measurements, magnetic force microscopy, and magneto-optical Kerr-effect magnetometry were compared with analytical predictions based on the curling model together with the results of other groups. It was found that the behavior of our wires that were electrochemically synthesized in the group of Kornelius Nielsch at the Institute of Applied Physics, University of Hamburg, is comparable to the one of others. The switching fields as well as the effective anisotropy calculated assuming magnetization reversal in an infinite cylinder tend to increase with decreasing diameter of the wires. The large scattering of the experimental values can likely be attributed to defects as well as to variations of the saturation magnetization and the effective anisotropy from wire to wire. Reasons for the latter are varying contributions of the shape anisotropy that has to compete with additional anisotropy contributions. These additional anisotropy contributions mainly originate from a non-negligible magnetocrystalline anisotropy combined with variations in the crystalline structures. Further indications for the existence of multiple anisotropy contributions and thereby even of multiple anisotropy axes are asymmetric angular dependencies of the switching field and shifts of up to (6 ± 2) degrees between the axis of a wire and the experimentally determined symmetry axis found for some wires.

The complexity of magnetization reversal that became apparent based on the analysis of switching fields was underlined by the direct insight into the magnetization patterns of nickel nanowires provided by methods that allow for magnetic imaging. In contrast to micromagnetic simulations, where nucleation occurs at the wire ends and - if present - at diameter modulations, magnetic force microscopy and photoemission electron microscopy (PEEM) reveal that domain nucleation can occur at arbitrary positions in a wire. We observe a curling of the magnetization along the entire wire axis rather than at the wire ends only. This explains the drop of resistivity at remanence. Not considering the magnetocrystalline anisotropy when applying analytical models was already taken flak by Aharoni [Aha99]. His criticism is clearly supported by this work. The applicability of the curling model was discussed in detail and is called into question by both our experimental and simulated results.

Stochastic scattering of switching fields around multiple accumulation values, each of which has its characteristic switching-field distribution, as well as magnetic force micrographs indicate that the reversal process in cylindrical nickel nanowires can take place via miscellaneous paths. This is characteristic for magnetization reversal through domain-wall motion. The idea of magnetization reversal based on the nucleation, depinning, and propagation of domain walls is supported by the angular dependence of the switching field being proportional to $1/\cos\theta$, where θ is the angle between the applied magnetic field and the wire axis.

In straight wires domain-wall pinning can occur at intrinsic defects. The pinning probability was found to increase with θ. This aspect is of interest when it comes to the intended pinning of domain walls. It was demonstrated that domain walls can be moved back and forth from one pinning site to another by an externally applied field.

For the controlled preparation of domain walls in cylindrical wires three methods were tested: local ion irradiation, application of an external field at a bent wire, and modulations of the cylinder diameter.

It was found that the manipulation of nickel nanowires with a focused Ga^+ ion beam is not suited to tailor pinning sites. The method rather decreases the field at which domain walls are injected into a wire by about 10 percent. This feature can be employed when it comes to the preparation of domain walls at other pinning sites, since lower injection fields increase the chance to observe pinning.

Applying a field at a bent wire is a dependable method that enables one to select between the preparation of tail-to-tail and head-to-head domain walls. Assuming that the domain walls prepared adopt the spin structure of transverse domain walls we found indications for the selectability of the chirality of a domain wall that does not change during the field-driven propagation of the wall.

In wires with one modulation of the cylinder diameter the thicker wire segment takes over the function of an injection pad in planar soft-magnetic wires. Several domain walls could reproducibly be prepared at intrinsic pinning sites in the thin segment by driving minor field sweeps, but no reliable pinning at modulations with aspect ratios up to four was found in wires with a single modulation. The synthesis approach of electrochemical deposition into alumina templates allows for the preparation of several diameter modulations. To enforce that domain walls have to pass from a thin towards a thicker segment, dumbbell-shaped wires were synthesized. It could be demonstrated both experimentally and through micromagnetic simulations that domain walls stop their propagation when approaching a modulation from a thin towards a thicker segment. A model based on magnetic charges was proposed that accounts for the observed behavior and explains what is confirmed by micromagnetic simulations: while the exact shape of a modulation is of minor importance, the force experienced by a domain wall is determined by the aspect ratio of a modulation. Now that a reliable method for the preparation of domain walls at pinning sites of tunable strength is found, the critical fields and currents that depin a domain wall can be studied. In principle, such experiments will allow for the determination of the effective mass of a domain wall in cylindrical wires [Sai04].

The complexity of the magnetic behavior found in electrochemically synthesized nickel wires imposes a stochastic nature on the nucleation, pinning, and propagation of domain walls that is undesirable with respect to applications. It can likely be reduced by fabricating either single-crystalline wires or wires of a material with negligible magnetocrystalline anisotropy such as nickel-iron or nickel-cobalt alloys of appropriate composition stoichiometry [Veg12]. A challenge will be the homogeneous concentration of the alloys across modulations. Another approach to obtain more simple domain patterns is the use of thinner wires or of structures that do not enforce a singularity of the magnetization, namely tubes.

Since the magnetic patterns observed appear to be a foot print of each particular wire, it is desirable to characterize the same wire by various methods. We suggest in-situ magnetoresistance measurements during PEEM imaging. Suited substrates, for example silicon wafers with a silicon-nitride coating, can be locally etched from the rear side leaving a suspended wire or a wire on a thin membrane allowing for high-resolution transmission-electron microscopy imaging. This approach will enable one to study the magnetization reversal and the crystalline structure of the same wire.

As clarified in this thesis, the detailed inspection of nanomagnets, like it is provided by our novel PEEM method, is indispensable for a fundamental understanding of the magnetization reversal processes. The method was developed at the synchrotron light source BESSY II in Berlin, Germany, and bases on conventionally surface-sensitive photoemission electron microscopy. Its capability for the investigation of complex nanostructures is demonstrated in publication [Kim11]. Recording both the electrons emitted directly from the surface of a nanoobject as well as the ones bounced out of the substrate by the transmitted x rays in the object's shadow, surface and bulk contributions can be probed separately. Element specificity enables one to individually image the magnetic states of composite nanomagnets, in this case iron-oxide tubes and enclosed nickel cores, even if components are buried deeper than the mean-free path of photoelectrons. Separate switching of the two coaxial nanomagnets was successfully demonstrated. The possibility to take images in magnetic fields, a potential spatial resolution of a few nanometers, and the option to implement time resolution in the picosecond range open new avenues for the study of complex three-dimensional nanomagnets.

The last chapter of this work includes publication [Kim13] and deals with domain nucleation and pinning of domain walls in Co/Pt multilayer wires patterned by electron-beam lithography, sputter deposition, and lift-off processing. The magnetization reversal of the nanowires was imaged by transmission x-ray microscopy at the Advanced Light Source in Berkeley, CA, USA. It was found that the nucleation field in these structures with perpendicular magnetic anisotropy can be tuned by changing the geometry of the wire ends. A reduction of the nucleation field by up to 60 percent is achieved when the wire ends are designed as triangular tip. In order to clarify the origin of the reduction of the nucleation field micromagnetic simulations were employed. The effect cannot be explained by the geometry variation alone, but is attributable to a local reduction of the perpendicular anisotropy caused by shadowing of the resist mask during sputter deposition of the multilayer. Our findings lay the foundation for the reliable preparation of domain walls at comparably weak pinning sites as they are desirable for current-driven experiments, since they enable one to inject domain walls into perpendicularly magnetized wires at the smallest possible fields. What remains is to find a reliable pinning site. In wires prepared by sputter deposition and lift-off processing, lateral modulations are not suited for this purpose, since pinning rather occurs at defects induced by thickness variations. It seems reasonable to prepare straight wires with triangular-pointed ends first, and to create pinning sites in an additional step. Promising methods for the latter are, for example, locally applied stray fields [Met09, O'B11] and local ion irradiation [Fas08, Fra12a], to mention a few. The feasibility of reliable domain-wall pinning at magnetic soft spots created by the implantation of chromium ions in permalloy nanowires was demonstrated in publication [Vog10].

In the frame of this work a variety of experimental methods was applied to gain new insights into the magnetization reversal in different kinds of ferromagnetic nanowires. Through the synergy of experiments, analytical models, and micromagnetic simulations, a profound understanding of the nucleation and the pinning of domain walls could be obtained. This lays the basis for systematic studies of domain-wall dynamics in these nanostructures as well as for potential future applications.

A Publications

A.1 Magnetic reversal of cylindrical nickel nanowires with modulated diameters

Publication [Pit11]

MAGNETIC REVERSAL OF CYLINDRICAL NICKEL NANOWIRES
WITH MODULATED DIAMETERS

by

Kristina Pitzschel, Julien Bachmann, Stephan Martens, Josep M.
Montero-Moreno, Judith Kimling, Guido Meier, Juan Escrig,
Kornelius Nielsch, and Detlef Görlitz

published in

Journal of Applied Physics **109**, 033907 (2011).

JOURNAL OF APPLIED PHYSICS **109**, 033907 (2011)

Magnetic reversal of cylindrical nickel nanowires with modulated diameters

Kristina Pitzschel,[1] Julien Bachmann,[1,a)] Stephan Martens,[1] Josep M. Montero-Moreno,[1]
Judith Kimling,[1] Guido Meier,[1] Juan Escrig,[2] Kornelius Nielsch,[1] and Detlef Görlitz[1]
[1]*Institute of Applied Physics, University of Hamburg, 20355 Hamburg, Germany*
[2]*Departamento de Física, Universidad de Santiago de Chile (USACH), Avda. Ecuador 3493,*
9170124 Santiago, Chile and Center for the Development of Nanoscience and Nanotechnology (CEDENNA),
9170124 Santiago, Chile

(Received 20 July 2010; accepted 12 December 2010; published online 3 February 2011)

Anodic alumina membranes with modulated pore diameters serve as template for the preparation of magnetic nanowires. Filling the pores with Ni by electrodeposition delivers wires replicating the variation in modulation in pore diameter from 80 to 160 nm. Such structures are of interest for the observation and control of magnetic domain wall motion. Single-object characterization utilizing the magneto-optical Kerr effect magnetometry evidences a strong correlation between geometric parameters and magnetic properties. Ensemble magnetization measurements with a superconducting quantum interference device show the effect of dipolar interactions. Analytical models can reproduce the lowering of coercivity due to the presence of enhanced stray fields within the array. Magnetic force microscopy at individual wires indicates the presence of a strong stray field in the vicinity of the diameter change. The preparation technique demonstrates a mass production method of nano-objects with designed geometric irregularities, which could be used to control the motions of magnetic domain walls. © *2011 American Institute of Physics*. [doi:10.1063/1.3544036]

I. INTRODUCTION

The controlled motions of magnetic domain walls would allow for the implementation of a novel data storage platform, that is, more robust and less energy-intensive than current hard disk drives, which base on the internal magnetization of Weiss domains.[1] The physical basis for this type of storage for the controlled manipulation of a large number of domain boundaries, however, has not been completly laid down to date. The basic experimental approach amounts in the definition of elongated submicron structures (wires) with geometrical features defined so as to either nucleate a domain wall or block (pin) its propagation at well-defined positions. Electron (e) beam lithography has been the most widely used preparative method to this goal, as it enables one to arbitrarily define notches or wire diameter changes as pinning centers.[2,3] However, e-beam lithography is a serial technique and limited to the definition of one nanostructure at a time. Additionally because it bases on structuring of a thin film, it is limited to generating wires of quadrangular cross-section. We have developed a general preparative strategy toward large numbers ($>10^8$) of cylindrical metal nanowires arranged in two-dimensional arrays and in which diameter modulations can be introduced at arbitrarily defined positions.

We base our work on the large body of literature dealing with the electrodeposition of magnetic wires in porous templates such as anodic alumina.[4–14] In this approach, (i) the utilization of a nanoimprinted, perfectly ordered anodic alumina membrane as a porous template defines length and diameter of the wires as well as their hexagonal order and (ii) the conformal filling of the cylindrical pores with magnetic substances by electrodeposition furnishes large numbers of objects in a simple procedure. In order to investigate the pinning of domain walls, diameter modulations can be introduced in this framework by combining the so-called "hard" and "mild" conditions for the electrochemical formation of the template, or anodization. A hard anodization is obtained when the voltage applied lies beyond the maximal value allowed for a stable mild procedure, which is more conventional. Hard porous alumina membranes are characterized by a smaller ratio between pore diameter and interpore distance: this is the characteristic utilized here.[15,16] Electrodeposition is used subsequently for the growth of metallic wires that replicate the diameter modulations defined in the template. As a proof of concept, we created modulated nickel nanowire arrays. This paper reports on their magnetic properties. At first, individual nanowires are investigated at the single-object level by spatially resolved magneto-optical Kerr effect (MOKE) magnetometry. Second, the wires are presented in organized arrays by ensemble superconducting quantum interference device (SQUID) measurements. At each step, a theoretical treatment sheds light on the relevant physical phenomena—at first, the influence of the diameter modulations, and then, the effect of dipolar interactions with neighboring magnets. The stray fields causing these interactions are evidenced by magnetic force microscopy (MFM).

II. PREPARATION

The procedure for the fabrication of the perfectly ordered Al_2O_3 nanopore arrays has been previously described.[17] Aluminum chips (99.999% from Goodfellow) were electropolished, a stamp with hexagonally ordered SiN pyramids and period of 235 nm was used to imprint the Al chips with a commercial hydraulic press under ≈ 9 tons/mm^2. The porous anodic alumina membrane is

---

[a)] Electronic mail: julien.bachmann@physik.uni-hamburg.de.

0021-8979/2011/109(3)/033907/6/$30.00

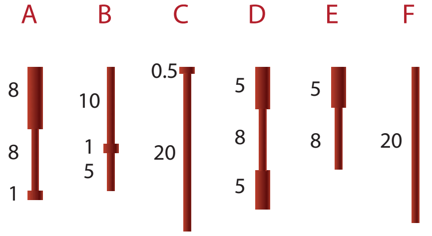

FIG. 1. (Color online) Schematic representation of the wire geometries investigated in this work: the individual segments are drawn on a common scale, their lengths are written in micrometers.

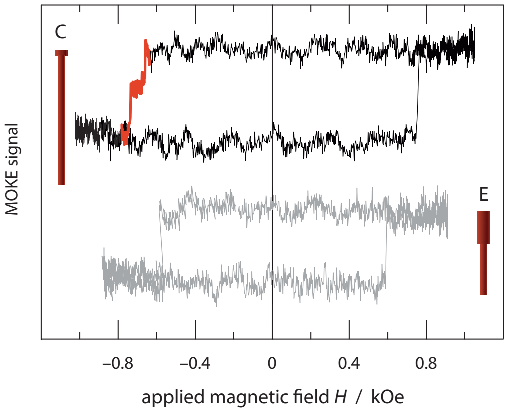

FIG. 3. (Color online) Single-wire magneto-optical (MOKE) hysteresis loops of two different modulated wires. One of them display more than one reversal event whereas the second wire (gray) reverses in a single step.

produced in several anodization steps. The applied voltages must be tuned to match the lithographically defined period. First, mild anodization is performed under 72 V in 0.4 M aqueous H_3PO_4 at 10 °C. Second, the hard segments are anodized under 93 V in 0.15 M $H_2C_2O_4$ at −5 °C in a water/ethanol mixture (H_2O:EtOH 4:1).[18] The different porosities obtained from the mild and hard anodizations at fixed periodicity amount to the formation of distinct diameter values for the individual segments. The nanowires are made of electrodeposited Ni. The series of wires (length $L \approx 1-40$ μm, radius $R=40-80$ nm, center-to-center distance $D=235$ nm) are prepared by electrodeposition in a porous alumina matrix. To prepare the template for electrodeposition, the so-called barrier layer of aluminum oxide closing the extremities of the pores is first removed by reactive ion etching in a CF_4/O_2 plasma. A thin layer of gold ($\approx$20 nm) is then sputtered onto the freshly etched backside of the membrane. The Au film is finally used as an electrode for the galvanostatic deposition of nickel. The Ni wires grow from the gold electrode up to the modulated pores at a typical rate of approximately 1 μm/min (300 g/l $NiSO_4 \cdot 6H_2O$, 45 g/l $NiCl_2 \cdot 6H_2O$, and 45 g/l H_3BO_3; current density roughly 10 mA/cm^2).

In this manner, large arrays ($\approx 10^8$) of parallel objects are obtained with geometric parameters (length, width, and number of modulations) defined at the experimentalist's discretion. Figure 1 displays the various types of wires prepared in this work. The labeling A–F will be followed consistently throughout the paper.

Figure 2 displays a transmission electron micrograph of a Ni wire obtained after release from the alumina matrix in chromic acid. The diameter modulations of the template between values of approximately 90 and 170 nm (±10 nm) are replicated by the magnetic nano-object with high accuracy. The thick central segment corresponds to the mild anodization, and the transition to the thinner section (hard anodization) is 100 nm wide. The samples prepared for magnetic characterization were protected by an extra 5-nm-thick SiO_2 layer deposited onto the alumina pore walls by atomic layer deposition[19] before electrodeposition. This prevents the formation of an antiferromagnetic NiO layer at the surface of isolated wires. In fact, we have not observed a significant difference between the hystereses from ensembles recorded for samples with and without the silica sheath, even though the diameters are reduced by the SiO_2 to 80 and 160 nm (±10 nm). The following measurements were done with samples including a silica sheath.

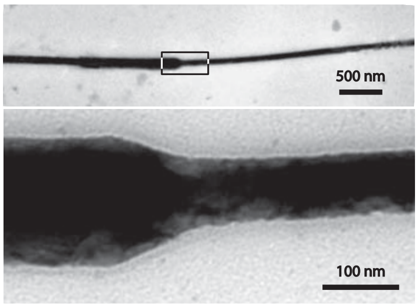

FIG. 2. Transmission electron micrographs of a single modulated Ni wire, isolated from the alumina template by chromic acid etching. Top, low magnification image showing two diameter changes. The area defined by the rectangle is further magnified in the lower panel.

III. PROPERTIES OF ISOLATED NICKEL NANOWIRES

We will first discuss the magnetic properties of a modulated wire as an isolated object—the interactions with neighbors will be considered in the next paragraph. In principle, a magnetic signature can be gleaned from a small amount of material using the MOKE (NanoMOKE™2). To prepare samples for MOKE measurement, the nickel nanowires dissolved from the matrix and suspended in an ethanol solution are dripped onto a Si substrate. The Si substrate carries gold markers fabricated by e-beam lithography, for locating the wires unambiguously. Figure 3 displays the data collected on a single wire consisting of a thick (160 nm diameter) and a thin segment (80 nm): a MOKE signal is measurable when a beam of *p*-polarized light is collimated down to a diameter of 3 μm on a flat Si substrate carrying cast individual Ni wires (after dissolution from the matrix). This is the first instance of MOKE results on cylindrical and modulated wires in this range of diameters. We note, however, that the MOKE signal only originates from the magnetization state of the structure near its surface. The hysteresis curves recorded in a field applied parallel to the wire axis are averaged during the measurement (500 to 1000 times), in order to obtain a better signal to noise ratio. Attention was paid to the fact that the laser spot contained one diameter modulation. Figure 3 displays typical hystereses recorded on individual Ni wires incorporating a change in diameter. Some of them yield two abrupt magnetization reversals on one branch of the hysteresis curve, highlighted in red color in the figure while others give rise to the standard square hysteresis shape typically measured on unmodulated wires. The presence of two distinct reversal events could originate from the pinning of the domain boundary at the diameter change. However, this curve shape may also arise from the addition of purely square individual hysteresis loops with two possible values of the switching field. Additionally, a symmetrical loop with two magnetization changes on both branches is never observed. Those contrasted observations make sense if we consider that domain walls propagating from one extremity of a wire to the other may be pinned by more than one type of irregularity—not only diameter changes but also crystal defects, roughness, and even magnetic impurities possibly present on the silicon substrate. The diameter modulation from 80 to 160 nm within a width of 100 nm in the present wire may not be sufficient to cause pinning on its own in 100% of the cases; a stochastic aspect comes into play, as has been amply documented in the case of wires fabricated by e-beam lithography.[20,21]

We will now use elementary theoretical models to calculate the coercive fields of modulated wires without taking domain wall pinning into account. The agreement with the experiment, or the lack thereof, can then be considered as an indication as to whether domain wall pinning plays a significant role or not. Based on the results of a published analytical model,[22] we consider that the magnetization reversal occurs by the propagation of a transverse (**T**) domain wall, in which a net magnetization component appears in the (x,y) plane (perpendicular to the wire axis). We note that the critical diameter (that is, the diameter at which the system crosses from the transverse domain wall to a vortex wall) depends on the theoretical method used as well as the exact parameters. Contrary to our analytical results,[22] numerical simulations have reached the conclusion that nickel wires of the diameter relevant here but much shorter length should switch through a vortex.[23–25] We will use the **T** mode in this work. It is much simpler to treat analytically, and its energy is quite similar to that of the **V** wall.[26]

For any given radius R of the wire, the coercive field H_c^T can be calculated based on an analytical treatment[27] in which the classical Stoner–Wohlfarth model[28] is adapted considering the width w_T of the domain wall,

$$\frac{H_c^T}{M_0} = \frac{2[K(w_T) - K_\alpha]}{\mu_0 M_0^2}, \tag{1}$$

where $K_\alpha = -1.6 \times 10^4$ J m^{-3} is the anisotropy constant,[29,30] $K(w_T) = \frac{1}{4}\mu_0 M_0^2 [1 - 3N_z(w_T)]$ [with $N_z(w_T)$ the demagnetization factor along z],[31] $M_0 = 4.85 \times 10^5$ A m^{-1}, and $A = 10^{-11}$ J m^{-1}.[32] We can approximate the effective coercive field of our modulated wires as the weighted average of the two H_c values calculated with the two radii involved. The comparison of the H_c values obtained in this manner with the coercive fields determined experimentally (MOKE) shows a systematic error. Figure 4 compares the values calculated in this manner (empty blue circles) with the experimentally determined switching fields (full blue disks). The agreement is acceptable for the wire types labeled E, C, and F (one diameter change or none), given the complexity of the system and the crudity of our approximations. In contrast to this, the value calculated for sample A, which consists of three segments, is off of our one experimental datapoint by a large difference. At this point, we will postpone an interpretation of this phenomenon due to the questionable statistical significance of a single experimental measurement. The study of wire ensembles will in this respect yield more positive evidence.

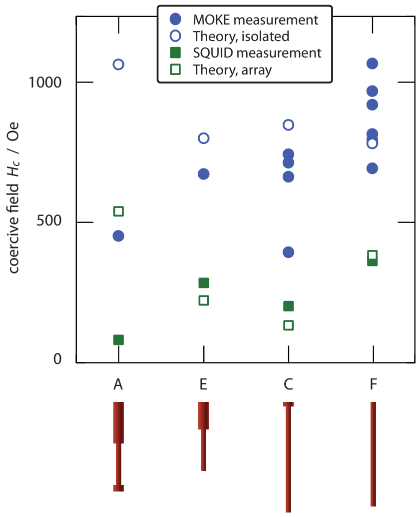

FIG. 4. (Color online) Summary of the coercive fields measured (full symbols) and calculated (empty symbols) for various types of modulated wires as single objects (circles) and ensembles (squares). From left to right the geometry is as sketched: A, thick 8 μm, thin 8 μm, thick 1 μm; E, thick 5 μm, thin 8 μm; C, thick 0.5 μm, thin 20 μm; F, thin 20 μm.

IV. INFLUENCE OF DIPOLAR INTERACTIONS IN NICKEL WIRE ENSEMBLES

When the modulated nanowires are investigated as arrays, interactions with the neighbors come into play.[33–35] Indeed, a hysteresis (SQUID MPMS2 by Quantum Design) loop measured at 300 K (with $\vec{H} \parallel \vec{z}$) on an ensemble of wires containing one short thick section and a long thinner one [geometry E, square symbols of Fig. 5(a)] shows a reduced squareness (remanence 45%) and coercive field (260 Oe) with respect to the single-object measurement for the same geometry (which yields 100% squareness and 670 Oe coercive field). The dipolar interactions, however, do not fully obscure the characteristics of the wires, as can be observed when the SQUID measurement is repeated with $\vec{H} \perp \vec{z}$ (circles). Due to the intrinsic shape anisotropy of the wires, the latter hysteresis yields even lower values of remanence and H_c (8% and 60 Oe, respectively). This fact and the values of H_c are consistent with previous reports on Ni wires without modulations.[36]

Figure 5(b) compares the SQUID hysteresis loops recorded on six samples of Ni wire arrays (labeled A–F) with

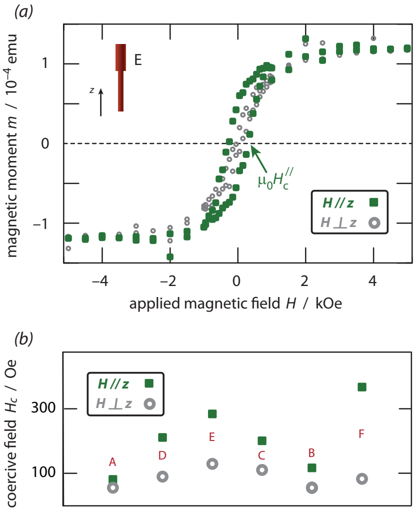

FIG. 5. (Color online) (a) Magnetic hysteresis loops of an array of Ni wires containing one modulation as sketched, oriented with the long axis (z) parallel to the applied field (squares) and orthogonal to it (circles). (b) Comparison of the coercive fields of different types of arrays of modulated Ni wires in a field applied parallel or perpendicular to the long axis of the wires at 300 K. The wire types are labeled according to Fig. 1 and ordered so that the fraction of thin segment(s) increases from left to right. From the experimental datapoints it is clear that the geometry has sizeable effect on H_c when the field is applied parallel to the long axis (full squares) but a much lower importance for the orthogonal orientation (empty circles).

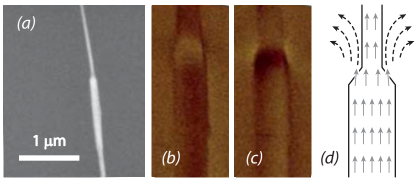

FIG. 6. (Color online) Magnetic imaging of an isolated Ni wire. (a) Electron microscopy furnishes the structural information. [(b) and (c)] Magnetic force micrographs of the central section of the wire taken in saturating positive and negative fields applied along the wire axis. The contrast originates from the magnetic stray fields generated by the ferromagnetic nanowire. Dark and bright areas reflect the presence of a magnetic field gradient perpendicular to the plane of the figure. (d) Sketch of the magnetization (gray arrows) within the wire and of the stray field lines (dashed black arrows) outside of it.

different types of diameter modulations, as sketched in Fig. 1. The coercive field stays in the vicinity of 100 Oe for all wire geometries when the field is applied $\vec{H} \perp \vec{z}$. In $\vec{H} \parallel \vec{z}$ orientation, however, differences emerge when the coercive field is considered as a function of the hard/mild ratio. Wires with smaller diameter have much larger values of $H_c^{\parallel}$ than the wider ones. This is due to the more pronounced geometric anisotropy,[37–39] as well as alleviated dipolar interactions between neighboring wires. More interestingly, one can observe that the introduction of one or two thick segments into a long narrow wire divides the coercive field value by a factor two or three. Clearly, $\vec{H}_c$ is not simply the weighted average of values that could be calculated[40,41] for wires of 80 nm, on the one hand, and 160 nm, on the other hand. This could be considered as an indication (albeit an indirect one) that the modulation serves as a nucleation point for the creation of domain walls and thereby facilitates the initiation of magnetization reversal. However, given the results presented in the previous paragraph, we contend that this effect is controlled by dipolar couplings in the ensemble. Indeed, the stray field generated by each wire is certainly strongly affected by the presence of modulations.

This aspect can be modeled: For this, we can consider the magnetostatic interaction between two modulated wires as the sum of the interactions between their individual segments, along the lines described more fully for the case of tubes.[17] In essence, the effective coercive field H_c in the array will be reduced from the value H_c^T calculated for an isolated object[42] by an amount H_{int} corresponding to the stray field:[43]

$$H_c = H_c^T - H_{\text{int}}. \tag{2}$$

This lowering in H_c is, qualitatively speaking, due to the spatial inhomogeneity of the stray field in such arrays of quite densely packed magnets.[42] In a mean-field approximation, only the remanence and not the coercive field would be affected.[44] Fig. 4 compares the theoretical values obtained for H_c in the ensemble according to the approach of Escrig *et al.*[43] (empty squares) with those calculated for single objects (empty circles) and with the corresponding experimental data—measured with SQUID and MOKE magnetometry for the ensemble (full green squares) and isolated objects (full disks). The dipolar interactions cause a major reduction of H_c in each sample. This appears both in the experimental and theoretical sets of data. This observation substantiates the primary importance of the stray fields generated in the vicinity of each diameter modulation. Experimentally, stray fields can be imaged by MFM, which was performed here with a Veeco DI Nanoscope IIIa built in a 1600 Oe magnet and operated with a cobalt-covered magnetic tip. Figure 6 displays the MFM data recorded on one horizontally lying wire under a saturating field applied along $+\vec{z}$ and $-\vec{z}$ [(c) and (d)]. A strong contrast is observed in the region with varying diameter, which is inverted when the applied field is reversed. Therefore, the contrast is magnetic in origin. However, the symmetry of the picture excludes its interpretation as originating from the presence of a domain boundary, as expected in the magnetic saturated state. Both a vortex and a transverse domain wall would introduce a difference in the perpendicular component of the stray field between the left and right sides of the wire, which is not observed in the MFM signal.[45–47] Thus, the contrast directly evidences the enhanced stray field present in the vicinity of the diameter modulation [sketched in Fig. 6(d)].

The comparison of the theoretically calculated coercive fields with the experimentally determined fields in Fig. 4 indicates a good agreement for samples E, C, and F [Eqs. (1) and (2)]. The experimental distribution of values at the single-object level reflects shape and size irregularities, which are averaged out in the ensemble and lead to an improved fit between theory and experiment. Among the factors that can account for the small differences are thermal fluctuations and the finite length of the wires. We conclude, therefore, that the hypotheses on which our analytical model bases are satisfactory. Most significantly, it need not be assumed that domain wall pinning occurs in order to account for the data. The situation is different for sample A, which consists of three segments. Here, the theoretical values differ from the measured counterparts by approximately 500 Oe both for an isolated object and the ensemble. We recall the results of a similar investigation on modulated nanotubes, where structures with more than two thick segments were not well described by the model, either.[17] We must attribute this behavior to a phenomenon not taken into account in the model. In this case, the magnetization reversal might take place via a more complex mechanism in which the modulations play a particular role. Additionally, the shape of the domain boundaries may deviate from the idealized structure in the analytical model [Eqs. (1) and (2)].

V. CONCLUSIONS

Porous alumina is a suitable template system for the creation of pseudo-one-dimensional cylindrical nano-objects with the controlled introduction of variations in diameter, which could function as pinning sites for magnetic domain boundaries. In single-object measurements, we were able to observe hints of domain boundary pinning in some cases. That the pinning occurs at the modulation remains to be shown. Additionally, in the nanowires presented here the pinning is not systematic. Most likely, the energy difference of a domain wall between thick and thin wire segments is too small with respect to the influence of magnetocrystalline anisotropy and thermal fluctuations. Such factors will introduce a stochastic component into the pinning phenomena. The difficulty can most logically be overcome by the use of soft magnetic materials and the creation of modulations between segments with diameters in a larger ratio.[48] Further, the presence of modulations also affects the magnetic properties of wire ensembles. In a simple theoretical framework we were able to account for the differences between the various types of modulated wires and calculate their enhanced interaction in the array. The model shows limitations for multiple modulations: we consider this as a likely sign that they influence either the nucleation of domain boundaries or their propagation.

ACKNOWLEDGMENTS

This work was supported by the German Research Council (DFG) in the framework of the Sonderforschungsbereich under Grant No. SFB668 "Magnetismus vom Einzelatom zur Nanostruktur" and by the Cluster of Excellence "Nanospintronics" funded by the "Forschungs-und Wissenschaftsstiftung Hamburg." J.M.M. acknowledges the Comissionat per a Universitats i Recerca from the Departament d'Innovació, Universitats i Empresa from Generalitat de Catalunya, and the Fons Social Europeu for financial support. J.E. acknowledges the "Millennium Science Nucleus Basic and Applied Magnetism" (Project No. P06-022F), Financiamiento Basal para Centros Científicos y Tecnológicos de Excelencia, and Fondecyt (Project No. 11070010).

[1] S. S. P. Parkin, M. Hayashi, and L. Thomas, Science **320**, 190 (2008).

[2] L. O'Brien, D. E. Read, H. T. Zeng, E. R. Lewis, D. Petit, and R. P. Cowburn, Appl. Phys. Lett. **95**, 232502 (2009).

[3] M. Hayashi, L. Thomas, R. Moriya, C. Rettner, and S. S. P. Parkin, Science **320**, 209 (2008).

[4] Y. Xia, P. Yang, Y. Sun, Y. Wu, B. Mayers, B. Gates, Y. Yin, F. Kim, and Y. Yan, Adv. Mater. **15**, 353 (2003).

[5] M. Law, J. Goldberger, and P. Yang, Annu. Rev. Mater. Res. **34**, 83 (2004).

[6] C. Yang, Z. Zhong, and C. Lieber, Science **310**, 1304 (2005).

[7] A. Hochbaum, R. Chen, R. Delgado, W. Liang, E. Garnett, M. Najarian, A. Majumdar, and P. Yang, Nature (London) **451**, 163 (2008).

[8] P. Aranda and J. M. Garcia, J. Magn. Magn. Mater. **249**, 214 (2002).

[9] W. Bruckner, J. Thomas, R. Hertel, R. Schäfer, and C.-M. Schneider, J. Magn. Magn. Mater. **283**, 82 (2004).

[10] N. B. Chaure, P. Stamenov, F. Rhen, and J. Coey, J. Magn. Magn. Mater. **290**, 1210 (2005).

[11] H. Hu, H. Chen, S. Yu, J. Chen, G. Wu, F. Meng, J. Qu, Y. Li, H. Zhu, and J. Xiao, J. Magn. Magn. Mater. **295**, 257 (2005).

[12] A. Fert and L. Piraux, J. Magn. Magn. Mater. **200**, 338 (1999).

[13] P. Paulus, F. Luis, M. Kroll, G. Schmid, and L. de Jongh, J. Magn. Magn. Mater. **224**, 180 (2001).

[14] M. Kröll, W. Blau, D. Grandjean, R. Benfield, F. Luis, P. Paulus, and L. de Jongh, J. Magn. Magn. Mater. **249**, 241 (2002).

[15] W. Lee, R. Scholz, and U. Gösele, Nano Lett. **8**, 2155 (2008).

[16] W. Lee, K. Schwirn, M. Steinhart, E. Pippel, R. Scholz, and U. Gösele, Nat. Nanotechnol. **3**, 234 (2008).

[17] K. Pitzschel, J. M. M. Moreno, J. Escrig, O. Albrecht, K. Nielsch, and J. Bachmann, ACS Nano **3**, 3463 (2009).

[18] Y. Li, M. Zheng, L. Ma, and W. Shen, Nanotechnology **17**, 5101 (2006).

[19] J. Bachmann, R. Zierold, Y. Chong, R. Hauert, C. Sturm, R. Schmidt-Grund, B. Rheinländer, M. Grundmann, U. Gösele, and K. Nielsch, Angew. Chem., Int. Ed. **47**, 6177 (2008).

[20] J. Briones, F. Montaigne, D. Lacour, M. Hehn, M. J. Carey, and J. R. Childress, Appl. Phys. Lett. **92**, 032508 (2008).

[21] G. Meier, M. Bolte, R. Eiselt, B. Kruger, D. H. Kim, and P. Fischer, Phys. Rev. Lett. **98**, 187202 (2007).

[22] P. Landeros, S. Allende, J. Escrig, E. Salcedo, D. Altbir, and E. E. Vogel, Appl. Phys. Lett. **90**, 102501 (2007).

[23] K. D. U. R. Wieser and U. Nowak, Phys. Rev. B **69**, 064401 (2004).

[24] R. Hertel, J. Magn. Magn. Mater. **249**, 251 (2002).

[25] D. Hinzke and U. Nowak, J. Magn. Magn. Mater. **221**, 365 (2000).

[26] A. Thiaville and Y. Nakatani, in *Spin Dynamics in Confined Magnetic Structures III*, Topics in Applied Physics Vol. 101, edited by B. Hillebrands and A. Thiaville (Springer, Berlin, 2006), p. 161.

[27] J. Escrig, J. Bachmann, J. Jing, M. Daub, D. Altbir, and K. Nielsch, Phys. Rev. B **77**, 214421 (2008).

[28] E. Stoner and E. C. Wohlfarth, Philos. Trans. R. Soc. London, Ser. A **240**, 599 (1948).

[29] C. A. Ross, M. Farhoud, M. Hwang, H. I. Smith, M. Redjdal, and F. B. Humphrey, J. Appl. Phys. **89**, 1310 (2001).

[30] J. Escrig, P. Landeros, J. C. Retamal, D. Altbir, and J. D. E. Castro, Appl. Phys. Lett. **82**, 3478 (2003).

[31] P. Landeros, J. Escrig, D. Altbir, D. Laroze, J. d'Albuquerque e Castro, and P. Vargas, Phys. Rev. B, **71**, 094435 (2005).

[32] R. C. O'Handley, *Modern Magnetic Materials: Principles and Applications* (Wiley, New York, 2000).

[33] O. Kazakova, D. Erts, T. Crowley, J. Kulkarni, and J. Holmes, J. Magn. Magn. Mater. **286**, 171 (2005).

[34] R. Kozhuharova, M. Ritschel, D. Elefant, A. Graff, I. Monch, T. Muhl, C. Schneider, and A. Leonhardt, J. Magn. Magn. Mater. **290**, 250 (2005).

[35] D. Navas, M. Hernández-Vélez, M. Vázquez, W. Lee, and K. Nielsch, Appl. Phys. Lett. **90**, 192501 (2007).

[36] K. Nielsch, R. B. Wehrspohn, J. Barthel, J. Kirschner, U. Gösele, S. F. Fischer, and H. Kronmüller, Appl. Phys. Lett. **79**, 1360 (2001).

[37] V. Raposo, J. Garcia, J. Gonzalez, and M. Vazquez, J. Magn. Magn. Mater. **222**, 227 (2000).

[38] J. Rivas, A. Bantu, G. Zaragoza, M. Blanco, and M. Lopez-Quintela, J. Magn. Magn. Mater. **249**, 220 (2002).

[39] Z. Hao, Y. Shaoguang, N. Gang, Y. Dongliang, and D. Youwei, J. Magn. Magn. Mater. **234**, 454 (2001).

[40] J. Escrig, R. Lavin, J. L. Palma, J. C. Denardin, D. Altbir, A. Cortes, and H. Gomez, Nanotechnology **19**, 075713 (2008).

[41] J. Escrig, D. Altbir, M. Jaafar, D. Navas, A. Asenjo, and M. Vazquez,

Phys. Rev. B **75**, 184429 (2007).
[42] R. Hertel, J. Appl. Phys. **90**, 5752 (2001).
[43] J. Escrig, S. Allende, D. Altbir, and M. Bahiana, Appl. Phys. Lett. **93**, 023101 (2008).
[44] P. Fodor, G. Tsoi, and L. Wenger, J. Appl. Phys. **93**, 7438 (2003).
[45] K. Miyake, K. Shigeto, K. Mibu, T. Shinjo, and T. Ono, J. Appl. Phys. **91**, 3468 (2002).
[46] J. M. García, A. Thiaville, and J. Miltat, J. Magn. Magn. Mater. **249**, 163 (2002).
[47] L. Belliard, J. Miltat, A. Thiaville, S. Dubois, J. Duvail, and L. Piraux, J. Magn. Magn. Mater. **190**, 1 (1998).
[48] S. Allende, D. Altbir, and K. Nielsch, Phys. Rev. B **80**, 174402 (2009).

A.2 Domain-wall pinning and depinning at soft spots in magnetic nanowires

Publication [Vog10]

DOMAIN-WALL PINNING AND DEPINNING AT SOFT SPOTS IN MAGNETIC NANOWIRES

by

Andreas Vogel, Sebastian Wintz, Judith Kimling, Markus Bolte,
Thomas Strache, Monika Fritzsche, Mi-Young Im, Peter Fischer,
Guido Meier, and Jürgen Fassbender

published in

IEEE Transactions on Magnetics **46**, 1708 (2010).

1708 IEEE TRANSACTIONS ON MAGNETICS, VOL. 46, NO. 6, JUNE 2010

Domain-Wall Pinning and Depinning at Soft Spots in Magnetic Nanowires

Andreas Vogel[1], Sebastian Wintz[2], Judith Kimling[1], Markus Bolte[1], Thomas Strache[2], Monika Fritzsche[2],
Mi-Young Im[3], Peter Fischer[3], Guido Meier[1], and Jürgen Fassbender[2]

[1]Institut für Angewandte Physik und Zentrum für Mikrostrukturforschung, Universität Hamburg, Hamburg, Germany
[2]Institut für Ionenstrahlphysik und Materialforschung, Forschungszentrum Dresden-Rossendorf, Dresden, Germany
[3]Center for X-ray Optics, Lawrence Berkeley National Laboratory, Berkeley, CA USA

The local modification of magnetic properties by ion irradiation opens the possibility to create pinning sites for domain walls in magnetic nanowires without geometric constrictions. Implantation of chromium ions into $\mathbf{Ni_{80}Fe_{20}}$ nanowires is used to cause a local reduction of the saturation magnetization M_s and thus a decrease of the energy associated with the domain wall. Field-driven pinning and depinning of a domain wall at the here so-called magnetic soft spots is directly observed using magnetic transmission soft X-ray microscopy. The pinning rate and the depinning field considerably depend on the wire width and the chromium fluence.

Index Terms—**Domain walls and domain structure, intrinsic properties of magnetically ordered materials, magnetic properties of nanostructures, magnetization reversal mechanisms.**

I. INTRODUCTION

THE controlled motion of magnetic domain walls (DWs) in nanowires is one of the fundamental issues for the realization of new concepts of high-density and ultrafast non-volatile data-storage devices [1]–[3]. Locally well-defined confining potentials, e.g., created by notches, act as pinning sites for individual DWs [4]–[6]. Spin polarized currents, driven through the nanowire, yield the possibility to manipulate the magnetic configuration due to a transfer of spin-angular momentum [7], [8]. For a reliable spin-torque induced domain-wall depinning, low threshold currents are required in order to reduce stochastic temperature effects by Joule heating and to avoid damage to the nanowire.

We investigate a concept to create pinning sites for DWs in magnetic nanowires without geometric constrictions: The local modification of magnetic properties by means of ion implantation (magnetic soft spots). Implantation of chromium ions into $\mathrm{Ni_{80}Fe_{20}}$ causes alloying and structural defects. This leads to a reduction of the Curie temperature and the saturation magnetization M_s as well as to small changes of the magnetocrystalline anisotropy [9]–[11]. The application of electron-beam lithography (EBL) or focused ion beam (FIB) on the other hand enables a spatial resolution below 50 nm for this kind of magnetic patterning [12]. Pinning of DWs at magnetic soft spots is expected to be preferred in comparison to the environment as the energy associated with the DW is locally reduced. In order to verify the suitability of this concept, we fabricate magnetic soft spots into $\mathrm{Ni_{80}Fe_{20}}$ nanowires by means of chromium ion irradiation through an EBL shadow mask and examine the pinning characteristics of DWs. Measurements have been performed for nanowires with different widths, spot sizes, and chromium fluences. We directly observe the field-driven pinning and depinning of a DW at magnetic soft spots using magnetic transmission soft X-ray microscopy (MTXM) [13]. Magnetic contrast is provided via X-ray magnetic circular dichroism (XMCD) [14] at the Ni $\mathrm{L_3}$-absorption edge.

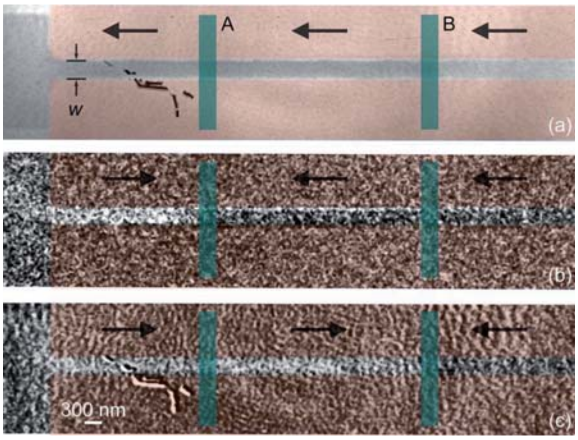

Fig. 1. Magnetization reversal of a 300 nm wide nanowire comprising two magnetic soft spots marked A and B with a width of 300 nm $(s = 1)$. (a) MTXM image in the saturated state. The arrows indicate the magnetization direction in the wire. An external magnetic field aligned parallel to the wire is successively reversed. Differential images with respect to the initial saturated state are shown for characteristic steps of the magnetization reversal: (b) domain-wall pinning at spot A, and (c) depinning at spot A/pinning at spot B.

II. SAMPLE PREPARATION AND EXPERIMENTAL METHOD

Ferromagnetic nanowires as shown in Fig. 1(a) with different wire widths are fabricated using electron-beam lithography and lift-off processing. Polycrystalline $\mathrm{Ni_{80}Fe_{20}}$ with a thickness of $L = 30\ \mathrm{nm}$ is thermally evaporated onto 100 nm thin silicon-nitride membranes. The wire width w is varied from 300 nm to 500 nm. Each wire comprises two individual soft spots induced by 15 kV chromium ion irradiation through an EBL shadow mask. The primary ion energy is chosen to achieve a mean chromium penetration depth of 6.8 nm which effectively suppresses the magnetic moment. We define the ratio s between the spot width and the wire width w to characterize the size of the magnetic soft spots. The parameter s is chosen between 0.5 and 2.0 for each wire width. Samples are fabricated with

Manuscript received October 30, 2009; revised January 13, 2010; accepted January 26, 2010. Current version published May 19, 2010. Corresponding authors: A. Vogel (e-mail: andreas.vogel@physnet.uni-hamburg.de) and S. Wintz (e-mail: s.wintz@fzd.de).

Color versions of one or more of the figures in this paper are available online at http://ieeexplore.ieee.org.

Digital Object Identifier 10.1109/TMAG.2010.2042285

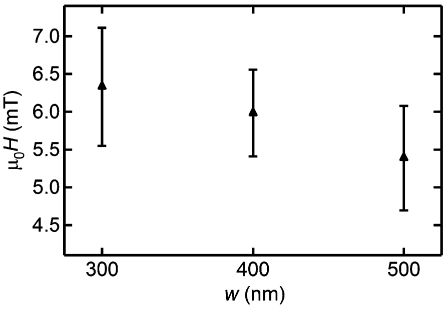

Fig. 2. Dependence of the saturation field of nanowires without pinning sites on the wire width w. Triangles and error bars depict the mean value and the standard deviation ($\pm\sigma$) for repeated measurements of several samples, respectively.

chromium fluences F of $5 \times 10^{15}\ \mathrm{cm}^{-2}$, $10 \times 10^{15}\ \mathrm{cm}^{-2}$, and $15 \times 10^{15}\ \mathrm{cm}^{-2}$, which reduces the magnetic moment to 80%, 66%, and 57% of the initial value (determined by magneto-optical Kerr effect (MOKE) magnetometry). At the chosen ion energy and fluences mixing of substrate atoms into $\mathrm{Ni}_{80}\mathrm{Fe}_{20}$ is mostly prevented. The reduction in layer thickness due to ion irradiation has been estimated by Rutherford backscattering (RBS) investigations and TRIDYN [15] simulations to be less than 6 nm for a film at the highest fluence. Thus, the effect of thickness reduction in the region of the submicrometer soft spots can be considered to be sufficiently small to ascribe the observed phenomena mainly to direct chromium implantation [16].

The measurements have been performed at beamline 6.1.2 of the Advanced Light Source in Berkeley, CA, USA. The full-field soft X-ray transmission microscope permits a spatial resolution down to 15 nm using Fresnel-zone plates [17]. Operated in a multibunch, top-off mode, the synchrotron delivers a constant electron-beam current of 500 mA. Samples are illuminated by circular polarized X-rays with an incident energy of 852.7 eV corresponding to the Ni L_3-absorption edge. Magnetic imaging is realized in an in-plane geometry where the nanowires are mounted under an angle of 60° with respect to the beam direction. Starting at a fully saturated state, an external magnetic field H aligned collinear to the nanowire is successively reversed in order to identify the specific pinning and depinning fields at the soft spots. The pinning field is determined as the external field necessary to get a DW into the spot. A contrast change in differential images reveals the magnetization switching in particular regions of the nanowire, see Fig. 1(b) and (c). Due to lower shape anisotropy in comparison to the narrow wire, the magnetic DW is created in the rectangular pad. With increasing strength of the external magnetic field, the DW propagates along the wire.

III. Experimental Data and Discussion

Reference nanowires without chromium irradiation have been investigated to determine their micromagnetic behavior. As expected, with the selected increment of the external magnetic field no pinning events are observed for wires without artificial pinning site. For each wire width w, all the nanowires switch within a range of about $2\sigma = 1.4\ \mathrm{mT}$. In agreement with previous results on $\mathrm{Ni}_{80}\mathrm{Fe}_{20}$ nanowires [18], the saturation fields are found to decrease with the width of the wire due to different shape anisotropy, see Fig. 2.

Pinning and subsequent depinning occurs in most of the nanowires with locally implanted chromium. The magnetic soft spots with reduced saturation magnetization act as a potential well for the motion of the DW. In the soft magnetic region, the energy associated with the DW is decreased and thus a DW position at the soft spot is energetically favorable. When the external force due to the magnetic field overcomes the pinning forces of the soft spots, the DW continues propagating towards the end of the wire where it is annihilated. Since the pinning and depinning fields exhibit a certain spread, multiple reversal measurements are required to gain information on the average pinning and depinning fields and the quality of the field distribution.

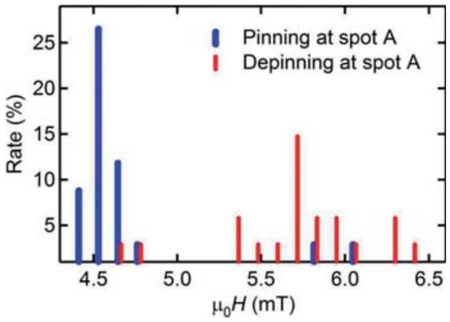

Fig. 3. Typical magnetic field distribution for pinning and depinning at a magnetic soft spot. The parameters of the present nanowire are: wire width $w = 400\ \mathrm{nm}$, ratio between spot width and wire width $s = 1.0$, and chromium fluence $F = 5 \times 10^{15}\ \mathrm{cm}^{-2}$. The total number of depinning events is 19.

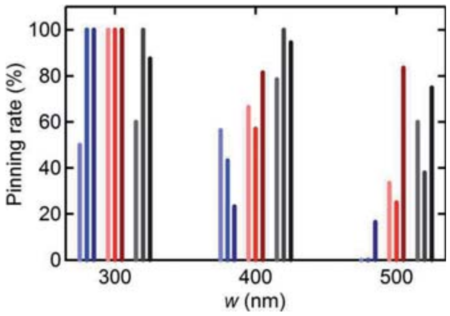

Fig. 4. Average pinning rate at spot A for different parameters w, s, and F. For each wire width w different colors depict the chromium fluence F (blue: $5 \times 10^{15}\ \mathrm{cm}^{-2}$; red: $10 \times 10^{15}\ \mathrm{cm}^{-2}$; black: $15 \times 10^{15}\ \mathrm{cm}^{-2}$) starting from the lowest on the left. The saturation of each color references to the spot size s where low color saturation means a small spot size (0.5, 1.0, 2.0).

Fig. 3 shows a typical field distribution for pinning and depinning at the magnetic soft spot A. Note that the pinning field at spot A corresponds to the switching field of the wire without artificial pinning site. The broadness of the depinning field distribution underlines the stochastic nature of the DW depinning process [6]. We do not distinguish between different types of DWs like transverse and vortex walls. In general, the pinning rate for the second spot B is lower than for the equivalent spot A. This is ascribed to prior depinning at spot A, involving magnetic fields that are already beyond the pinning potential of spot B. In the following, we concentrate on the analysis of pinning and depinning at the magnetic soft spot A depending on the parameters of the nanowire.

Fig. 4 shows the pinning rates at spot A as a function of the wire width w, the chromium fluence F, and the ratio s between width of the magnetic soft spot and wire width. For several configurations a pinning rate of 100% is observed. Multiple measurements reveal that the average pinning rate of a DW decreases with increasing width of the nanowire. For wires with

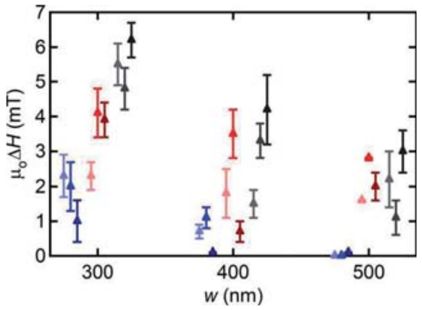

Fig. 5. Average gap $\mu_0\Delta H$ between pinning and depinning field at spot A for different parameters w, s, and F. For each wire width w different colors depict the chromium fluence F (blue: $5 \times 10^{15}\ \mathrm{cm}^{-2}$; red: $10 \times 10^{15}\ \mathrm{cm}^{-2}$; black: $15 \times 10^{15}\ \mathrm{cm}^{-2}$) starting from the lowest on the left. The saturation of each color references to the ratio s (0.5, 1.0, 2.0) of spot width to wire width where low color saturation means small spot size. Triangles and error bars depict the mean value and the standard deviation for repeated measurements of different nanowires, respectively.

$w = 400\ \mathrm{nm}$ and $w = 500\ \mathrm{nm}$, the pinning rate increases with increasing chromium fluence. No significant trend can be determined concerning the influence of the size of the magnetic soft spot.

Depending on the parameters of the wire, we observe clear trends regarding the gap ΔH in the magnetic field between pinning and depinning of DWs. Fig. 5 shows the average gap at spot A as a function of the width w of the wire, the chromium fluence F, and the ratio s characterizing the size of the magnetic soft spot. The difference between the pinning and the depinning field provides information about the pinning strength of the spot. We determine the additional field necessary to move the DW beyond the magnetic soft spot in comparison to the switching field of the wire without artificial pinning site. Taking into account the results for the reference nanowires presented in Fig. 2, ΔH is a measure for the pinning potential of the spot with respect to the wire. The gap is observed to decrease with increasing wire width. For each width, ΔH and thus the pinning potential increases with an increase of chromium ion irradiation resulting in a stronger decrease of the saturation magnetization. Again no significant dependence on the size of the soft spot is observed.

IV. CONCLUSION

Magnetic transmission soft X-ray microscopy has been used to directly observe field-driven DW pinning and depinning at magnetic soft spots in $\mathrm{Ni}_{80}\mathrm{Fe}_{20}$ nanowires. The pinning rate and the depinning field considerably depend on the width of the nanowire and the saturation magnetization of the soft spot. For several configurations a pinning rate of 100% has been observed. The strength of the pinning potential can be tuned by the chromium ion fluence applied to induce the soft spots. In conclusion, magnetic soft spots realized via implantation of chromium are suitable as pinning site for DWs and avoid supplementary spatial constrictions. Further investigations concerning the geometric shape of the soft spots and current-induced DW motion are under way.

ACKNOWLEDGMENT

The measurements were performed at the Advanced Light Source which is supported by the U.S. Department of Energy under Contract DE-AC02-05-CH11231. This work was support in part by the Deutsche Forschungsgemeinschaft via the Graduiertenkolleg 1286 and the Sonderforschungsbereich 668. The authors would like to thank M. Volkmann and I. Winkler for superb technical support.

REFERENCES

[1] D. A. Allwood, G. Xing, M. D. Cooke, C. C. Faulkner, D. Atkinson, N. Vernier, and R. P. Cowburn, “Submicrometer ferromagnetic NOT gate and shift register,” *Science*, vol. 296, pp. 2003–2006, Jun. 2002.

[2] S. S. P. Parkin, “Shiftable Magnetic Shift Register and Method of Using the Same,” U.S. Patent 683 400 5, Dec. 2004.

[3] T. Ono, H. Miyajima, K. Shigeto, K. Mibu, N. Hosoito, and T. Shinjo, “Propagation of a magnetic domain wall in a submicrometer magnetic wire,” *Science*, vol. 284, pp. 468–470, Apr. 1999.

[4] M. Kläui, C. A. F. Vaz, J. A. C. Bland, W. Wernsdorfer, G. Faini, E. Cambril, L. J. Heyderman, F. Nolting, and U. Rüdiger, “Controlled and reproducible domain wall displacement by current pulses injected into ferromagnetic ring structures,” *Phys. Rev. Lett.*, vol. 94, pp. 106601-1–106601-4, Mar. 2005.

[5] P. Lendecke, R. Eiselt, G. Meier, and U. Merkt, “Temperature dependence of domain-wall depinning fields in constricted Permalloy nanowires,” *J. Appl. Phys.*, vol. 103, pp. 073909-1–073909-4, Apr. 2008.

[6] M.-Y. Im, L. Bocklage, P. Fischer, and G. Meier, “Direct observation of stochastic domain-wall depinning in magnetic nanowires,” *Phys. Rev. Lett.*, vol. 102, pp. 147204-1–147204-4, Apr. 2009.

[7] L. Thomas, M. Hayashi, X. Jiang, R. Moriya, C. Rettner, and S. S. P. Parkin, “Oscillatory dependence of current-driven magnetic domain wall motion on current pulse length,” *Nature (London)*, vol. 433, pp. 197–200, Sep. 2006.

[8] G. Meier, M. Bolte, R. Eiselt, B. Krüger, D.-H. Kim, and P. Fischer, “Direct imaging of stochastic domain-wall motion driven by nanosecond current pulses,” *Phys. Rev. Lett.*, vol. 98, pp. 187202-1–187202-4, May 2007.

[9] J. Fassbender, J. von Borany, A. Mücklich, K. Potzger, W. Möller, J. McCord, L. Schultz, and R. Mattheis, “Structural and magnetic modifications of Cr-implanted Permalloy,” *Phys. Rev. B*, vol. 73, pp. 184410-1–184410-8, May 2006.

[10] J. Fassbender, T. Strache, M. O. Liedke, D. Marko, S. Wintz, K. Lenz, A. Keller, S. Facsko, I. Moench, and J. McCord, “Introducing artificial length scales to tailor magnetic properties,” *New J. Phys.*, vol. 11, pp. 125002-1–125002-19, Dec. 2009.

[11] L. Folks, R. E. Fontana, B. A. Gurney, J. R. Childress, S. Maat, J. A. Katine, J. E. E. Baglin, and A. J. Kellock, “Localized magnetic modification of permalloy using Cr^{+} ion implantation,” *J. Phys. D*, vol. 36, pp. 2601–2604, Oct. 2003.

[12] J. Fassbender and J. McCord, “Magnetic patterning by means of ion irradiation and implantation,” *J. Magn. Mag. Matter.*, vol. 320, pp. 579–596, Feb. 2008.

[13] P. Fischer, D.-H. Kim, W. Chao, J. A. Liddle, E. H. Anderson, and D. T. Attwood, “Soft X-ray microscopy of nanomagnetism,” *Mater. Today*, vol. 9, pp. 26–33, Jan.–Feb. 2006.

[14] C. T. Chen, F. Sette, Y. Ma, and S. Modesti, “Soft-x-ray magnetic circular dichroism at the $\mathrm{L}_{2,3}$ edges of nickel,” *Phys. Rev. B*, vol. 42, pp. 7262–7265, Oct. 1990.

[15] W. Möller, W. Eckstein, and J. P. Biersack, “Tridyn-binary collision simulation of atomic collisions and dynamic composition changes in solids,” *Comput. Phys. Commun.*, vol. 51, pp. 355–368, Nov. 1988, The TRIDYN code is available at www.fzd.de.

[16] J. Fassbender and J. McCord, “Control of saturation magnetization, anisotropy, and damping due to Ni implantation in thin $\mathrm{Ni}_{81}\mathrm{Fe}_{19}$ layers,” *Appl. Phys. Lett.*, vol. 88, pp. 252501-1–252501-3, Jun. 2006.

[17] W. Chao, B. H. Harteneck, J. A. Liddle, E. H. Anderson, and D. T. Attwood, “Soft X-ray microscopy at a spatial resolution better than 15 nm,” *Nature (London)*, vol. 435, pp. 1210–1213, Jun. 2005.

[18] Y. Yokoyama, Y. Suzuki, S. Yuasa, K. Ando, K. Shigeto, T. Shinjo, P. Gogol, J. Miltat, A. Thiaville, T. Ono, and T. Kawagoe, “Kerr microscopy observations of magnetization process in microfabricated ferromagnetic wires,” *J. Appl. Phys.*, vol. 87, pp. 5618–5620, May 2000.

B Experimental details

B.1 Synthesis parameters for cylindrical wires

The main steps for the electrochemical synthesis of cylindrical nanowires are:

1. Preparation of the template.
2. Filling of the template by electrochemical deposition.

Between steps 1 and 2 both the aluminum substrate and the alumina barrier layer are removed, and a gold electrode is sputter deposited on the rear side of the template.

For selected wires studied the parameters for the main steps are listed in the following sections. If no standards solutions were used the recipes for these are given as well. Otherwise details on the synthesis are given in the publications cited.

B.1.1 Nickel wires with one diameter modulation

Synthesis by Shadyar Farhangfar, Institut für Angewandte Physik und Zentrum für Mikrostrukturforschung Hamburg, Universität Hamburg, Germany.
Scanning electron micrographs of these wires are shown in Fig. 6.10(c) and Fig. 6.18(a). The modulation is from about 240 nm to 340 nm.

Template: The membrane was fabricated in a three-step anodization process. To this end, we used 1 weight percent phosphoric acid (H_3PO_4) as electrolyte. The first anodization step was performed under potentiostatic condition with an applied voltage of 195 V at 1.5 °C for about six hours. After elimination of the first anodized alumina layer in a mixture of H_3PO_4 (6 weight percent)/H_2CrO_4 (1.8 weight percent), the second anodization step was repeated under similar conditions for about 15 hours. Next, subsequent to the removal of the electrolyte and cleaning of the samples with distilled water, we used a stirred 10 weight percent solution of H_3PO_4 at 32 °C to chemically widen the pores. The pore widening rate was about 120 $\frac{\mathrm{nm}}{\mathrm{h}}$. In the last step, the anodization was continued as in the first two ones for several hours.

Electrochemical deposition: Galvanostatic electrochemical deposition of the nickel nanowires from a Ni electrolyte through the narrower channels to the template following the standard procedure detailed in Ref. [Nie02b].

B.1.2 Nickel-iron wires with one diameter modulation

Synthesis by Víctor Vega Martínez, Laboratorio de Membranas Nanoporosas, Unidad de Nanotecnología de los Servicios Científico-Técnicos de la Universidad de Oviedo, Spain.
Scanning electron micrographs of these wires with an average nickel content of 83 ± 2 percent are depicted in Figs. 6.10(g) and (h). The modulations of these wires are from about 70 nm to 225 nm.

Template: The membrane was prepared by hard anodization of a high purity aluminum foil in 0.3 M oxalic acid containing 5 percent in volume of ethanol, at an anodization voltage of 140 V at $0 - 3\,^{\circ}$C, during 1800 seconds. Afterwards, the membrane was covered by 3 nm of SiO_2 by atomic layer deposition. The sample was then re-anodized in the same electrolyte and conditions for 300 s. After removal of the aluminum substrate the membrane was immersed in H_3PO_4 (5 weight percent) at $45\,^{\circ}$C for 2 hours, resulting in both, alumina barrier layer removal (pore opening) and pore size increase in the second segment, while the pore diameter of the first segment keeps constant due to the SiO_2 protective layer. Finally, the whole membrane was coated with 3 nm more of SiO_2.

Electrochemical deposition: Galvanostatic electrodeposition at $0.51\frac{\text{mA}}{\text{cm}^2}$ from 100 ml of aqueous solution containing:

0.1 g	$C_6H_8O_6$
2.5 g	H_3BO_3
21.3 g	$NiSO_4{\cdot}6H_2O$
0.1 g	$C_7H_5NO_3S$
0.35 g	$FeSO_4{\cdot}7H_2O$
pH = 3	(by adding NaOH)

The deposition lasted for 9 hours.

B.1.3 Nickel wires with three modulations

Synthesis by Víctor Vega Martínez, Laboratorio de Membranas Nanoporosas, Unidad de Nanotecnología de los Servicios Científico-Técnicos de la Universidad de Oviedo, Spain.
One of these wires with three diameter modulations is displayed in Fig. 6.18(b) and in Fig. 6.19. Typical diameters of the four segments are 220 nm, 170 nm, 220 nm, and 300 nm. Since no highly-ordered membranes were used as template, the size distribution of the pore diameters is about 15 percent. As a consequence the aspect ratios of the individual modulations vary strongly.

Template: Combination of anodizations in mild and hard conditions:

1. Hard anodization: Oxalic 0.3 M + 5 percent in volume of ethanol, 140 V, $0-3\,^{\circ}$C, 1800 s (employed to get an ordered pore distribution and uniform pore size).
2. Mild anodization: Phosphoric 5 weight percent, 130 V, $5\,^{\circ}$C, 1800 s.
3. Hard anodization: Oxalic 0.3 M + 5 percent in volume of ethanol, 140 V, $0-3\,^{\circ}$C, 150 s.
4. Mild anodization: Phosphoric 5 weight percent, 130 V, $5\,^{\circ}$C, 1800 s.
5. Coating of the membrane with 2 nm of SiO_2 by atomic layer deposition.
6. Mild anodization: Phosphoric 5 weight percent, 130 V, $5\,^{\circ}$C, 1800 s.
7. Immersion in H_3PO_4 (5 weight percent) at $45\,^{\circ}$C for 2 hours to widen the pore diameter of the last grown segment.
8. Coating of the membrane with 3 nm of SiO_2.

The parts that were finally filled with nickel are the segments grown in steps 2, 3, 4 and 6.

Electrochemical deposition: Potentiostatic deposition at -1.2 V measured versus Ag/AgCl reference electrode from 100 ml of aqueous solution containing:

30 g	$NiSO_4 \cdot 6H_2O$
4.5 g	$NiCl_2 \cdot 6H_2O$
4.5 g	H_3BO_3
pH = 3	(by adding NaOH)

The deposition time was adjusted to achieve the desired filling degree.

B.2 Wafer substrates

For PEEM imaging:

Material:	Silicon
Orientation:	< 1 0 0 >
Thickness:	50 µm or 500 µm
Resistivity:	$5-10\ \Omega$ cm
Dopant:	N/Phos
Particles:	< 30 @ 0.3 µm
TTV:	< 10 µm

from Si-Mat Silicon Materials, Viktor-Frankl-Str. 20, 86916 Kaufering, Germany.

The 50 µm wafers have little defects (see for example Figs. 6.22(a), (e), and (k) below the thick wire segment) the origin of which is unclear. It was found that these defects with a width of about 50 nm are perfect for the drift correction of PEEM images.

For magnetoresistance measurements:

If contacts were not defined on substrates that have to be suited for PEEM imaging, standard silicon wafers with a thickness of 500 µm and a 150 − 200 nm thick silica layer on top were used.

B.3 Electron-beam lithography

B.3.1 Process parameters

In the following paragraphs the process parameters for electron-beam lithography are given and examples are discussed. The individual steps of sample preparation are illustrated in Fig. 4.4.

Resist: Polymethyl methacrylate (PMMA) in anisol from MicroChem (A4) or PMMA in ethyllactat from Allresist (600K, 6 percent) was used as positive resist. To facilitate the lift-off step a two-layer system consisting of a copolymer resist (EL6 from MicroChem) and a PMMA resist as shown in Fig. B.1 was used in some cases. The parameters for the spin-coating of a resist are given in the following table:

Step	Time (s)	Ramping	Spin speed (rpm)
1	4.5	30	400
2	90	0	x

The spin speed x depends on the resist and on the required thickness. The spin speed x was usually between 4000 rpm and 8000 rpm. Such high spin speeds are required to ensure a homogeneous thickness, in particular on not perfectly flat substrates as silicon-nitride membranes or on substrates with high structures as nanowires on them.
Prior to each spin-coating step the sample was put on a hot plate at 160 °C for 2 minutes. The bake-out after the last spin-coating step was done in an oven at 170 °C for 30 minutes.

Exposure: The exposure of the electron-sensitive resist was done with a Gemini Supra 55 scanning electron microscope (SEM) from Zeiss and the use of a Raith

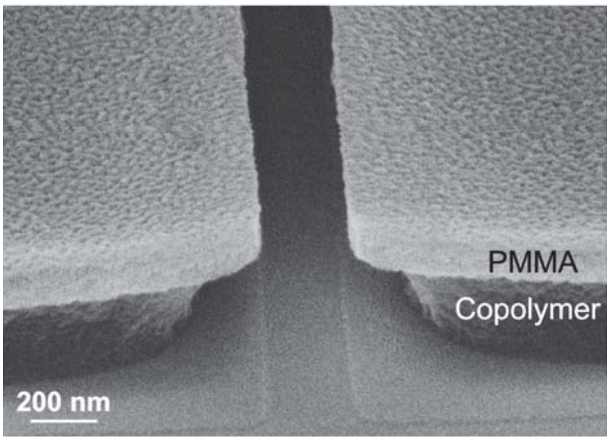

Figure B.1: Scanning electron micrograph of a two layer resist system consisting of 300 nm copolymer topped with 150 nm PMMA.

lithography package including the software Elphy. Typical exposure parameters are an acceleration voltage of 10 kV and a current of 23 pA (aperture 10 μm) for fine structures written in 200 μm × 200 μm write fields or 780 pA (aperture 60 μm) for input leads and bond pads written in 2000 μm × 2000 μm write fields. The area dose was typically 130 - 200 $\frac{\mu\mathrm{C}}{\mathrm{cm}^2}$ and the dwell time was always set above 1 μs resulting in step sizes of 6.1 nm and 61 nm for small and large write fields, respectively.

Development: After exposure the samples were developed in AR 600-56 from Allresist for 30 seconds. To stop the development they were swirled in isopropanol for 120 seconds where the copolymer (if present) is further removed due to its better resolvability and thus the undercut is increased. In a last step the samples were blown dry with nitrogen.

The next steps are the application of an RF plasma and the deposition of a metal film. Details on these are given in Sec. B.5.

Lift-off: For the lift-off of the resist and the undesired metal film the samples were put in acetone for several hours. Scratches at the edge of the substrate facilitate the dissolution of the resist. Finally the samples were rinsed with isopropanol and water before being blown dry with nitrogen.

The resist used for electron-beam lithography is usually thinner than optical resist, what makes the lift-off step more critical. To enable a proper lift off, it has to be ensured that the metal film to be removed together with the resist is not connected to the metal film of the contact pads. Crucial for this are the height of the resist and an undercut. For the definition of the contacts shown in Fig. B.2(c) a bilayer of 120 nm copolymer and 180 nm PMMA was used as resist (MicroChem CoPoEL6@4000rpm + A4@8000rpm, RF plasma: 200sec, 30W). The copolymer is dissolved stronger than the PMMA during the development step, thus the undercut is large. Since sputter deposition is a rather undirected process, the edges of the contacts are not well defined but smeared out. The total thickness of the resist (300 nm) was not high enough, thus the wire broke during the lift off. For the definition of the contacts

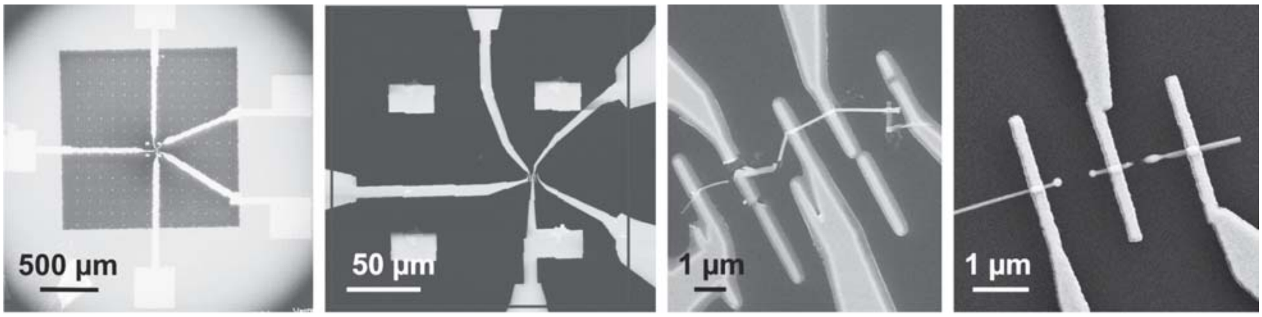

(a) (b) (c) (d)

Figure B.2: Scanning electron micrographs of gold contacts for magnetoresistance measurements. (a) Overview of a sample consisting of five bond pads, input leads, and inner contact pads defined by electron-beam lithography. The substrate is a silicon-nitride membrane as used for transmission x-ray microscopy. The membrane itself appears dark, the surrounding silicon frame appears bright. (b) For the positioning of the contact pads on the nanowire markers are used. Due to the limited size of write fields several illuminations are required and the respective write fields have to be stitched. The red square marks the inner write field (200 µm × 200 µm) in which the contact pads and the first part of the input leads are written. (c) Close-up of five contact pads on a modulated nanowire that broke during the lift-off of the resist. (d) Modulated nanowire destroyed by discharges.

shown in Fig. B.2(d) a layer of 520 nm PMMA was used (Allresist 600K@4000rpm, RF-plasma: 200sec, 20W). In this case the undercut was created by the halo of the electrons during exposure of the resit. It is not as strong as for the bilayer resist, thus the contacts are well defined. The resist was high enough to avoid the breaking of the wire during lift off. The wire got destroyed later by discharges.

B.3.2 Definition of contacts on self-arranged nanostructures

In contrast to fully lithographically designed structures, both the location and dimensions of self-arranged nanowires on a substrate are unknown. Therefore, the definition of contacts on these structures is not trivial. It consists of the following steps: Writing of markers by lithography, application of the wires, localization of the wires and designing of the contacts, as well as the final definition of contacts in a second lithography step. This section explains the lithography system and the experimental procedure.

During lithography both stage and electron beam are controlled by the Raith software. The software uses three different coordinate systems. They are illustrated in Fig. B.3. (X/Y) refers to the absolute position of the stage with the sample holder (blue). (U/V) refers to the coordinate system on the sample (gray) and therewith on the position of the write fields on the sample relative to (X/Y). (U/V) is adjusted by

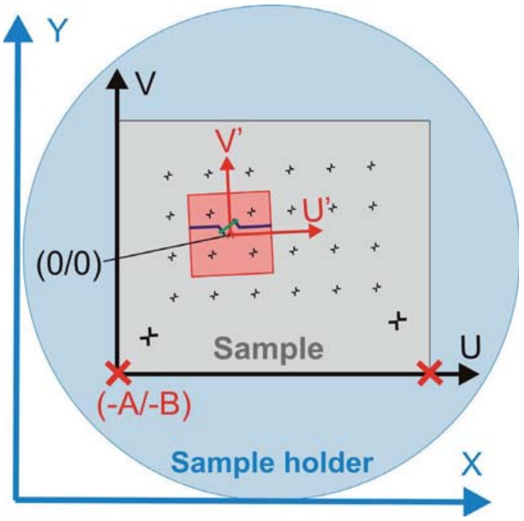

Figure B.3: Schematic of a sample in the scanning electron microscope for lithography and illustration of the three different coordinate systems used by the Elphy software.

reading out the two points on the lower edge of the sample marked with red crosses. The coordinates of the lower left corner are set such that the origin of the (U/V) coordinate system is at the desired position, for example in the center of the sample. (U'/V') refers to the position of the elements within a write field. When it comes to writing structures, the Raith software reverts to correction parameters parallel to (X/Y) for which stretching factors and a tilt angle have to be added.
To define contacts on an individual nanowire located at an arbitrary position on the substrate, two lithography steps are required. The first step is the writing of markers that can be employed for the placing of the contacts during the second lithography step (compare black crosses on sample sketched in Fig. B.3). In the first step gold markers with a size of about 20 µm are written in a cubic lattice with a lattice constant of 100 µm on an area of 4 mm × 2 mm. After the application of the nanowires the sample is imaged by SEM to locate a wire (green) suited for electrical characterization. The stage of the SEM can only be moved with an accuracy of about 1 µm what is not sufficient when it comes to the placement of contacts. Thus, once a wire is selected the center between the four markers closest to this wire is set as (U/V)=(0/0). From that state on the stage must not be moved anymore until the exact position of the wire is determined using beam shift only. This is done employing the Elphy software. The four markers closest to the wire selected are read out as manual marks in a 200 µm × 200 µm write field and the software automatically adjusts the (U'/V') coordinate system by offsets, stretching, and tilt. Then, two scan windows are set in the software and placed such that their centers hit the extremities of the wire. If there are more points of interest, for example diameter modulations of the wire, more than two scan windows can be set. The coordinates of the scan windows (in (U'/V')) are then used to design the contact pads with the Elphy software. Once this is done, the (U/V) position of the center of the write field is to be determined with respect to the sample edges. For this purpose the stage of the SEM is usually moved such that the lower left corner of the substrate is centered. The

coordinates (U/V)=(-A/-B) of the corner are set again on this position during the second lithography step to find the write field of interest again. Since the accuracy of the stage is limited, and since the position of the target write field has to be hit with a high precision to not accidentally expose a region on the wire when reading out the manual marks, usually a pair of markers located about 1 mm away from the write field of interest is used as intermediate step for the positioning.

The lithography parameters are given in Sec. B.3.1. Due to the limited size of write fields several illuminations are required during the lithography of the contacts and the respective write fields have to be stitched, compare Figs. B.2(a) and (b). Possible sources of error are mismatches between the different write fields and the displacement of a wire when the resist is spin-coated on the sample.

B.4 Optical projection lithography

Typical process parameters for the definition of contacts on individual nanowires by optical projection lithography.

Resist: Two-layer resist of photon-sensitive positive resist spin-coated according to the table in Sec.B.3 with the following parameters for step 2 and soft bake:

Resist	Time (s)	Spin speed (rpm)	Soft bake
LOR 3B (MicroChem)	45	3500	5 min @ 160 °C
ma-P 1205 (Microresist)	30	3500	30 s @ 100 °C

Exposure: The resist was exposed with a Vanox light microscope from Olympus that was extended by a Hg lamp and other components for projection lithography. Details on the setup are given in the diploma thesis of Tim Böhnert [Böh09]. The exposure time was varied between 20 seconds and 35 seconds.

Development: Samples were developed in ma-D 331 from Microresist for 30 seconds, rinsed with water, and blown dry with nitrogen.

The next steps are the application of an RF plasma and the deposition of a metal film. Details on these are given in Sec. B.5.

Lift-off: The lift-off was done by putting the samples in Microposit remover 1165 for several hours. Finally, the samples were rinsed with water and blown dry with nitrogen.

B.5 Parameters for RF-plasma and sputter deposition

To define ohmic contacts on the cylindrical nickel nanowires studied, the following sputter and deposition parameters were used:

Wire name		RF-plasma			Metal film
	Chamber	Ar pressure	Power	Time	
3w	K	15 sccm	20 W	480 s	Ti(5 nm)/Pt(75 nm)
T4-05	N	$1 \cdot 10^{-}2$ mbar	20 W	400 s	Al(2 nm)/Au(120 nm)
T5-03	N	$1 \cdot 10^{-}2$ mbar	20 W	400 s	Al(2 nm)/Au(120 nm)
Ni-test-O	N	$1 \cdot 10^{-}2$ mbar	20 W	100 s	Al(2 nm)/Au(100 nm)
Jan7-01	N	$1 \cdot 10^{-}2$ mbar	20 W	300 s	Al(2 nm)/Au(200 nm)
Jan4-02	N	$1 \cdot 10^{-}2$ mbar	20 W	300 s	Al(2n m)/Au(200 nm)
Jan4-01	N	$1 \cdot 10^{-}2$ mbar	20 W	300 s	Al(2 nm)/Au(200 nm)

K and N denote the two sputtering chambers in which the samples were prepared. K is a commercial CRC 600 sputtering chamber from Torr. N is a self-built system details on which are given in Ref. [Pel04].

B.6 Transmission x-ray microscopy

B.6.1 Setup

Transmission x-ray microscopy was performed at the XM-1 full field microscope of beamline 6.1.2 at the Advanced Light Source in Berkeley, CA, USA [Fis06]. Off-orbit elliptically polarized soft x-ray photons are provided by the storage ring of the Advanced Light Source using a bending magnet. A schematic of the XM-1 microscope is depicted in Fig. B.4. Consisting of a condenser, an objective lens, and a detector, the setting is to some extend comparable to the one of a light microscope. Due to the refractive index for soft x rays however, the use of Fresnel zone plates instead of conventional lenses is required. A pinhole between the condensor zone plate and the sample makes for monochromation. The x rays transmitted by the sample are projected onto a soft x-ray sensitive charge-coupled device (CCD) camera by a micro zone plate. State of the art is a resolution of about 12 nm [Fis10]. For a more detailed description of the microscope and possible applications the reader may refer to the website *http://www-cxro.lbl.gov/BL612/* as well as Refs. [Fis01, Fis06]. While the x-ray optics is in high vacuum to reduce absorption, the sample is located at room conditions. The application of external magnetic fields perpendicular to (≈ 200 mT) and along (≈ 100 mT) the sample surface is enabled by coil pairs that are fixed next to the sample holder. The field of view is limited to about 10 µm.

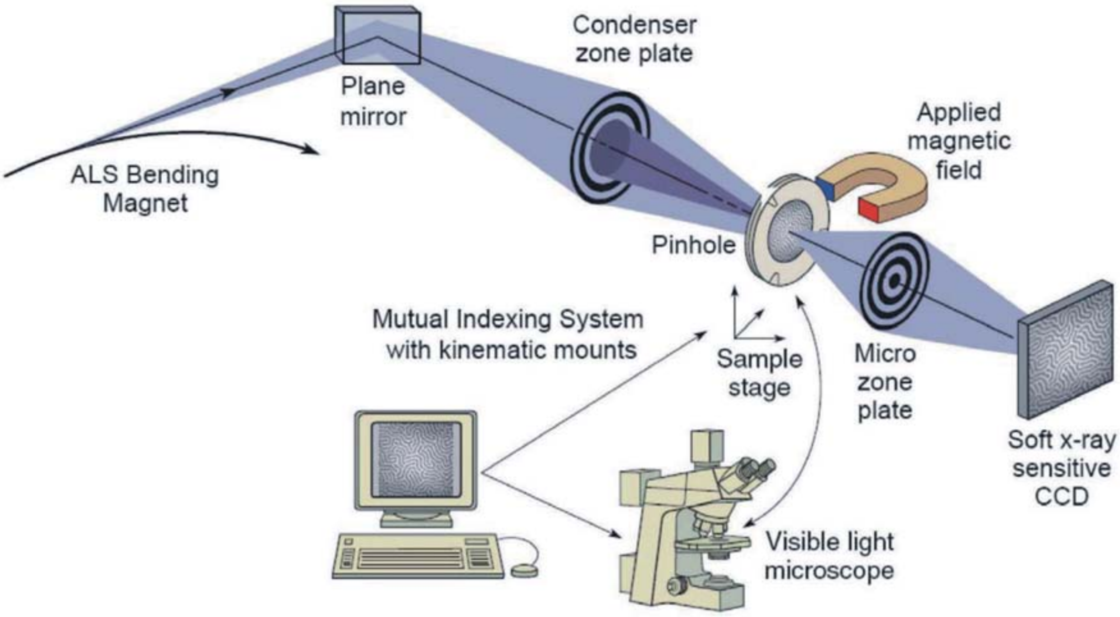

Figure B.4: Schematic of the XM-1 microscope at beamline 6.1.2 of the Advanced Light Source in Berkeley, CA, USA. From Ref. [Fis06].

B.6.2 Magnetic imaging of cylindrical nickel nanowires

We studied electrochemically synthesized nickel wires with diameters of 80 nm, 160 nm, 200 nm, and 300 nm during three beamtimes at the XM-1 microscope. For imaging the wires were dispersed on silicon-nitride membranes from Silson with a thickness of 150 nm. To locate the wires of interest, the membranes had markers written by electron-beam lithography. Magnetic contrast at the XM-1 microscope bases on the XMCD effect described in Sec. 2.4 and is thus proportional to the magnetization components along the projection of the x-ray beam. In-plane magnetized samples as the cylindrical nickel nanowires are therefore mounted at an angle of 60 degrees with respect to the beam axis. In principle it makes no difference for the XMCD signal, whether the helicity of the x-ray beam or the sample magnetization is inverted. Since beamline 6.1.2 at the Advanced Light Source does not come with an undulator to set the photon helicity, magnetic contrast can only be obtained by inverting the sample's magnetization. To obtain magnetic contrast two images of a wire were taken and subtracted from each other. The two images were either acquired in saturation at ±100 mT, after saturation at remanence, or during field sweeps with varying step widths. Despite exposure times up to several minutes, no convincing or reproducible magnetic contrast was obtained for all wire diameters studied.

Besides technical aspects such as the instability of the x-ray beam, which restricts the maximum exposure time, there are some fundamental aspects that could account for the impossibility of imaging cylindrical wires at the XM-1 microscope. One aspect is the thickness of the wires that remarkably reduces the intensity of transmitted x-ray photons. Our PEEM experiments, however, demonstrate, that magnetic contrast at the nickel L_3 and L_2 edges can be obtained in the shadow of nickel nanowires. As exemplified in publication [Kim11], this contrast is caused by the x-rays traversing the bulk of the nanostructure. Therefore, a fundamental impossibility of obtaining magnetic contrast in transmission geometry on nickel wires in the diameter range under consideration can be excluded.

The results on the magnetic behavior of nickel nanowires presented in chapter 5 imply, that the magnetic states in these nanostructures are rather complex and can thus not simply be reversed by driving opposite field sweeps. The continuous rotation of the magnetic moments away from the wire's axis under the application of a reverse field reduces the magnetic contrast that can be expected when subtracting two images recorded right before and after switching in comparison to a structure as flat permalloy wires where the in-plane component of the magnetization stays mainly constant at all times. The above aspects could account for the fact that during non of the various experiments at the XM-1 microscope a reliable magnetic contrast on cylindrical nickel nanowires was obtained.

B.7 Procedure for the elimination of thermal drift in Fig. 5.11(b)

While the switching-field distributions presented in Fig. 5.11(b) were recorded, the temperature in setup 3 was unstable. The temperature drift $\Delta T = \frac{\Delta R}{R \cdot \alpha}$ plotted in Fig. B.5 is calculated from the variation of the first resistance value R measured during each field sweep at ± 20 mT and using a temperature coefficient $\alpha = 0.004\ \Omega/\mathrm{K}$ [Joh]. The green data points in the lower panels of Fig. B.5 depict the switching fields as measured. With increasing sweep numbers a drift of the switching fields towards higher values is observed that can be correlated with the decrease in temperature ΔT. The underlying mechanism is thermal activation as explicated in Sec. 2.2.2. Even though the exact relation between H_{SF} and ΔT is unknown, the data was corrected as indicated by the red data points to eliminate the thermal drift. The indicator for the shifting of the data points was the observation that the switching fields associated with one accumulation value only scatter towards lower fields (compare (Fig. 5.11(a)). As a reference the ‘upper row’ of switching field was used here. It cannot be excluded that the switching-field distributions are actually broader than it is now indicated in Fig. 5.11(b).

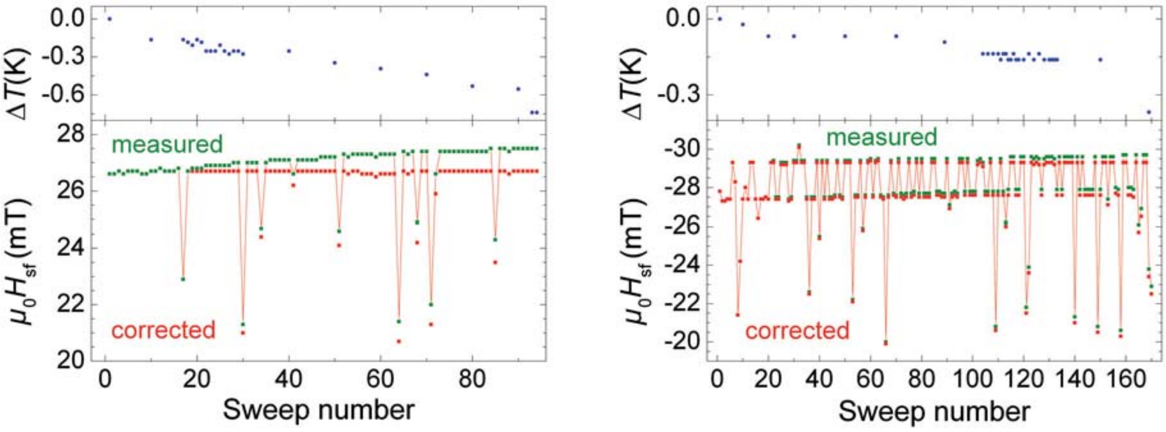

(a) (b)

Figure B.5: Data underlying Fig. 5.11(b). (a) and (b) depict the switching fields H_{SF} for positive and negative reverse fields, respectively. ΔT is the estimated temperature offset.

B.8 Magnetization reversal in cobalt-nickel nanowires

The synthesis of cobalt-nickel nanowires of various compositions as well as their structural and magnetic properties are described in Ref. [Veg12]. Figure B.6 reveals the magnetization reversal of an individual wire with a diameter of about 130 nm imaged by photoemission electron microscopy at the Co L_3 edge (776.6 eV). According to energy dispersive x-ray microanalysis on an ensemble of wires the composition stoichiometry of the wire is about $Co_{71}Ni_{29}$. X-ray diffraction measurements reveal a polycrystalline structure with a coexistence of fcc and hcp phases. Due to the high cobalt content and a broad distribution of magnetocrystalline anisotropy axes the magnetization reversal in the wire occurs via local magnetization rotation processes as it is already concluded by Vega *et al.* based on their results obtained by magneto-optical Kerr-effect magnetometry and vibrating sample magnetometry.

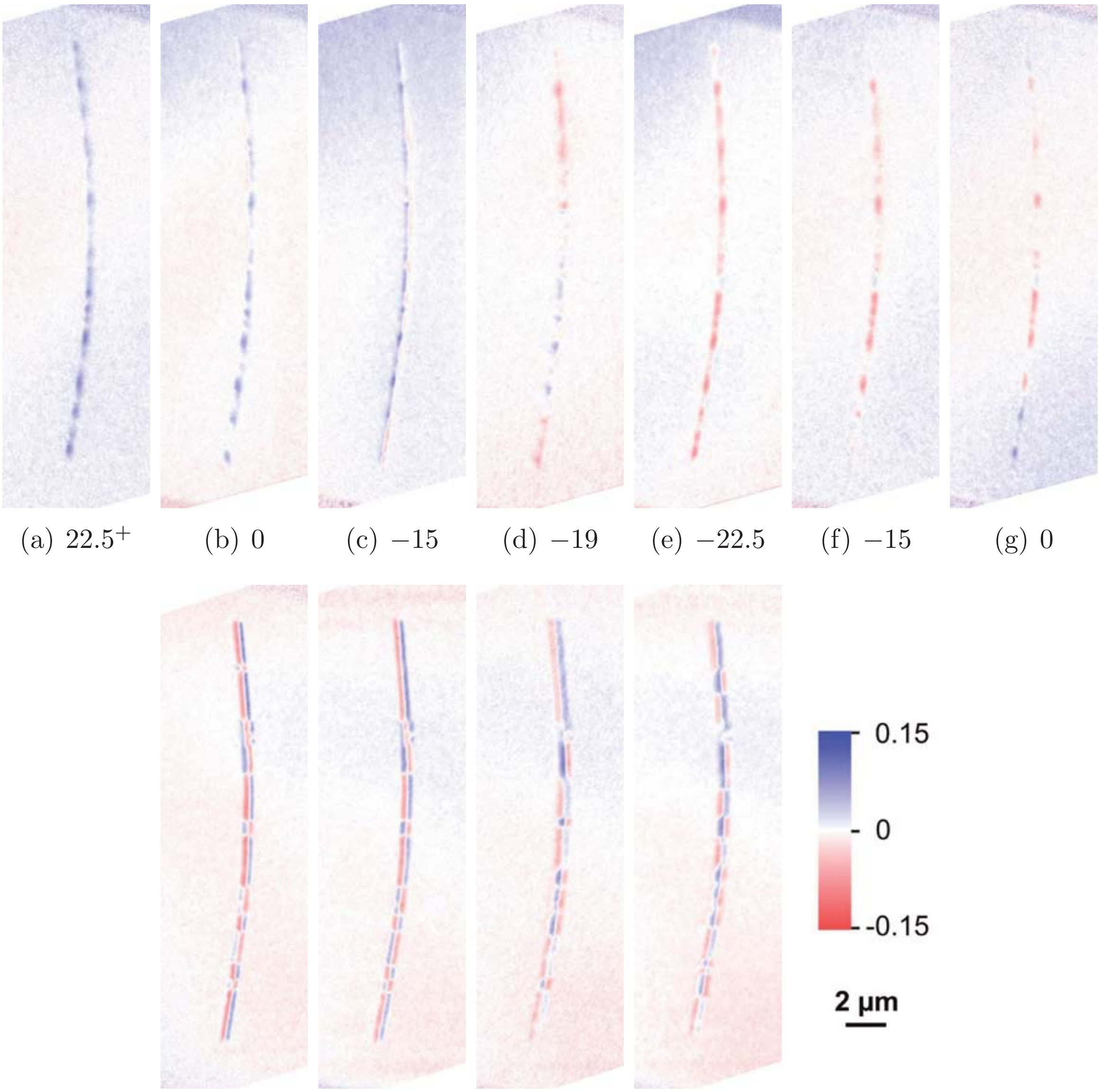

(a) 22.5^+ (b) 0 (c) -15 (d) -19 (e) -22.5 (f) -15 (g) 0

(h) 0^+ (i) -15 (j) -26 (k) -24 (l)

Figure B.6: Differential photoemission electron micrographs revealing the magnetization reversal of an electrochemically synthesized $Co_{71}Ni_{29}$ wire. (a) through (g) depict the magnetization components along the wire axis, (h) through (k) are the perpendicular components. Note that in (h) through (k) the contrast on the right hand side originates from the surface of the nanowire, while the inverted pattern to the left represents the XMCD contrast caused by the x rays that passed through the wire and thus probed the bulk magnetization. If not marked, the images were acquired in a row at the field values stated below the panels (values in mT). $^+$ or * indicates that an image was recorded in the respective applied field after saturation at ±68 mT, respectively. Images were acquired at 776.6 eV (Co L_3 edge). Estimated field constant: $0.075\frac{\mathrm{mT}}{\mathrm{mA}}$.

Bibliography

[Abe98] L. Abelmann, C. Lodder, A. Moser, M. E. Best, P. J. van Schendel, B. Stiefel, H. J. Hug, G. P. Heydon, A. Farley, S. R. Hoon, T. Pfaffelhuber, R. Proksch, K. Babcock, S. Porthun, and M. Haast, *Comparing the resolution of magnetic force microscopes using the CAMST reference samples*, J. Magn. Magn. Mater. **190**, 135 (1998). 58

[Aha58] A. Aharoni and S. Shtrikman, *Magnetization curve of the infinite cylinder*, Phys. Rev. **109**, 1522 (1958). 88

[Aha86] A. Aharoni, *Perfect and imperfect particles*, IEEE Trans. Magn. **22**, 478 (1986). 19, 20, 78

[Aha97a] A. Aharoni, *Angular dependence of nucleation by curling in a prolate spheroid*, J. Appl. Phys. **82**, 1281 (1997). 2, 20, 21, 54, 75, 76, 77, 81

[Aha97b] A. Aharoni, *Nucleation modes in ferromagnetic prolate spheroids*, J. Phys.: Condens. Matter **9**, 10009 (1997). 89

[Aha99] A. Aharoni, *Incoherent magnetization reversals in elongated particles*, J. Magn. Magn. Mater. **196-197**, 786 (1999). 85, 151

[Ake10] J. Akerman, M. Muñoz, M. Maicas, and J. L. Prieto, *Stochastic nature of the domain wall depinning in permalloy magnetic nanowires*, Phys. Rev. B **82**, 064426 (2010). 117

[All05] D. A. Allwood, G. Xiong, C. C. Faulkner, D. Atkinson, D. Petit, and R. P. Cowburn, *Magnetic domain-wall logic*, Science **309**, 1688 (2005). 1, 23

[All11] S. Allende and R. Arias, *Transverse domain wall propagation in modulated cylindrical nanostructures and possible geometric control*, Phys. Rev. B **83**, 174452 (2011). 124

[Alv10] L. S. E. Alvarez, K. Y. Wang, S. Lepadatu, S. Landi, S. J. Bending, and C. H. Marrows, *Spin-transfer-torque-assisted domain-wall creep in a Co/Pt multilayer wire*, Phys. Rev. Lett. **104**, 137205 (2010). 2

[Azi06] A. Aziz, S. J. Bending, H. G. Roberts, S. Crampin, P. J. Heard, and C. H. Marrows, *Angular dependence of domain wall resistivity in artificial magnetic domain structures*, Phys. Rev. Lett. **97**, 206602 (2006). 2

[Bac07] J. Bachmann, J. Jing, M. Knez, S. Barth, H. Shen, S. Mathur, U. Gösele, and K. Nielsch, *Ordered iron oxide nanotube arrays of controlled geometry and tunable magnetism by atomic layer deposition*, J. Am. Chem. Soc. **129**, 9445 (2007). 47

[Bai88] M. N. Baibich, J. M. Broto, A. Fert, F. N. Van Dau, F. Petroff, P. Eitenne, G. Creuzet, A. Friederich, and J. Chazelas, *Giant magnetoresistance of (001)Fe/(001)Cr magnetic superlattices*, Phys. Rev. Lett. **61**, 2472 (1988). 29

[Bar04] M. Barthelmess, C. Pels, A. Thieme, and G. Meier, *Stray fields of domains in permalloy microstructures - Measurements and simulations*, J. Appl. Phys. **95**, 5641 (2004). 58

[Bau90] L. Baumgarten, C. M. Schneider, H. Petersen, F. Schäfers, and J. Kirschner, *Magnetic x-ray dichroism in core-level photoemission from ferromagnets*, Phys. Rev. Lett. **65**, 492 (1990). 62

[Bel98] L. Belliard, J. Miltat, A. Thiaville, S. Dubois, J. L. Duvail, and L. Piraux, *Observing magnetic nanowires by means of magnetic force microscopy*, J. Magn. Magn. Mater. **190**, 1 (1998). 58

[Ber74] L. Berger, *Prediction of a domain-drag effect in uniaxial, non-compensated, ferromagnetic metals*, J. Phys. Chem. Solids **35**, 947 (1974). 22

[Ber78] L. Berger, *Low-field magnetoresistance and domain drag in ferromagnets*, J. Appl. Phys. **49**, 2156 (1978). 22, 32

[Ber84] L. Berger, *Exchange interaction between ferromagnetic domain wall and electric current in very thin metallic films*, J. Appl. Phys. **55**, 1954 (1984). 1

[Ber11] L. Berger, *Spin relaxation in metallic ferromagnets*, Phys. Rev. B **83**, 054410 (2011). 31

[BES] *http://www.helmholtz-berlin.de/*. 63

[Böh09] T. Böhnert, *Magneto-Widerstandsmessungen an fotolithografisch kontaktierten Nickel-Nanodrähten*, Diplomarbeit, Universität Hamburg (2009). 49, 174

[Bie07] A. Biehler, M. Kläui, M. Fonin, C. König, G. Güntherodt, and U. Rüdiger, *Domain structures and the influence of current on domains and domain walls in highly spin-polarized CrO_2 wire elements*, Phys. Rev. B **75**, 184427 (2007). 107

[Bin89] G. Binasch, P. Grünberg, F. Saurenbach, and W. Zinn, *Enhanced magnetoresistance in layered magnetic structures with antiferromagnetic interlayer exchange*, Phys. Rev. B **39**, 4828 (1989). 29

[Blü95] S. Blügel, *Magnetism of 4d and 5d transition metal adlayers on Ag(001): Dependence on the adlayer thickness*, Phys. Rev. B **51**, 2025 (1995). 8

[Bla94] J. A. C. Bland and B. Heinrich, *Ultrathin magnetic structures I*, Springer, Berlin (1994). 8

[Blu01] S. Blundell, *Magnetism in condensed matter*, Oxford University Press Inc., New York (2001). 6

[Bob04] J. F. Bobo, L. Gabillet, and M. Bibes, *Recent advances in nanomagnetism and spin electronics*, J. Phys.: Condens. Matter **16**, 471 (2004). 8

[Boc09] L. Bocklage, B. Krüger, T. Matsuyama, M. Bolte, U. Merkt, D. Pfannkuche, and G. Meier, *Dependence of magnetic domain-wall motion on a fast changing current*, Phys. Rev. Lett. **103**, 197204 (2009). 28

[Boc11] L. Bocklage, *Current-induced magnetization dynamics of ferromagnetic nanostructures*, Dissertation, Universität Hamburg (2011). 50

[Bou08] O. Boulle, J. Kimling, P. Warnicke, M. Kläui, U. Rüdiger, G. Malinowski, H. J. M. Swagten, B. Koopmans, C. Ulysse, and G. Faini, *Nonadiabatic spin transfer torque in high anisotropy magnetic nanowires with narrow domain walls*, Phys. Rev. Lett. **101**, 216601 (2008). 2, 28

[Bou11] O. Boulle, G. Malinowski, and M. Kläui, *Current-induced domain wall motion in nanoscale ferromagnetic elements*, Mat. Sci. Eng. R **72**, 159 (2011). 2, 28

[Bré07] C. Bréchignac, P. Houdy, and M. Lahmani, *Nanomaterials and nanochemistry*, Springer, Berlin (2007). 9

[Bri11] J. Briones, F. Montaigne, M. Hehn, D. Lacour, J. R. Childress, and M. J. Carey, *Stochastic and complex depinning dynamics of magnetic domain walls*, Phys. Rev. B **83**, 060401 (2011). 27, 94, 117

[Bro45] W. F. Brown, *Virtues and weaknesses of the domain concept*, Rev. Mod. Phys. **17**, 15 (1945). 84

[Bro91] F. J. A. den Broeder, W. Hoving, and P. J. H. Bloemen, *Magnetic anisotropy of multilayers*, J. Magn. Magn. Mater. **93**, 562 (1991). 11

[Bry10] M. T. Bryan, J. Dean, T. Schrefl, F. E. Thompson, J. Haycock, and D. A. Allwood, *The effect of trapping superparamagnetic beads on domain wall motion*, Appl. Phys. Lett. **96**, 192503 (2010). 1

[Cab74] G. G. Cabrera and L. M. Falicov, *Theory of the residual resistivity of Bloch walls - I. Paramagnetic effects*, Phys. Status Solidi B **61**, 539 (1974). 32

[Cam70] I. A. Campbell, A. Fert, and O. Jaoul, *The spontaneous resistivity anisotropy in Ni-based alloys*, J. Phys. C: Solid State **3**, S95 (1970). 31

[Cam82] I. A. Campbell and A. Fert, Ferromagnetic Materials **3**, 747 (1982). 30

[Cay04] F. Cayssol, D. Ravelosona, C. Chappert, J. Ferré, and J.-P. Jamet, *Domain wall creep in magnetic wires*, Phys. Rev. Lett. **92**, 107202 (2004). 28

[Cha98] C. Chappert, H. Bernas, J. Ferré, V. Kottler, J.-P. Jamet, Y. Chen, E. Cambril, T. Devolder, F. Rousseaux, V. Mathet, and H. Launois, *Planar patterned magnetic media obtained by ion irradiation*, Science **280**, 1919 (1998). 25

[Che90] C. T. Chen, F. Sette, Y. Ma, and S. Modesti, *Soft-x-ray magnetic circular dichroism at the $L_{2,3}$ edges of nickel*, Phys. Rev. B **42**, 7262 (1990). 33, 99, 102

[Che91] D.-X. Chen, J. Brug, and R. Goldfarb, *Demagnetizing factors for cylinders*, IEEE Trans. Magn. **27**, 3601 (1991). 75

[Che10] A. P. Chen, K. Y. Guslienko, and J. Gonzalez, *Magnetization configurations and reversal of thin magnetic nanotubes with uniaxial anisotropy*, J. Appl. Phys. **108**, 083920 (2010). 40, 82, 107

[Cho69] K. L. Chopra, *Thin Film Phenomena Vol. 1*, McGraw-Hill Book Company, New York (1969). 8, 11

[Cho10] Y. T. Chong, D. Görlitz, S. Martens, M. Y. E. Yau, S. Allende, J. Bachmann, and K. Nielsch, *Multilayered core/shell nanowires displaying two distinct magnetic switching events*, Adv. Mater. **22**, 2435 (2010). 2

[Cra63] J. Crangle and G. C. Hallam, *The magnetization of face-centred cubic and body-centred cubic iron + nickel alloys*, Proc. R. Soc. London A **272**, 119 (1963). 75

[Don98] M. J. Donahue, *A variational approach to exchange energy calculations in micromagnetics*, J. Appl. Phys. **83**, 6491 (1998). 108

[Don99] M. J. Donahue and D. G. Porter, *OOMMF User's Guide, Version 1.0* (1999), interagency Report NISTIR 6376. 36

[Dör38] W. Döring, *Die Abhängigkeit des Widerstandes von Nickelkristallen von der Richtung der spontanen Magnetisierung*, Ann. Phys. **424**, 259 (1938). 32

[Dür09] H. A. Dürr, T. Eimüller, H.-J. Elmers, S. Eisebitt, M. Farle, W. Kuch, F. Matthes, M. Martins, H.-C. Mertins, P. M. Oppeneer, L. Plucinski, C. M. Schneider, H. Wende, W. Wurth, and H. Zabel, *A closer look into magnetism: Opportunities with synchrotron radiation*, IEEE Trans. Magn. **45**, 15 (2009). 62

[Ehl88] J. Ehlert, F. K. Hübner, and W. Sperber, *Micromagnetics of cylindrical particles*, Phys. Status Solidi A **106**, 239 (1988). 84

[Fan] H. Fangohr, T. Fischbacher, M. Franchin, G. Bordignon, J. Generowicz, A. Knittel, M. Walter, and M. Albert, *Nmag User Manual.* 36

[Fas04] J. Fassbender, D. Ravelosona, and Y. Samson, *Tailoring magnetism by light-ion irradiation*, J. Phys. D: Appl. Phys. **37**, R179 (2004). 25

[Fas08] J. Fassbender and J. McCord, *Magnetic patterning by means of ion irradiation and implantation*, J. Magn. Magn. Mater. **320**, 579 (2008). 110, 154

[Fer69] A. Fert, *Two-current conduction in ferromagnetic metals and spin wave-electron collisions*, J. Phys. C: Solid State **2**, 1784 (1969). 31

[Fer97] R. Ferré, K. Ounadjela, J. M. George, L. Piraux, and S. Dubois, *Magnetization processes in nickel and cobalt electrodeposited nanowires*, Phys. Rev. B **56**, 14066 (1997). 73, 107

[Fis01] P. Fischer, T. Eimüller, G. Schütz, G. Denbeaux, A. Pearson, L. Johnson, D. Attwood, S. Tsunashima, M. Kumazawa, N. Takagi, M. Köhler, and G. Bayreuther, *Element-specific imaging of magnetic domains at 25 nm spatial resolution using soft x-ray microscopy*, Rev. Sci. Instrum. **72**, 2322 (2001). 176

[Fis06] P. Fischer, *Studies of magnetic microstructures with soft x-ray transmission microscopy*, IEEE J. Quantum. Electron. **42**, 36 (2006). 176

[Fis07] T. Fischbacher, M. Franchin, G. Bordignon, and H. Fangohr, *A systematic approach to multiphysics extensions of finite-element-based micromagnetic simulations: Nmag*, IEEE Trans. Magn. **43**, 2896 (2007). 37

[Fis10] P. Fischer, *Viewing spin structures with soft x-ray microscopy*, Mater. Today **13**, 14 (2010). 176

[Flo] Florian Kronast, private communication. 64

[For02] H. Forster, T. Schrefl, W. Scholz, D. Suess, V. Tsiantos, and J. Fidler, *Micromagnetic simulation of domain wall motion in magnetic nano-wires*, J. Magn. Magn. Mater. **249**, 181 (2002). 86

[FR10] A. Fraile Rodríguez, A. Kleibert, J. Bansmann, A. Voitkans, L. J. Heyderman, and F. Nolting, *Size-dependent spin structures in iron nanoparticles*, Phys. Rev. Lett. **104**, 127201 (2010). 100

[Fra12a] J. H. Franken, M. Hoeijmakers, R. Lavrijsen, and H. J. M. Swagten, *Domain-wall pinning by local control of anisotropy in Pt/Co/Pt strips*, J. Phys.: Condens. Matter **24**(2), 024216 (2012). 154

[Fra12b] J. H. Franken, M. Hoeijmakers, H. J. M. Swagten, and B. Koopmans, *Tunable resistivity of individual magnetic domain walls*, Phys. Rev. Lett. **108**, 037205 (2012). 2

[Fra12c] J. H. Franken, H. J. M. Swagten, and B. Koopmans, *Shift registers based on magnetic domain wall ratchets with perpendicular anisotropy*, Nat. Nanotechnol. **7**, 499 (2012). 1

[Fre57] E. H. Frei, S. Shtrikman, and D. Treves, *Critical size and nucleation field of ideal ferromagnetic particles*, Phys. Rev. **106**, 446 (1957). 20, 21, 80

[Fre85] P. P. Freitas and L. Berger, *Observation of s-d exchange force between domain walls and electric current in very thin permalloy films*, J. Appl. Phys. **57**, 1266 (1985). 22

[Fre90] D. Fredkin and T. Koehler, *Hybrid method for computing demagnetizing fields*, IEEE Trans. Magn. **26**, 415 (1990). 38

[Gar95] A. Garg, *Escape-field distribution for escape from a metastable potential well subject to a steadily increasing bias field*, Phys. Rev. B **51**, 15592 (1995). 27, 28

[Gar01] J. M. García, A. Thiaville, J. Miltat, K. J. Kirk, J. N. Chapman, and F. Alouges, *Quantitative interpretation of magnetic force microscopy images from soft patterned elements*, Appl. Phys. Lett. **79**, 656 (2001), and references therein. 61

[Gla12] S. Glathe and R. Mattheis, *Magnetic domain wall pinning by kinks in magnetic nanostripes*, Phys. Rev. B **85** (2012). 26

[Gol03] D. Goll, G. Schütz, and H. Kronmüller, *Critical thickness for high-remanent single-domain configurations in square ferromagnetic thin platelets*, Phys. Rev. B **67**, 094414 (2003). 10

[Gor99] R. P. van Gorkom, A. Brataas, and G. E. W. Bauer, *Negative domain wall resistance in ferromagnets*, Phys. Rev. Lett. **83**, 4401 (1999). 32

[Has06] C. Hassel, M. Brands, F. Y. Lo, A. D. Wieck, and G. Dumpich, *Resistance of a single domain wall in (Co/Pt)$_7$ multilayer nanowires*, Phys. Rev. Lett. **97**, 226805 (2006). 2

[Hay06a] M. Hayashi, L. Thomas, Y. B. Bazaliy, C. Rettner, R. Moriya, X. Jiang, and S. S. P. Parkin, *Influence of current on field-driven domain wall motion in permalloy nanowires from time resolved measurements of anisotropic magnetoresistance*, Phys. Rev. Lett. **96**, 197207 (2006). 27

[Hay06b] M. Hayashi, L. Thomas, C. Rettner, R. Moriya, X. Jiang, and S. S. P. Parkin, *Dependence of current and field driven depinning of* *domain walls on their structure and chirality in permalloy nanowires*, Phys. Rev. Lett. **97**, 207205 (2006). 2, 26, 117

[Hei28] W. Heisenberg, *Zur Theorie des Ferromagnetismus*, Z. Phys. **49**, 619 (1928). 6

[Her90] G. Herzer, *Grain size dependence of coercivity and permeability in nanocrystalline ferromagnets*, IEEE Trans. Magn. **26**, 1397 (1990). 82

[Her02] R. Hertel, *Computational micromagnetism of magnetization processes in nickel nanowires*, J. Magn. Magn. Mater. **249**, 251 (2002). 84

[Her04] R. Hertel and J. Kirschner, *Magnetization reversal dynamics in nickel nanowires*, Physica B **343**, 206 (2004). 37, 41, 84, 85, 124

[Him03] A. Himeno, T. Ono, S. Nasu, K. Shigeto, K. Mibu, and T. Shinjo, *Dynamics of a magnetic domain wall in magnetic wires with an artificial neck*, J. Appl. Phys. **93**, 8430 (2003). 24, 26

[Hor71] R. Hornreich, H. Rubinstein, and R. Spain, *Magnetostrictive phenomena in metallic materials and some of their device applications*, IEEE Trans. Magn. **7**, 29 (1971). 10

[Hub09] A. Hubert and R. Schäfer, *Magnetic Domains*, Springer, Berlin (2009). 9, 11, 14, 15, 17, 19, 20, 21, 23, 80, 82

[Iba99] H. Ibach and H. Lüth, *Festkörperphysik*, Springer, Berlin (1999). 7

[Im09] M.-Y. Im, L. Bocklage, P. Fischer, and G. Meier, *Direct observation of stochastic domain-wall depinning in magnetic nanowires*, Phys. Rev. Lett. **102**, 147204 (2009). 26, 95

[Ima02] S. Imada, S. Suga, W. Kuch, and J. Kirschner, *Magnetic microspectroscopy by a combination of XMCD and PEEM*, Surf. Rev. Lett. **9**, 877 (2002). 62

[Jao77] O. Jaoul, I. Campbell, and A. Fert, *Spontaneous resistivity anisotropy in Ni alloys*, J. Magn. Magn. Mater. **5**, 23 (1977). 31

[Jes98] O. Jessensky, F. Müller, and U. Gösele, *Self-organized formation of hexagonal pore arrays in anodic alumina*, Appl. Phys. Lett. **72**, 1173 (1998), and references therein. 46

[Joh] Johannes Kimling, private communication. 178

[Joh96] M. T. Johnson, P. J. H. Bloemen, F. J. A. den Broeder, and J. J. de Vries, *Magnetic anisotropy in metallic multilayers*, Rep. Prog. Phys. **59**, 1409 (1996). 11

[Ken01] A. D. Kent, J. Yu, U. Rüdiger, and S. S. P. Parkin, *Domain wall resistivity in epitaxial thin film microstructures*, J. Phys.: Condens. Matter **13**, R461 (2001). 32

[Kim11] J. Kimling, F. Kronast, S. Martens, T. Böhnert, M. Martens, J. Herrero-Albillos, L. Tati-Bismaths, U. Merkt, K. Nielsch, and G. Meier, *Photoemission electron microscopy of three-dimensional magnetization configurations in core-shell nanostructures*, Phys. Rev. B **84**, 174406 (2011). 1, 3, 40, 45, 66, 138, 153, 177

[Kim11b] J. Kim, S. Kim, S. Lee, and J. Hong, *Domain wall types and field-induced domain wall motion in L-shaped nanowires*, Thin Solid Films **519**, 8263 (2011). 117

[Kim13] J. Kimling, T. Gerhardt, A. Kobs, A. Vogel, S. Wintz, M.-Y. Im, P. Fischer, H. P. Oepen, U. Merkt, and G. Meier, *Tuning of the nucleation field in nanowires with perpendicular magnetic anisotropy*, J. Appl. Phys. **113**, 163902 (2013). 3, 143, 144, 153

[Kis03] M. Kisielewski, A. Maziewski, M. Tekielak, J. Ferré, S. Lemerle, V. Mathet, and C. Chappert, *Magnetic anisotropy and magnetization reversal processes in Pt/Co/Pt films*, J. Magn. Magn. Mater. **260**, 231 (2003). 15

[Kit49] C. Kittel, *Physical theory of ferromagnetic domains*, Rev. Mod. Phys. **21**, 541 (1949). 9, 14, 15

[Kit05] C. Kittel, *Introduction to solid state physics*, John Wiley & Sons, Ltd (2005). 8

[Klä03a] M. Kläui, C. A. F. Vaz, J. A. C. Bland, W. Wernsdorfer, G. Faini, E. Cambril , and L. J. Heyderman, *Domain wall motion induced by spin polarized currents in ferromagnetic ring structures*, Appl. Phys. Lett. **83**, 105 (2003). 1

[Klä03b] M. Kläui, C. A. F. Vaz, J. Rothman, J. A. C. Bland, W. Wernsdorfer, G. Faini, and E. Cambril, *Domain wall pinning in narrow ferromagnetic ring structures probed by magnetoresistance measurements*, Phys. Rev. Lett. **90**, 097202 (2003). 26

[Klä05] M. Kläui, P.-O. Jubert, R. Allenspach, A. Bischof, J. A. C. Bland, G. Faini, U. Rüdiger, C. A. F. Vaz, L. Vila, and C. Vouille, *Direct observation of domain-wall configurations transformed by spin currents*, Phys. Rev. Lett. **95**, 026601 (2005). 27

[Klä08] M. Kläui, *Head-to-head domain walls in magnetic nanostructures*, J. Phys.: Condens. Matter **20**, 313001 (2008). 27

[Kne07] M. Knez, K. Nielsch, and L. Niiniströ, *Synthesis and surface engineering of complex nanostructures by atomic layer deposition*, Adv. Mater. **19**, 3425 (2007). 46

[Kop07] K. Kopitzki, *Einführung in die Festkörperphysik*, Teubner, Wiesbaden (2007). 6

[Kor] Kornelius Nielsch, private communication. 83

[Koy11] T. Koyama, D. Chiba, K. Ueda, H. Tanigawa, S. Fukami, T. Suzuki, N. Ohshima, N. Ishiwata, Y. Nakatani, and T. Ono, *Wire width dependence of threshold current density for domain wall motion in Co/Ni nanowires*, IEEE Trans. Magn. **47**, 3089 (2011). 24

[Krü07] B. Krüger, D. Pfannkuche, M. Bolte, G. Meier, and U. Merkt, *Current-driven domain-wall dynamics in curved ferromagnetic nanowires*, Phys. Rev. B **75**, 054421 (2007). 22

[Krü12] B. Krüger, *The interaction of transverse domain walls*, J. Phys.: Condens. Matter **24**, 024209 (2012). 126

[Kri] Kristina Pitzschel, private communication. 77

[Kro62] H. Kronmüller, *Mikromagnetisehe Berechnung der Magnetisierung in der Umgebung unmagnetischer Einschlüsse in Ferromagnetika*, Z. Phys. **168**, 478 (1962). 18

[Kro87] H. Kronmüller, *Theory of nucleation fields in inhomogeneous ferromagnets*, Phys. Status Solidi B **144**, 385 (1987). 89

[Kro07] H. Kronmüller and S. Parkin, Handbook of Magnetism and Advanced Magnetic Materials Vol. 2, John Wiley & Sons, Ltd (2007). 89

[Kro10] F. Kronast, J. Schlichting, F. Radu, S. K. Mishra, T. Noll, and H. A. Dürr, *Spin-resolved photoemission microscopy and magnetic imaging in applied magnetic fields*, Surf. Interface Anal. **42**, 1532 (2010). 62, 63, 64

[Kub87] R. L. Kubena and J. W. Ward, *Current-density profiles for a Ga$^+$ ion microprobe and their lithographic implications*, Appl. Phys. Lett. **51**, 1960 (1987). 111

[Led95] M. Lederman, R. O'Barr, and S. Schultz, *Experimental study of individual ferromagnetic sub-micron cylinders*, IEEE Trans. Magn. **31**, 3793 (1995). 73, 76, 77, 78, 107

[Lee71] E. W. Lee and M. A. Asgar, *The magnetostriction of nickel*, Proc. R. Soc. London A **326**, 73 (1971). 10

[Lee06] W. Lee, R. Ji, U. Gösele, and K. Nielsch, *Fast fabrication of long-range ordered porous alumina membranes by hard anodization*, Nat. Mater. **5**, 741 (2006). 2, 46

[Lee09] J. Lee, S. Farhangfar, R. Yang, R. Scholz, M. Alexe, U. Gösele, J. Lee, and K. Nielsch, *A novel approach for fabrication of bismuth-silicon dioxide core-shell structures by atomic layer deposition*, J. Mater. Chem. **19**, 7050 (2009). 46

[Len10] P. Lendecke, U. Merkt, and G. Meier, *Hall micromagnetometry of domain-wall depinning in permalloy nanowires*, J. Magn. Magn. Mater. **322**, 1399 (2010). 27

[Lev97] P. M. Levy and S. Zhang, *Resistivity due to domain wall scattering*, Phys. Rev. Lett. **79**, 5110 (1997). 32

[Li98] A. P. Li, F. Müller, A. Birner, K. Nielsch, and U. Gösele, *Hexagonal pore arrays with a 50 - 420 nm interpore distance formed by self-organization in anodic alumina*, J. Appl. Phys. **84**, 6023 (1998). 46

[Lil50] B. A. Lilley, *Energies and widths of domain boundaries in ferromagnetics*, Phil. Mag. Ser. **41**, 792 (1950). 17

[Liu05] Y. Liu, D. Shindo, and D. J. Sellmyer, *Handbook of Advanced Magnetic Materials*, Vol. 1, Springer, Berlin (2005). 19

[Loh99] J. Lohau, S. Kirsch, A. Carl, G. Dumpich, and E. F. Wassermann, *Quantitative determination of effective dipole and monopole moments of magnetic force microscopy tips*, J. Appl. Phys. **86**, 3410 (1999). 58

[Mar87] Y. Martin and H. K. Wickramasinghe, *Magnetic imaging by "force microscopy" with 1000 Å resolution*, Appl. Phys. Lett. **50**, 1455 (1987). 58

[Mar94] C. R. Martin, *Nanomaterials: A membrane-based synthetic approach*, Science **266**, 1961 (1994). 45

[Mar05] C. H. Marrows, *Spin-polarised currents and magnetic domain walls*, Adv. Phys. **54**, 585 (2005). 32

[Mat61] B. T. Matthias, R. M. Bozorth, and J. H. Van Vleck, *Ferromagnetic interaction in EuO*, Phys. Rev. Lett. **7**, 160 (1961). 6

[Mat01] J. Mathon and A. Umerski, *Physics of low dimensional systems*, Kluwer Academic / Plenum Publishers, New York, New York (2001). 33

[McG75] T. McGuire and R. Potter, *Anisotropic magnetoresistance in ferromagnetic 3d alloys*, IEEE Trans. Magn. **11**, 1018 (1975). 31

[Mei96] J. Meier, B. Doudin, and J.-P. Ansermet, *Magnetic properties of nanosized wires*, J. Appl. Phys. **79**, 6010 (1996). 46, 83

[Met07] P. J. Metaxas, J.-P. Jamet, A. Mougin, M. Cormier, J. Ferré, V. Baltz, B. Rodmacq, B. Dieny, and R. L. Stamps, *Creep and flow regimes of magnetic domain-wall motion in ultrathin* Pt/Co/Pt *films with perpendicular anisotropy*, Phys. Rev. Lett. **99**, 217208 (2007). 28

[Met09] P. J. Metaxas, P.-J. Zermatten, J.-P. Jamet, J. Ferré, G. Gaudin, B. Rodmacq, A. Schuhl, and R. L. Stamps, *Periodic magnetic domain wall pinning in an ultrathin film with perpendicular anisotropy generated by the stray magnetic field of a ferromagnetic nanodot array*, Appl. Phys. Lett. **94**, 132504 (2009). 154

[Mil07] M. J. Miltat, Jacques E. et Donahue, *Numerical micromagnetics: Finite difference methods*, Handbook of Magnetism and Advanced Magnetic Materials Vol. 2, John Wiley & Sons, Ltd (2007). 12

[MM] *http://micromagnum-tis.informatik.uni-hamburg.de;* MicroMagnun is developed by the group Arbeitsbereich Technische Informatik Systeme of the Department of Informatics and the Nanostructure Physics of the Institute of Applied Physics of the Universität Hamburg. 37

[Mot36] N. F. Mott, *The electrical conductivity of transition metals*, Proc. R. Soc. London A **153**, 699 (1936). 29, 30, 31

[Mot64] N. F. Mott, *Electrons in transition metals*, Adv. Phys. **13**, 325 (1964). 29, 31

[Mou07] A. Mougin, M. Cormier, J. P. Adam, P. J. Metaxas, and J. Ferré, *Domain wall mobility, stability and Walker breakdown in magnetic nanowires*, Europhys. Lett. **78**, 57007 (2007). 28

[Nah09] G. Nahrwold, L. Bocklage, J. M. Scholtyssek, T. Matsuyama, B. Krüger, U. Merkt, and G. Meier, *Current-induced domain-wall depinning in curved permalloy nanowires*, J. Appl. Phys. **105**, 07D511 (2009). 23

[Nav07] D. Navas, M. Hernández-Vélez, W. Lee, K. Nielsch, and M. Vázquez, *Ordered Ni nanohole arrays with engineered geometrical aspects and magnetic anisotropy*, Appl. Phys. Lett. **90**, 192501 (2007). 47

[New93] A. J. Newell, W. Williams, and D. J. Dunlop, *A generalization of the demagnetizing tensor for nonuniform magnetization*, J. Geophys. Res. **98**, 9551 (1993). 38

[Nie00] K. Nielsch, F. Müller, A.-P. Li, and U. Gösele, *Uniform nickel deposition into ordered alumina pores by pulsed electrodeposition*, Adv. Mater. **12**, 582 (2000). 47

[Nie02a] K. Nielsch, *Hochgeordnete ferromagnetische Nano-Stabensembles: Elektrochemische Herstellung und magnetische Charakterisierung*, Dissertation, Martin-Luther-Universität Halle-Wittenberg (2002). 82

[Nie02b] K. Nielsch, J. Choi, K. Schwirn, R. B. Wehrspohn, and U. Gösele, *Self-ordering regimes of porous alumina: The 10 porosity rule*, Nano Lett. **2**, 677 (2002). 46, 47, 167

[Nix69] W. C. Nixon, *Scanning electron microscopy*, Contemp. Phys. **10**, 71 (1969). 45

[Nma] *http://www.nmag.soton.ac.uk*. 86

[Nol86] W. Nolting, *Quantentheorie des Magnetismus*, Vol. 1, Teubner, Stuttgart (1986). 6

[O'B11] L. O'Brien, D. Petit, E. R. Lewis, R. P. Cowburn, D. E. Read, J. Sampaio, H. T. Zeng, and A.-V. Jausovec, *Tunable remote pinning of domain walls in magnetic nanowires*, Phys. Rev. Lett. **106**, 087204 (2011). 154

[O'H00] R. C. O'Handley, *Modern magnetic materials: Principles and applications*, John Wiley & Sons, Ltd (2000). 7, 9, 10, 15, 26, 29, 30, 32, 80, 84

[Pan03] Q. A. Pankhurst, J. Connolly, S. K. Jones, and J. Dobson, *Applications of magnetic nanoparticles in biomedicine*, J. Phys. D: Appl. Phys. **36**, R167 (2003). 1

[Pan05] H. Pan, H. Sun, C. Poh, Y. Feng, and J. Lin, *Single-crystal growth of metallic nanowires with preferred orientation*, Nanotechnology **16**, 1559 (2005). 82

[Par02] C.-M. Park and J. Bain, *Local degradation of magnetic properties in magnetic thin films irradiated by Ga$^+$ focused-ion-beams*, IEEE Trans. Magn. **38**, 2237 (2002). 110

[Par05] S. S. P. Parkin, *US Patents 6834005, 6898132, 6920062, 7031178* (2004-2005). 1

[Par08] S. S. P. Parkin, M. Hayashi, and L. Thomas, *Magnetic domain-wall racetrack memory*, Science **320**, 190 (2008). 1, 23, 27

[Pel04] C. Pels, *Ferromagnetic electrodes for spin-polarized transport - Technology and experiments*, Dissertation, Universität Hamburg (2004). 175

[Pet08] D. Petit, A.-V. Jausovec, D. Read, and R. P. Cowburn, *Domain wall pinning and potential landscapes created by constrictions and protrusions in ferromagnetic nanowires*, J. Appl. Phys. **103**, 114307 (2008). 26

[Pig00] S. Pignard, G. Goglio, A. Radulescu, L. Piraux, S. Dubois, A. Declémy, and J. L. Duvail, *Study of the magnetization reversal in individual nickel nanowires*, J. Appl. Phys. **87**, 824 (2000). 73, 74, 76, 77, 84, 87, 107

[Pir97] L. Piraux, S. Dubois, E. Ferain, R. Legras, K. Ounadjela, J. George, J. Maurice, and A. Fert, *Anisotropic transport and magnetic properties of arrays of sub-micron wires*, J. Magn. Magn. Mater. **165**, 352 (1997). 73

[Pit09] K. Pitzschel, J. M. Montero Montero, J. Escrig, O. Albrecht, K. Nielsch, and J. Bachmann, *Controlled introduction of diameter modulations in arrayed magnetic iron oxide nanotubes*, ACS Nano **3**, 3463 (2009). 2, 47

[Pit11] K. Pitzschel, J. Bachmann, S. Martens, J. M. Montero Moreno, J. Kimling, G. Meier, J. Escrig, K. Nielsch, and D. Görlitz, *Magnetic reversal of cylindrical nickel nanowires with modulated diameters*, J. Appl. Phys. **109**, 033907 (2011). 2, 46, 47, 77, 120, 134, 155

[Pos70] G. E. Possin, *A method for forming very small diameter wires*, Rev. Sci. Instrum. **41**, 772 (1970). 45

[Qin99] W. Qin, Z. Chen, P. Huang, and Y. Zhuang, *Crystal lattice expansion of nanocrystalline materials*, J. Alloy. Compd. **292**, 230 (1999). 84

[Qui72] J. A. Quinn, J. L. Anderson, W. S. Ho, and W. J. Petzny, *Model pores of molecular dimension: The preparation and characterization of track-etched membranes*, Biophys. J. **12**, 990 (1972). 45

[Ram96] K. Ramstöck, W. Hartung, and A. Hubert, *The phase diagram of domain walls in narrow magnetic strips*, Phys. Status Solidi A **155**, 505 (1996). 17

[Rap12] E. Rapoport and G. S. D. Beach, *Dynamics of superparamagnetic microbead transport along magnetic nanotracks by magnetic domain walls*, Appl. Phys. Lett. **100**, 082401 (2012). 1

[Raq02] B. Raquet, M. Viret, E. Sondergard, O. Cespedes, and R. Mamy, *Electron-magnon scattering and magnetic resistivity in* 3d *ferromagnets*, Phys. Rev. B **66**, 024433 (2002). 31

[Rhe07a] Y. Rheem, B.-Y. Yoo, W. P. Beyermann, and N. V. Myung, *Electro- and magneto-transport properties of a single CoNi nanowire*, Nanotechnology **18**, 125204 (2007). 87

[Rhe07b] Y. Rheem, B.-Y. Yoo, W. P. Beyermann, and N. V. Myung, *Magnetotransport studies of a single nickel nanowire*, Nanotechnology **18**, 015202 (2007). 73, 77, 79, 82

[Rij95] T. G. S. M. Rijks, R. Coehoorn, M. J. M. de Jong, and W. J. M. de Jonge, *Semiclassical calculations of the anisotropic magnetoresistance of NiFe-based thin films, wires, and multilayers*, Phys. Rev. B **51**, 283 (1995). 32, 100

[Rud54] M. A. Ruderman and C. Kittel, *Indirect exchange coupling of nuclear magnetic moments by conduction electrons*, Phys. Rev. **96**, 99 (1954). 6

[Sai04] E. Saitoh, H. Miyajima, T. Yamaoka, and G. Tatara, *Current-induced resonance and mass determination of a single magnetic domain wall*, Nature **423**, 203 (2004). 153

[Sal12] M. S. Salem, P. Sergelius, R. Zierold, J. M. Montero Moreno, D. Görlitz, and K. Nielsch, *Magnetic characterization of nickel-rich NiFe nanowires grown by pulsed electrodeposition*, J. Mater. Chem. **22**, 8549 (2012). 47, 84, 120, 121

[San11] A. Santos, J. M. Montero Moreno, J. Bachmann, K. Nielsch, P. Formentín, J. Ferré-Borrull, J. Pallarès, and L. F. Marsal, *Understanding pore rearrangement during mild to hard transition in bilayered porous anodic alumina membranes*, ACS Appl. Mater. Interfaces **3**, 1925 (2011). 46

[Sar91] D. Sarid, *Scanning force microscopy (with applications to electric, magnetic, and atomic forces)*, Oxford Series on Optical Sciences, Oxford University Press, Oxford (1991). 58

[Sau02] G. Sauer, G. Brehm, S. Schneider, K. Nielsch, R. B. Wehrspohn, J. Choi, H. Hofmeister, and U. Gösele, *Highly ordered monocrystalline silver nanowire arrays*, J. Appl. Phys. **91**, 3243 (2002). 46

[Sch74] N. L. Schryer and L. R. Walker, *The motion of 180° domain walls in uniform dc magnetic fields*, J. Appl. Phys. **45**, 5406 (1974). 28

[Sch87] G. Schütz, W. Wagner, W. Wilhelm, P. Kienle, R. Zeller, R. Frahm, and G. Materlik, *Absorption of circularly polarized x rays in iron*, Phys. Rev. Lett. **58**, 737 (1987). 33

[Sch91] M. E. Schabes, *Micromagnetic theory of non-uniform magnetization processes in magnetic recording particles*, J. Magn. Magn. Mater. **95**, 249 (1991). 10, 79

[Sch97] C. Schneider, *Soft x-ray photoemission electron microscopy as an element-specific probe of magnetic microstructures*, J. Magn. Magn. Mater. **175**, 160 (1997). 62

[Sel01] D. J. Sellmyer, M. Zheng, and R. Skomski, *Magnetism of Fe, Co and Ni nanowires in self-assembled arrays*, J. Phys.: Condens. Matter **13**, R433 (2001). 73

[Shi99] K. Shigeto, T. Shinjo, and T. Ono, *Injection of a magnetic domain wall into a submicron magnetic wire*, Appl. Phys. Lett. **75**, 2815 (1999). 24, 54, 105, 113

[Sko06] R. Skomski and J. Zhou, *Advanced Magnetic Nanostructures - Chapter 3: Nanomagnetic models*, Springer, Berlin (2006). 20

[Slo96] J. Slonczewski, *Current-driven excitation of magnetic multilayers*, J. Magn. Magn. Mater. **159** (1996). 22

[Smi51] J. Smit, *Magnetoresistance of ferromagnetic metals and alloys at low temperatures*, Physica **17**, 612 (1951). 31

[Smi55] K. C. A. Smith and C. W. Oatley, *The scanning electron microscope and its fields of application*, Br. J. Appl. Phys. **6**, 391 (1955). 45

[Smy91] J. F. Smyth, S. Schultz, D. R. Fredkin, D. P. Kern, S. A. Rishton, H. Schmid, M. Cali, and T. R. Koehler, *Hysteresis in lithographic arrays of permalloy particles: Experiment and theory (invited)*, J. Appl. Phys. **69**(8), 5262 (1991). 15

[Spa11] N. A. Spaldin, *Magnetic materials: Fundamentals and applications, 2nd edition*, Cambridge University Press, Cambridge (2011). 5

[Stö93] J. Stöhr, Y. Wu, B. D. Hermsmeier, M. G. Samant, G. R. Harp, S. Koranda, D. Dunham, and B. P. Tonner, *Element-specific magnetic microscopy with circularly polarized x-rays*, Science **259**, 658 (1993). 62

[Stö98] J. Stöhr, H. A. Padmore, S. Anders, T. Stammler, and M. R. Scheinfein, *Principles of x-ray magnetic dichroism spectromicroscopy*, Surf. Rev. Lett. **5**, 1297 (1998). 33, 34, 62

[Stö06] J. Stöhr and H. C. Siegmann, *Magnetism - From fundamentals to nanoscale dynamics*, Springer, Berlin (2006). 5, 6, 11, 12, 17, 18, 22, 31

[Ste12] F.-U. Stein, L. Bocklage, T. Matsuyama, and G. Meier, *Generation and annihilation of domain walls in nanowires by localized fields*, Appl. Phys. Lett. **100**, 192403 (2012). 24

[Sto38] E. C. Stoner, *Collective electron ferromagnetism*, Proc. R. Soc. London **165**, 372 (1938). 6, 7

[Sto48] E. C. Stoner and E. P. Wohlfarth, *A mechanism of magnetic hysteresis in heterogeneous alloys*, Philos. Trans. R. Soc. London A **240**, 599 (1948). 18

[Sto66] T. G. Stockham, *High speed convolution and correlation*, Spring Joint Comput. Conf. Proc. **28**, 229 (1966). 38

[Tan08] C. Tannous and J. Gieraltowski, *The Stoner-Wohlfarth model of ferromagnetism*, Eur. J. Phys. **29**, 475 (2008). 18

[Tat97] G. Tatara and H. Fukuyama, *Resistivity due to a domain wall in ferromagnetic metal*, Phys. Rev. Lett. **78**, 3773 (1997). 32

[Tat04] G. Tatara and H. Kohno, *Theory of current-driven domain wall motion: Spin transfer versus momentum transfer*, Phys. Rev. Lett. **92**, 086601 (2004). 2

[Tay68] G. R. Taylor, A. Isin, and R. V. Coleman, *Resistivity of iron as a function of temperature and magnetization*, Phys. Rev. **165**, 621 (1968). 32

[Ter05] B. D. Terris and T. Thomson, *Nanofabricated and self-assembled magnetic structures as data storage media*, J. Phys. D: Appl. Phys. **38**, R199 (2005). 1

[Thi05] A. Thiaville, Y. Nakatani, J. Miltat, and Y. Suzuki, *Micromagnetic understanding of current-driven domain wall motion in patterned nanowires*, Europhys. Lett. **69**, 990 (2005). 22, 28

[Tho56] W. Thomson, *On the electro-dynamic qualities of metals: Effects of magnetization on the electric conductivity of nickel and of iron*, Proc. R. Soc. London **8**, pp. 546 (1856). 31

[Tho07] L. Thomas and S. S. P. Parkin, *Current induced domain-wall motion in magnetic nanowires*, Handbook of Magnetism and Advanced Magnetic Materials Vol. 2, John Wiley & Sons, Ltd (2007). 1, 129

[Tia08] F. Tian, J. Chen, J. Zhu, and D. Wei, *Magnetism of thin polycrystalline nickel nanowires*, J. Appl. Phys. **103**, 013901 (2008). 107

[Ton96] B. Tonner, D. Dunham, T. Droubay, J. Kikuma, and J. Denlinger, *X-ray photoemission electron microscopy: Magnetic circular dichroism imaging and other contrast mechanisms*, J. Electron Spectrosc. **78**, 13 (1996). 62

[Víc] Víctor Vega, private communication. 120

[Veg12] V. Vega, T. Böhnert, S. Martens, M. Waleczek, J. M. Montero Moreno, D. Görlitz, V. M. Prida, and K. Nielsch, *Tuning the magnetic anisotropy of Co-Ni nanowires: comparison between single nanowires and nanowire arrays in hard-anodic aluminum oxide membranes*, Nanotechnology **23**, 465709 (2012). 141, 153, 179

[Vir96] M. Viret, D. Vignoles, D. Cole, J. M. D. Coey, W. Allen, D. S. Daniel, and J. F. Gregg, *Spin scattering in ferromagnetic thin films*, Phys. Rev. B **53**, 8464 (1996). 32

[Vog10] A. Vogel, S. Wintz, J. Kimling, M. Bolte, T. Strache, M. Fritzsche, M.-Y. Im, P. Fischer, G. Meier, and J. Fassbender, *Domain-wall pinning and depinning at soft spots in magnetic nanowires*, IEEE Trans. Magn. **46**, 1708 (2010). 25, 110, 154, 162

[Weg98] J.-E. Wegrowe, S. Gilbert, D. Kelly, B. Doudin, and J.-P. Ansermet, *Anisotropic magnetoresistance as a probe of magnetization reversal in individual nono-sized nickel wires*, IEEE Trans. Magn. **34**, 903 (1998). 46, 73, 90

[Weg99] J.-E. Wegrowe, D. Kelly, A. Franck, S. E. Gilbert, and J.-P. Ansermet, *Magnetoresistance of ferromagnetic nanowires*, Phys. Rev. Lett. **82**, 3681 (1999). 32, 73, 84, 90

[Wer95] W. Wernsdorfer, K. Hasselbach, D. Mailly, B. Barbara, A. Benoit, L. Thomas, and G. Suran, *DC-SQUID magnetization measurements of single magnetic particles*, J. Magn. Magn. Mater. **145**, 33 (1995). 73, 78

[Wer96] W. Wernsdorfer, B. Doudin, D. Mailly, K. Hasselbach, A. Benoit, J. Meier, J.-P. Ansermet, and B. Barbara, *Nucleation of magnetization reversal in individual nanosized nickel wires*, Phys. Rev. Lett. **77**, 1873 (1996). 73, 75, 76, 77, 78, 107

[Whi93] T. M. Whitney, P. C. Searson, J. S. Jiang, and C. L. Chien, *Fabrication and magnetic properties of arrays of metallic nanowires*, Science **261**, 1316 (1993). 82

[Whi07] R. M. White, *Quantum theory of magnetism, 3rd edition*, Springer, Berlin (2007). 6

[Wik] *http://www.wikipedia.org/*. 80

[Wu94] C.-G. Wu and T. Bein, *Conducting polyaniline filaments in a mesoporous channel host*, Science **264**, 1757 (1994). 45

[Wut12] C. Wuth, P. Lendecke, and G. Meier, *Temperature-dependent dynamics of stochastic domain-wall depinning in nanowires*, J. Phys.: Condens. Matter **24**, 024207 (2012). 27

[Xia06] J. Xiao, A. Zangwill, and M. D. Stiles, *Spin-transfer torque for continuously variable magnetization*, Phys. Rev. B **73**, 054428 (2006). 2

[Yan10] M. Yan, A. Kákay, S. Gliga, and R. Hertel, *Beating the Walker limit with massless domain walls in cylindrical nanowires*, Phys. Rev. Lett. **104**, 057201 (2010). 2, 28

[Zaa86] J. Zaanen, C. Westra, and G. A. Sawatzky, *Determination of the electronic structure of transition-metal compounds: 2p x-ray photoemission spectroscopy of the nickel dihalides*, Phys. Rev. B **33**, 8060 (1986). 62

[Zah98] P. Zahn, J. Binder, I. Mertig, R. Zeller, and P. H. Dederichs, *Origin of giant magnetoresistance: Bulk or interface scattering*, Phys. Rev. Lett. **80**, 4309 (1998). 30

[Zha04] S. Zhang and Z. Li, *Roles of nonequilibrium conduction electrons on the magnetization dynamics of ferromagnets*, Phys. Rev. Lett. **93**, 127204 (2004). 22, 28

[Zhe00] M. Zheng, R. Skomski, Y. Liu, and D. J. Sellmyer, *Magnetic hysteresis of Ni nanowires*, J. Phys.: Condens. Matter **12**, L497 (200). 107

[Zim63] J. Ziman, *Electrons and phonons*, Clarendon, London (1963). 31

[Zou08] X. Zou and G. Xiao, *Electronic transport and magnetoresistance in polycrystalline and epitaxial* CrO_2 *nanowires*, Phys. Rev. B **77**, 054417 (2008). 107

Acknowledgment

Thanks!

- ... to Guido Meier and Ulrich Merkt for supporting me and my projects.
- ... to Manfred Albrecht, Kornelius Nielsch, and Guido Meier for reviewing.
- ... for financial support to the Helmholtz-Zentrum Berlin, the DOE, the Fachbereich Physik Universität Hamburg, as well as to the DFG for funding via GrK 1286 and SFB 668.
- ... for supplying nanowires and for interesting discussions to:
  Victor Vega Martinez, Kristina Pitzschel, Mohamed Shaker Salem, Shadyar Farhangfar, Yuen Tung Chong, Robert Zierold, Julien Bachmann, Kornelius Nielsch, and others from group K.
- ... for supporting PEEM measurements at BESSY II in Berlin to:
  Stephan Martens, Tim Böhnert, Michael Martens, Lars Bocklage, Peter Lendecke, Julia Herrero-Albillos, Logane Tati-Bismaths, and Florian Kronast.
- ... for supporting transmission x-ray microscopy at the XM-1 in Berkeley to:
  Andreas Vogel, Sebastian Wintz, Lars Bocklage, Jeannette Wulfhorst, Markus Bolte, Guido Meier, Mi-Young Im, and Peter Fischer.
- ... for Co/Pt multilayers and fruitful discussions to:
  André Kobs, Hans Peter Oepen and others from group G.
- ... for technical support to Michael Volkmann and the workshops at the IAP and at the Helmholtz-Zentrum Berlin.
- ... to all colleagues at the IAP, especially group N and the graduate class GrK1286.
- ... to Gesche Nahrwold and Jeannette Wulfhorst for maintaining the sputtering chamber, as well as to Sedat Dogan, Kim Martens, Christian Swoboda, and Nils Kuhlmann for deposition.
- ... to Lars Bocklage for providing the HF setup.
- ... to Sebastian Allende for interesting discussions.
- ... to Theo Gerhardt for micromagnetic simulations.

- ... to Neele Grenda for assistance with sample and data processing.
- ... to Tim Böhnert for the good collaboration, in particular the magnetoresistance measurements during his diploma thesis.
- ... to Stephan Martens for support in several fields, e.g. nanoMOKE.
- ... to Michael Martens for his instructions and support concerning micromagnetic simulations and many other things as well as for being such a good friend and god father.
- ... to all other people that enabled me to focus on my work through child care.
- ... to my parents, other family, and friends for their advice and support.
- ... to my husband Johannes Kimling for experimental support and all the other little and not so little things.
- ... to my daughters Sophie and Reija for being delightful distractions and for bringing me closer to wisdom.